

https://dspace.org/

Near-surface geophysical investigation of the Far Western Limb of the Bushveld Complex, South Africa

Nadan, Thiashen

2023-10

University of the Witwatersrand, Johannesburg

https://hdl.handle.net/10539/41761

Nadan, Thiashen. (2023). Near-surface geophysical investigation of the Far Western Limb of the Bushveld Complex, South Africa. [Master's dissertation, University of the Witwatersrand, Johannesburg]. WIReDSpace. https://hdl.handle.net/10539/41761

Downloaded from a DSpace repository. https://dspace.org/

Near-surface geophysical investigation of the Far Western Limb of the Bushveld Complex, South Africa

By

Thiashen Nadan

Supervisors:
Prof. Musa Manzi
Dr. Stephanie Scheiber-Enslin

A dissertation submitted to the Faculty of Science, University of the Witwatersrand, in fulfilment of the requirements for the degree of Master of Science

School of Geosciences
University of the Witwatersrand
Johannesburg, 2023

Declaration

I declare that this dissertation is my own, unaided work. It is being submitted for the Degree of Master of Science at the University of the Witwatersrand, Johannesburg. It has not been submitted before for any degree or examination at any other University.



Thiashen Nadan

27th day of October 2023, at The University of the Witwatersrand, Johannesburg.

Abstract

Platinum Group Elements (PGE's) and chromium are the main economic minerals that are found within the Bushveld Complex. In particular, the Far Western Limb of the Bushveld Complex has not been completely explored, as it is overlain by a thick Quaternary sedimentary deposit which masks the contacts between the different underlying lithological units. Chromium outcrops within the Far Western Limb have already been identified and mined. The study aims to assess the feasibility of extended geophysical surveys which will further identify the shallow subsurface lithologies and evaluate the future mining potential in the area. Results of this study show that the quaternary cover is approximately eighty meters thick, implying a shallow bedrock within the Far Western Limb. This was used to delineate a contact between the Transvaal Supergroup and the Rustenburg Layered Suite that was lost beneath the sedimentary cover. This shows that shallow geophysical investigations and drilling can prove useful in delineating the lithologies hosting the chromium ores.

Acknowledgements

I would like to thank my main supervisor Prof Musa Manzi for his technical advice and guidance throughout the course of the report. A special thanks to Dr Stephanie Scheiber-Enslin for her consistent support and guidance.

I would like to acknowledge the following companies for providing the necessary software facilities to complete this research: Seequent for providing (Geosoft) Oasis Montaj, Globe Claritas for their reflection seismic processing software, Tesseral technologies for their seismic modelling software, The Council for Geosciences for allowing the use of their equipment in their petrophysics lab, the Wits seismic research centre for providing the facilities to conduct the research.

I would like to acknowledge the National Research Foundation for the financial support received throughout my MSc.

Lastly and certainly not least, a special thanks to my family. Thank you for your love and support throughout my studies. Your encouragement and motivation have helped me every step of the way. To my life partner Kiyona Moodley, thank you for your continued patience and support. You have been my pillar of strength throughout this MSc.

Table of Contents

Declaration 1
Abstract i
Acknowledgements ii
Table of Contents iii
List of Figures viii
List of Tables xviii
1 Introduction 1
2 Geological background 6
2.1 Ventersdorp Supergroup 6
2.2 Transvaal Supergroup 7
2.2.1 Tectonics of the Pretoria Group 13
2.2.2 Correlation between the Transvaal Basin, the Southeast Bushveld Basin and the Kanye Basin 14
2.3 Waterberg Group 17
2.4 Bushveld Complex 18
2.4.1 Rooiberg Group 18
2.4.2 Rustenburg Layered Suite 19
2.5 Intrusions (Nietverdiend Complex) 23
2.5.1 Structural controls on the Nietverdiend Basin 24
2.6 Lithologies in the study area 26
3 Geophysical Theory 28
3.1 Seismic method 28
3.1.1 Wave velocities 30
3.1.2 Reflection 31
3.1.3 Refractions 31

3.1.4 Seismic surveys 32

3.2 Resistivity Method 33

3.2.1 Field measurements 33

3.2.2 Layering in the subsurface 36

3.2.3 Apparent resistivity 37

3.2.4 Arrays 39

3.3 Magnetics Method 41

3.3.1 The Earth's magnetic field 41

3.3.2 Types of magnetism 41

3.3.3 Magnetic surveys 42

3.3.4 Recording the Earth's magnetic field 43

4 Methods 45

4.1 Physical property measurements 45

4.1.1 Preparing the samples for laboratory measurements 47

4.1.2 Bulk magnetic susceptibility 47

4.1.3 Density 48

4.1.4 Ultrasonic velocity analysis 49

4.1.5 Resistivity 51

4.2 Geophysical surveys 53

4.2.1 Survey study areas 53

4.2.2 Seismic data acquisition 54

4.2.3 Resistivity data acquisition 56

4.2.4 Magnetic data acquisition 57

4.3 Seismic data processing 58

4.3.1 Reflection seismic processing for seismic line 1 58

4.3.2 Reflection seismic processing for seismic line 2 66

4.3.3 Reflection seismic processing for seismic line 3 74

4.4 Legacy seismic data acquisition 83

5 Results 85

5.1 Thin section analysis 85

5.1.1 Area 1 85

5.1.2 Area 2 86

5.2 Physical property data 89

5.2.1 Area 1 89

5.2.2 Area 2 89

5.3 Field seismic data 91

5.3.1 Seismic line 1 91

5.3.2 Seismic line 2 92

5.3.3 Seismic line 3 94

5.4 Field resistivity data 97

5.4.1 Resistivity line 1 97

5.4.2 Resistivity line 2 98

5.4.3 Resistivity line 3 100

5.5 Field magnetic data 102

5.6 Legacy 2D reflection seismic data 104

6 Interpretation 109

6.1 Petrographic analysis 109

6.2 Geophysical data analysis area 1 111

6.2.1 Seismic line 1 111

6.2.2 Modelling for seismic line 1 113

6.2.3 DC Resistivity line 1 118

6.2.4 Magnetics 123

6.3 Geophysical data analysis for area 2 127

6.3.1 Seismic line 2 128

6.3.2 Modelling for Seismic line 2 130

6.3.3 Seismic line 3 133

6.3.4 Modelling for seismic line 3 135

6.3.5 DC resistivity line 2 140

6.3.6 DC resistivity line 3 145

6.4 2D legacy seismic data analysis 149

6.4.1 P-wave refraction tomography analysis 149

6.4.2 Geological description of lithologies along the legacy seismic line 154

6.4.3 Integration with the regional magnetic data 155

7 Discussion 158

7.1 Geochemical vs physical property data 158

7.1.1 Area 1 158

7.1.2 Area 2 159

7.2 Comparison of the physical properties with existing datasets 161

7.3 Correlation between the physical property and the field geophysical data 163

7.3.1 Area 1 163

7.3.2 Area 2 166

7.4 Assessment of the regional legacy seismic data 170

7.5 Integration of the legacy seismic data with the local geophysical survey 171

8 Conclusion 174

8.1 Recommendations 176

9 References 177

List of Figures

Figure 1.1: The Kaapvaal Craton (green outline) with the outcrops from the Transvaal Supergroup (blue) basins (Griqualand West Basin, Transvaal Basin, Bushveld Basin, the Kanye Basin and the Rustenburg Layered Suite (red) from Bushveld Large Igneous Province marked. 1

Figure 1.2: Regional geological map with historic 2D reflection seismic lines RZ-254, 255 and 256 indicated, along with a local survey completed in 2018 (red box, sites marked 1 and 2)..... 3

Figure 1.3: Interpreted 2D reflection seismic data (RZ-254) tending North-South over the entire Far Western Limb (modified after Tinker et al., 2002) with lithologies responsible for the reflections indicated..... 4

Figure 2.1 Rustenburg Layered Suite stratigraphy, with the occurrence of the various chromitite layers marked (Kinnaird et al., 2002): Lower Group (LG), Middle Group (MG) and Upper Group (UG). ... 19

Figure 2.2: Geological map of the Far Western Limb showing the outcropping Rustenburg Layered Suite lithologies and Nietverdiend Basin and the existing boreholes that have been drilled (green dots) and existing chromite layers (red lines) (after Engelbrecht, 1985)..... 24

Figure 2.3: Local geological map with survey areas (blue blocks)..... 26

Figure 3.1: General seismic wave paths as they propagate through the subsurface (Burger et at., 1992, p. 36). 31

Figure 3.2: Plot showing the recorded arrival times of different seismic waves (Burger et al., 1992, p. 38). 32

Figure 3.3: Electrode configuration for a Wenner array. Current source (C1), current sink (C2) and potential electrodes (P1 and P2) with their specified spacings (A-D) and the density of the subsurface (p) (Burger et al., 1992, p. 278). 34

Figure 3.4: Current paths (black arrows) identified from the equipotential surfaces (Burger et al., 1992, p. 271). 34

Figure 3.5: Two current electrodes survey setup (Burger et al., 1992, p. 272).P1 is the measurement point,r1 and r2 are the radial distances from the electrodes to the measurement point with d the horizontal distance between the two current electordes..... 35

Figure 3.6: Current paths and equipotential surfaces determined for a current source and current sink. Not drawn to scale (Burger et al., 1992, p. 277). 35
Figure 3.7: The changes in the current paths caused by resistivity contrasts. a) Layers have equal resistivities (p1=p2), b) top layer has a lower resistivity (p1<p2), c) Bottom layer has a lower resistivity (p1>p2). Not drawn to scale (Burger et al., 1992, p. 286). 37
Figure 3.8: Electrode configuration for a Schlumberger array. Current source (C1), current sink (C2) and potential electrodes (P1 and P2) with their specified spacings (A-C) and the density of the subsurface (p) (Burger et al., 1992, p. 318). 39
Figure 3.9: Electrode configuration for a Dipole-Dipole array. Current source (C1), current sink (C2) and potential electrodes (P1 and P2) with their specified spacings (A) and the density of the subsurface (p) (Burger et al., 1992, p. 318). 40
Figure 3.10: Earth's magnetic field lines showing perpendicular field lines at the poles and, parallel field lines at the equator (Dentith and Mudge, 2015). 41
Figure 3.11: Amplitude response created by a magnetic survey that crosses a magnetic source located in South Africa. Not drawn to scale, (Dentith and Mudge, 2015, p. 95). 43
Figure 4.1: AGICO MFK1-FA used to measure the bulk magnetic susceptibility of the samples. Sample (red arrow) within the holder (blue arrow). 47
Figure 4.2: Measuring the weight in air and water of Sample S008A using the METTLER TOLEDO MS-DNY-54 density kit A) Sample on top of the universal basket measuring its weight in air, B) sample inside the universal basket measuring its weight in distilled water. 49
Figure 4.3: The Proceq Pundit PL-200 used to measure seismic velocities: A) Touchscreen, B) 150 kHz Transducers and calibration rod used to calibrate the transducer C) 250 kHz Transducers and calibration rods used to calibrate the transducer. 49
Figure 4.4: GDD SAMPLE CORE I.P TESTER used to measure the resistivity of the samples. This consists of the Archer field computer (blue arrow), the SCIP tester model TDLV (red arrow), the transmitting cable (purple arrow), the receiving cable (green arrows), and finally the computer connected to represent the data visually. 51
Figure 4.5: Rock samples wrapped with non-conductive tape to retain the moisture..... 51

Figure 4.6: Area 1 with the magnetic lines (red lines), the seismic line 1 (blue line), and the resistivity line 1 (yellow line) marked. A wire fence (black line) and outcrop (green line) are also marked (Google Earth Image)..... 53
Figure 4.7: Area 2 with the resistivity profiles (orange and dark green lines, resistivity lines 2 and 3 respectively) and the seismic lines (light green and purple lines, seismic lines 2 and 3 respectively). Pink block in the figure indicates where the rock samples were collected (Google Earth Image). 54
Figure 4.8: Survey layout along seismic profile 1 showing the weight drop (blue arrow), seismic station at the centre of the profile (red arrow), and the seismic profile with geophones (yellow arrow). 54
Figure 4.9: Geophones (red arrow), sledgehammer source (blue arrow), metal plate (yellow arrow), and the take-out cable (orange arrow)utilised during seismic data acquisition. 55
Figure 4.10: A) Electrodes fixed to the steel rods (blue arrow), B) Resistivity meter (ARES) (green arrow) with the multicore take-out electrode cable and the external battery (red arrow). 57
Figure 4.11: Caesium vapour walk magnetometer used for the magnetics data acquisition. 58
Figure 4.12: Raw shot gathers of seismic line 1 (Area 1) showing the far offset noise present in the data. 59
Figure 4.13: Frequency spectrum of the raw shot gathers for line 1 showing the dominant frequency at 65 Hz. 59
Figure 4.14: Interpreted raw shot gathers for line 1, D is the direct wave, R1 and R2 are the refracted waves, A is the air wave, G is the ground roll and R is the potential reflections in the data. 60
Figure 4.15: Pre-stack processing steps applied to seismic line 1: A) Raw shot gathers; B) Shot gathers after top mute and scaled window; C) Shot gather after predictive deconvolution; D Shot gathers after bandpass filtering; E) Shot gathers after f-k filtering and top mute; F) Shot gathers after automatic gain control and time cut; G) Velocity analysis of pre-stack shot gathers. D is the direct wave, R1 and R2 are the refracted waves, A is the air wave, G is the ground roll and R is the reflections in the data. ... 63
Figure 4.16: Stack and post-stack processing steps applied to seismic line 1: A) NMO correction and stacking; B) Bandpass frequency filtering; C) Static correction; D) Migration; E) Time-depth conversion; F) Final seismic section for seismic line 1. 65

Figure 4.17: Frequency spectrum of shot gathers for seismic line 1: Original frequency (red line); After top mute and scaled window processing (blue line). The frequency content after this processing is from 40 to 150 Hz, compared to the previous 30 to 200 Hz; After predictive deconvolution (orange line): the frequency that got enhanced is from 30 to 250 Hz; After bandpass filtering (green line): this filter preserved the frequencies from 50 to 250 Hz; After top mute and f-k filtering (purple line): the frequency that has been preserved is that from 60 to 250 Hz; After top mute and automatic gain control (pink line). Final frequency spectrum shows that the frequency for the weight drop is significantly enhanced and preserved (light blue line). 66
Figure 4.18: Raw shot gathers of seismic line 2 showing the noise in the far offsets. 66
Figure 4.19: Frequency spectrum of the raw shot gathers for line 2..... 67
Figure 4.20: Interpreted raw shot gathers for line 2, D is the direct wave, R1 and R2 are the refracted waves, A is the air wave, G is the ground roll and R is the potential reflections in the data. 68
Figure 4.21: Pre-stack processing steps applied to seismic line 2: A) Raw shot gathers; B) Shot gathers after top mute and scaled window; C) Shot gather after deconvolution; D) Shot gathers after bandpass filtering; E) Shot gathers after f-k filtering and top mute; F) Velocity analysis of pre-stack shot gathers after automatic gain control and time cut. D is the direct wave, R1 and R2 are the refracted waves, A is the air wave, G is the ground roll and R is the reflections in the data. 71
Figure 4.22: Post-stack processing steps applied to seismic line 2: A) NMO correction and stacking; B) Bandpass frequency filtering; C) Static correction; D) Migration; E) Time-depth conversion; F) Final seismic section for seismic line 2..... 73
Figure 4.23: Frequency spectrum of shot gathers for seismic line 2: Original (red line) and after top mute and scaled window processing (blue line). The frequency content after this processing is from 20 to 150 Hz, compared to the previous 25 to 200 Hz; After deconvolution (orange line): the frequency that got enhanced is from 30 to 200 Hz; After bandpass filtering (green line); this filter preserved the frequencies from 50 to 150 Hz; After top mute and f-k filtering (purple line): the frequency that has been preserved is that from 60 to 200 Hz; After top mute and automatic gain control (pink line): the frequency that is preserved is that from 50 to 150 Hz; Final frequency spectrum (light blue line) shows that the frequency for the weight drop is significantly enhanced and preserved. 74

Figure 4.24:Raw shot gathers of seismic line 3 showing the noise in the far offsets..... 74
Figure 4.25: Frequency spectrum of the raw shot gathers for line 3..... 75
Figure 4.26: Interpreted raw shot gathers for line 3, D is the direct wave, R1 and R2 are the refracted waves, A is the air wave, G is the ground roll and R is the potential reflections in the data. 76
Figure 4.27: Pre-stack processing steps applied to seismic line 2: A) Raw shot gathers; B) Shot gathers after top mute and scaled window; C) Shot gather after deconvolution; D) Shot gathers after bandpass filtering; E) Shot gathers after f-k filtering and top mute; F) Shot gathers after automatic gain control and time cut; G) Velocity analysis of pre-stack shot gathers. D is the direct wave, R1 and R2 are the refracted waves, A is the air wave, G is the ground roll and R is the reflections in the data..... 79
Figure 4.28: Post-stack processing steps applied to seismic line 3: A) NMO correction and stacking; B) Static correction; C) Migration; D) Time-depth conversion; E) Final seismic section for seismic line 3. 81
Figure 4.29: Frequency spectrum of shot gathers for seismic line 3:) Original (red line) and after top mute and scaled window processing (blue line). The frequency content after this processing is from 30 to 150 Hz, compared to the previous 25 to 200 Hz; After deconvolution (orange line): the frequency that got enhanced is from 30 to 200 Hz: After bandpass filtering (green line): this filter preserved the frequencies from 50 to 120 Hz; After top mute and f-k filtering (purple line): the frequency that has been preserved is that from 65 to 150 Hz; Automatic gain control and time cut (pink line): the frequency that is preserved is that from 50 to 100 Hz; G) Final frequency spectrum (light blue line) shows that the frequency for the hammer is significantly enhanced and preserved. 82
Figure 4.30: First break picks along the legacy seismic line RZ-254 indicated by the red arrows..... 84
Figure 5.1: Cross and plain polarised light of samples A) S001, B) S001 exhibiting fracture and C) S004. 86
Figure 5.2: Cross and plain polarised light of samples A) S002, B) S005, C) S003, D) S007. E) S006 shows plain, cross polarised and reflect light. 88
Figure 5.3: A) Ray tracing and B) seismic tomography of seismic line 1. 91
Figure 5.4: Seismic section for line 1. 92
Figure 5.5: Frequency spectrum for the seismic section of seismic line 1..... 92

Figure 5.6: A) Ray tracing and B) seismic tomography of seismic line 2. 93
Figure 5.7: Seismic section for line 2. 94
Figure 5.8: Frequency spectrum for the seismic section of seismic line 2..... 94
Figure 5.9: A) Ray tracing and B) seismic tomography of seismic line 3. 95
Figure 5.10: Seismic section for line 3. 96
Figure 5.11: Frequency spectrum for the seismic section of seismic line 3..... 96
Figure 5.12: Dipole-Dipole array representing the resistivity inversion section of resistivity line 1. .. 98
Figure 5.13: Schlumberger array representing the resistivity inversion section of resistivity line 1. ... 98
Figure 5.14: Dipole-Dipole array representing the resistivity inversion section of resistivity line 2. .. 99
Figure 5.15: Schlumberger array representing the resistivity inversion section of resistivity line 2. . 100
Figure 5.16: Schlumberger array representing the resistivity inversion section of resistivity line 3. . 100
Figure 5.17: Raw magnetic data for Area 1 with high magnetic anomaly (red arrow) and low magnetic anomalies (blue and purple arrows) indicated. 102
Figure 5.18: Diurnal data for day 1 (A) and day 2 (B) during the magnetic data acquisition (Geosoft map data)..... 103
Figure 5.19: A) Ray tracing and B) refraction seismic tomography for section A of seismic line RZ-254. 105
Figure 5.20: A) Ray tracing and B) refraction seismic tomography for section B of seismic line RZ-254. 106
Figure 5.21: A) Ray tracing and B) refraction seismic tomography for section C of seismic line RZ-254. 107
Figure 5.22: A) Ray tracing and B) refraction seismic tomography for section C of seismic line RZ-254. 108
Figure 6.1: Interpreted seismic tomography for seismic line 1 with the different weathering surfaces marked. 111
Figure 6.2: Interpreted seismic section for seismic line 1 with the different weathering surfaces marked, discontinuities (blue dashed lines) and indication of the potential fault (red arrow). 112

Figure 6.3: Integration between seismic section and tomography for seismic line 1with the different weathering surfaces marked and discontinuities (blue dashed lines). 113
Figure 6.4: Geological model for seismic line 1. 114
Figure 6.5: A) Synthetic shot gathers, B) Processed shot gathers for seismic line 1 showing reflections picked. Yellow arrow showing a velocity of 1000 m/s and the green arrow showing the velocity of 3000 m/s. 115
Figure 6.6: Synthetic seismogram using the minimum phase wavelet for area 1, OPX is the orthopyroxenite. 116
Figure 6.7: Synthetic seismogram using the Ricker wavelet for area 1, OPX is the orthopyroxenite. 117
Figure 6.8: Correlation of the reflections in the seismic section with the minimum phase (MP) and ricker (R) synthetic seismograms for area 1. 118
Figure 6.9: Interpreted resistivity section and marked weathering profiles for the Dipole-Dipole array from resistivity line 1. 119
Figure 6.10: Interpreted resistivity section and marked weathering profiles for the Schlumberger array from resistivity line 1. 120
Figure 6.11: Geological model for Resistivity line 1. 121
Figure 6.12: Dipole-Dipole array, comparison of: A) Forward model of the geological model for resistivity line 1; B) Inversion of the measured data 122
Figure 6.13: Schlumberger array, comparison of: A) Forward model of the geological model for resistivity line 1; B) Inversion of the measured data 123
Figure 6.14: Regional magnetic map over the Far Western Limb with the legacy vibroseis seismic lines (Black lines) and the two study areas (Red blocks). 124
Figure 6.15: Interpreted Total Magnetic Intensity Map. Regions with less weathered Orthopyroxenite possibly shown by the purple and blue arrows. The green surrounding these less weathered orthopyroxenites may indicate a higher degree of weathering of these orthopyroxenites. The high magnetic anomaly (red arrow) is one of the east-west trending dykes that can be found in the regional magnetic data. The pink line shows the location of the seismic and resistivity lines in the area with the black lines showing the lines where the magnetic data are collected. 125

Figure 6.16: Integrated geophysical data for Area 1. A) The surveys lines used to collect the data; B) The interpreted magnetic data; C) the general geological model for the area; D) Interpreted resistivity data for resistivity line 1 and E) Interpreted seismic..... 127
Figure 6.17: Interpreted seismic tomography for seismic line 2 with the different weathering surfaces marked. 128
Figure 6.18: Interpreted seismic section for seismic line 2, with the different weathered surfaces, discontinuities (blue dashed line) and agricultural digging (dashed pink lines) marked. 129
Figure 6.19: Integrated interpretations for seismic section and seismic tomography data along seismic line 2 with the weathering surfaces, discontinuities (blue dashed lines) and agricultural digging (dashed pink lines) marked..... 129
Figure 6.20: Model for seismic line 2. 131
Figure 6.21: A) Synthetic shot gathers, B) Processed shot gathers for seismic line 2 showing reflections picked. Yellow arrow showing a velocity of 600 m/s, the green arrow showing the velocity of 2000 m/s and the pink arrow showing a velocity of 3000 m/s. 132
Figure 6.22: Interpreted seismic tomography for seismic line 3 with the different weathering surfaces marked. 133
Figure 6.23: Interpreted seismic section for seismic line 3 with the different weathering surfaces, discontinuities (blue dashed lines) and agricultural digging (dashed pink line) marked. 134
Figure 6.24: Integrated seismic section with the seismic tomography for seismic line 3 with the different weathering surfaces, discontinuities (blue dashed lines) and agricultural digging (pink dashed line) marked. 134
Figure 6.25: Geological model for seismic line 3. 136
Figure 6.26: A) Synthetic shot gathers, B) Processed shot gathers for seismic line 3 showing reflections picked. Yellow arrow showing a velocity of 600 m/s, the green arrow showing the velocity of 1200 m/s and the pink arrow showing a velocity of 1600-2000 m/s. 137
Figure 6.27: Synthetic seismogram using the minimum phase wavelet for area 2, GN represents gabbronorite. 138

Figure 6.28: Synthetic seismogram using the Ricker wavelet for area 2, GN represents gabbronorite. 139
Figure 6.29: Correlation of the real and synthetic reflections in the seismic section with the with the minimum phase (MP) and ricker (R) synthetic seismograms for line 2 in area 2..... 139
Figure 6.30: Correlation of the real and synthetic reflections in the seismic section with the with the minimum phase (MP) and ricker (R) synthetic seismograms for line 3 in area 2..... 140
Figure 6.31: Interpreted resistivity section with marked weathering profiles, agricultural digging (black circle) and possible fractures (pink dashed line) for the Dipole-Dipole array from resistivity line 2. 141
Figure 6.32: Interpreted resistivity section with marked weathering profiles for the Schlumberger array from resistivity line 2. 142
Figure 6.33: Geological model for resistivity line 2. 143
Figure 6.34: Dipole-Dipole section, comparison of A) Forward model of the geological model for resistivity line 2, B) Inversion of the measured data..... 144
Figure 6.35: Schlumberger section, comparison of A) Forward model of the geological model for resistivity line 2, B) Inversion of the measured data..... 145
Figure 6.36: Interpreted resistivity section with marked weathering profiles and agricultural digging (black circle) for the Schlumberger array from resistivity line 3. 145
Figure 6.37: Geological model for resistivity line 3. 147
Figure 6.38: Schlumberger section, comparison of: A) Forward model of the geological model for resistivity line 3; B) Inversion of the measured data..... 147
Figure 6.39: Integrated geophysical data for area 2. A) The surveys lines used to collect the data; B) Seismic models for the east-west trending line; C) Seismic models for the North-South trending line; D) Seismic data for the east-west trending seismic line; E) Seismic data for the North-South trending seismic line; F) Resistivity data for the east-west trending seismic line and G) Resistivity data for the North-South trending seismic line. 148
figure 6.40: Elevation profile for legacy seismic line RZ-254. Mountainous peaks represented by the red arrows and paleo river valleys represented by the blue arrows. 149

Figure 6.41: A) Geological map with legacy seismic line RZ-254 interpolated (with 5 km intervals marked in red and green), high magnetic anomalies from the regional magnetic data represented (black line); B) the interpreted legacy P-wave refraction seismic tomography of the RZ-254 seismic line. The blue boxes indicate the area where the Transvaal Supergroup lithologies occur. Similarly, the red box indicates with the Bushveld Complex lithologies occur. The blue arrows indicate where the paleo river valleys were found on the Google Earth imagery and the descriptions of the lithologies contacts are as in Table 6.18. 153

Figure 6.42: Regional magnetic data over the Far Western Limb with seismic line RZ254 running over it (5 km intervals marked in yellow and blue). Black stars represent the survey areas 1 and 2, blue and white circles represent boreholes in the area. Green and yellow arrow indicating Silverton Formation and Goudini Complex, respectively. 156

Figure 6.43: Interpreted seismic tomography for legacy seismic data showing the position of the Goudini Complex (yellow arrow) and the potential contact between the Transvaal Supergroup and the Rustenburg layered Suite in the North (red arrow). 157

Figure 7.1: Velocity vs Density plot of the local data and the previous data collected from the Bushveld Complex (Shithigona et al., 2018). Trendlines show the relationship between the 2 dataset that have been plotted. 162

Figure 7.2: Survey lines for area 1 with the potential fault (orange dashed line) offsetting the outcrops to the North (green outline). 164

Figure 7.3: Integration of the seismic and resistivity profile for area 1 showing the weathered profiles within the subsurface and discontinuities (blue dashed lines). 165

Figure 7.4: Interpreted magnetic data collected in area 1. Less weathered Orthopyroxenite (purple and blue arrows) with a higher degree of weathering (green surrounding these less weathered orthopyroxenites). East-west trending dyke (red arrow) identified in the regional magnetic data. Position of the seismic and resistivity lines (pink line) in the area and the magnetic survey lines (black lines). 166

Figure 7.5: Integration of seismic line 2 with Schlumberger array for resistivity line 2 showing the weathered profiles within the subsurface, discontinuities (blue dashed lines) and the agricultural digging (pink dashed lines). 167
Figure 7.6: Integration of seismic line 2 with dipole-dipole array for resistivity line 2 showing the weathered profiles within the subsurface, discontinuities (blue dashed lines) and the agricultural digging (pink dashed lines). 168
Figure 7.7: Integration of seismic line 3 with Schlumberger array for resistivity line 3 showing the weathered profiles within the subsurface, discontinuities (blue dashed lines) and the agricultural digging (pink dashed lines). 169
Figure 7.8: A) Geological map showing the lithologies present along the legacy seismic line; B) Interpreted refraction tomography of the legacy seismic line and C) 2D reflection seismic data tending North-South over the entire Far Western Limb (modified after Tinker et al., 2002) with the interpreted seismic data and the suggested lithologies responsible for the reflections present. 170
Figure 7.9: Regional geological map with the study areas and the potential contact between the Lower Zone of the Bushveld Complex and the Rayton Formation of the Transvaal Supergroup (Red dashed line). 173

List of Tables

Table 2.1: Stratigraphic column of the prominent lithologies in the Far Western Limb (Armstrong et al., 1991, Eriksson et al., 1993, Maré et al., 2006, Bumby et al., 2012, Fanchi et al., 2019 and all references within). The Ventersdorp Supergroup through to the Magaliesburg Formation of the Transvaal Supergroup was mapped in the study area using 2D vibroseis surveys (Tinker et al., 2002) while most of the remaining lithological units were mapped in outcrop (Engelbrecht, 1985, 1990; Eriksson et al., 1993, 1995 and 1998). 10
Table 2.2: Lithologies of the Rustenburg Layered Suite and Rooiberg Group in the Far Western Limb, with their thicknesses based on borehole data. References within table. 21
Table 2.3: Physical property data for lithologies from the Rustenburg Layered Suite obtained from the Council for Geosciences South Africa. 27

Table 4.1: Outline of Physical Properties measured for samples collected in the study area. This includes what physical property will be measured, how the data will be collected, the number of measurements that are required, and how the data will be analysed. 46
Table 4.2: Data acquisition parameters for seismic lines. 56
Table 4.3: Resistivity data acquisition parameters for the resistivity lines. 57
Table 4.4: Pre-stack processing steps that are taken to produce the seismic section for seismic line 1. 61
Table 4.5: Stack and post-stack processing steps for seismic line 1. 64
Table 4.6: Pre-stack processing steps that are taken to produce the seismic section for seismic line 2. 69
Table 4.7: Stacking and post-stack processing of seismic line 2. 72
Table 4.8: Pre-stack processing steps that are taken to produce the seismic section for seismic line 3. 77
Table 4.9: Stacking and post-stack processing of seismic line 3. 80
Table 4.10: Acquisition parameters for the legacy 6 second TWT 2D seismic reflection data. 83
Table 5.1: Descriptions of geological samples for Area 1. 85
Table 5.2: Descriptions of geological samples for Area 2. 87
Table 5.3: Physical property measurements for sample S001 and S004. 89
Table 5.4: Physical property measurements for samples S002, S003, S005, S006, S007 and S008. 89
Table 5.5: Inversion results for resistivity line 1 97
Table 5.6: Inversion results for resistivity line 2 98
Table 5.7: Inversion results for resistivity line 3 100
Table 6.1: Sample Classifications. 109
Table 6.2: Velocity ranges and correlating thicknesses for the interpreted subsurface weathering profiles on seismic line 1 113
Table 6.3: Geological model for seismic line 1. 114
Table 6.4: Geological section for reflectivity modelling in area 1 116

Table 6.5: Resistivity ranges and correlating thicknesses for the interpreted subsurface weathering profiles of the Dipole-Dipole array (resistivity line 1).....119
Table 6.6: Resistivity ranges and correlating thicknesses for the interpreted subsurface weathering profiles of the Schlumberger array (resistivity line 1). 120
Table 6.7: Physical characteristics of lithological units in area 1 with their thicknesses found from interpreted data.....120
Table 6.8: Velocity ranges and correlating thicknesses for the interpreted subsurface weathering profiles on seismic line 2.....130
Table 6.9: Geological model for seismic line 2. 130
Table 6.10: Velocity ranges and correlating thicknesses for the interpreted subsurface weathering profiles on seismic line 3. 135
Table 6.11: Geological model for seismic line 3. 135
Table 6.12: Geological section for reflectivity modelling in area 2.....138
Table 6.13: Resistivity ranges and correlating thicknesses for the interpreted subsurface weathering profiles of the Dipole-Dipole array (resistivity line 2).....141
Table 6.14: Resistivity ranges and correlating thicknesses for the interpreted subsurface weathering profiles of the Schlumberger array (resistivity line 2). 142
Table 6.15: Physical characteristics of lithological units in area 2 with their thicknesses found from interpreted data.....142
Table 6.16: Resistivity ranges and correlating thicknesses for the interpreted subsurface weathering profiles of the Schlumberger array (resistivity line 3). 146
Table 6.17: Physical characteristics of lithological units in area 2 with their thicknesses found from interpreted data.....146
Table 6.18: Lithological correlation with the P-wave seismic velocities found in the legacy seismic data together with their horizontal thickness and location along the legacy seismic tomography. 152
Table 7.1: Average seismic anisotropy together with the modal abundance for each geological sample collected. 158

1 Introduction

There have been extensive studies conducted on the Bushveld Complex, due to it being the largest known layered igneous intrusion and its large contribution to the world's platinum and chromium reserves (Crowson., 2001). Almost half of the world's platinum, chromium, vanadium and some other refractory minerals come directly from the Bushveld Complex.

The Bushveld Large Igneous Province (ca. 2.05 Ga), commonly known as the Bushveld Complex, intruded into the Transvaal Supergroup in the form of sills (Lendhardt et al., 2012; Basson, 2019). It consists of the Northern Limb, Southern Limb, Eastern Limb, Western Limb, and Far Western Limb. The contacts between the Bushveld Complex and the Transvaal Supergroup can only be seen within the Transvaal and Kanye Basins (Figure 1.1).

The Palaeo-proterozoic Transvaal Supergroup (ca. 2.65 – 2.06 Ga) was deposited onto the Kaapvaal Craton (ca. 3.7–2.6 Ga) while it was experiencing thermal subsidence to a point where it was below sea level (Clendenin et al., 1989, 1991; Eriksson et al., 1993, 1995; Bumby et al., 2012). This subsidence allowed for a shallow continental shelf to be established upon which the Transvaal Supergroup was deposited. This volcano-sedimentary sequence is still preserved in the Transvaal (South Africa), Kanye (Botswana), Bushveld (Southeast Botswana), and the Griqualand West (South Africa) structural basins (Figure 1.1) (Eriksson et al., 1995; Eriksson and Altermann, 1998).

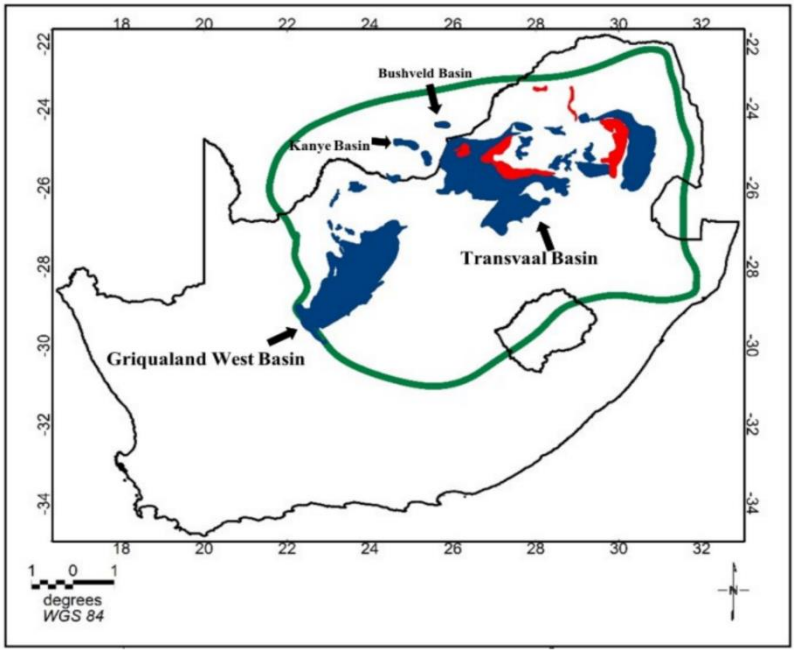

Figure 1.1: The Kaapvaal Craton (green outline) with the outcrops from the Transvaal Supergroup (blue) basins (Griqualand West Basin, Transvaal Basin, Bushveld Basin, the Kanye Basin and the Rustenburg Layered Suite (red) from Bushveld Large Igneous Province marked.

The economic minerals (platinum, chromium and vanadium) are found in several economic layers in the complex, as the Bushveld Complex sills intruded possible magma mixing allowing for the cyclic layering within the Rustenburg Layered Suite (Irvine, 1977; Kinnaird et al., 2002). Chromium ore from the Bushveld Complex occurs in the Rustenburg Layered Suite. The chromium ore occurring within the chromitite layers is enriched up to 30%. This is significantly higher than the average basaltic lava which has 0.002% chromium. The formation of the chromitite layers has not yet been identified although several ideas do exist (Kinnaird et al., 2002). The thickest chromitite layers are approximately 1 m thick and originate within the Critical Zone of the Rustenburg Layered Suite.

The Far Western Limb does not draw much attention due to the absence of the major lithologies hosting the platinum and chromium reserves, although it does host the chromitite layers from the Lower Critical Zone within its centre (Engelbrecht., 1985; 1990). These chromitite layers are currently being mined where they outcrop. To fully understand the extent of the chromitite in the Far Western Limb, the subsurface lithologies and structures need to be identified. This presents a challenge due to the vast Quaternary cover over the centre of the Far Western Limb, which limits the mappable contacts between the lithological units and structures within the basin (Figure 1.2). Geophysical methods have proven useful to describe the subsurface geology of the Far Western Limb, including three 2D 6-second TWT vibroseis surveys that were previously acquired in the area (RZ-254, RZ-255, RZ-256) (Tinker et al., 2002) (Figure 1.2). An existing outcrop along the rim of the Far Western Limb was used to correlate lithologies to the reflections seen on the seismic sections.

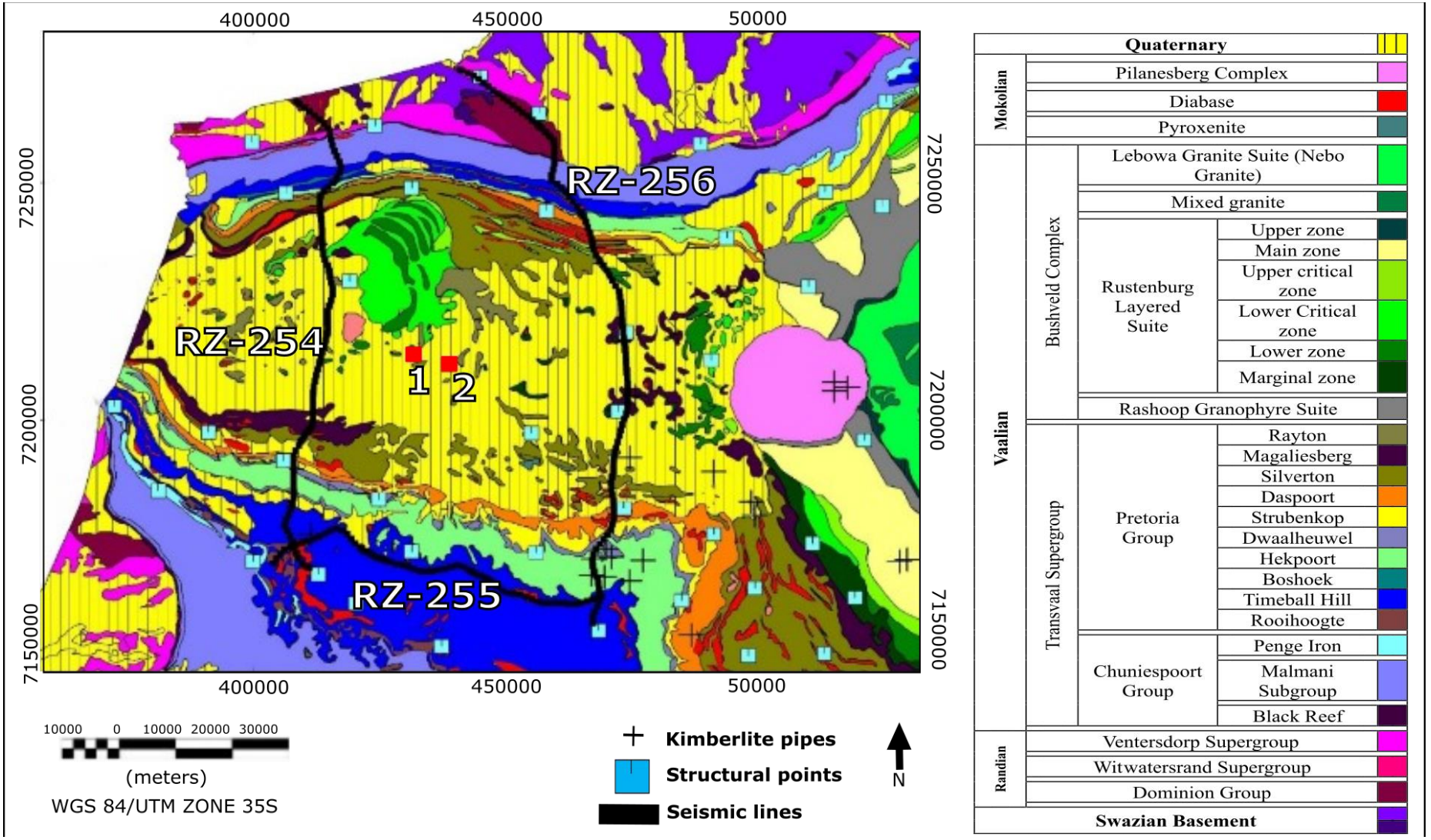

Figure 1.2: Regional geological map with historic 2D reflection seismic lines RZ-254, 255 and 256 indicated, along with a local survey completed in 2018 (red box, sites marked 1 and 2).

The legacy 2D reflection seismic survey identified lithologies from the Pretoria Group, the Chuniespoort Group, and the Black Reef Formation of the Transvaal Supergroup unconformably overlying the Ventersdorp Supergroup (Figure 1.3). Within this seismic section, there is an unknown lithological unit (Figure 1.3, green arrow) that was not identified. This is due to the lack of outcropping lithologies along the centre of the seismic profile and due to the study mainly focusing on the deeper structures.

One of these legacy seismic lines (RZ-254) was reprocessed and reinterpreted in this study. Reprocessing only focused on the P-wave first break refraction tomography, which provided a clearer understanding of the shallow subsurface (first 100 m) lithologies within the centre of the Far Western Limb and the unclassified lithological unit from the seismic section (Figure 1.3, green arrow).

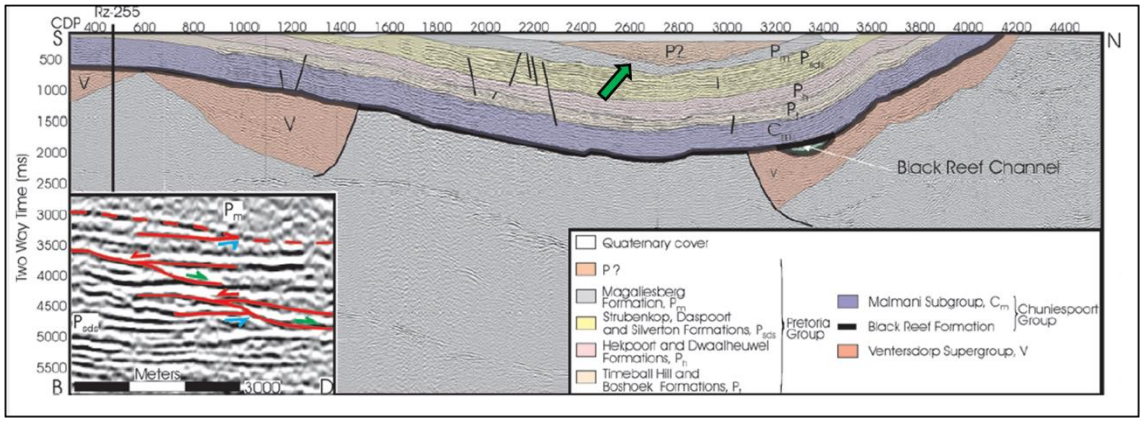

Figure 1.3: Interpreted 2D reflection seismic data (RZ-254) tending North-South over the entire Far Western Limb (modified after Tinker et al., 2002) with lithologies responsible for the reflections indicated.

Near-surface geophysical studies (see Figure 1.2 red boxes for location) were conducted in 2018 to identify the shallow subsurface in the Far Western Limb and map the potential extension of the chromitite from its outcrop towards the North of the study areas. The survey consisted of reflection seismic, DC resistivity, and magnetic methods.

Previously, only the refraction tomography was processed from the seismic data collected. During the course of this study, I will better characterise the subsurface in the Far Western Limb by processing the new reflection seismic data (first 15 m) and interpreting the first break refraction tomography of the legacy 2D reflection seismic data to provide a clearer understanding of the shallow subsurface (first 100 m) lithologies within the centre of the Far Western Limb and the unclassified lithological unit at the centre of the seismic section.

Field samples were collected and analysed. The physical properties of these samples were measured which allowed for seismic, DC resistivity, and magnetic data modelling. Geochemical analysis of the

samples was used to identify which lithological unit these samples belong to, and provided more information on the shallow subsurface.

Integrating and interpreting these datasets will allow for the tectonic history of the Far Western Limb to be further understood by identifying the undefined lithology seen on the seismic section, as well as help with the planning of future exploration within the Far Western Limb. In addition, it may possibly present the lateral extent of the Bushveld Complex metamorphism.

The understanding of the geological history of the Bushveld Complex is vital, as it potentially allows for similar layered intrusions to be identified worldwide in particular, the outlier intrusions like the Far Western Limb that were previously thought to not contain any economic minerals.

2 Geological background

A few attempts have been made to constrain the geological history of the Far Western Limb, although none have proven to be successful due to the inability to map and classify all the lithologies present in the area due to Quaternary cover. The lack of deep boreholes in the centre of the Limb that penetrate the Transvaal Supergroup also makes it difficult to map and classify any of the shallow lithologies. The existing boreholes that are within the Far Western Limb were sunk close to the outcropping Lower Critical Zone and only revealed the thickness of the Rustenburg Layered Suite lithologies (Engelbrecht, 1985).

In this study, we investigate historic seismic data and two more recent geophysical surveys. These surveys pass over lithologies of the Transvaal Supergroup, as well as the Bushveld Complex. The legacy reflection seismic line images the Ventersdorp Supergroup contact with the Transvaal Supergroup at a maximum of 2 s depth. A dyke also mapped by magnetic data is thought to be part of the Marico Hypabyssal Suite (Engelbrecht, 1990).

2.1 Ventersdorp Supergroup

This volcanic sequence is suspected to be extruded unconformably over the Archean granite basement (Tinker et al., 2002) within the Far Western Limb. It consists of predominantly three Groups: a basal unit known as the Klipriviersberg Group which is a komatiitic flood basalt (2787 ± 2 Ma) (Stamsnijder, 2017: U-Pb ID-TIMS, baddeleyite from the dolerite) unconformably overlain by the Platberg Group (2709 ± 4 Ma) (Armstrong et al., 1991: ion probe U-Pb Zircon) which is a volcano-sedimentary sequence. This is then overlain by the Pniel Group which is also a volcano-sedimentary sequence (Bumby et al., 2012).

2.2 Transvaal Supergroup

As mentioned, the Transvaal Supergroup is still preserved in the Transvaal (South Africa), Kanye (Botswana), Bushveld (Southeast Botswana), and the Griqualand West structural basins (Eriksson et al., 1995; Eriksson and Altermann, 1998). All of these basins have similar deposits, although the nomenclature for lithologies within each basin is not standardized. As this study focuses on the Far Western Limb of the Bushveld Complex, the Transvaal Supergroup basins that are of interest since they are all in the proximity of the study area, are the Kanye, Bushveld and the Transvaal basins.

The basins that were created by the subsidence formed a shallow sea where the river channels drained into and formed the beach and shallow water marine deposits (conglomerates, sandstones and mudrocks) (Henry et al., 1990; Eriksson et al., 1995; Eriksson et al., 2006) of the Black Reef Formation (2642 ± 3 Ma) (Walraven and Martini, 1995: U-Pb zircon crystallization). This formation is considered to be the erosional contact with the underlying Ventersdorp Supergroup (Henry et al., 1990; Clendenin et al., 1991; Eriksson et al., 1993; Eriksson et al., 2006).

The uppermost mudrocks of the Black Reef Formation are followed unconformably by the Malmani dolomites (2550 ± 3 Ma) (Barton et al., 1994: U-Pb zircon dating) of the Chunniespoort Group which represents a transgressive flat carbonate platform (Clendenin, 1989; Eriksson et al., 2006). The Penge Iron Formation (2431 ± 31 Ma) (Walraven and Martini., 1995: Pb-Pb zircon evaporation) consisting of the banded ironstones known for their asbestos and manganese ores (Beukes, 1983; Eriksson et al., 1995; Fanchi et al., 2019) conformably overlies the Malmani dolomites and represents the chemical sedimentation that occurred within the Transvaal basin. This also marks the end of the Chuniespoort Group which has a minimum age of 2432 ± 31 Ma (Trendall et al., 1990). It was unconformably followed by the Duitchsland Formation (2424 ± 24 Ma) (Rasmussen et al., 2013: SHRIMP U-Pb zircon) which consists of the carbonaceous mudrocks, limestones, dolomites, conglomerates, diamictites and lavas which are said to represent the final regressive stage of the Transvaal epeiric sea (Clendenin et al., 1988; Fanchi et al., 2019).

The last group of the Transvaal Supergroup is the Pretoria Group (maximum age of 2316 ± 7 Ma (Hannah et al., 2004). The group lies unconformably over the Duitchsland Formation which formed due to the uplift of the basin that allowed for the deposition of a shallow marine to muddy tidal flats facies. The Pretoria Group consists of sandstones, mudstones, conglomerates, diamictites and carbonate beds (Eriksson et al., 1991). Amongst these sediments, there are also various volcanic sequences which can be found within the stratigraphy (Eriksson et al., 1995).

The Pretoria Group begins with the Rooihoogte Formation consisting of quartzites, mudrocks and breccia. This is conformably overlain by the Timeball Hill Formation (2250 ± 14/15 Ma) (Mapeo et al., 2006: SHRIMP U-Pb detrital zircon) which consists of mudrocks and quartzites. It contains the Lower Mudrocks which host the lavas of the Bushy Bend Lava Member (2316 ± 7Ma) (Hannah et al., 2004: Re/Os dating of Bushy Bend Lavas) overlain by the Quartzite Member and finally the Upper Mudrocks which contain some diamictite. The Boshoek Formation conformably overlies the Timeball Hill Formation and consists of conglomerates and sandstones. Each of these formations represents a period of glacial activity as they all contain diamictites (Beukes, 1987; Eriksson et al., 1991, 1993). The diamictites are characterized by a periglacial basin deposit starting with a shallow basin followed by a deep basin (which includes turbidites and some fluvial deltaic deposits) and finally a periglacial till and fan deposit respectively (Eriksson et al., 1995).

The volcanics consist of the Bushy Bend Lavas and conformably overlying the Boshoek Formation is the Hekpoort Formation consisting of basaltic andesites (2224 ± 21 Ma) (Walraven and Martini, 1995: whole-rock Rb/Sr isochron).

The Hekpoort andesites have localized pyroclastic sedimentary interbeds that underlie the alluvial fans and deltaic sequence (sandstones and conglomerates) of the Dwaalheuwel Formation, which also contains some diamictite.

The Strubenkop mudrocks overlie the Dwaalheuwel Formation and represent a shallower basin deposit with minor tuffs. Overlying this is the Daspoort sandstones (2236 ± 13 Ma) (Mapeo et al., 2006: SHRIMP U-Pb detrital zircon) which represent both a distal fan deposit together with a braided fluvial deposit (Eriksson et al., 1991, 1993; Eriksson et al., 1995).

The Daspoort Formation is conformably overlain by the Silverton Formation which consists of predominantly shales and has an overlying sandstone lens as a cap. It hosts the Boven Shale Member, the Machadodorp Volcanic Member, the Lydenburg Shale Member and some carbonates all conformably overlying one another. This formation is characterized by a deep basin suspension deposit with some pyroclastics within the basin (Eriksson et al., 1991, 1993; Eriksson et al., 1995).

The overlying Magaliesburg Formation sandstones (2193 ± 20 Ma) (Mapeo et al., 2006: SHRIMP U-Pb detrital zircon) which have intermittent lenses of mudrock represent an environment where there may be a fluvial reworking of the shoreline deposits.

The final formation of the Pretoria Group is the Rayton Formation which consists of the Vermont, Lakenvlei, Nederhorst, Steenkampsberg and Houtenbek Members. This formation is represented

potentially by a fan, fan-delta, delta and lacustrine sedimentation as it has interbedded mudrocks and tuffaceous mudstones within a sandstone deposit which recrystallized into a quartzite (Eriksson et al., 1991, 1993; Eriksson et al., 1995; Eriksson et al., 1998).

Lithologies from the Transvaal Supergroup which are present in the Far Western Limb with their correlating deposits from respective sub-basins are listed in Table 2.1. Many of the lithological units have been exposed to different geological and structural events that affect the thickness of the lithology that outcrops at the surface.

Table 2.1: Stratigraphic column of the prominent lithologies in the Far Western Limb (Armstrong et al., 1991, Eriksson et al., 1993, Maré et al., 2006, Bumby et al., 2012, Fanchi et al., 2019 and all references within). The Ventersdorp Supergroup through to the Magaliesburg Formation of the Transvaal Supergroup was mapped in the study area using 2D vibroseis surveys (Tinker et al., 2002) while most of the remaining lithological units were mapped in outcrop (Engelbrecht, 1985, 1990; Eriksson et al., 1993, 1995 and 1998).

Units from the South African Stratigraphy						**Western Transvaal Basin thickness (meters) Formation**	**Corresponding deposits in the Kanye Basin**	**Corresponding unit in the Southeast Botswana Bushveld Basin deposit**		
Supergroup	**Group**		**Formation**	**Members**	**Lithology**		**Formation**	**Formation**	**Group**	**Supergroup**
	Waterberg (ca. ~2.06 Ga to ~1.88 Ga)	Kransberg Sub-Group	Vaalwater Formation		Feldspathic	475		Palla Sandstone	Waterberg 2.06 Ga	
			Claremont Formation		Quartzarenites	125				
			Sandriviersberg Formation		Quartzitic sublitharenites	1250				
		Matlabas Sub-Group	Aasvoëlkop Formation		Quartzitic sublitharenites	300-600		Ramatlobake Siltstone Formation Masma Sandstone Formation Lokgalo Siltstone Formation		
			Skilpadkop Formation		Arkosic litharenites	450-600 >130	Mannyelanong Hills Formation	Mannyelanong Hills Formation ~1973 Ma (U-Pb baddeleyite crystallization)		
		Nylstroom Sub-Group	Alma Formation		Arenaceous beds	<3000		Upper Woodlands Formation?	Otse	
			Wilge River Formation /Swaershoek		Quartzites and shales	50-1000 Otse Group ≤ 1400				
Bushveld Large Igneous Province intrusion										
	Rooiberg Fragment		Smelterskop and Leeuwpoort		Sandstones and Shales	?				
Transvaal Supergroup (ca. 2.65 – 2.06 Ga)	Pretoria Group (maximum age of 2316 ± 7	Upper Pretoria Group	Rayton Formation (Central Transvaal basin)	Houtenbek	Mudrocks Sandstones Limestones Tuffaceous mudrocks	<200	Lomugau	Lower Woodlands Formation	Segwagwa	Upper Transvaal Supergroup
				Steenkampsberg	Sandstones					

	Ma (Hannah et al., 2004)			Nederhorst	Sandstones Mudrocks and tuffaceous mudrocks					
				Lakenvlei	Sandstones					
				Vermont	Mudrocks and tuffaceous mudrocks					
			Magaliesberg (2193 ± 20 Ma) (Mapeo et al., 2006: SHRIMP U-Pb detrital zircon)		Sandstones and mudrocks	150 - 430	Monotoholwane	Sengoma Quartzite		
			Silverton		Carbonate	117 - 167	Gatsepane	Sengoma Argillite		
					Lydenburg Shale Member	500 - 1328				
					Machadodorp Volcanic Member Mudrocks	Absent				
					Boven Shale Member	0 - 5				
			Daspoort (2236 ± 13 Ma) (Mapeo et al., 2006: SHRIMP U-Pb detrital zircon)		Sandstone	65 - 120	Mogapinyana Gatsepane	Ditlhojana Quartzite		
			Strubenkop		Mudrocks	50 - 360	Tsatsu			
			Dwaalheuwel or Droogedal		Diamictite and conglomerate Sandstone	Droogedal 15 -70				Lower Transvaal Supergroup
			Hekpoort 2224 ± 21 Ma (whole-rock Rb–Sr isochron; Walraven and Martini, 1995)		Basaltic andesite	190 - -890		Ditlhojana Volcanic		
			Boshoek		Diamictite, conglomerate and sandstone	35 - -70	Tlaameng	Ditlhojana Shale		
			Timeball Hill (2250 ± 14/15 Ma) (Mapeo et al., 2006: SHRIMP U-Pb detrital zircon)		Upper Mudrocks Diamictite Klapperkop	Upper Mudrocks: 200 – 430 which thickness to the west No diamictite	Ditlhojana			
					Quartzite Member	Quartzite: 90 - 620 which thickens westwards		Sckwane Quartzite		

				Lower Mudrocks Bushy Bend Lava Member Lavas (2316 ± 7Ma) (Hannah et al., 2004: Re/Os dating of Bushy Bend Lavas)	Lower Mudrocks: 160 - 460 which thickens westwards		Lephale		
			Rooihoogte	Polo Ground Quartzite Member Mudrock Bevets Conglomerate (Breccia)	Quartzite: 0 – 1 Mudrocks: 0 – 150 Breccia: 17 – 232				
	Duitchsland (2424 ± 24 Ma) (Rassmussen et al., 2013: SHRIMP U-Pb zircon)			Muddy flats deposit	1100	Kgwakgwe chert breccia	Ramotswa Masoke	Taupone Dolomite Group	
	Chuniespoort (2642 ± 3 Ma) (Bumby et al., 2012) (2432 ± 31 Ma) (Trendall et al., 1990)	Penge Iron (2431 ± 31 Ma) (Walraven., 1995: Pb-Pb zircon evaporation)		Iron formation	Up to 640	Masoke			
		Malmani Subgroup	Malmani Dolomites (2550 ± 3 Ma) (Barton et al., 1994: U-Pb zircon dating)	Dolomites	1200	Ramonnedi	Magobane Maholoba Ramotswa dolomites		
	Black Reef Formation correlated to the Vryburg Formation dated at ~2642 ± 3 Ma. (Mapeo et al., 2006)				200	Black Reef Formation	Black Reef Formation		
Ventersdorp	Pniel			Volcano-sedimentary	400 clastic Bothaville Formation 750m Allanridge flood basalts	Mogobane (2774 ± 10 Ma)	Kanye Volcanics	Lobatse	
	Platberg (2709 ± 4 Ma) (Armstrong et al., 1991: ion probe U-Pb Zircon)			Volcano-sedimentary	≤1800	Nnywane			
	Klipriversberg (2787 ± 2 Ma)			Komatiitic basalt	1500 to 2000	Kanye Volcanic			
Archean Granite Basement									

2.2.1 Tectonics of the Pretoria Group

The tectonic setting for the deposition of the Pretoria Group is associated potentially with a fault-controlled graben basin (Eriksson et al., 1991, 1993; Schreiber et al., 1992) and is said to be related to the Thabazimbi-Murchison lineament, the Barbeton greenstone belt and the Sugarbush fault system (Eriksson et al., 1995). This was followed by various glacial deposits within a shallow closed basin deposit (Eriksson et al., 1991, 1993). The Silverton Formation may represent a time where there was the subsidence of the basin related to the fault-controlled basin deposit. After this, there was tectonic instability which created many sub-basins within the Western and Eastern Transvaal basins which were potentially separated by the intruding Rooiberg magmas of the Bushveld Complex (Engelbrecht., 1988; Schreiber et al., 1992; Eriksson et al., 1993).

Of these different sub-basin deposits, there is the Woodlands Formation in the west, the Vermont to Houtenbek formation in the east, and the Rayton Formation North-Northeast of Pretoria which are suggested to all correlate to one another (Eriksson et al., 1998).

A clear understanding of these deposits is required as they are the main units which will be investigated in this study in particular, the Rayton Formation of the South African stratigraphy and the Woodlands Formation of the Botswana stratigraphy, since these two deposits border one another within the Far Western Limb. The Rayton Formation (Pretoria Group of the Transvaal Supergroup) is an example of a lithological unit that may be present in the Far Western Limb and imaged on seismic data with very little outcrop. Understanding the corresponding lithological units between the different sub-basins can allow for easier identification of the shallow subsurface lithologies in the study area.

2.2.2 Correlation between the Transvaal Basin, the Southeast Bushveld Basin and the Kanye Basin

Within the Far Western Limb, the Magaliesburg Quartzites border the entire Far Western Limb through the Dwarsberg, the Enzelsburg and the Tshwenyane mountains (Engelbrecht, 1985; Eriksson et al., 1998). These quartzites are predominantly striking in an east-west direction creating mountains that dip in various directions within the basin. The southern rim of these mountains dips 9° towards the north while the northern rims dip 25° towards the south (Engelbrecht, 1985). This correlates with the Sengoma Quartzites on the eastern side of Botswana which is suggested to be structurally more complex. The Far Western Limb is characterized by a flat topography with traces of quartzites, shales, mafic sills, dykes and some marble-calcsilicate lithologies (Engelbrecht, 1990; Eriksson et al., 1998). The quartzites and shales have not been accurately allocated to any of the formations within the Pretoria Group and are suggested to potentially represent the lithologies from the Woodlands Formation of the Southeast Bushveld Basin and the Vermont, the Lakenveli and the Nederhorst formations of the Transvaal Basin (Hartzer, 1995).

Another opinion is that these quartzites and shales belong to the Magaliesberg and Silverton formation where there could have been thrust faulting in the area (Engelbrecht, 1985) which would have caused the repetition within the sequence, although currently there is no major evidence from geophysical and satellite data to prove this (Eriksson et al., 1998). Therefore, the lithologies have been attributed to folding that was followed by the later deposits of the Woodlands Formation (post-Magaliesberg deposits).

Within the flat-lying area in the Far Western Limb there are metamorphosed carbonate rocks known as the Kalkfontein outcrop (Eriksson et al., 1998). This is suggested to be a localized metamorphosed unit within the Woodlands Formation (Rayton Formation).

Woodlands Formation

The Woodlands Formation is suggested to be the unknown lithological unit in the shallow subsurface of the legacy seismic line RZ-254 (Tinker et al., 2002). Eriksson (1998) compared the Woodlands Formation in Lobatse Botswana (Southeast Botswana) to the deposits within the Pretoria Group. It showed that the sandstones were of similar composition although the siltstones varied completely. The thickness of this formation was suggested at first to be up to 1200 m thick (Key, 1983). Due to the tectonic behaviour in the area, gravity sliding may have contributed to the thickness being overestimated, leaving the formation of having a potential maximum thickness of 120 m (Eriksson et al., 1998).

The Woodlands Formation itself is split up into the Lower Woodlands Formation which incorporates a sequence of alternating mudrocks and fine-grained quartzites. The Upper Woodlands Formation is uniquely found in Botswana within the Otse-Ramotswa Basin. It unconformably (Key 1983; Crokett, 1969; Eriksson et al., 1998) overlies the siltstones of the Lower Woodlands Formation and comprises a chaotic slump deposit with shale, quartzitic pebbles and boulder hosted within an andesitic matrix with 300 m of it being penetrated by the various boreholes drilled in the area (Eriksson et al., 1995; 1998).

The current understanding is that the Lower Woodlands Formation correlates to the Upper Pretoria Group (Rayton Formation), with the Upper Woodlands Formation being a younger deposit formed within an unstable tectonic environment and approximately Bushveld-Rooiberg in age (ca. 2050 Ma) (Eriksson et al., 1998). Specifically, the Upper Woodlands Formation is part of the Otse Basin deposits together with the Otse Group from the Southeast Botswana Bushveld Basin (Carney et al., 1994).

In the Otse Basin these deposits are suggested to be older than the Waterberg Group (ca. ~2.06 Ga to ~1.88 Ga) as they are unconformably overlain by the red arkosic and lithic sandstones of the Mannyelanong Hill Formation (correlated with the Skilpad Formation in the Transvaal Basin) which also forms part of the Waterberg Group of the Botswana stratigraphy.

Tectonic History

The lithologies within the Far Western Limb of the Bushveld Complex have been subjected to a three-fold deformation history (Hartzer, 1995). Here, a 200 m lithological sequence potentially from the Woodlands Formation has a similar dip and strike as the underlying Magaliesberg Formation (Engelbrecht, 1985; Hartzer, 1995; Eriksson et al., 1998).

The lithological units (Pretoria Group, inferred Woodlands Formation and the Marico Hypabyssal Suite) in the area were first subjected to northeast-southwest shortening (F1), followed by a northwest-southeast shortening (F2) and finally a tightening in the F1 direction (F3). Together with this, there is an apparent strike-slip faulting which has extended into Eastern Botswana where the same deformation occurred and resulted in the creation of a dome structure (Hartzer 1995).

The Mannyleanong Fault which is similar to the F3 faulting, exposes rocks from the younger Waterberg Group. By unpopular opinion, given that Waterberg Group rocks cannot be found on either side of the fault, the fault post-dates the Waterberg Group. Eriksson et al., 1998 suggests through the restoration of the Mannyleanong Fault, a sequence of interference folding can be observed.

The Upper Woodlands Formation correlates well with the rocks deposited post-Mannyleanong faulting. This again suggests that the Lower Woodlands Formation belongs to the uppermost Pretoria Group (Rayton Formation) while the Upper Woodlands Formation belonged to a post-Pretoria Group depositional episode (Eriksson et al., 1998). All of these lithologies, together with the Marico Hypabyssal Suite, were deformed during the pre-Bushveld basin-inversion except for the Nietverdiend lobe (both described later). The Nietverdiend lobe includes the Rustenburg Layered Suite in the Far Western Limb, together with various other igneous intrusions.

In conclusion, the Lower Woodlands forms part of the Upper Pretoria Group with the Upper Woodlands being a younger deposit formed within an unstable tectonic environment and approximately Bushveld-Rooiberg in age (ca. 2050 Ma) suggesting an unconformable contact (Key 1983; Crokett, 1969; Eriksson et al., 1998).

Since the geology of the Far Western Limb is so complex; it may be possible that the equivalent of the Upper Woodlands Formation (potentially Waterberg Group lithologies) may be present in the Far Western Limb basin. This may be possible, as the shallow subsurface lithologies of the Far Western Limb have not been identified as yet due to the thick Quaternary deposit. The current geological maps show very little evidence of the Rayton Formation, and this is possibly due to the thick Quaternary cover as only minor outcrops of it can be found throughout the basin.

2.3 Waterberg Group

At the base of the Waterberg Group is the Nylstroom Sub-Group. This unconformably overlies the Bushveld Complex that intruded within and between the Transvaal Supergroup. The Nylstroom Sub-Group contains the Wilger River Formation overlain conformably by the Alma Formation. The Wilge Formation consists of arenaceous beds which originate primarily from the Transvaal Supergroup (Visser and de Villiers, 1961, Jansen, 1982). It is also distributed similarly to the Rooiberg Group (Bilijon, 1976, Coertze et al., 1977). The Swaershoek Formation is similar to the Wilge Formation and is suggested to have been deposited immediately after with the Bushveld Granites (Maré et al., 2006).

Conformably overlying the Nylstroom Sub-Group is the Matlabas Sub-Group which conformably contains the Skilpadkop Formation and the Aasvoëlkop Formation which consist predominantly of arkosic litharenites and quartzitic sublitharenites respectively. The Mannyelanong Formation which is an equivalent deposit in Botswana is dated at ~1973 Ma (Hanson et al., 2004: U-Pb baddeleyite crystallization). The final unit within the Waterberg Group is the Kransberg Sub-Group which contains the Sandrivierberg Formation, conformably overlain by the Claremont Formation and finally conformably by the Vaalwater Formation. They consist of quartzitic sublitharenites, quartzarenites and feldspathic arenites, respectively.

2.4 Bushveld Complex

The Bushveld Complex formed as a result of three magmatic events. The first was the lavas of the Rooiberg Group (2061 ± 2 Ma) (Walraven, 1997: Pb evaporation age of zircons in rhyolites), consisting of two events: a basaltic lava followed by a thicker flow of rhyolites. This then led to the intrusion of the Rustenburg Layered Suite (2058.9 ± 0.8 Ma) (Buick et al., 2001: U-Pb isotope from newly grown titanite found in calc-silicate xenoliths); 2054.4 ± 1.3 Ma (Scoates and Friedman, 2008: U-Pb zircon from Merensky Reef) which is known for its economic minerals.

2.4.1 Rooiberg Group

This group forms the uppermost portion of the Transvaal Supergroup and is considered to be the most silicic volcanic unit in the Transvaal Supergroup, but it is linked to and precedes the Bushveld Complex (Eriksson et al., 1995; Lendhardt et al, 2012). It consists of the Dullstroom, Damwal, Kwaggasnek, and Schrikkloof formations all conformably overlying one another respectively (Schweitzer et al., 1995). The Dullstroom Formation consists of the basaltic lavas dated 2037 ± 92 Ma (Harmer and Farrow, 1995: $^{87}Sr/^{86}Sr$), the Damwal Formation consists of the dacite (2071 ± 94 Ma) (Buchanan et al., 2004: Rb-Sr dating), the Kwaggasnek Formation estimated to be 2057.3 ± 3.8 Ma (Harmer and Armstrong, 2000) contains some shales, and the Schrikkloof Formation contains the rhyolites which are also present in each one of the formations.

The Rooiberg Group consists of a few kilometres of a lava flow which is said to have erupted from fissural volcanism containing minor units of shales, tuff and greywacke (Twist and French, 1983; Twist, 1985; Harmer and Farrow, 1995; Schweitzer et al., 1995; Hatton and Schweitzer, 1995). These minor units represent the breaks in the volcanism that was taking place in the area where fluvial deposits took over (Eriksson et al., 1995; Schweitzer et al., 1995; Lendhardt et al., 2012). The thickest deposit can be found at Loskop Dam and is suggested to have formed due to a structural feature of Transvaal age (Eriksson et al., 1996).

These lavas were unconformably deposited onto the younger Transvaal Supergroup during its last stages, which had been exposed to various forms of compressive deformation. The physical contact between the Transvaal basin and The Rooiberg Group can be found to the South Eastern parts of the Rooiberg Group where the Dullstroom Formation lies unconformably over the Pretoria Group (Cheney and Twist, 1991). The remaining formations all overlie the Bushveld Complex as they were detached during the intrusion of the Bushveld Complex. In some cases, the Kwaggasnek and the Schrikkloof formations disconformably overlie the Smelterskop Formation of the Transvaal Supergroup (Richards, 1987) and is referred to as the Rooiberg Fragment (Lendhardt et al., 2012). Similarly, there is the

Crocodile Fragment in the west and there are Dennilton, Makeckaan, and Marble Hall fragments in the east (Hartzer, 1995). The Rustenburg Layered Suite thermally altered the Kwaggasnek and the Schrikkloof formations as it intruded while the Lebowa Granite Suite had altered the entire Pretoria Group (Buchanan, 2006).

2.4.2 Rustenburg Layered Suite

The Rustenburg Layered Suite is subdivided into five zones: The Marginal Zone (MZ), the Lower Zone (LZ), the Critical Zone (CZ), the Main Zone (MZ) and the Upper Zone (UZ). The Critical Zone is further subdivided into an Upper Critical Zone (UCZ) and Lower Critical Zone (LCZ) and hosts the various chromitite layers (Figure 2.1).

<table>
<tr><th colspan="2">Zone</th><th>Distribution of chromite layers</th></tr>
<tr><td colspan="2">Upper Zone</td><td></td></tr>
<tr><td colspan="2">Main Zone</td><td></td></tr>
<tr><td rowspan="2">Critical Zone</td><td>Upper Critical Zone</td><td>Merensky Reef

UG 2
UG 1

MG 4

MG 3</td></tr>
<tr><td>Lower Critical Zone</td><td>MG 2

MG 1

LG 7

LG 6

LG 5

LG 4

LG 3
LG 2

LG 1</td></tr>
<tr><td colspan="2">Lower Zone</td><td></td></tr>
<tr><td colspan="2">Marginal Zone</td><td></td></tr>
</table>

Figure 2.1 Rustenburg Layered Suite stratigraphy, with the occurrence of the various chromitite layers marked (Kinnaird et al., 2002): Lower Group (LG), Middle Group (MG) and Upper Group (UG).

The Marginal Zone mainly consists of norites but does contain gabbronorites and meta-sediments, which are considered to be the xenoliths from the basal contact with the Transvaal Supergroup (Kinnaird et al., 2002, Kinnaird, 2005, Kruger, 2005; Basson, 2019). The Marginal zone has a varying thickness (400 m to 800 m) and is hardly present in the stratigraphy. The Lower Zone lithologies found in the limbs of the Bushveld Complex reach their maximum thickness at 1600 m. It can mostly be found in the Eastern, Western and Northern Limbs where the thickness is controlled by local/regional structures, and predominantly consists of, harzburgites, pyroxenites and dunites (Viljoen and Schűrmann, 1998).

The Critical Zone mainly occurs in the Western and Eastern Limbs and is subdivided into a Lower Critical Zone and an Upper Critical Zone (Basson, 2019). The Lower Critical Zone is composed of ultramafic rocks which consist of orthopyroxenite, harzburgite and chromite layers while the Upper Critical Zone contains chromite layers, feldspathic orthopyroxenite, norite and anorthosite/troctolite layers (Kinnaird et al., 2002, Kruger, 2005; Basson, 2019).

The Main Zone is more than 4000 m thick and consists of gabbronorites, anorthosites and pyroxenites which also contains identification markers such as the Pyroxenite Marker and the Mottled Anorthosite (Upper and Main) (Eales and Cawthorn, 1996; Cawthorn and McKenna, 2006; Kinnaird, 2005). The Upper Zone is made up of anorthosite, troctolite and ferrogabbro to diorite which is around 2000 m in thickness, also containing up to 25 magnetite layers (Kinnaird et al., 2002).

Given the vast extent of the Quaternary cover over the Far Western Limb, various geological mapping expeditions have taken place and have revealed that within (and surrounding) the Far Western Limb there are traces of the chromitites from the Lower Critical zone (LG 1 to LG 5) which is surrounded by various lithologies from the Pretoria Group (Engelbrecht, 1985, 1990). Table 2.2 summarises the lithologies from the Bushveld Complex which are present in the Far Western Limb.

Table 2.2: Lithologies of the Rustenburg Layered Suite and Rooiberg Group in the Far Western Limb, with their thicknesses based on borehole data. References within table.

Intrusive body	Subdivision	Member		Lithologies	Far Western Limb lithologies thickness (meters)
Bushveld Complex (~2.06 Ga)	Rustenburg Layered Suite (2058.9 ± 0.8 Ma) (Buick et al., 2001;U-Pb isotope from newly grown titanite found in calc-silicate xenoliths) (2054.4 ± 1.3 Ma) (Scoates and Friedmann, 2008: U-Pb zircon from Merensky Reef)	Upper Zone		-	~ 2000
		Main Zone		Gabbronorites, Anorthosites and Pyroxenites	≥ 4000
		Critical Zone	Lower Critical Zone	orthopyroxenites, Harzburgites and Chromite layers	~ 800 300 (Engelbrecht, 1985) >200 (Engelbrecht, 1990)
		Lower Zone		Dunites, Harzburgites and Pyroxenites containing Chromite layers	<1600 1030 (Engelbrecht, 1985) 1050 (Engelbrecht, 1990)
		Marginal Zone		Norites, Gabbronorites and Metasediments	<800 m, mostly around 400 814 (Engelbrecht, 1985) 790 (Engelbrecht, 1990)
	Rooiberg	Schrikkloof		Rhyolite	200 -3000
		Kwaggasnek 2057.3 ± 3.8 Ma (Harmer and Armstrong, 2000)		Rhyolite and Shale	500 – 2500
		Damwal (2071 ± 94/65 Ma) (Buchanan et al., 2004: Rb-Sr dating)		Rhyolite and Dacite	1000 – 2500
		Dullstroom (2037 ± 92 Ma) (Harmer and Farrow, 1995: $^{87}Sr/^{86}Sr$)		Basalt to Rhyolite	< 2000

The boreholes used to obtain the thicknesses of the Critical, Marginal and Lower Zones were all drilled into outcrop and ceased once it reached the Transvaal Sequence. The outcrop of the Rustenburg Layered Suite in the Far Western Limb together with various other igneous intrusions is also known as the Nietverdiend Complex. Together with its immediate surroundings - it is also known as the Nietverdiend basin.

Mineralisations and occurrence of the chromitite

The chromitite mineralisation is found in layers within the Critical zones of the Rustenburg Layered Suite. These chromitite layers are accompanied with significant levels of Platinum Grade Elements (PGE) but have variable thicknesses and are discontinuous. The mineralisation has been subdivided into 3 categories, namely: the Lower Group (LG), the Middle Group (MG) and the Upper Group (UG) (Figure 2.1) (Viljoen and Schűrmann, 1998).

The LG consists of 7 layers found within the feldspathic pyroxenite which are labelled with increasing order from the base upwards. The LG 6 layer is the thickest of these layers and is commonly known as

the Steelpoort seam (Schűrmann et al., 1998). The LG 1 to LG 4 layers are distinguishable from the higher chromitites as they are associated with olivine (Hatton and von Gruenewaldt, 1989). The MG mainly consists of four layers depending on the thickness of each layer. It is found at the contact between the Lower Critical Zone and the Upper Critical Zone with the MG 1 and MG 2 found below the first anorthosite while the MG 3 and MG 4 are found above. Within the UG, there are two layers namely the UG 1 and UG 2, with the UG 3 and UG 3a found only in the eastern portion of the Bushveld Complex (Kinnaird et al., 2002). The UG2 is one of the largest deposits of PGEs in the world (Kinnaird, 2005).

The Rustenburg Layered Suite includes two cyclic units within the Critical Zone which are the Merensky Reef and the Bastard unit (Kruger and Marsh, 1982). The Merensky Reef is considered to be the contact between the Critical Zone and the Main Zone and is characterized by the greatest concentration of chromitite and consists of thin persistent layers (Kinnaird et al., 2002).

The lower layers of chromitite tend to have the highest concentrations of Cr_2O_3, with the LG 6 having 46 – 47%, the MG chromitites 44 – 46% and the UG 43% Cr_2O_3 (Viljoen and Schűrmann, 1998). Together with the chromitite enrichment, there is also PGE and minor sulphide enrichments within the lower chromitite layers. The ratio between the sum of the Pt, Rh, and Pd to the sum of Ru, Ir and Os is used to identify the different chromitite mineralisations. The chromitites hosted within the harzburgite-pyroxenite cycles generally have a Cr:Fe ratios greater than 1.8 although have a low PGE content (< 1000 ppb) with the ratio less than 1. The chromitites which are hosted within the pyroxenites, norite and anorthosite cycles have Cr:Fe ratio less than 1.5 and have a higher PGE content (5000 ppb) (Scoon and Teigler, 1994).

2.5 Intrusions (Nietverdiend Complex)

The Nietverdiend Complex is within the Far Western Limb and can be considered as one of the unique intrusions within the area. Along with the Rustenburg Layered Suite, it consists of the Marico Hypabyssal Suite (MHS) which is said to have intruded before the Rustenburg Layered Suite (Engelbrecht, 1990). The maximum thickness of the overburden at the time of intrusion was constrained between 1 and 2 km (Roberts, 1970) suggesting the presence of only the Transvaal sedimentary sequence. The MHS consists of sills and dykes which intruded the Transvaal sediments and is overlain by warped lithologies of the Rustenburg Layered Suite (Engelbrecht, 1988). The sills have a tholeiitic basaltic composition which is chemically noritic and amphibolitic, accompanied by similar dykes (Engelbrecht, 1990).

The noritic sills can be found in close proximity to the contact between the Rustenburg Layered Suite and the Transvaal Supergroup. As the noritic sills become hydrated, they are suggested to form the amphibolitic sills (Engelbrecht, 1990). The MHS is chemically and mineralogically distinct from the Marginal Zone of the Bushveld Complex (Engelbrecht, 1990) with the noritic sills shown to potentially belong to the parental magma of the Rustenburg Layered Suite (Engelbrecht, 1990).

2.5.1 Structural controls on the Nietverdiend Basin

The Nietverdiend basin, which includes the Nietverdiend Complex, is structurally controlled by the Dwarsberg mountain range to the north, together with the Enzelsburg and Tshwenyane mountains to the south.

The basin itself is surrounded by the metasedimentary floor rocks suggested to originate from the Pretoria Group. To the east of this basin, there is an anticlinal flexure along which the Marico River flows. The surrounding rocks here are argillites from the Silverton Formation and are capped by the quartzites from the Magaliesberg Formation (Engelbrecht, 1990). This cap forms the hill at Zelikatskjop and Piet Zyn Kop (Figure 2.2). These two hills are suggested to be part of a ridge within the basin. Since there is no evidence for stress or deformation, gravity sliding (Crokett, 1971) is accepted as the mechanism for the location of these lithologies and origin of the fold structures.

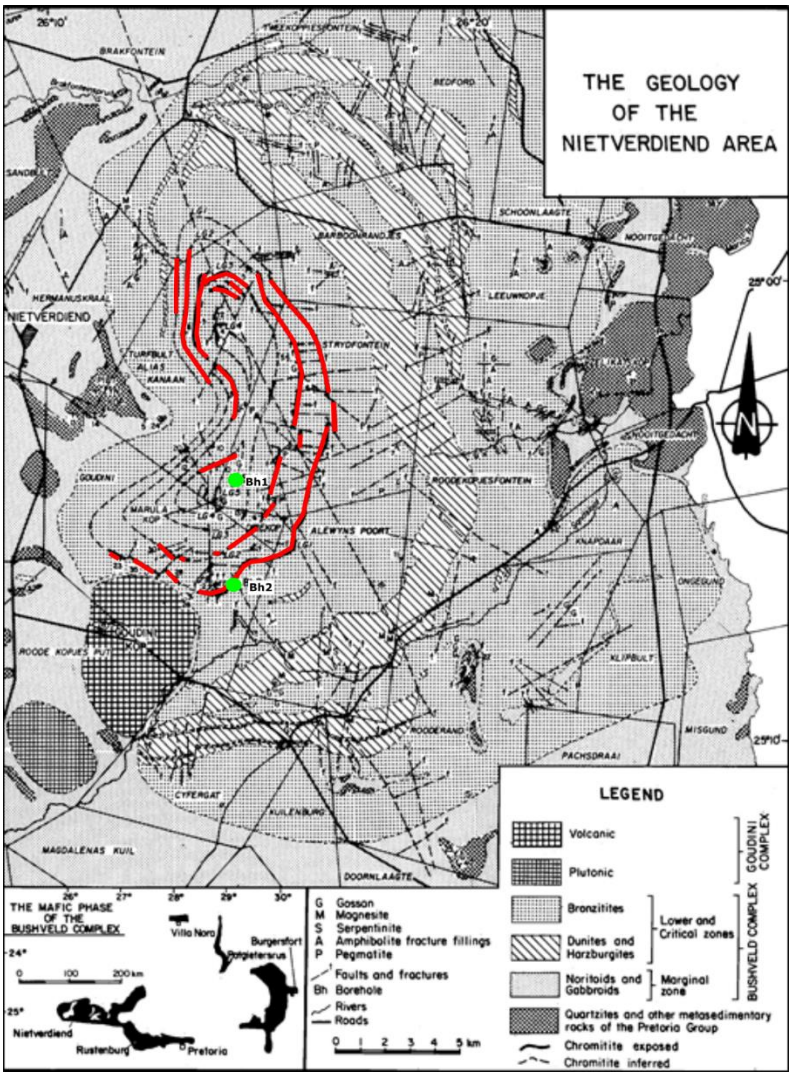

Figure 2.2: Geological map of the Far Western Limb showing the outcropping Rustenburg Layered Suite lithologies and Nietverdiend Basin and the existing boreholes that have been drilled (green dots) and existing chromite layers (red lines) (after Engelbrecht, 1985).

When the magma intruded into the basin, fold structures influenced the existing north-south trend of the mafic magma deposits and the hills were responsible for the embayments which formed. Minor folding and multiple east-west trending faults are found to offset the chromite layers (Figure 2.2) with some fracture filling attributes to the self-metamorphism of the mafic minerals during cooling (Engelbrecht, 1990).

The Goudini Complex together with the Roode Kopjies Put are the two late (post-Bushveld Complex) intrusive suites within the basin. The Roode Kopjies Put is a plutonic plug, while the Goudini Complex is said to be a volcanic intrusion that is the deepest portion and centre of the magmas for the Bushveld Complex (Biesheuvel, 1970).

2.6 Lithologies in the study area

From borehole data within the study area (Figure 2.2, Bh1 and Bh2), there are estimates of lithology thicknesses. The existing rocks of the Rustenburg Layered Suite within the study area consist of 790 m of cyclic olivine melanonorites, gabbroic melanonorites and norites from the Marginal Zone, which have a general increase in anorthite content upwards (Engelbrecht, 1985; 1990). The underlying rocks here consist of the pyroxene-cordierite-biotite hornfelses from the Transvaal Supergroup.

There are 1050 m of cyclic dunites, harzburgites and bronzitites from the Lower Zone which overlie the Marginal Zone in the basin. At the contact there is a 50 m transitional zone which consists of olivine norite, norites and bronzitites followed by a cyclic unit of harzburgite dunite and bronzitite which are extremely weathered at the outcrops such that there are traces of opal, serpentine, magnesite and haematite (Engelbrecht, 1985; 1990).

There are 300 m of cyclic chromitites, dunites, harzburgites and bronzitites from the Critical Zone that are also found within the basin (Engelbracht, 1985). The remaining lithologies in the study area are suggested to belong to the Transvaal Supergroup. A local geological map (Figure 2.3) with the study areas shows the different lithological units that have been mapped in close vicinity to the study areas.

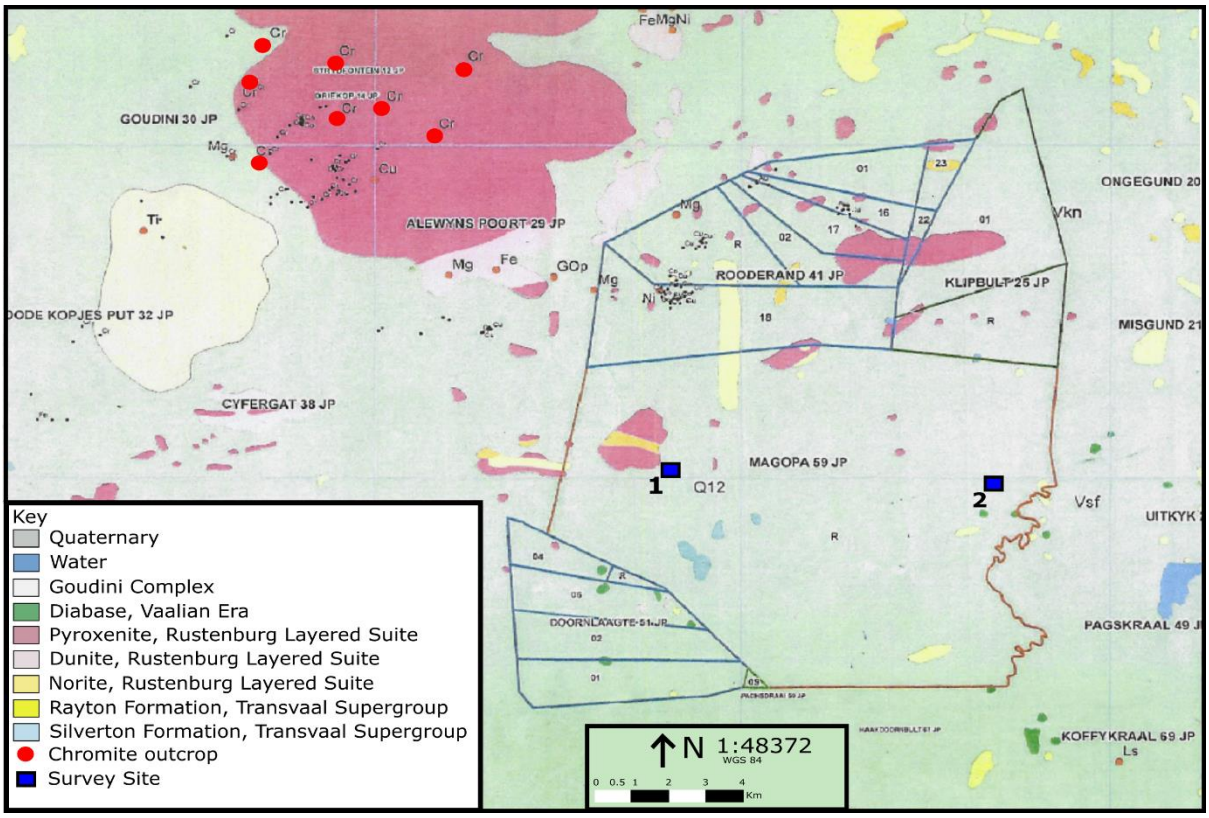

Figure 2.3: Local geological map with survey areas (blue blocks).

Regional physical property data made available by the Council for Geosciences South Africa shows the properties of some of the Rustenburg Layered Suite lithologies that have been collected. Table 2.3 below shows the results of some of the physical properties that were tested.

Table 2.3: Physical property data for lithologies from the Rustenburg Layered Suite obtained from the Council for Geosciences South Africa.

Samples	Density (g/cm^3)	P-wave Velocity
Chromite	3.906 - 4.182	4827 - 5274
Harzburgite	3.276	6532
Pyroxenite	3.266 - 3.295	6100 - 6547

3 Geophysical Theory

The seismic, resistivity and magnetics methods were all used to collect the geophysical data in this study. Understanding the basic theory for each of these methods is vital to understand the data that are acquired. This chapter describes the basic background and theory for each of these geophysical methods.

3.1 Seismic method

Seismic surveying is an active geophysical method that is dependent on the acoustic impedance contrast and the wave propagation through the subsurface (Telford et al., 1990, p. 136). A simplification of a seismic wave is a sinusoidal wave (Milson and Eriksen, 2011, p. 211). This allows for the wave to have properties such as a crest, a trough, an amplitude, a frequency and a wavelength. By intentionally setting the frequency and the wavelength of the wave which is dependent on the source (Heiland, 1940, p. 25), the velocity of it through the medium can be determined. High frequencies produce shorter wavelengths, resulting in a higher resolution of the shallow subsurface. Similarly, low frequencies produce longer wavelengths, resulting in a higher resolution of the deep subsurface. The depth of investigation for the seismic survey determines the type of seismic source that must be used.

Particles that are concurrently in phase within a homogeneous subsurface medium will create a wavefront (Milson and Eriksen, 2011, p. 211). The direction of the wave is perpendicular to the wavefront (similar to an equipotential surface) and is called a ray. The paths of these rays are recorded through the use of seismic receivers (geophones).

A material's elastic properties affect the waves produced by a source that impacts its surface (Telford et al., 1990, p. 140). The particles within the material are subjected to a stress, causing a change to their shape as the wave passes. They then return to their original shape once the wave has passed. Materials with these properties have Hookean behaviour. Here, the relationship between the strain and the stress are linear as described by equation 1 (Burger et al., 1992, p. 12) when the material experiences a constant compression or tension along one axis.

$$\sigma = E\varepsilon \qquad (1)$$

Here σ is the stress, E is the Young's modulus and ε is the strain.

Equation 2 describes the change in the lengths of the sides of the material (the elasticity) and is known as the elongation coefficient (Burger et al., 1992, p. 12) (Dobrin, 1976, p. 26) (Heiland, 1940, p. 443).

$$\varepsilon = \frac{l_f - l_o}{l_o} = \frac{\Delta l}{l_o} \quad (2)$$

Here ε is the elongation, l_f is the length in the deformed or final state and $l_o$is the length in the initial state.

Poisson's ratio (Burger et al., 1992, p. 12) (Heiland, 1940, p. 443) (Telford et al., 1990, p. 143) describes the ratio between the elongation in each direction as in equation 3.

$$\mu = -\frac{\varepsilon_1}{\varepsilon_2} \; where \; \mu \leq 0.5 \quad (3)$$

where μ is the Poisson's ratio.

The incompressibility of an isotropic material (its ability to change its volume when it experiences a change in pressure) is known as the bulk modulus coefficient and is described by equation 4 (Burger et al., 1992, p. 12) (Dobrin, 1976, p. 26) (Heiland, 1940, p. 443) (Telford et al., 1990, p. 143).

$$K = \frac{\Delta P}{\left(\frac{V_f - V_o}{V_o}\right)} \quad (4)$$

where K is the bulk modulus, V_f is the final volume, V_o is the initial volume and ΔP is the change in pressure on the material.

The ability of a material to shear when it experiences a shear stress is known as the rigidity modulus (Equation 5) (Burger et al., 1992, p. 13) (Dobrin, 1976, p. 29).

$$G = \frac{\sigma_s}{\gamma} \quad (5)$$

where G is the rigidity modulus, σ_s is the shear stress and γ is the shear strain.

The elastic capabilities of a material are described by these coefficients which can be tested in a laboratory.

The transmission of waves through the material can be described by using the various elastic properties (Milson and Eriksen, 2011, p. 211). This allows for different types of waves to be identified. A back-and-forth motion among the particles within a medium is created by the Longitudinal wave (P-wave) along the direction of propagation (Dobrin, 1976, p. 35) (Milson and Eriksen, 2011, p. 211). This creates dilations and compressions between the particles as the wave propagates through the medium (Telford et al., 1990, p. 147). Particles within a medium shear pass one another at 90° to the direction of propagation under the influence of a Transverse wave (S-wave) (Dobrin, 1976, p. 35) (Milson and

Eriksen, 2011, p. 211). This slows down the velocity of the wave. Longitudinal and Transverse waves are also named body waves (Telford et al., 1990, p. 147).

There are two types of surface waves that can be considered when working with homogenous waves. These are the Raleigh waves and Love waves. Raleigh waves cause particles to move in an elliptical manner within the vertical plane of the direction of propagation. They lose their effectiveness as they propagate downwards into the surface, and their velocity changes with the wavelength of the wave (Milson and Eriksen, 2011, p. 211). Love waves cause the particles within the medium to move parallel to the surface and perpendicular to the direction of propagation (Telford et al., 1990, p. 147). Air waves are faster than the surface waves and travel from the source to the geophone through the air.

3.1.1 Wave velocities

Elastic coefficients and the density (ρ) of a material are used to calculate the wave velocities (Burger et al., 1992, p. 18). Equation 6 shows the wave velocity for the Longitudinal waves (P-waves) (Milson and Eriksen, 2011, p. 212).

$$V_P = \sqrt{\frac{K+\frac{4}{3}G}{\rho}} = \sqrt{\frac{E(1-\mu)}{\rho(1-2\mu)(1+\mu)}} \quad (6)$$

Equation 7 shows the wave velocity for the Transverse waves (S-waves).

$$V_S = \sqrt{\frac{G}{\rho}} = \sqrt{\frac{E}{\rho 2(1+\mu)}} \quad (7)$$

Equation 8 shows the ratio between the two.

$$\frac{V_P}{V_S} = \sqrt{\frac{1-\mu}{\frac{1}{2}-\mu}} \quad (8)$$

The Transverse waves' velocity is zero when the rigidity modulus coefficient is zero. This shows Transverse waves do not move through liquids.

Huygens principle, Fermat's principle and Snell's Law will need to be considered when an inhomogeneous surface is surveyed.

All points on a wavefront act as point sources, as explained by Huygens principle. The constructive and destructive interfaces of all the point sources along the initial wavefront create a secondary wavefront (Dobrin, 1976, p. 40). Fermat's principle explains that the path of a wave propagating between two points is proportional to the lowest travel time between the two points. These principles are used to further understand how the waves reflect and refract when they interact with a surface.

3.1.2 Reflection

A planar, horizontal boundary which has a change in the acoustic impedance (a product of seismic velocity and density), creates a reflection and refraction of an incident wave that is moving at a constant velocity. The angle at which the incident wave interacts with the boundary is known as the angle of incidence (angle between the normal of the surface and the incident wave) (Telford et al., 1990, p. 152). The reflection of the incident wave off the boundary creates an angle of reflection (angle between the normal of the boundary and the reflected wave). An assumption is made in reflection seismics that every wave which is recorded at the surface, is a reflected wave where the angle of incidence is equal to the angle of reflection. This creates a peak travel time for the wave (Burger et al., 1992, p. 25) (blue path in Figure 3.1). Measuring the time that these waves reach the surface provides more information about the depth of the subsurface boundary.

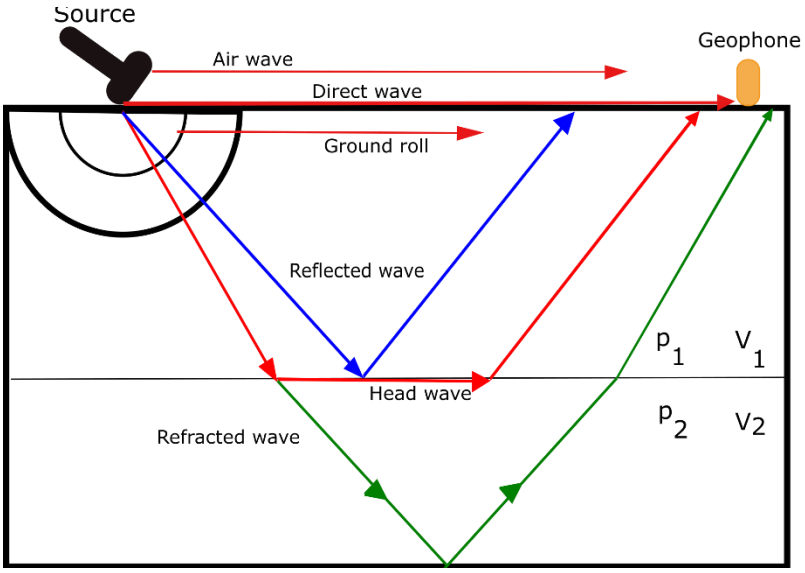

Figure 3.1: General seismic wave paths as they propagate through the subsurface (Burger et at., 1992, p. 36).

3.1.3 Refractions

The angle of refraction is the angle between the normal of the boundary and the refracted wave. This differs from the angle of reflection when the incident wave interacts with the boundary (containing a seismic velocity variation) (Milson and Eriksen, 2011, p. 215).

Equation 9 describes the critical angle as the angle at which the refracted wave propagates along the boundary (green path in Figure 3.1) (Milson and Eriksen, 2011, p. 215). If the incident wave exceeds this angle, there would be no refraction as a result of total internal reflection (Burger et al., 1992, p. 27).

$$\theta_{ic} = \left(\frac{V_1}{V_2}\right) \quad (9)$$

Here the seismic velocities of each layer are defined as v_1 and v_2. If there is a sharp discontinuity in the subsurface, the observed waves begin to diffract.

Equation 10 shows Snell's Law which describes the relationship between the reflections and the refractions (Burger et al., 1992, p. 28) (Telford et al., 1990, p. 152).

$$\frac{\sin\theta_i}{\sin\theta_r} = \frac{V_1}{V_2} \qquad (10)$$

The angles shown between the refracted and the incident ray with the normal to the surface are described as θ_r and θ_i. Incident Longitudinal and Transverse waves on a boundary will result in both reflected and refracted Longitudinal and Transverse waves being produced.

3.1.4 Seismic surveys

The arrival times of the different seismic waves are recorded using a geophone when energy is entered into the surface. The velocity of the seismic waves depend on the acoustic impedance of the subsurface which causes them to either speed up or slow down as they propagate through the medium. This would cause the different waves (Figure 3.1) to be recorded at different time intervals. Figure 3.2 shows a time vs distance plot that would be created as the geophones along a survey line record the seismic waves that have travelled from the source. Air waves travel through the air, direct waves travel along the surface, the top layer of the subsurface hosts the ground roll waves, while the interface between the subsurface layers hosts the head wave.

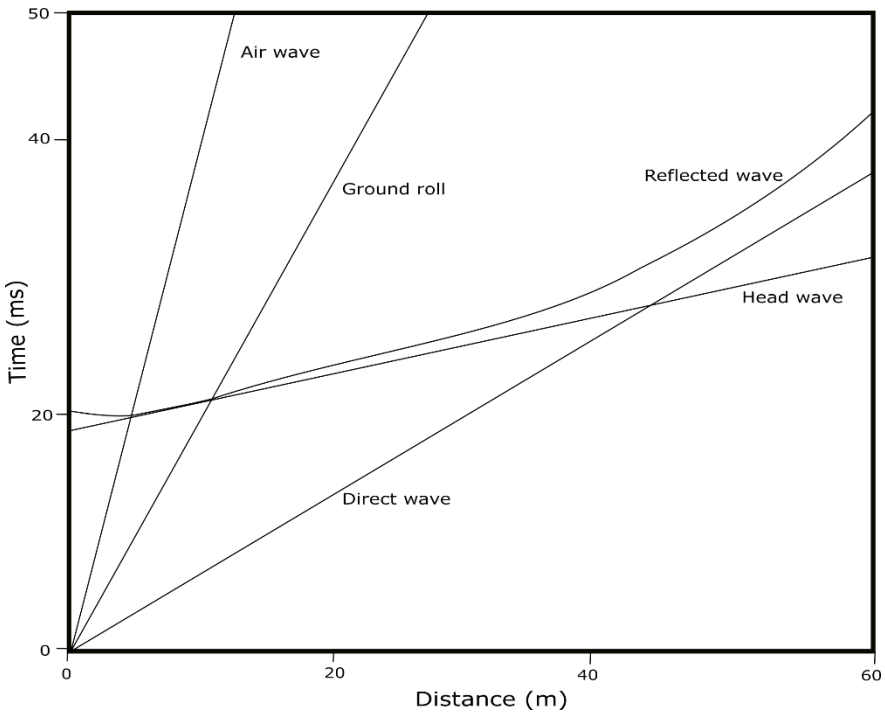

Figure 3.2: Plot showing the recorded arrival times of different seismic waves (Burger et al., 1992, p. 38).

3.2 Resistivity Method

This resistivity geophysical method is an active geophysical technique that is rooted within Ohms law (Milson and Eriksen, 2011, p. 109). Ohms law explains the proportional relationship between the potential measured over a resistor to the current flowing through it, while the resistance of the resistor is constant throughout (Telford et al., 1990, p. 522) (Dobrin, 1976, p. 569). The resistance is influenced by the geometry of the material. A wire which has a small diameter and a longer length has a higher resistance as compared to a wire with a larger diameter and shorter length. Ohms law does not consider the dimensions of the wire which is not suitable for geophysical surveying. This prompts one to consider the resistivity. Equation 11 describes the resistivity as the ability to hinder the flow of electrical current (Dobrin, 1976, p. 569).

$$\rho = \frac{RA}{L} \qquad (11)$$

Here the resistivity (ρ) has units of Ohm.m, the resistance of the wire (R) is in Ohms, the cross-sectional area of the wire (A) is in square meters, and the length of the wire (L) is in meters. This equation considers the dimensions of the wire. A high resistance is correlated with a high resistivity while a low resistance implies a low resistivity.

Properties such as, conductivity, porosity, permeability, temperature of the subsurface, and the presence of metallic ores and groundwater (containing dissolved salts), allows different rock types to have different resistivities (Milson and Eriksen, 2011, p. 121). Fracturing within the rocks and its ability to host fluids is another factor that influences a rock's resistivity. This is dependent on the conditions to which the rocks are exposed. Igneous rocks naturally occur with lower porosity, low conductivity and low permeability which allows them to have the highest resistivities. Fracturing within the igneous rocks allows them to obtain a reasonably lower resistivity. Sedimentary rocks have high porosity and permeability. Ground water seepage into the sedimentary rocks allows the electrical current to flow more easily, creating a lower resistivity.

3.2.1 Field measurements

Specific configurations of current and potential electrodes are used to determine the resistivity of the rock layers within the subsurface. This configuration used is dependent on the depth of investigation for the geophysical survey. The Wenner (Figure 3.3), Schlumberger and Dipole-Dipole Array are the three most relevant configurations.

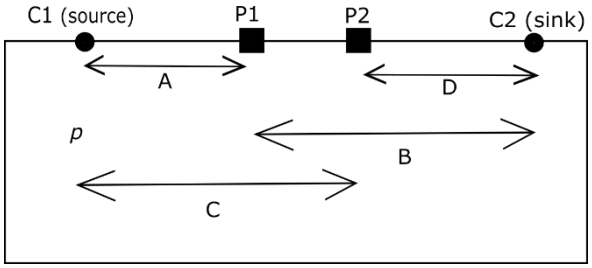

Figure 3.3: Electrode configuration for a Wenner array. Current source (C1), current sink (C2) and potential electrodes (P1 and P2) with their specified spacings (A-D) and the density of the subsurface (p) (Burger et al., 1992, p. 278).

Single point source

Current is injected into the subsurface through a single current electrode, creating a single point current source (Figure 3.4). Air has an infinite resistivity therefore the current is restricted to flowing downwards into the subsurface. The current distribution is equal, as it flows radially from the point source. An equipotential surface propagating from the point source in a hemispherical pattern is created (Telford et al., 1990, p. 523). Current paths are determined as they flow perpendicular to the equipotential surfaces.

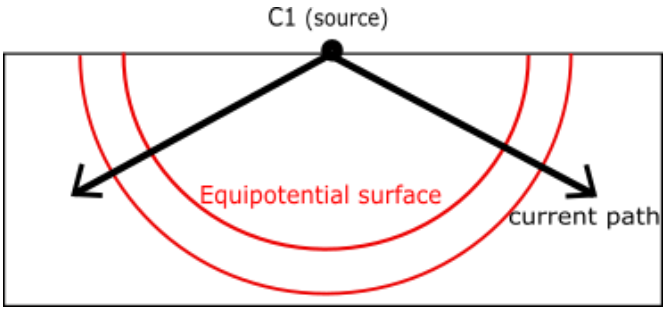

Figure 3.4: Current paths (black arrows) identified from the equipotential surfaces (Burger et al., 1992, p. 271).

Two current electrodes

A current source injects the current into the medium, while a current sink records the current once it has passed through the medium. Equation 12 is used to calculate the potential created by the current source and current sink (Telford et al., 1990, p. 523).

$$V_{P_1} = \frac{i\rho}{2\pi}\left(\frac{1}{\left[\left(\frac{d}{2}+x\right)^2+z^2\right]^{\frac{1}{2}}} - \frac{1}{\left[\left(\frac{d}{2}-x\right)^2+z^2\right]^{\frac{1}{2}}}\right) \qquad (12)$$

Where d is the distance between the two electrodes, the origin which is situated in the middle of the two electrodes represents the x and z with the z-axis being negative upwards (Figure 3.5). P_1 is the position anywhere below the surface and ρ is the assumed resistivity of the surface (Burger et al., 1992, p. 272).

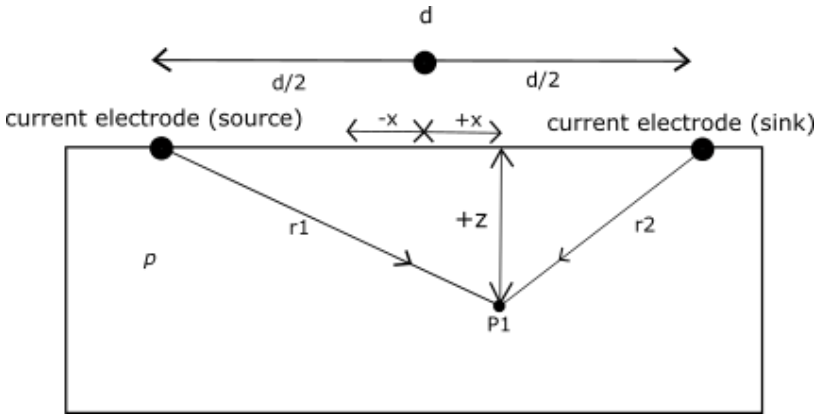

Figure 3.5: Two current electrodes survey setup (Burger et al., 1992, p. 272).P1 is the measurement point,r1 and r2 are the radial distances from the electrodes to the measurement point with d the horizontal distance between the two current electordes.

An equipotential surface is created after the potential is calculated for each point within the subsurface by connecting the points with equal potential. This is done with the assumption that the subsurface is homogenous (Figure 3.4). Once the equipotential surface has been established, the current path (Figure 3.6) can be obtained.

The current is confined to a specific depth which is controlled by the distance between the current electrodes. Burger (1992) uses a simple calculation to described the confines of the current which is restricted to a homogenous and isotropic medium. Here, half of the distance between the two current electrodes contains 50 % of the current while 75 % of the current is confined to a depth equal to the distance between the current electrodes.

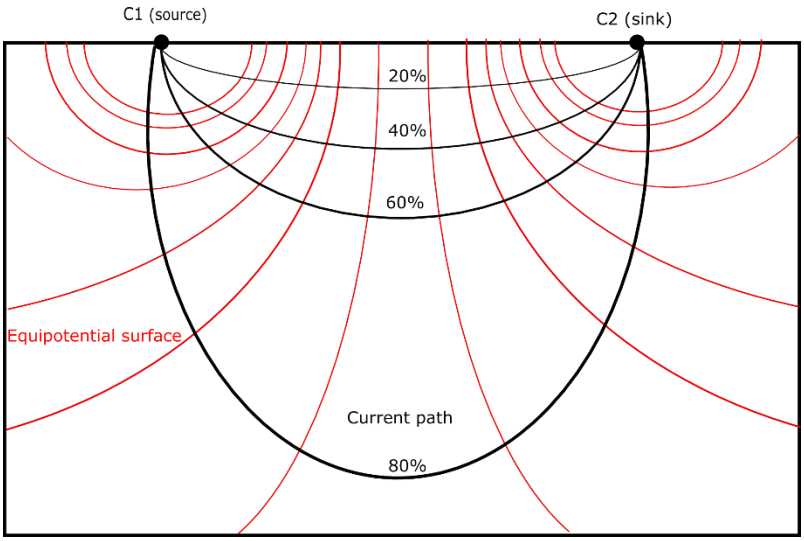

Figure 3.6: Current paths and equipotential surfaces determined for a current source and current sink. Not drawn to scale (Burger et al., 1992, p. 277).

Two current and two potential electrodes

Figure 3.3 shows two potential electrodes which are placed between the two current electrodes. The resistivity between the electrodes can be determined by measuring the potential from each potential electrode at a given point once the current has been injected into the ground. Equation 13 describes the resistivity ρ (units: Ohm.m) (Telford et al., 1990, p. 524).

$$\rho = \frac{2\pi\Delta V}{i}\left(\frac{1}{\frac{1}{A}-\frac{1}{B}-\frac{1}{C}+\frac{1}{D}}\right) \quad (13)$$

A through to D is the measured distances between respective electrodes, (corresponding to Figure 3.3), while V is the potential difference and i is the current.

If the potential difference from each electrode, the current injected into the subsurface and the spacing between the electrodes are known, the resistivity can be found. This assumes that the resistivity is constant and does not consider the variations that can occur due to natural exposure. Equation 14 shows the change in the potential (ΔV) from P1 to P2 (using Figure 3.3) (Telford et al., 1990, p. 524).

$$\Delta V = V_{P_1} - V_{P_2} = \left(\frac{ip}{2\pi A} - \frac{ip}{2\pi B}\right) - \left(\frac{ip}{2\pi C} - \frac{ip}{2\pi D}\right) \quad (14)$$

3.2.2 Layering in the subsurface

The Earth has natural variations in physical properties between the subsurface layers. The single layered Earth is not a reasonable simplification (Figure 3.7 A). It is therefore important to understand how the variations in the physical properties within the subsurface layers will affect the measurements that are being made.

Current paths behave differently at the interface between subsurface layers that have different resistivities. The current distribution (Burger et al., 1992, p. 280) can be found by understanding the resistivities of the subsurface layers. Current flowing from a high to a low resistivity layer causes the current paths to deflect or shift away from the normal to the interface (Figure 3.7 B). Additionally, when the current is flowing from a low to a higher resistivity layer, the current paths deflect towards the normal to the interface (Figure 3.7 C). This results in the current paths being more closely spaced and parallel in a lower resistivity layer.

Equation 15 shows the relationship between the deflection and the resistivity of the layers (Burger et al., 1992, p. 284).

$$\frac{tan\,(\theta_1)}{tan\,(\theta_2)} = \frac{\rho_1}{\rho_2} \quad (15)$$

θ is the angle between the current path and the normal to the interface for each identified layer while ρ is their resistivities.

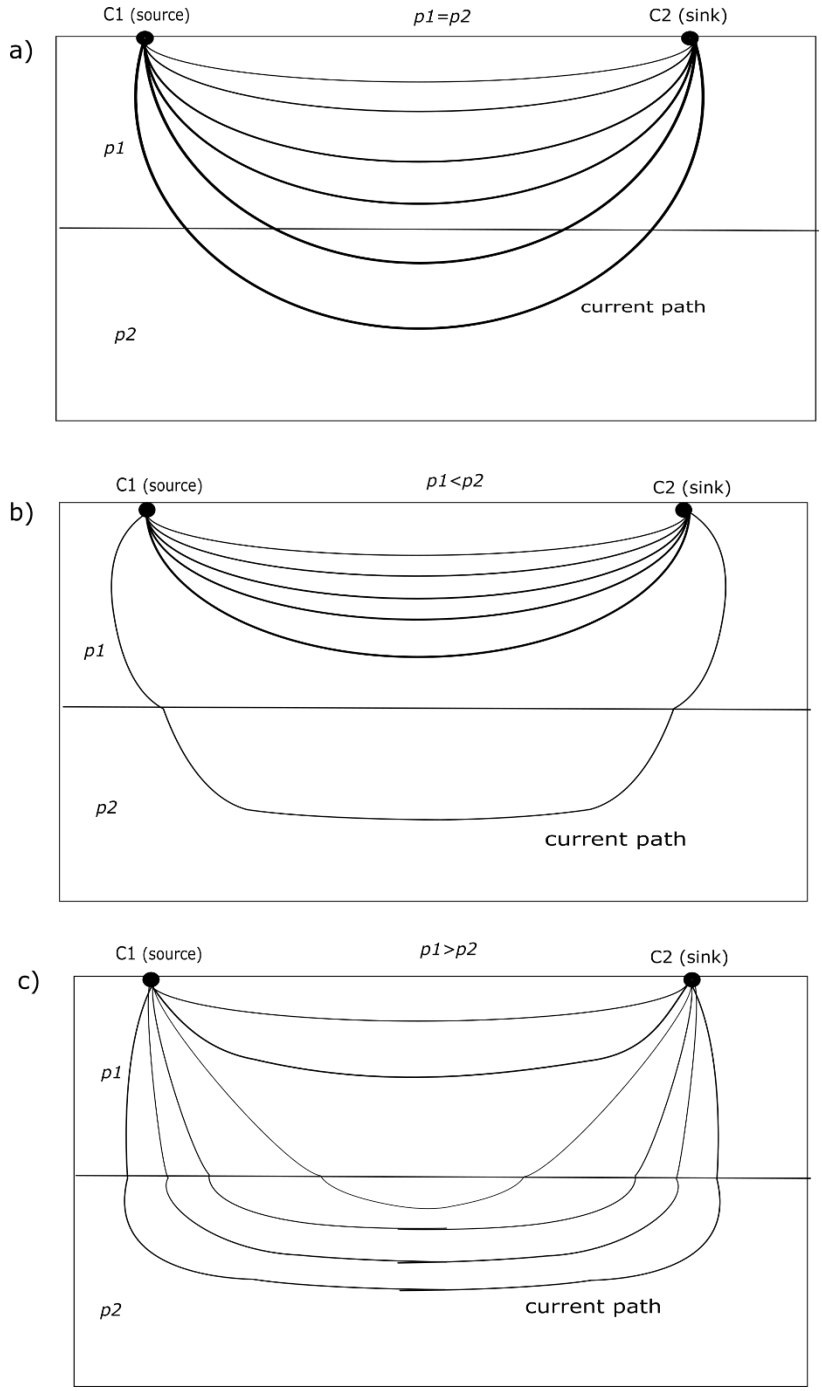

Figure 3.7: The changes in the current paths caused by resistivity contrasts. a) Layers have equal resistivities (p1=p2), b) top layer has a lower resistivity (p1<p2), c) Bottom layer has a lower resistivity (p1>p2). Not drawn to scale (Burger et al., 1992, p. 286).

3.2.3 Apparent resistivity

The examples above (Figure 3.7), are for homogeneous surfaces. In reality, however, the subsurface layers are inhomogeneous and actual resistivity of a layer cannot be calculated. The resistivity that has been discussed above is the apparent resistivity. Changes in the current density affect the potential

measured between the potential electrodes and the apparent resistivity with depth (Burger et al., 1992) (Dobrin, 1976, p. 577).

In two-layer Earth scenarios where the layers are homogeneous (Figure 3.7 A), the apparent resistivity is equivalent to the resistivity of the subsurface layers. In inhomogeneous cases (Figure 3.7 B and 3.7 C) the apparent resistivity varies to the actual resistivity of the subsurface layers. Current paths that are in close proximity to one another have a higher current density causing the measured apparent resistivity to be larger than the actual resistivity of the layer (top layer in Figure 3.7 B). Current paths that are more sparsely spaced have a lower current density causing the measured apparent resistivity to be smaller than the actual resistivity of the layer (top layer in Figure 3.7 C).

The apparent resistivity recorded is also dependent on the distance between the electrodes. Closely spaced electrodes provide a higher resolution of the shallow subsurface as the current paths are concentrated within the shallow subsurface layers. A larger electrode spacing allows the current paths to penetrate the deeper subsurface layers providing more information about the deep subsurface. This is still affected by the variations of the current density.

By increasing the distance between the electrodes from a central point, the apparent resistivity measured will change depending on the subsurface layering. This allows for boundaries between subsurface layers and the resistivities of these layers to be identified. For example, an increasing apparent resistivity suggests a higher resistivity layer, while a decreasing apparent resistivity suggests a lower resistivity layer with depth.

The thickness of the subsurface layers affects the readings even if there is a significant resistivity contrast within a multi-layered subsurface. Most equipment can only account for 13 Ohm.m which implies that narrow resistivity contrasts are less likely to be mapped.

A vertical resistive contact is caused by rapid changes in the subsurface resistivity. This is as a result of lithological contacts or from structural displacements in an area of interest.. It is important to use the correct configuration to map the relevant contacts of interest, as the subsurface can be poorly mapped if the wrong configuration is implemented. This is completed by using various resistivity sounding and profiling configurations. To complete a resistivity sounding, the innermost electrodes are initially used while the remaining electrodes are inactive. Once a measurement is completed, the next set of electrodes used has a larger electrode spacing. This allows for a deeper measurement to be completed. This provides a vertical profile of the subsurface resistivities.

Resistivity profiling concentrates on mapping the lateral variations. The depth of investigation is constant so the spacing between the electrodes remains the same. The different arrays are used to obtain resistivity profiles and soundings.

3.2.4 Arrays

Multiple electrodes spread out over an area are used for each array. The electrodes are used as either potential electrodes or current electrodes. Most of the electrodes remain inactive until their operation is required.

Wenner array

The Wenner array is the most commonly used array (Figure 3.3). Here, two potential and two current electrodes (current source and current sink) are used with a constant electrode spacing.

The calculation of the apparent resistivity for the Wenner array and the setup are simple.(Telford et al., 1990, p. 537). The Wenner array is best suited for shallow investigations as it is sensitive to near surface variations. This allows for noise to be interpreted as resistivity variations with depth, which is why this array is more reliable for resistivity profiling.

Schlumberger array

The Schlumberger array (Figure 3.8) has variations in the electrode spacings. Figure 3.8 shows the relationship between the spacing of the potential and the current electrodes (2A > 5BC) where the current electrodes have a larger distance to the midpoint (A) as compared to the potential electrodes (B and C). As measurements are being made, the distance from the midpoint of the current electrodes is increased. This is done until there is a null measurement recorded by the potential electrodes. At this point, the distances from the midpoint to the potential electrodes (B and C) are increased (Telford et al., 1990, p. 537).

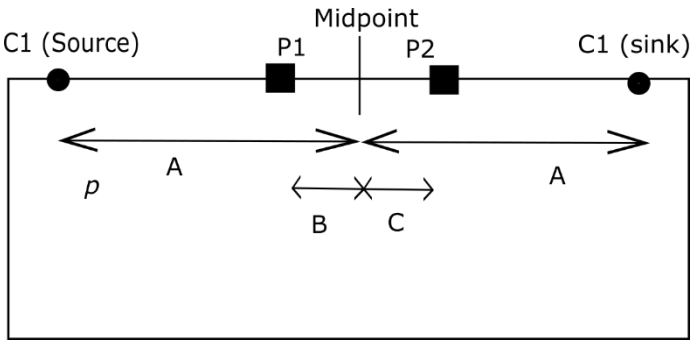

Figure 3.8: Electrode configuration for a Schlumberger array. Current source (C1), current sink (C2) and potential electrodes (P1 and P2) with their specified spacings (A-C) and the density of the subsurface (p) (Burger et al., 1992, p. 318).

The Schlumberger array has a higher resolution than the Wenner array for resistivity soundings (Dobrin, 1976, p. 580). It also has a faster setup time. The near-surface/shallow resolution is not comparable to the Wenner array although it is best suited for resistivity soundings.

Dipole-Dipole array

Detailed cross-section of the subsurface are obtained using the Dipole-Dipole array (Figure 3.9) (Burger et al., 1992, p. 318). The current and potential electrodes are placed on either end of the midpoint and a specified distance (A). An apparent resistivity measurement is at taken at the midpoint. A new measurement is completed at a new midpoint created by moving only the potential electrodes one step away from the current electrodes. This process continues until the signal recorded at the potential electrodes is too low. The current electrodes are then moved one step towards the potential electrodes and the process is repeated until a pseudo-cross section of the subsurface is created. The actual resistivity of the subsurface layers can be calculated using various inversion softwares.

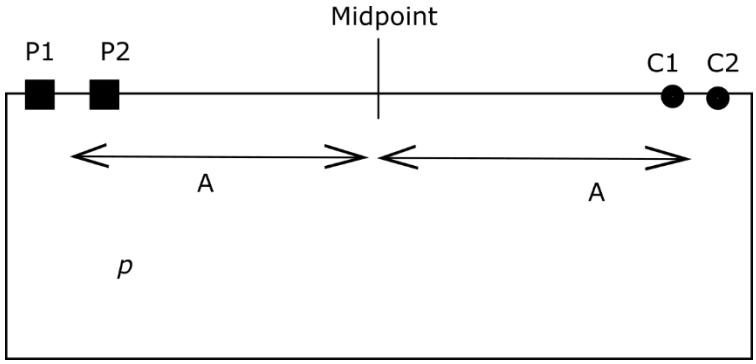

Figure 3.9: Electrode configuration for a Dipole-Dipole array. Current source (C1), current sink (C2) and potential electrodes (P1 and P2) with their specified spacings (A) and the density of the subsurface (p) (Burger et al., 1992, p. 318).

The Dipole-Dipole array is easy to work with, provides a detailed cross section of the subsurface and is more sensitive to lateral changes in resistivity along a profile (best suited for resistivity profiling). The electrode spacing is a key component for the Dipole-Dipole array. If the electrode spacing is too large, reliable measurements will not be made as the signal would be too weak.

3.3 Magnetics Method

The magnetic susceptibility and the ability for a rock to get magnetised is the basis of magnetic surveys. It is a passive geophysical technique (Milson and Eriksen, 2011, p. 65). The magnetic mineral grain size, microstructure lattice structures, electron spins, concentrations of the magnetic atoms or ions, orbital motions and mineral content are the properties that control the magnetic susceptibility of the rock (Dentith and Mudge, 2015).

3.3.1 The Earth's magnetic field

An electric current produced from the flow of the outer core creates the Earth's magnetic field. The magnetic field can be considered as a magnetic dipole that does not align with the Earth's geographic pole (Dentith and Mudge, 2015). The magnetic declination is the angle between the axis of the magnetic field and that of the Earth. Magnetic field lines (Figure 3.10) perpendicular to the surface that occur at the poles are the strongest, while those parallel to the surface at the equator are the weakest (Dobrin, 1976, p. 477). Inclination is known as the angle of these field lines to the Earth's surface.

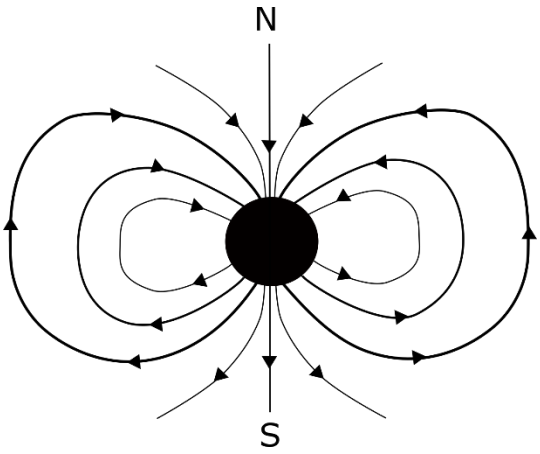

Figure 3.10: Earth's magnetic field lines showing perpendicular field lines at the poles and, parallel field lines at the equator (Dentith and Mudge, 2015).

3.3.2 Types of magnetism

The magnetic domains that are present in materials (as a result of the electron spins) cause the material to have variable magnetic susceptibilities as they interact with an external magnetic field (Telford et al., 1990, p. 73). The parallel alignment of the electron spins with Earth's magnetic field in a paramagnetic material creates a weak positive magnetic susceptibility only visible in high resolution surveys. The electron spins align in the opposite direction to the Earth's magnetic field in a diamagnetic material creating a weak negative magnetic susceptibility, not measurable on high resolution surveys. Both

parallel and opposite alignments of the electron spins with the Earth's magnetic field occur in a ferromagnetic material, creating a high magnetic susceptibility if these domains align the Earth's external magnetic field. Ferromagnetic materials have the largest susceptibilities (Dentith and Mudge, 2015).

Permanent/remanent magnetism and induced magnetism are two types of magnetism that some materials are able to host. The vector sum of the induced and the remanent magnetism is considered as the overall magnetism of a mineral (Dentith and Mudge, 2015).

Permanent or Remanent magnetism

A material that retains the orientation of its initial magnetisation caused by the presence of a strong external magnetic field is considered to have a high magnetic susceptibility. Magnetic minerals with a high magnetic susceptibility, occurring in a newly formed magma, will align with the Earth's magnetic field at its time of formation (Telford et al., 1990, p. 72). The magnetic alignment is retained as the magma cools. This process is known as permanent or remanent magnetisation. The orientation of the magnetic alignment varies as new magmas form due to the Earth's shifting magnetic field. Changes in the Earth's magnetic field can be tracked in this way. Plate tectonics allows for changes in the magnetic alignment to occur as the rocks get re-magnetised due to partial melting. The sum of the permanent magnetisms is considered to be the overall remanent magnetism (natural remanent magnetism) (Dentith and Mudge, 2015).

Induced magnetism

An external magnetic field will magnetise a material that has a high magnetic susceptibility (known as induced magnetism) (Telford et al., 1990, p. 72). This differs from permanent magnetisation as initial magnetisation that it obtains is not retained. Magnetic domains existing on the surface of the rock will realign to the Earth's existing magnetic field as the rock moves to a different magnetic orientation. The remaining domains within the rock retain their original magnetisation. By this occurrence, rocks can have both the induced magnetism and permanent magnetism.

3.3.3 Magnetic surveys

In magnetic surveys, the Earth's total magnetic field intensity are measured at every point along the survey line. A high magnetic susceptibility feature within the subsurface will affect the resultant magnetic field that is recorded along the line (Figure 3.11). A larger magnetic intensity will be recorded where the rocks' magnetic field lines align with the Earth's magnetic field lines. Similarly, a lower

magnetic intensity will be recorded where the field lines oppose one another. Additionally, a higher density of the magnetic field lines (at the poles) will create a higher magnetic response.

The response that can be expected at a latitude of -26° (South Africa) if measurements of the total magnetic field intensity were made over the magnetised source, is shown in Figure 3.11.

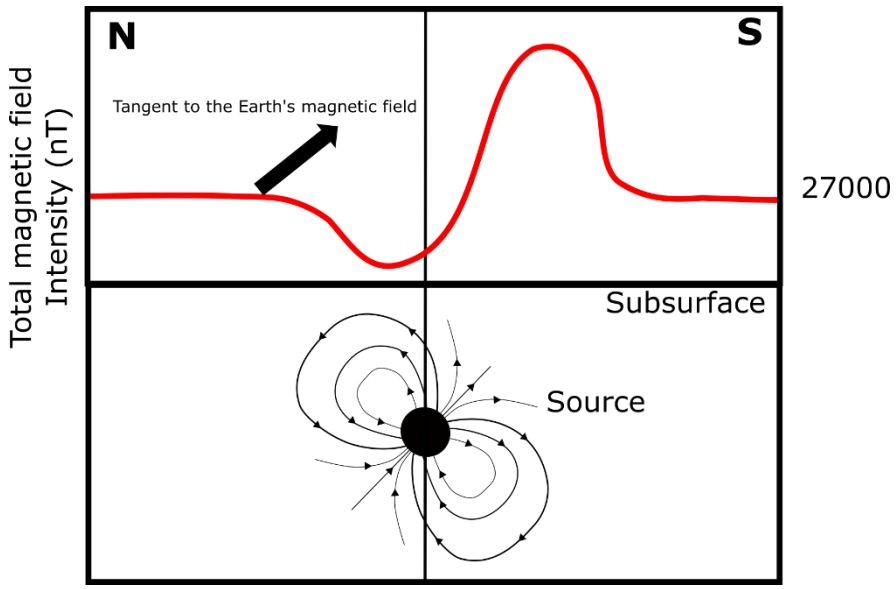

Figure 3.11: Amplitude response created by a magnetic survey that crosses a magnetic source located in South Africa. Not drawn to scale, (Dentith and Mudge, 2015, p. 95).

3.3.4 Recording the Earth's magnetic field

The Earth's magnetic field strength can be recorded with the use of a proton procession magnetometer (Milson and Eriksen, 2011, p. 72). The magnetometer contains a proton-rich fluid which aligns with a magnetic field created by a current carrying coil that surrounds the container. When the magnetic field stops, the protons realign with the existing Earth's magnetic field. The frequency (Larmors frequency as in Equation 16) at which the protons begin to precess, is dependent on the magnitude of the Earth's magnetic field. A proton procession magnetometer has a resolution of 0.1 nanotesla (nT) (Hollos and Hollos, 2008).

$$L_f = \frac{m}{2\pi I}\vec{B} = \frac{G}{2\pi}\vec{B} \qquad (16)$$

This equation is described by the Larmor frequency (L_f), proton magnetic moment (m), proton angular momentum I, ambient magnetic field $\vec{B}$ and the gyrometric ratio (G) for protons 0.267513 $nT^{-1}s^{-1}$.

The scalar quantity of the Earth's magnetic field is measured by the cesium vapour magnetometer (Milson and Eriksen, 2011, p. 73). The cesium vapour is held in a glass cell through which a laser light is transmitted. This laser light has a frequency and wavelength that is equivalent to that of the first

absorption line of the cesium vapour. The electrons within the cesium vapour absorb the photons, causing the decrease in the light's intensity. The electrons then move to higher energy level which will increase their intensity which is measurable with a photoelectric cell.

A spin alignment is created as the electrons move to a higher energy level. The frequency at which these spin alignments precess is the Larmor frequency which varies with the ambient magnetic field and can be used to describe the total magnetic field (Geometrics, inc., 2004). High shifts are required as the initial precessions are small. A decrease in the intensity of the light registered by the photoelectric cell activates an alternating current in the coil that is tuned to match the precession frequency. This will allow the electrons to shift to a higher energy level that is measurable. This allows the photons to be absorbed by the electrons changing the light's intensity. The precession frequency is then recorded (using equation 16) and the total magnetic intensity is calculated. Most cesium vapour magnetometers have a resolution of 0.001 nT (SCINTREX., 2012).

4 Methods

To achieve the aims and objectives of this study, physical property and geophysical data analysis are required. The methods used to acquire the bulk magnetic susceptibility, density, ultrasonic velocity and resistivity data for the physical property analysis are described here, together with the acquisition parameters for the geophysical field data that are analysed.

4.1 Physical property measurements

Through the petrographic analysis and physical property measurements of the rock samples, the samples can be classified stratigraphically. The P- and S-wave seismic velocities, the time-domain resistivity, density, and the bulk magnetic susceptibility, are the physical properties measured.

The seismic velocities and the densities will allow for numerical simulations, i.e. computation of synthetic seismograms. The synthetic seismograms will aid in the interpretation of the seismic data by identifying the lithologies responsible for the reflections in the 2018 reflection seismic data. In turn, this 2018 seismic section and the refraction tomography of the 2D legacy reflection seismic data will assist in constraining the near-subsurface geology.

Measuring the resistivities of the samples will allow for a better understanding of the lithologies responsible for the various anomalies found on the resistivity data and go hand in hand with the identification of the shallow stratigraphic units.

The regional magnetic data over the Far Western Limb shows that there are linear east-west trending positive magnetic anomalies that have not been attributed to any of the geological units in the area. The positive magnetic anomalies could be related to one of the structural phases that the Far Western Limb experienced during its formation. Measuring the bulk magnetic susceptibility of the rock samples will potentially allow for the identification of the lithological unit and structure responsible for this linear positive magnetic anomaly.

To do the physical properties, the equipment listed in Table 4.1 was used at the Petrophysics Section of the Analytical Services Unit, Council for Geoscience.

Table 4.1: Outline of Physical Properties measured for samples collected in the study area. This includes what physical property will be measured, how the data will be collected, the number of measurements that are required, and how the data will be analysed.

Equipment used	Physical property measured	How data are collected	Number of measurements required	How data are analysed
Agico MFK1-FA multifunction kappabridge (susceptibility meter)	Bulk magnetic susceptibility	Place sample in the tube Run the program	10	Use the data to create models in mag2dc to further understand the geometry of the positive magnetic anomalies
Proceq PUNDITPL-200 (Ultrasonic meter)	Obtain P-wave velocities. Obtain S-wave velocities. Measure the anisotropy	Measure the respective velocities in 3 different directions	10 measurements per orientation (X, Y, Z direction)	Compared with known velocities to see which lithologies they match
METTLER TOLEDO MS-DNY-54 density kit (density meter)	Find the density of the samples in g/cm^3	Measure the weight of the sample in air and then in water	10 measurements per sample	Calculate densities from the weights. Use the density and P-wave velocity data to calculate the acoustic impedance and create the synthetic seismograms
GDD SAMPLE CORE I.P TESTER (time-domain resistivity meter)	Finding the resistivity of the samples in Ohm.m	Submerge the sample in water then measure the time domain resistivity	10 measurements per sample	Use the data for forward modelling and to further understand the subsurface lithologies imaged on the resistivity data

4.1.1 Preparing the samples for laboratory measurements

To prepare the rock samples that were collected in the field, the samples were first cut into 2 cm × 2 cm ×2 cm blocks. This was done through the use of a rock cutting saw in a laboratory at the South African Council for Geosciences. These samples were of sufficient size for the physical properties of the samples to be measured. A total of 21 blocks were created from all the collected rock samples, and their dimensions can be found in the Appendix A. However, the volumes for each sample were not exactly 8 cm^3 as they were irregularly shaped, this may cause possible discrepancies between samples.

4.1.2 Bulk magnetic susceptibility

The bulk magnetic susceptibility is measured using the AGICO MFK1-FA (Figure 4.1) and the Safyr7 software. Calibration of the equipment is required before the measurements can be taken. This begins with the instrument's calibration and is followed by the holder calibration.



Figure 4.1: AGICO MFK1-FA used to measure the bulk magnetic susceptibility of the samples. Sample (red arrow) within the holder (blue arrow).

- To measure the bulk magnetic susceptibility, the magnetic field intensity is set to 200 A/m, the measuring mode is set to measure the Individual Measurements Mode (bulk susceptibility) and the operating frequency is set to 976 Hz.
- Once completed, the normalization mode for the bulk susceptibility measurement is set to volume normalized since the dimensions of each sample is known.
- The equipment measures the total susceptibility κ_T which is then used to obtain the volumetric susceptibility κ_V through the following formula in equation 17:

$$\kappa_V = \frac{V_0}{V}\kappa_T \qquad (17)$$

where V_0 is the nominal volume of 10 cm^3 and V is the actual volume of the sample.

- Each sample can then be placed within the holder in the y-direction. Once completed a new measurement is initiated where the sample name and the calculated volume are added on the computer linked to the instrument.
- The measurements are set to 10 measurements per sample, followed by saving the data into its respective file. This is then repeated for each sample.

4.1.3 Density

To measure the bulk density, the samples were dried in the oven for 24 hours at 110 °C. Measurements were made once the samples returned to ambient temperature. To measure the density of the sample the METTLER TOLEDO MS-DNY-54 density kit was used (Figure 4.2). A glass beaker containing a known fluid (distilled water) is fitted with a precision thermometer attached to it. The beaker is placed on a platform situated over the bracket which holds the universal basket in which the samples were placed.

The weight of the sample was measured in air and then in water for the density to be calculated. This was done by following several steps described below:

- The equipment first needs to be calibrated before any measurements can be made. Known weights are placed onto the basket and the value for each one is recorded. This allows for the accuracy of the equipment to be monitored.
- Next, the density of the liquid in the water needs to be found. To do this, the temperature of the liquid (usually distilled water) is measured, followed by a correlation with a density table for distilled water, which gives the density of the liquid which is then entered into the system. Once completed, the equipment is zeroed. The sample of interest is then placed onto the universal basket (Figure 4.2 A) and its weight in air is recorded once the value stabilizes. The equipment struggled on certain measurements to stabilize the values and this might result in discrepancies between samples.
- The sample is then placed into the universal basket (Figure 4.2 B) and the measurement is taken once more while the sample is now immersed into the liquid.
- The system records the results into an excel spreadsheet and the process is then repeated for the next sample.

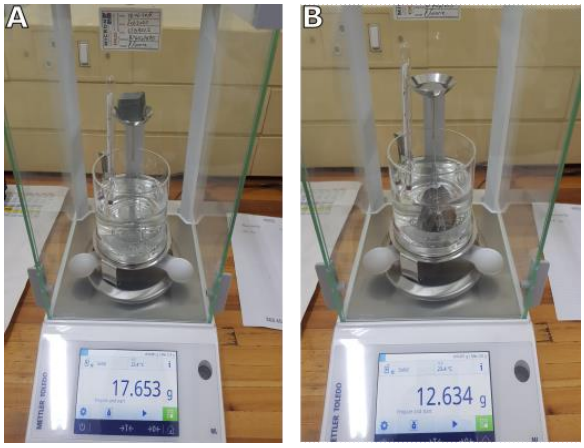

Figure 4.2: Measuring the weight in air and water of Sample S008A using the METTLER TOLEDO MS-DNY-54 density kit A) Sample on top of the universal basket measuring its weight in air, B) sample inside the universal basket measuring its weight in distilled water.

Once these measurements were completed, equation 18 is used to provide the density of the sample.

$$\rho = \frac{A}{A-B}(\rho_0 - \rho_L) + \rho_L \qquad (18)$$

where ρ is the density of the sample, A is the weight of the sample in air, B is the weight of the sample in the liquid, ρ_0 is the density of the liquid and ρ_L is the density of air at 0.0012g/cm^3.

4.1.4 Ultrasonic velocity analysis

To measure the ultrasonic velocities of the samples, the Proceq Pundit PL-200 was used. This piece of equipment provides the P- and S-wave velocities for each of the samples. It consists of a Pundit Touchscreen (Figure 4.3 A), transducers and calibration rods with their respective connecting cables. To measure the P-wave velocities, the 150 kHz transducers (Figure 4.3 B) were chosen, while for the S-wave velocities the 250 KHz transducers were used (Figure 4.3 C).

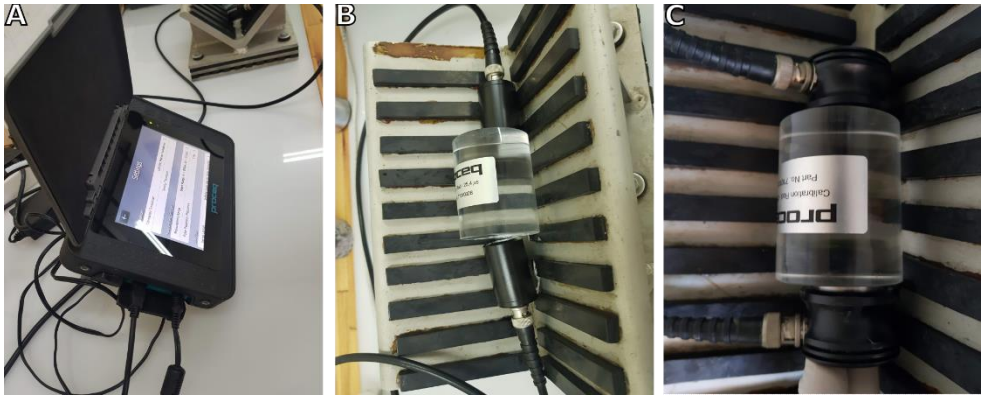

Figure 4.3: The Proceq Pundit PL-200 used to measure seismic velocities: A) Touchscreen, B) 150 kHz Transducers and calibration rod used to calibrate the transducer C) 250 kHz Transducers and calibration rods used to calibrate the transducer.

The following steps were followed:

- Since each sample is a block, measurements were made in all three directions (x, y and z). The setup of the Procep Pundit PL-200 requires that the measurement mode be set to the pulse velocity, the voltage of the transmitter to be 100 V, and the transmission to be continuous. The gain, file name, and distance (length of the side) are adjusted accordingly for each sample. The first step is to zero the instrument. Here the calibration rod is placed between the transducers and the velocity recorded is compared to its actual velocity. Only when the values match, can the experiment continue. To make the measurements, liquid soap is placed between the sample and the transducers as a contact medium.
- The first arrival for the P-wave is picked automatically by the software while the S-wave's first arrival is picked manually.
- The software automatically calculates the respective velocities once the first arrivals are confirmed.
- Each sample was measured in each direction a total of ten times.
- The measurements are recorded and saved onto the system until they are downloaded later onto the computer.

Possible problems causing discrepancies:

- Not having enough soap on the samples causes the samples to be in direct contact with the transducers which causes the velocities to be much lower.
- When holding the transducers to the samples, if they are pressed too little or too much into the samples the velocities are affected.
- The irregular shape of the samples can cause the velocities to be affected. This is due to air between the transducer and sample slowing down the wave, or misalignment of transducers due to nonparallel sample edges.
- The system automatically picks the first arrival on the seismogram. The S-wave velocities were picked by hand.

Multiple seismic P-and S-wave velocities measurements in the x, y and z orientations allows for the anisotropy of each sample to be collected. The formula for calculating the seismic anisotropy is shown by equation 19 (Shithigona et al., 2018):

$$\frac{V_{pmax}-V_{pmin}}{V_{pmean}} \qquad (19)$$

where V_{pmax}, V_{pmin} and V_{pmean} is equivalent to the maximum, minimum and mean P-wave velocity in each sample collected, respectively. The same was done for the S-wave measurements.

4.1.5 Resistivity

To measure the time domain resistivity of the samples the GDD SAMPLE CORE I.P TESTER (time-domain resistivity meter) was used (Figure 4.4).

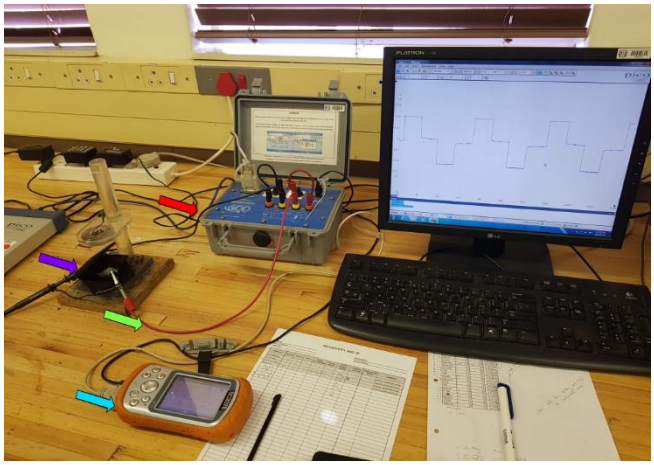

Figure 4.4: GDD SAMPLE CORE I.P TESTER used to measure the resistivity of the samples. This consists of the Archer field computer (blue arrow), the SCIP tester model TDLV (red arrow), the transmitting cable (purple arrow), the receiving cable (green arrows), and finally the computer connected to represent the data visually.

<u>The following steps were carried out:</u>

- Once the SAMPLE CORE I.P TESTER is switched on and all the necessary cables are connected it requires calibration . Known resistors are placed between the transmitting and receiving terminals and the resistivity is recorded. This helps in monitoring the accuracy of the equipment. Each sample was prepared by submerging them in water overnight. To stop the samples from drying out quickly, they were wrapped in a rubber tape (Figure 4.5) for it to retain its moisture.



Figure 4.5: Rock samples wrapped with non-conductive tape to retain the moisture.

- For each sample, X × Y is used as the area therefore the sample is placed with the z-axis vertical between the two terminals.
- To make the measurements, the transmitting terminal is set to a constant voltage of 12 V and each sample is labelled accordingly in the system.

- A total of 6 stacks is used and the data is then saved to the computer.

Possible problems causing discrepancies.

- Samples drying out too quickly before measurements are completed.
- Terminals could touch while measurements are being completed.

4.2 Geophysical surveys

This section describes the different acquisition parameters for the geophysical methods that were employed in this study.

4.2.1 Survey study areas

The two study areas shown in Figure 1.2 are where the surveys took place. The magnetic survey lines are represented by the numbered red lines in Area 1 shown in Figure 4.6. Seismic line 1 is represented by the blue line and the resistivity line 1 is represented by the yellow line. There are outcropping lithologies outlines by the green line North of the survey lines where samples were collected. A fence represented by the black line in the area runs north-west/south-east. This is why the surveyed area was restricted and why the lines terminate against the fence.

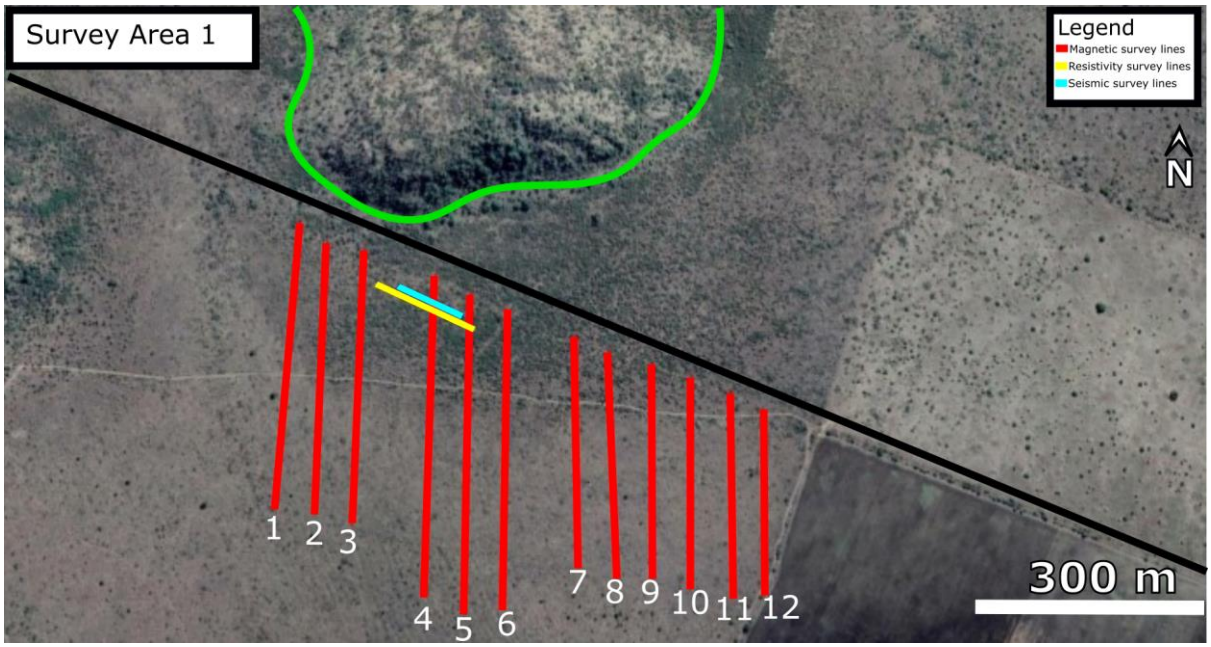

Figure 4.6: Area 1 with the magnetic lines (red lines), the seismic line 1 (blue line), and the resistivity line 1 (yellow line) marked. A wire fence (black line) and outcrop (green line) are also marked (Google Earth Image).

Area 2 (Figure 4.7) contains resistivity profiles (orange, resistivity line 2 and dark green, resistivity line 3) and seismic profiles (light green, seismic line 2 and purple, seismic line 3). This area does not contain any outcropping units but due to the agricultural digging (pink box), some of the rock samples were exposed and therefore recovered.



Figure 4.7: Area 2 with the resistivity profiles (orange and dark green lines, resistivity lines 2 and 3 respectively) and the seismic lines (light green and purple lines, seismic lines 2 and 3 respectively). Pink block in the figure indicates where the rock samples were collected (Google Earth Image).

4.2.2 Seismic data acquisition

Equipment utilised for the seismic data acquisition consisted of forty-eight 14 Hz uniaxial vertical geophones connected to a take-out cable. Two Geometric Geodes (32 bit) were utilised, each connected to 24 geophones, a power source and acquisition laptop for all the seismic lines and was located at the seismic station (centre of the profile) (Figure 4.8). The geometry was set on the laptop with the seismic data acquisition software.



Figure 4.8: Survey layout along seismic profile 1 showing the weight drop (blue arrow), seismic station at the centre of the profile (red arrow), and the seismic profile with geophones (yellow arrow).

The energy sources used were the 9 kg sledgehammer (Figure 4.9) and the accelerated weight drop (23 kg). A metal base plate (30 ×30 × 2.5 cm^3) was utilised for both the sledgehammer and the accelerated weight drop. A sampling interval of 0.5 ms sampling was used to record the data with a total recording length of 500 ms.



Figure 4.9: Geophones (red arrow), sledgehammer source (blue arrow), metal plate (yellow arrow), and the take-out cable (orange arrow)utilised during seismic data acquisition.

A summary of the acquisition parameters for the seismic lines that were collected in this survey can be found in Table 4.2.

Table 4.2: Data acquisition parameters for seismic lines.

Item	Parameters		
Line	1 (Area 1)	2 (Area 2)	3 (Area 2)
Orientation	WNW-ESE	WNW-ESE	N-S
Geophones type	14 Hz		
Geometry	Split spread		
Seismograph	Geometric Geode (32)		
Source	Weight drop(23 kg)	Sledgehammer (9 kg)	Sledgehammer (9 kg)
Record length (ms)	500		
Sampling interval (ms)	0.5		
Vertical stacks	4	4	4
Receiver number	48	48	48
Receiver spacing (m)	2	2	2
Number of shots	26	50	50
Shot spacing (m)	4	2	2
Profile length (m)	94	94	94
Min/Max offset (m)	-4/96	-2/96	-2/96
CMP fold	12	24	24

4.2.3 Resistivity data acquisition

Resistivity data acquisition included steel electrodes (Figure 4.10 A) and the fully automated ARES Resistivity meter (Figure 4.10 B). Electrodes (found in the multicore take-out cable) were fixed to steel rods that were placed into the ground. The ARES resistivity meter was connected to an external battery and the multicore cables, measurements were then taken.

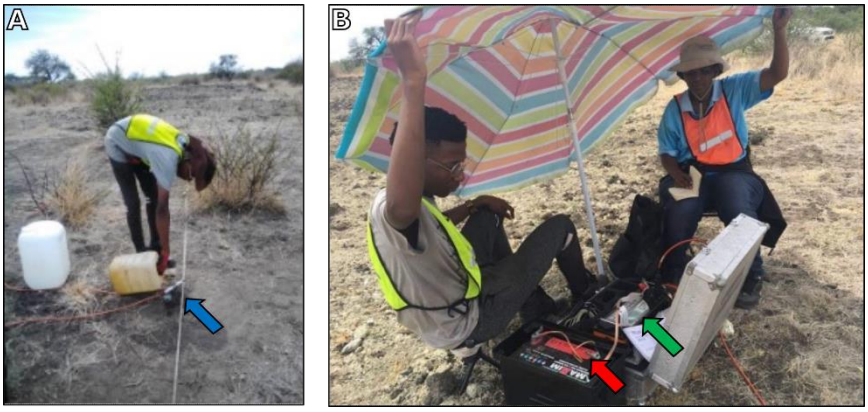

Figure 4.10: A) Electrodes fixed to the steel rods (blue arrow), B) Resistivity meter (ARES) (green arrow) with the multicore take-out electrode cable and the external battery (red arrow).

Three electrical resistivity lines were used in this study. The parameters of the lines can be found in Table 4.3 below.

Table 4.3: Resistivity data acquisition parameters for the resistivity lines.

Line	1 (Area 1)	2 (Area 2)	3 (Area 2)
Profile length	150 m	100 m	100 m
Number of electrodes	31	48	48
Electrode spacing	5 m	2 m	2 m

4.2.4 Magnetic data acquisition

The Cesium vapour walk magnetometer (Figure 4.11) was used to acquire the magnetic data while the Proton Precession magnetometer was used as a base station. A total of twelve magnetic lines were acquired with the Cesium vapour walk magnetometer ranging between 200 m and 350 m with an average line spacing of 50 m. The lines all trend North-South.



Figure 4.11: Caesium vapour walk magnetometer used for the magnetics data acquisition.

4.3 Seismic data processing

The profile for seismic line 1 (Area 1) can be seen in Figure 4.6 and seismic lines 2 and 3 (Area 2) can be seen in Figure 4.7. During data collection, airwave padding was added such that the effects of the airwaves were minimised. This entails that the models all start at 1.5 m below the ground level.

Refraction seismic processing

The refraction tomography was primarily created to understand the velocities and thicknesses of the near-surface lithologies. The first arrivals were picked using ReflexW software while the Tomoplus software was used to process and invert the refraction tomography. The ray paths contain six 50 cm cells as padding which means that the data starts at -3 m in the tomography.

Reflection seismic section

The seismic sections were processed using ReflexW.

4.3.1 Reflection seismic processing for seismic line 1

The raw shot gathers for line 1 (Area 1) (Figure 4.12) show some noise that was incurred in the far offsets for each shot. The major reflections within the data are not necessarily clear as they have a smaller amplitude than the surface waves within the data.

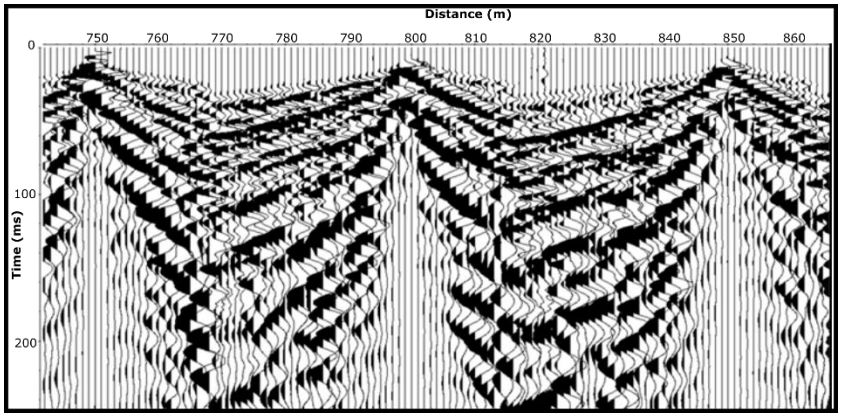

Figure 4.12: Raw shot gathers of seismic line 1 (Area 1) showing the far offset noise present in the data.

The seismic source for this survey was a 23 kg accelerated weight drop. . This has a dominant frequency around 65 Hz (Figure 4.13) which will need to be enhanced through further data processing for a better identification of the reflections within the raw shot gathers.

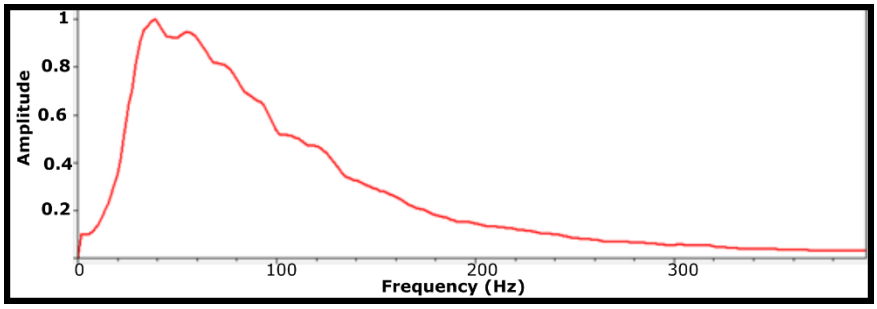

Figure 4.13: Frequency spectrum of the raw shot gathers for line 1 showing the dominant frequency at 65 Hz.

Figure 4.14 shows the interpreted seismic events that are clear on the raw shot gathers. Within the raw shot gathers there are the direct waves (D), refracted waves (R1 and R2), potential reflections (R) and the surface waves (air waves (A) and the ground roll (G)). The direct waves occur within the first 10 m of the shot gathers and have a velocity ranging from 600 to 1000 m/s. The refracted waves (R1 and R2) can be found from 10 m to 52 m from the shot and have velocities of 1800-2000 and 4500-5500 m/s. The surface waves (air wave and ground roll) fall within a range of 270 to 450 m/s. Due to the padding that the raw data has, the air waves are not very clear within the shot gathers. The reflections are also not entirely clear in the raw shot gathers.

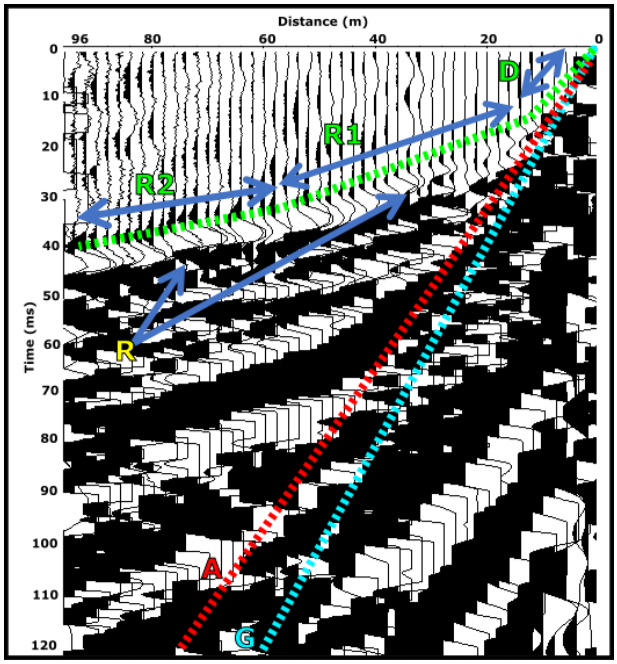

Figure 4.14: Interpreted raw shot gathers for line 1, D is the direct wave, R1 and R2 are the refracted waves, A is the air wave, G is the ground roll and R is the potential reflections in the data.

Table 4.4 represents the pre-stack processing steps that are taken to produce the seismic section for seismic line 1 followed by Figure 4.15 which shows the shot gathers for each step.

Table 4.4: Pre-stack processing steps that are taken to produce the seismic section for seismic line 1.

Processing step	Justification	Parameters
Top mute	From the raw shot gathers and observations during the data collection, the area was windy and had loose soil which caused some of the geophones to have less contact with the ground. This created the noisy traces seen in the far offsets of the raw shot gathers. The top mute was applied in order to remove this surface noise. Frequency content remains unaffected.	
Scaled window	To increase the amplitude of the shallow reflections and correct for the spherical divergence effects. The raw shot gathers show that the major reflections are well within this window and are enhanced through this process. Frequency content becomes 40 to 150 Hz.	0-300 ms (Figure 4.15 B).
Deconvolution	This step helps to remove the multiples within the data and the effect of source receiver coupling. The amplitudes of the multiples have been reduced. Frequency content becomes 30 to 250 Hz.	Predictive deconvolution of 0 to 150 ms with the 60 ms filter length and a 10 % lag (Figure 4.15 C).
Bandpass frequency	This removes the dominant surface waves within the data which occur at the lower frequencies. It is clear at this point that the reflections that were initially picked out exist and have been revealed by decreasing the noise caused by the surface waves in these data. Frequency content becomes 50 to 250 Hz.	The best filter used was a 3rd order Butterworth bandpass from 80 to 220 Hz (Figure 4.15 D).
Top mute	This was employed again in order to remove any noise that has been enhanced in the data. Frequency content remains unaffected.	
f-k filter	To remove the remaining low frequency signal in the data. Frequency content becomes 60 to 250 Hz.	A velocity filter is used ranging from 600 ms to 1000000 ms with a Hanning ^2. taper with a taper width of 5 for the f and k domains.
Top mute	This was employed again in order to remove any artefacts that have been enhanced in the data from the f-k filter. Frequency content remains unaffected.	Shot gathers with f-k filtering and top mute (Figure 4.15 E).

Automatic gain control (AGC) and time cut.	The AGC was used to enhance the late arriving events in the data and a time cut was used to remove the chance of overinterpreting the data. Frequency content remains unaffected on 60 to 250 Hz. AGC enhanced all of the noise in the first 100 ms creating spikes in the frequency spectrum.	100 ms AGC window and time cut of 120 ms (Figure 4.15 F).
Velocity analysis	The velocities were carefully picked for each reflection within the data. Frequency content remains unaffected.	The first reflection was ~ 1000 m/s (20 and 25 ms) while the second reflection has a velocity of ~ 3000 m/s and was (35 and 40 ms) (Figure 4.15 G).

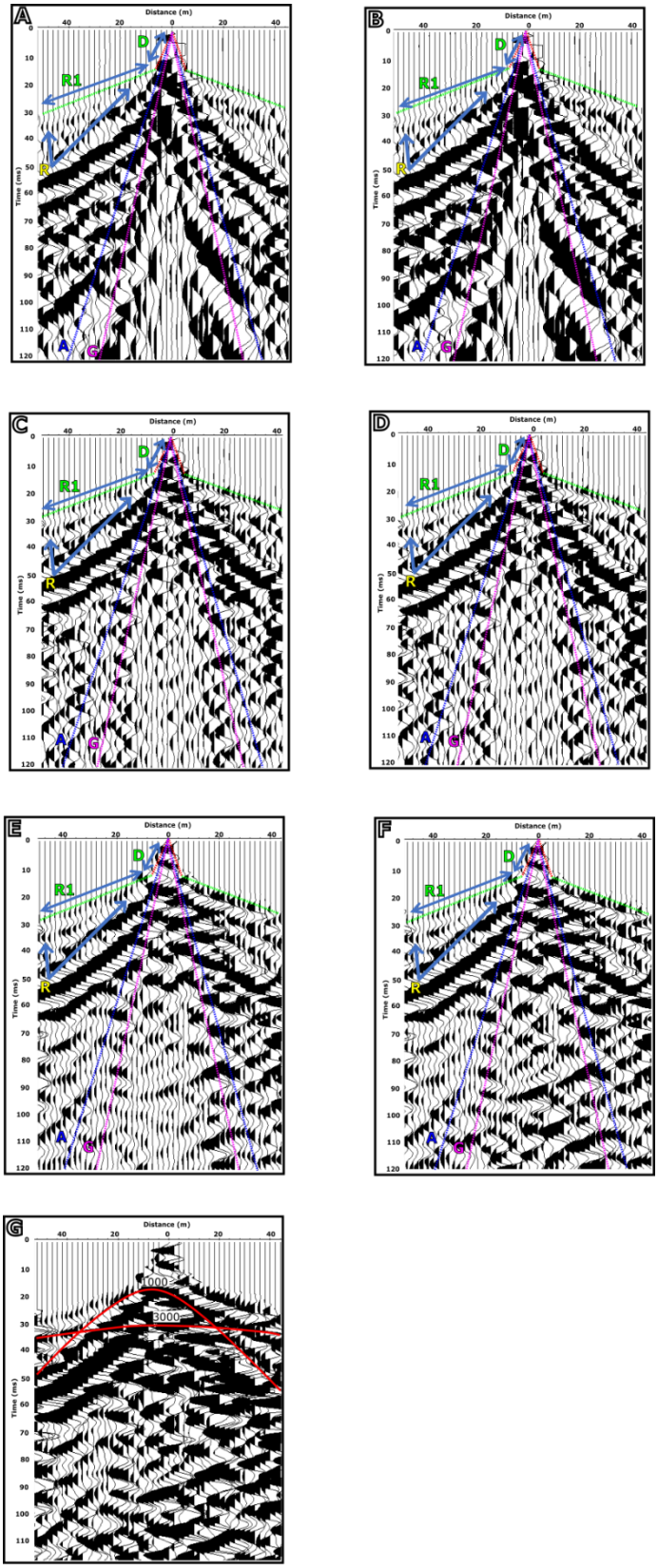

Figure 4.15: Pre-stack processing steps applied to seismic line 1: A) Raw shot gathers; B) Shot gathers after top mute and scaled window; C) Shot gather after predictive deconvolution; D Shot gathers after bandpass filtering; E) Shot gathers after f-k filtering and top mute; F) Shot gathers after automatic gain control and time cut; G) Velocity analysis of pre-stack shot gathers. D is the direct wave, R1 and R2 are the refracted waves, A is the air wave, G is the ground roll and R is the reflections in the data.

Table 4.5 represents the stacking and post-stack processing of seismic line 1.

Table 4.5: Stack and post-stack processing steps for seismic line 1.

Processing step	Justification	Parameters
NMO correction/ Stacking	The velocity model was used to correct the normal moveout of the reflections within the shot gathers. Once completed, the common midpoints for the data are then stacked to create the stacked section. Frequency content remains unaffected.	To avoid stretching of the data after the NMO corrections, a 45 % stretch mute was applied to the data with the correction (Figure 4.16 A).
Bandpass frequency	Applied to enhance the existing data within the targeted frequency range and remove any noise that the data inherited due to stacking. Frequency content becomes 50 to 150 Hz.	Filter created to preserve the frequency from 50 to 150 Hz (Figure 4.16 B).
Static correction	To correct for any surface inherited delays in the shot gathers. Frequency content remains unaffected.	(Figure 4.16 C).
Migration	Kirchoff migration applied to the stacked section to remove the effect of dipping strata. Frequency content remains unaffected.	Stacking velocity of 2000 m/s which is an average of all the velocities picked up in the tomography (Figure 4.16 D).
Time-depth conversion	To convert the seismic section to depth to allow for comparisons between the data collected. Frequency content remains unaffected.	This was also completed using a constant stacking velocity of 2000 m/s (Figure 4.16 E).
Bandpass	To remove any unwanted signal from the data. Frequency content remains unaffected.	The 3rd order Butterworth bandpass filter was applied to preserve the frequency between 50 and 150 Hz so only the original signal is in the data.
Automatic gain control	Applied so the reflections within the seismic section become enhanced. Frequency content remains unaffected.	20 ms intervals.
Bandpass	Applied to directly enhance only signal in the data from the weight drop. Frequency content becomes 65 to 130 Hz. The final frequency spectrum for line 1 shows that the frequency for the weight drop is significantly enhanced and preserved.	A final 3rd order Butterworth bandpass filter to preserve the frequency from 65 to 130 Hz (Figure 4.16 F).

Figure 4.16 displays the stack and post stack processing steps for seismic line 1.

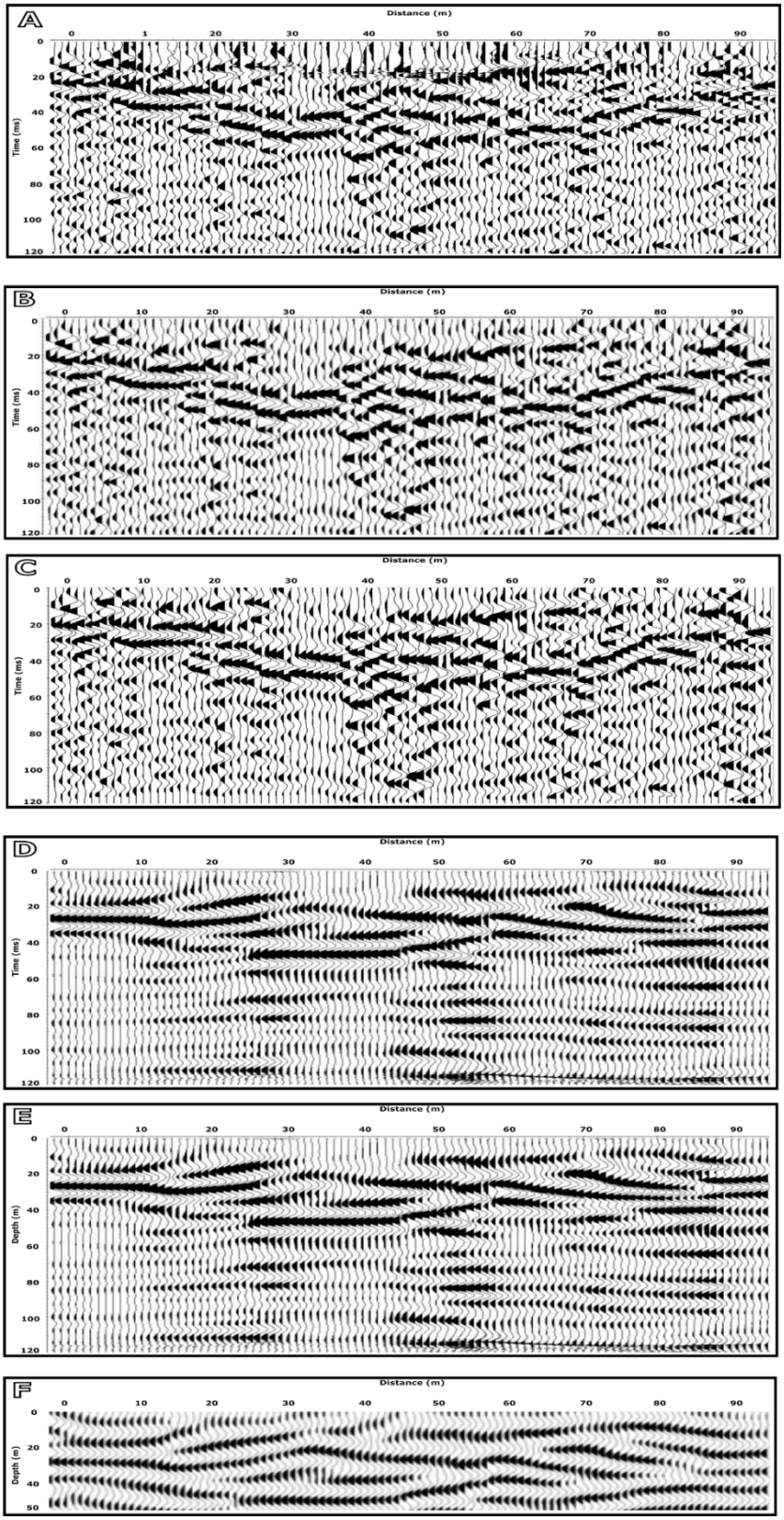

Figure 4.16: Stack and post-stack processing steps applied to seismic line 1: A) NMO correction and stacking; B) Bandpass frequency filtering; C) Static correction; D) Migration; E) Time-depth conversion; F) Final seismic section for seismic line 1.

Frequency spectrum for reflection seismic processing of seismic line 1 (Figure 4.17).

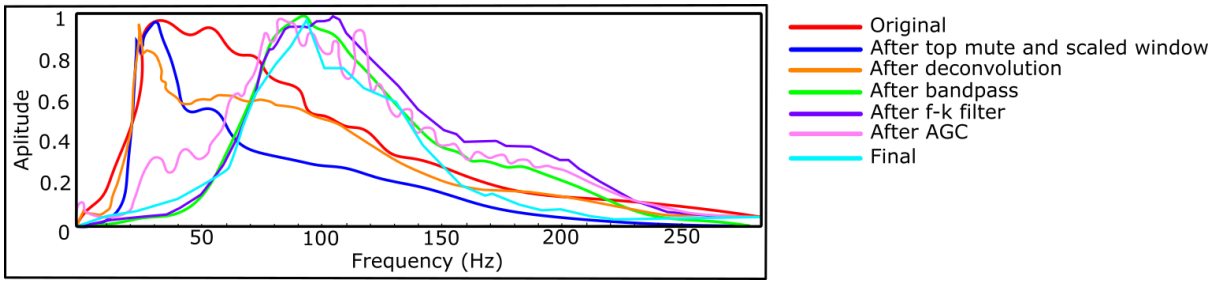

Figure 4.17: Frequency spectrum of shot gathers for seismic line 1: Original frequency (red line); After top mute and scaled window processing (blue line). The frequency content *after this processing is from 40 to 150 Hz, compared to the previous 30 to 200 Hz; After predictive deconvolution (orange line): the frequency that got enhanced is from 30 to 250 Hz; After bandpass filtering (green line): this filter preserved the frequencies from 50 to 250 Hz; After top mute and f-k filtering (purple line): the frequency that has been preserved is that from 60 to 250 Hz; After top mute and automatic gain control (pink line). Final frequency spectrum shows that the frequency for the weight drop is significantly enhanced and preserved (light blue line).*

4.3.2 Reflection seismic processing for seismic line 2

The raw shot gathers seismic line 2 (Figure 4.18) show some noise that was incurred in the far offsets for each shot. The major reflections within the data are not necessarily clear as they have a smaller amplitude than the surface waves within the data.

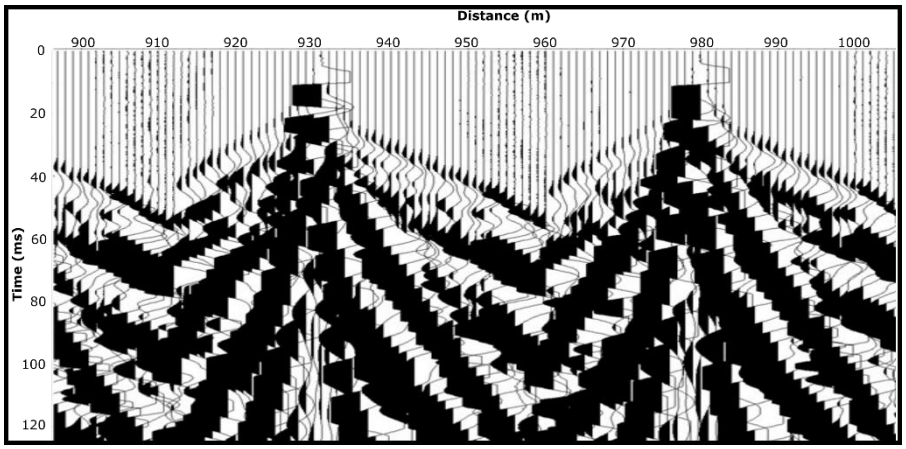

Figure 4.18: Raw shot gathers of seismic line 2 showing the noise in the far offsets.

The frequency content within the raw data is from 25 Hz to 200 Hz (Figure 4.19). The seismic source for this survey was a 9 kg hammer hitting a metal plate. This has a dominant frequency around 60 Hz which will need to be enhanced through further data processing for a better identification of the reflections within the raw shot gathers.

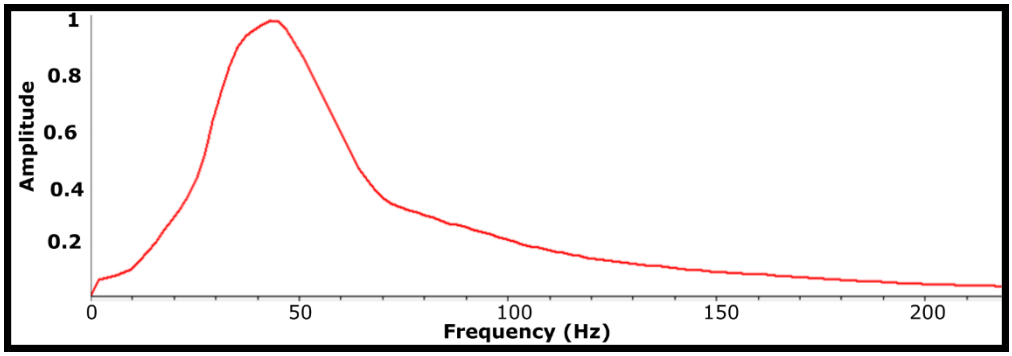

Figure 4.19: Frequency spectrum of the raw shot gathers for line 2.

Figure 4.20 shows the interpreted seismic events that are clear on the raw shot gathers. Within the raw shot gathers there are the direct waves (D), refracted waves (R1 and R2), potential reflections (R), the surface waves (air waves (A) and the ground roll (G)). The direct waves occur within the first 10 m of the shot gathers and have a velocity ranging from 350 to 400 m/s. The refracted waves (R1 and R2) can be found from 10 m and 52 m from the shot and have velocities of 1200-1500 and 1800-2500 m/s. The reflections are not entirely clear in the raw shot gathers. Surface waves (air wave and ground roll) fall within a range of 270 to 350 m/s. Due to the padding that the raw data has, the air waves are not very clear within the shot gathers.

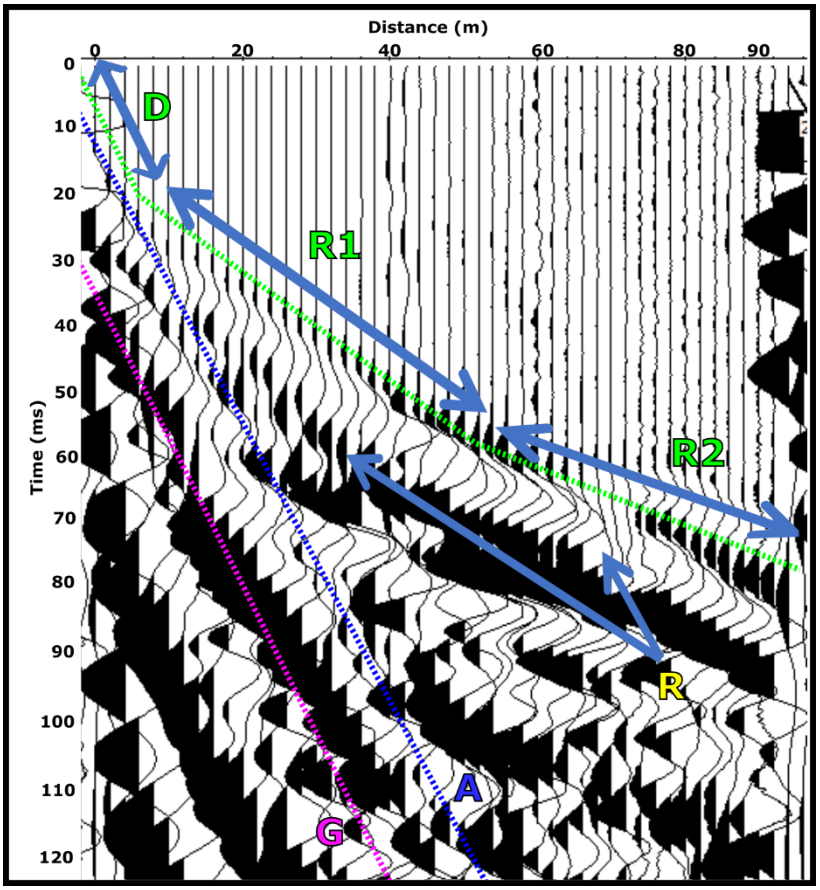

Figure 4.20: Interpreted raw shot gathers for line 2, D is the direct wave, R1 and R2 are the refracted waves, A is the air wave, G is the ground roll and R is the potential reflections in the data.

Table 4.6 represents the pre-stack processing steps that are taken to produce the seismic section for seismic line 2 followed by Figure 4.21 which shows the shot gathers for each step.

Table 4.6: Pre-stack processing steps that are taken to produce the seismic section for seismic line 2.

Processing step	Justification	Parameters
Top mute	From the raw shot gathers and observations during the data collection, the area was windy and had loose soil which caused some of the geophones to have less contact with the ground. This created the noisy traces seen in the far offsets of the raw shot gathers. The top mute was applied in order to remove this surface noise. Frequency content remains unaffected.	
Scaled window	To increase the amplitude of the shallow reflections and correct for the spherical divergence effects. The raw shot gathers show that the major reflections are well within this window and are enhanced through this process. Frequency content becomes 20 to 150 Hz.	0-300 ms (Figure 4.21 B).
Deconvolution	This step helps to remove the multiples within the data and the effect of source receiver coupling. The amplitudes of the multiples have been reduced. Frequency content becomes 30 to 200 Hz.	Deconvolution of 50 to 150 ms with the 60 ms filter length and a 5 % lag (Figure 4.21 C).
Bandpass frequency	This removes the dominant surface waves within the data which occur at the lower frequencies. It is clear at this point that the reflections that were initially picked out exist and have been revealed by decreasing the noise caused by the surface waves in these data. Frequency content becomes 50 to 150 Hz.	The best filter used was a 3rd order Butterworth bandpass to preserve the frequency from 50 to 150 Hz (Figure 4.21 D).
Top mute	This was employed again in order to remove any noise that has been enhanced in the data. Frequency content remains unaffected.	
f-k filter	To remove the remaining low frequency signal in the data Frequency content becomes 60 to 200 Hz.	A velocity filter is used ranging from 300 ms to 1000000 ms with a Hanning ^2 taper with a taper width of 5 for the f and k domains.
Top mute	This was employed again in order to remove any artefacts that have been enhanced in the data from the f-k filter. Frequency content remains unaffected.	Shot gathers with f-k filtering and top mute (Figure 4.21 E).

Automatic gain control (AGC) and time cut.	The AGC was used to enhance the late arriving events in the data and a time cut was used to remove the chance of overinterpreting the data. Frequency content remains unaffected on 60 to 200 Hz. AGC enhanced all of the noise in the first 100 ms creating spikes in the frequency spectrum.	100 ms AGC window and time cut of 150 ms.
Velocity analysis	The velocities were carefully picked for each reflection within the data. Frequency content remains unaffected.	The first reflection was ~ 800 m/s (20 and 30 ms) while the second reflection has a velocity of ~ 1000 m/s and (40 and 50 ms). The third reflection has a velocity of ~ 2000-3000 m/s (50 and 70 ms) (Figure 4.21 F).

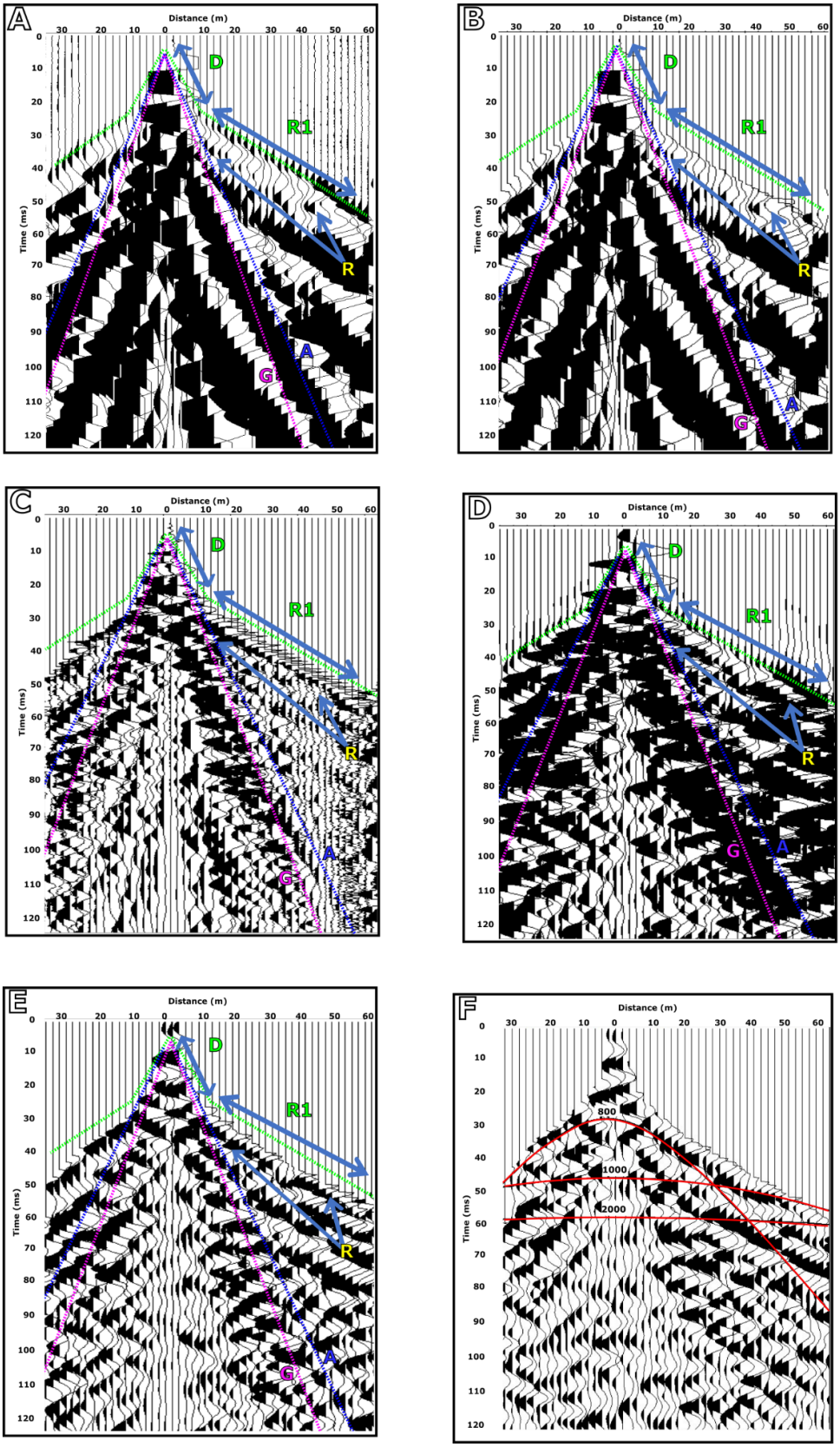

Figure 4.21: Pre-stack processing steps applied to seismic line 2: A) Raw shot gathers; B) Shot gathers after top mute and scaled window; C) Shot gather after deconvolution; D) Shot gathers after bandpass filtering; E) Shot gathers after f-k filtering and top mute; F) Velocity analysis of pre-stack shot gathers after automatic gain control and time cut. D is the direct wave, R1 and R2 are the refracted waves, A is the air wave, G is the ground roll and R is the reflections in the data.

Table 4.7 represents the stacking and post-stack processing of seismic line 2.

Table 4.7: Stacking and post-stack processing of seismic line 2.

Processing step	Justification	Parameters
NMO correction/ Stacking	The velocity model was used to correct the normal moveout of the reflections within the shot gathers. Once completed, the common midpoints for the data are then stacked to create the stacked section. Frequency content remains unaffected.	To avoid stretching of the data after the NMO corrections, a 45 % stretch mute was applied to the data with the correction (Figure 4.22 A).
Bandpass frequency	Applied to enhance the existing data within the targeted frequency range and remove any noise that the data inherited due to stacking. Frequency content becomes 50 to 150 Hz.	Filter created to preserve the frequency from 50 to 150 Hz (Figure 4.22 B).
Static correction	To correct for any surface inherited delays in the shot gathers. Frequency content remains unaffected.	(Figure 4.22 C).
Migration	Kirchoff migration applied to the stacked section to remove the effect of dipping strata. Frequency content remains unaffected.	Stacking velocity of 2000 m/s which is an average of all the velocities picked up in the tomography (Figure 4.22 D).
Time-depth conversion	To convert the seismic section to depth to allow for comparisons between the data collected. Frequency content remains unaffected.	This was also completed using a constant stacking velocity of 2000 m/s. (Figure 4.22 E).
Bandpass	To remove any unwanted signal from the data. Frequency content remains unaffected.	The 3rd order Butterworth bandpass filter was applied to preserve the frequency between 50 and 150 Hz so only the original signal is in the data
Automatic gain control	Applied so the reflections within the seismic section become enhanced. Frequency content remains unaffected.	20 ms intervals
Bandpass	Applied to directly enhance only signal in the data from the weight drop. Frequency content becomes 65 to 130 Hz. The final frequency spectrum for line 2 shows that the frequency for the hammer is significantly enhanced and preserved.	A final 3rd order Butterworth bandpass filter to preserve the frequency from 50 to 150 Hz (Figure 4.22 F).

Figure 4.22 displays the stack and post-stack processing steps for seismic line 2.

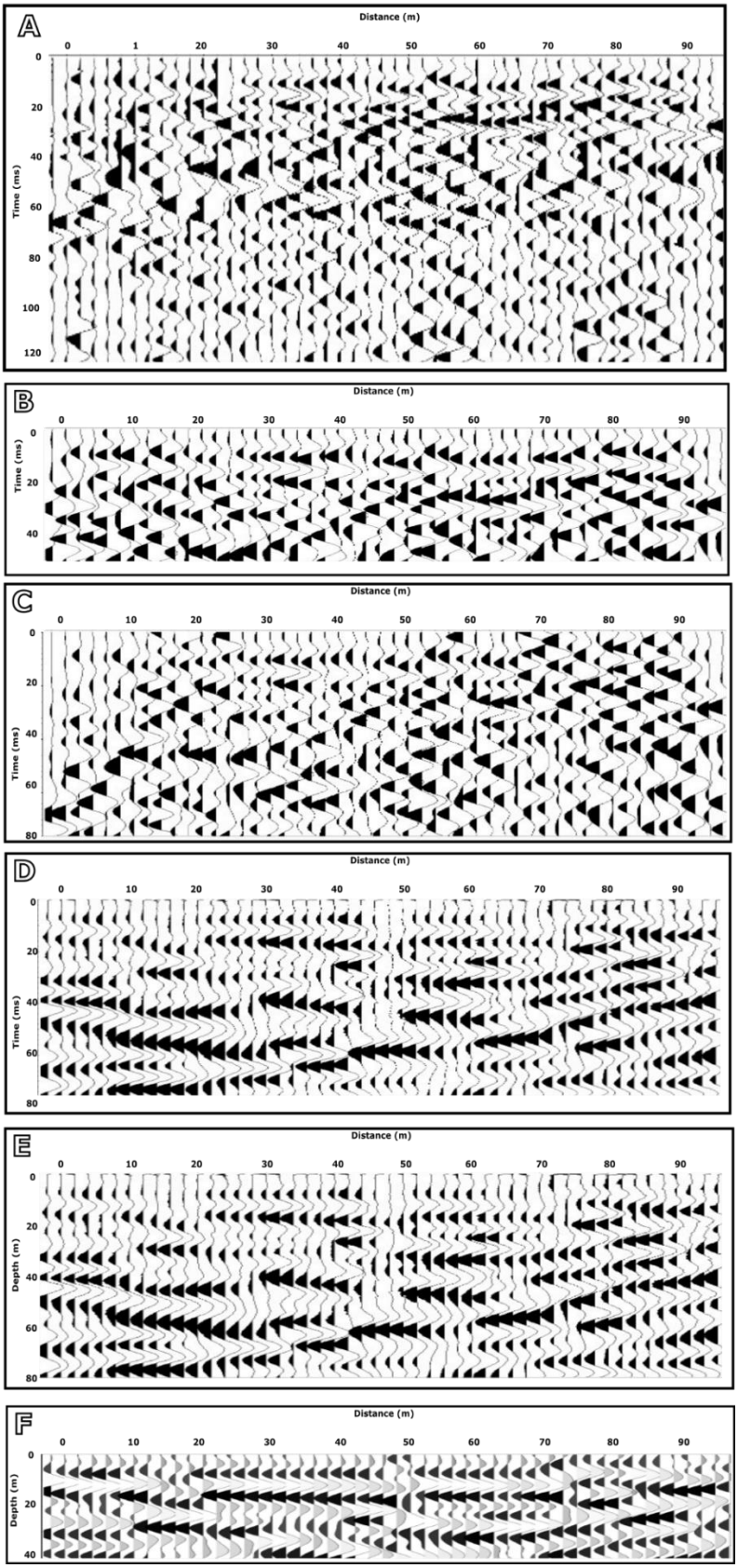

Figure 4.22: Post-stack processing steps applied to seismic line 2: A) NMO correction and stacking; B) Bandpass frequency filtering; C) Static correction; D) Migration; E) Time-depth conversion; F) Final seismic section for seismic line 2.

Frequency spectrum for reflection seismic processing of seismic line 2 (Figure 4.23).

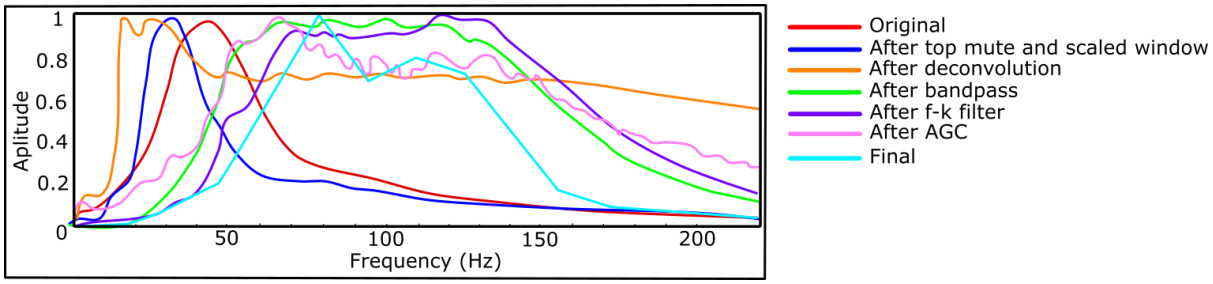

Figure 4.23: Frequency spectrum of shot gathers for seismic line 2: Original (red line) and after top mute and scaled window processing (blue line). The frequency content after this processing is from 20 to 150 Hz, compared to the previous 25 to 200 Hz; After deconvolution (orange line): the frequency that got enhanced is from 30 to 200 Hz; After bandpass filtering (green line); this filter preserved the frequencies from 50 to 150 Hz; After top mute and f-k filtering (purple line): the frequency that has been preserved is that from 60 to 200 Hz; After top mute and automatic gain control (pink line): the frequency that is preserved is that from 50 to 150 Hz; Final frequency spectrum (light blue line) shows that the frequency for the weight drop is significantly enhanced and preserved.

4.3.3 Reflection seismic processing for seismic line 3

The raw shot gathers for seismic line 3 (Figure 4.24) show some noise that was incurred in the far offsets for each shot. The major reflections within the data are not necessarily clear as they have a smaller amplitude than the surface waves within the data.

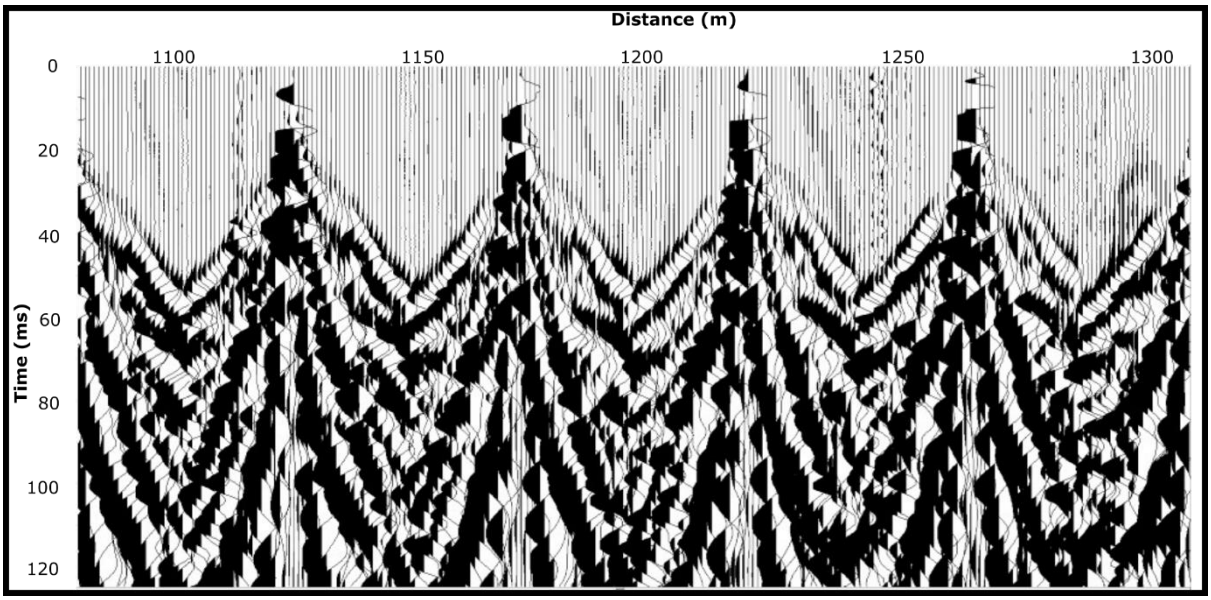

Figure 4.24:Raw shot gathers of seismic line 3 showing the noise in the far offsets.

The frequency content within the raw data is from 25 Hz to 200 Hz (Figure 4.25). The seismic source for this survey was a 9 kg hammer hitting a metal plate providing a dominant frequency around 60 Hz.

Enhancing this frequency will allow for a better identification of the reflections within the raw shot gathers.

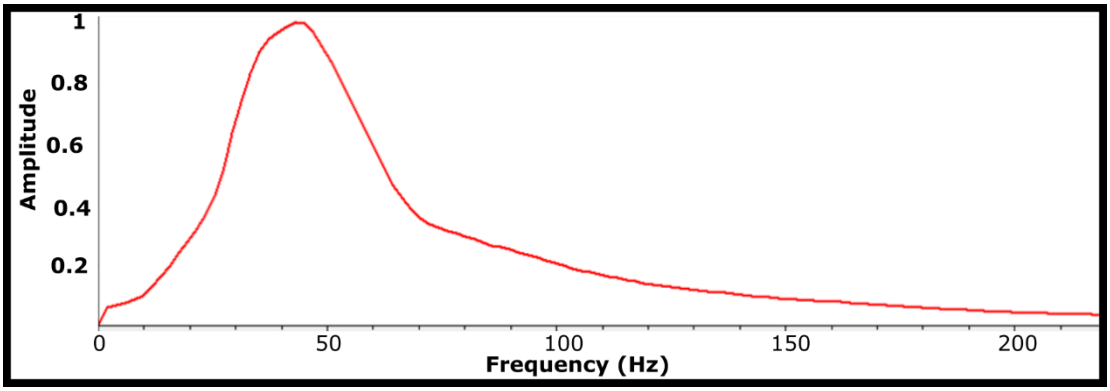

Figure 4.25: Frequency spectrum of the raw shot gathers for line 3.

Figure 4.26 shows the interpreted seismic events that are clear on the raw shot gathers. Within the raw shot gathers there are the direct waves (D), refracted waves (R1 and R2) , potential reflections (R), the surface waves (air waves (A) and the ground roll (G)). The direct waves occur within the first 10 m of the shot gathers and have a velocity ranging from 270 to 350 m/s. The refracted waves (R1 and R2) can be found from 10 m and 50 m from the shot and have velocities of 400-900 and 1000-1600 m/s. The reflections are not entirely clear in the raw shot gathers. Surface waves (air wave and ground roll) fall within a range of 270 to 350 m/s. Due to the padding that the raw data has, the air waves are not very clear within the shot gathers.

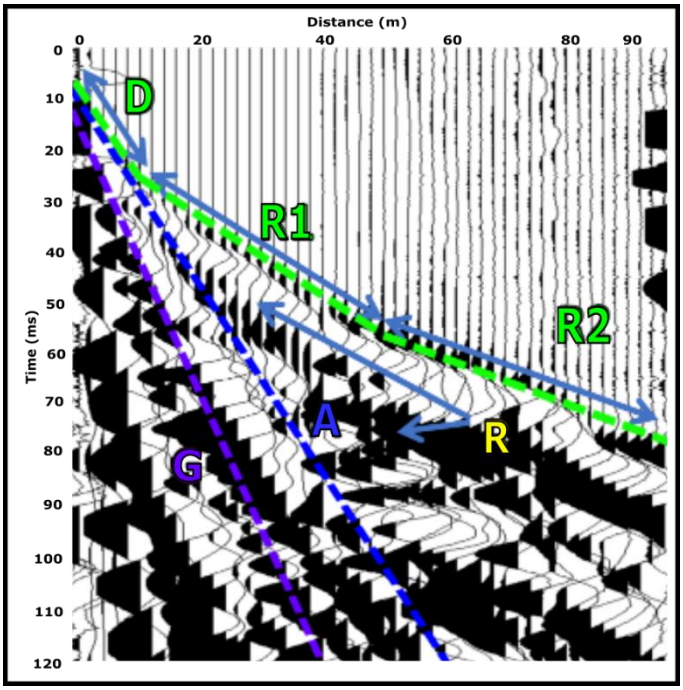

Figure 4.26: Interpreted raw shot gathers for line 3, D is the direct wave, R1 and R2 are the refracted waves, A is the air wave, G is the ground roll and R is the potential reflections in the data.

Table 4.8 represents the pre-stack processing steps that are taken to produce the seismic section for seismic line 3 followed by Figure 4.27 which shows the shot gathers for each step.

Table 4.8: Pre-stack processing steps that are taken to produce the seismic section for seismic line 3.

Processing step	Justification	Parameters
Top mute	From the raw shot gathers and observations during the data collection, the area was windy and had loose soil which caused some of the geophones to have less contact with the ground. This created the noisy traces seen in the far offsets of the raw shot gathers. The top mute was applied in order to remove this surface noise. Frequency content remains unaffected.	
Scaled window	To increase the amplitude of the shallow reflections and correct for the spherical divergence effects. The raw shot gathers show that the major reflections are well within this window and are enhanced through this process. Frequency content becomes 30 to 150 Hz.	0-300 ms (Figure 4.27 B).
Deconvolution	This step helps to remove the multiples within the data and the effect of source receiver coupling. The amplitudes of the multiples have been reduced. Frequency content becomes 30 to 200 Hz.	Deconvolution of 50 to 150 ms with the 60 ms filter length and a 5 % lag (Figure 4.27 C).
Bandpass frequency	This removes the dominant surface waves within the data which occur at the lower frequencies. It is clear at this point that the reflections that were initially picked out exist and have been revealed by decreasing the noise caused by the surface waves in these data. Frequency content becomes 50 to 120 Hz.	The best filter used was a 3rd order Butterworth bandpass to preserve the frequency from 50 to 100 Hz (Figure 4.27 D).
Top mute	This was employed again in order to remove any noise that has been enhanced in the data. Frequency content remains unaffected.	
f-k filter	To remove the remaining low frequency signal in the data. Frequency content becomes 65 to 150 Hz.	A velocity filter is used ranging from 300 ms to 1000000 ms with a Hanning ^2 taper with a taper width of 5 for the f and k domains.
Top mute	This was employed again in order to remove any artefacts that have been enhanced in the data from the f-k filter. Frequency content remains unaffected.	Shot gathers with f-k filtering and top mute (Figure 4.27 E).
Automatic gain control	The AGC was used to enhance the late arriving events in the data and a time cut was used to remove the chance of overinterpreting the data.	100 ms AGC window and time cut of 150 ms (Figure 4.27 F).

(AGC) and time cut.	Frequency content remains unaffected on 65 to 150 Hz. AGC enhanced all of the noise in the first 100 ms creating spikes in the frequency spectrum.	
Velocity analysis	The velocities were carefully picked for each reflection within the data. Frequency content remains unaffected.	The first reflection was ~ 600-800 m/s (20 and 30 ms) while the second reflection has a velocity of ~ 1000-1200 m/s (30 and 40 ms). The third reflection has a velocity of ~ 1400-3000 m/s (50 and 60 ms) (Figure 4.27 G).

Figure 4.27 shows the pre-stack processing steps for seismic line 3.

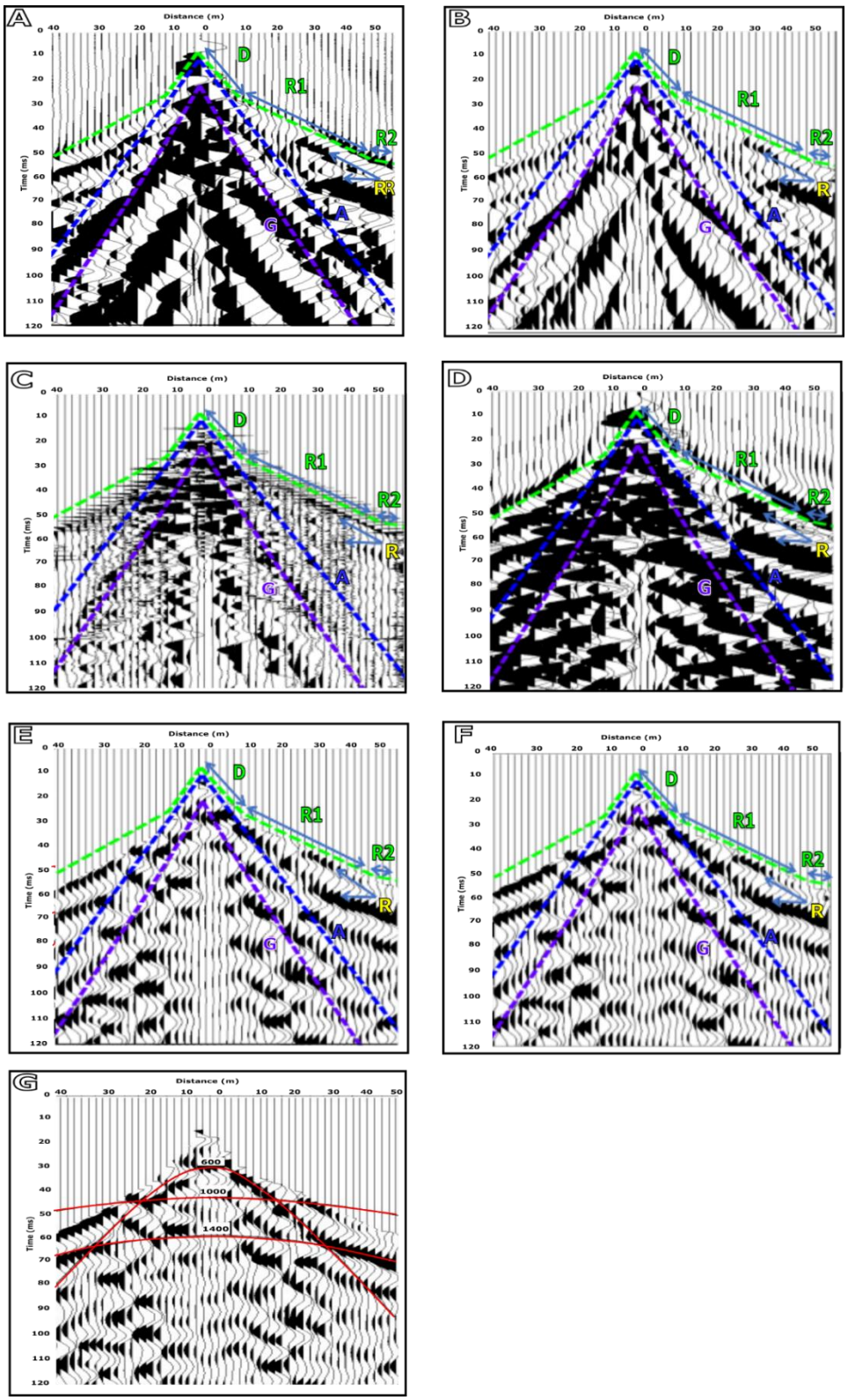

Figure 4.27: Pre-stack processing steps applied to seismic line 2: A) Raw shot gathers; B) Shot gathers after top mute and scaled window; C) Shot gather after deconvolution; D) Shot gathers after bandpass filtering; E) Shot gathers after f-k filtering and top mute; F) Shot gathers after automatic gain control and time cut; G) Velocity analysis of pre-stack shot gathers. D is the direct wave, R1 and R2 are the refracted waves, A is the air wave, G is the ground roll and R is the reflections in the data.

Table 4.9 represents the stacking and post-stack processing of seismic line 3.

Table 4.9: Stacking and post-stack processing of seismic line 3.

Processing step	Justification	Parameters
NMO correction/ Stacking	The velocity model was used to correct the normal moveout of the reflections within the shot gathers. Once completed, the common midpoints for the data are then stacked to create the stacked section. Frequency content remains unaffected.	To avoid stretching of the data after the NMO corrections, a 45 % stretch mute was applied to the data with the correction (Figure 4.27 A).
Static correction	To correct for any surface inherited delays in the shot gathers. Frequency content remains unaffected.	(Figure 4.27 B)
Migration	Kirchoff migration applied to the stacked section to remove the effect of dipping strata. Frequency content remains unaffected.	Stacking velocity of 1000 m/s which is an average of all the velocities picked up in the tomography (Figure 4.27 C).
Time-depth conversion	To convert the seismic section to depth to allow for comparisons between the data collected. Frequency content remains unaffected.	This was also completed using a constant stacking velocity of 1000 m/s (Figure 4.27 D).
Bandpass	To remove any unwanted signal from the data. Frequency content remains unaffected.	The 3rd order butterworth bandpass filter was applied to preserve the frequency between 50 and 150 Hz so only the original signal is in the data.
Automatic gain control	Applied so the reflections within the seismic section become enhanced. Frequency content remains unaffected.	20 ms intervals.
Bandpass	Applied to directly enhance only signal in the data from the weight drop. Frequency content becomes 65 to 130 Hz. The final frequency spectrum for line 3 shows that the frequency for the hammer is significantly enhanced and preserved.	A final 3rd order butterworth bandpass filter to preserve the frequency from 60 to 180 Hz (Figure 4.16 E).

Figure 4.28 displays the stack and post stack processing steps for seismic line 3.

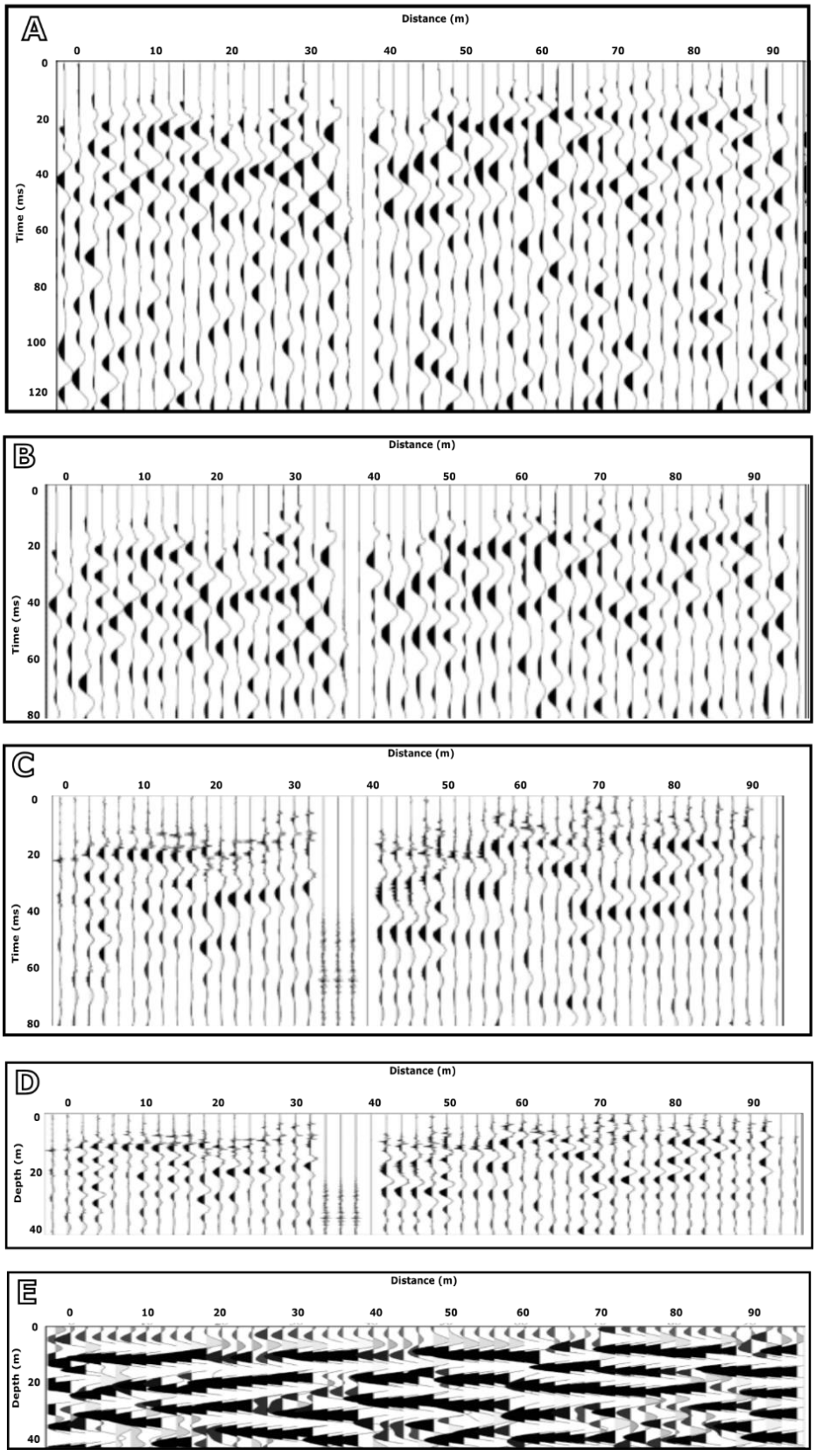

Figure 4.28: Post-stack processing steps applied to seismic line 3: A) NMO correction and stacking; B) Static correction; C) *Migration;* D) *Time-depth conversion;* E) *Final seismic section for seismic line 3.*

Frequency spectrum for reflection seismic processing of seismic line 3 (Figure 4.29).

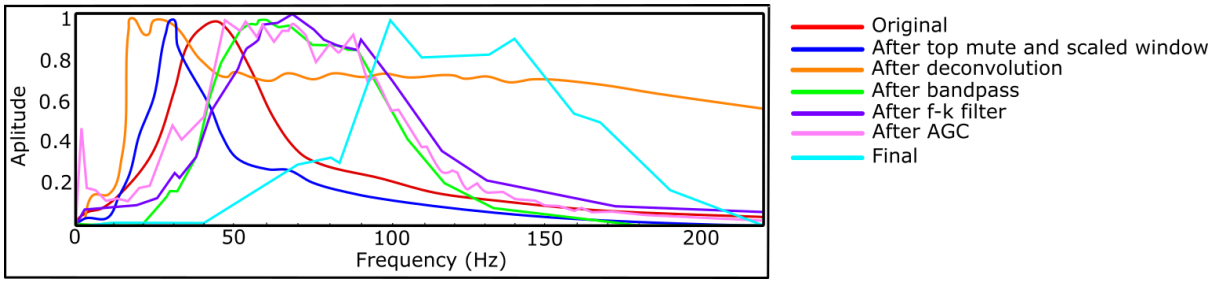

Figure 4.29: Frequency spectrum of shot gathers for seismic line 3:) Original (red line) and after top mute and scaled window processing (blue line). The frequency content after this processing is from 30 to 150 Hz, compared to the previous 25 to 200 Hz; After deconvolution (orange line): the frequency that got enhanced is from 30 to 200 Hz: After bandpass filtering (green line): this filter preserved the frequencies from 50 to 120 Hz; After top mute and f-k filtering (purple line): the frequency that has been preserved is that from 65 to 150 Hz; Automatic gain control and time cut (pink line): the frequency that is preserved is that from 50 to 100 Hz; G) Final frequency spectrum (light blue line) shows that the frequency for the hammer is significantly enhanced and preserved.

4.4 Legacy seismic data acquisition

The RZ-254 six second TWT vibroseis lines that is 105 km long and crosses the study area as seen in Figure 1.2 will be further analysed in this study. The refraction tomography images will be used to further understand the shallow subsurface over the entire Far Western Limb. This was not done in the previous study (Tinker et al., 2002) that mapped the deeper subsurface along the section. The acquisition parameters for this study can be found in Table 4.10.

Table 4.10: Acquisition parameters for the legacy 6 second TWT 2D seismic reflection data.

Survey parameters	
Type of survey	2D
Year	1988
Profile length	105 km
Trend	NNE-SSW
Split spread	2975-25-X-25-2975 (m)
Nominal fold	60
Recording system	
Recording device	Sercel 368
Sampling rate	4ms
Record length	6 s
Sweep length	18 s
Sweep frequencies	10-61 Hz
Source information	
Source spacing	50 m
Source type	4 Pelton MK II vibrators in a line
Receiver information	
Receiver spacing	50 m
Geophone type	10Hz (SM4U)

The data are used to create the refraction tomography representing the seismic velocities that dominate the subsurface. This requires the first break picking for each shot (in Globe Claritas) and setting up the geometry of the data. Figure 4.30 shows the first break picks for one on the shots along the RZ-254 legacy seismic line.

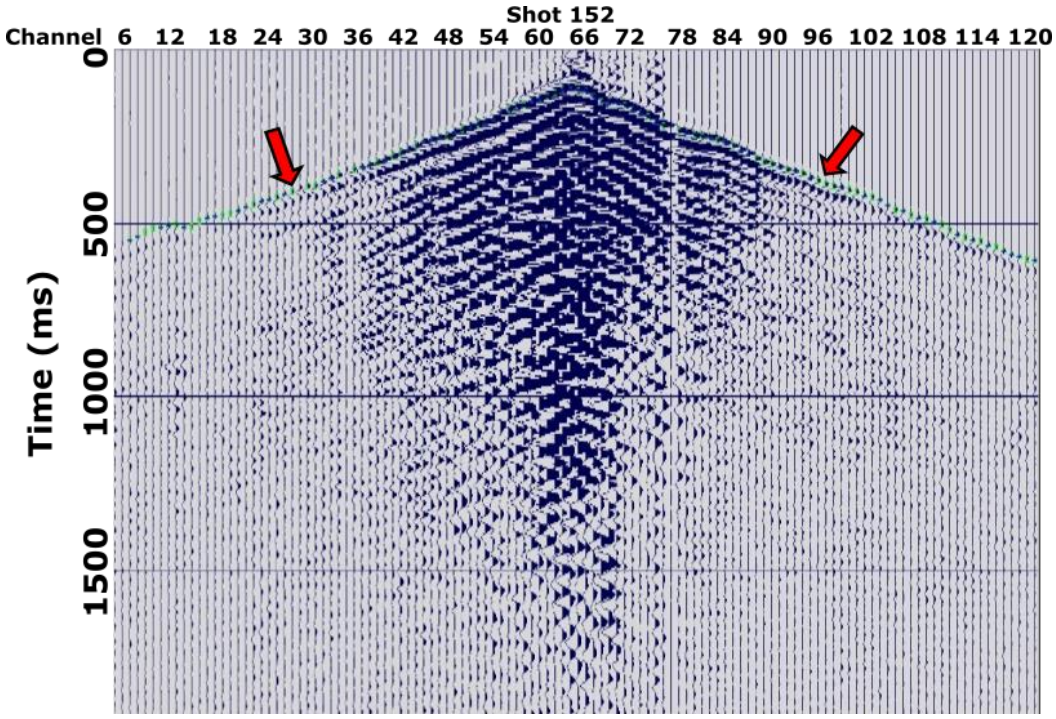

Figure 4.30: First break picks along the legacy seismic line RZ-254 indicated by the red arrows.

The trace headers in the raw data first needed to be reassigned and defined to allow the SEG-Y files to be compatible with Globe Claritas. Then receiver and shot pegs needed to be assigned peg numbers. This then shows that the shot and receiver elevations were not coinciding along the same tomography. The geometry file was exported into SPS files, where the receiver elevation was corrected from using the nearest neighbour scattered interpolation function in MATLAB. This then corrected the geometry files, which were then merged with the SEG-Y files and then run though Tomoplus on a smoothed 5 x 5 m grid, creating the seismic tomography for each section. The comparison between the synthetic first break picks for the modelled tomography and the actual first break picks shows that they all occur within 10 ms of each other for the seismic lines.

5 Results

This chapter lays out the thin section and geophysical data used to characterise the subsurface of area 1 and 2. The geophysical data include reflection seismic, resistivity and magnetic data.

5.1 Thin section analysis

5.1.1 Area 1

Table 5.1 describes the geological samples that were collected for analysis in area 1 and Figure 5.1 shows the corresponding thin sections.

Table 5.1: Descriptions of geological samples for Area 1.

Sample	Outcrop/Loose	Hand sample description	Thin section description	Figure
S001	Loose bolder – not from surrounding outcrop.	Dark brown. fresh surface of this sample showing light grey to white grains (< 1 mm) within an unidentifiable matrix.	0.5 to 1 mm of quartz grains (~ 90 %) which have a fine-grained unidentifiable matrix (10 %) forming a granular texture. Shows evidence of both overgrowth and compaction with minor fracturing amongst the grains.	5.1 A 5.1 B
S004	Boulders from the existing outcrops.	Rusted brown colour on the weathered side while the fresh surface has ~ 2 mm size grains which are either dark grey (90 %) or green in colour (10 %).	Fractured euhedral to anhedral grains (< 3 mm) of orthopyroxene (90 %) with some intercumulus clinopyroxene (10 %). Adcumulate texture with evidence for annealing. All the grains are highly fractured.	5.1 C

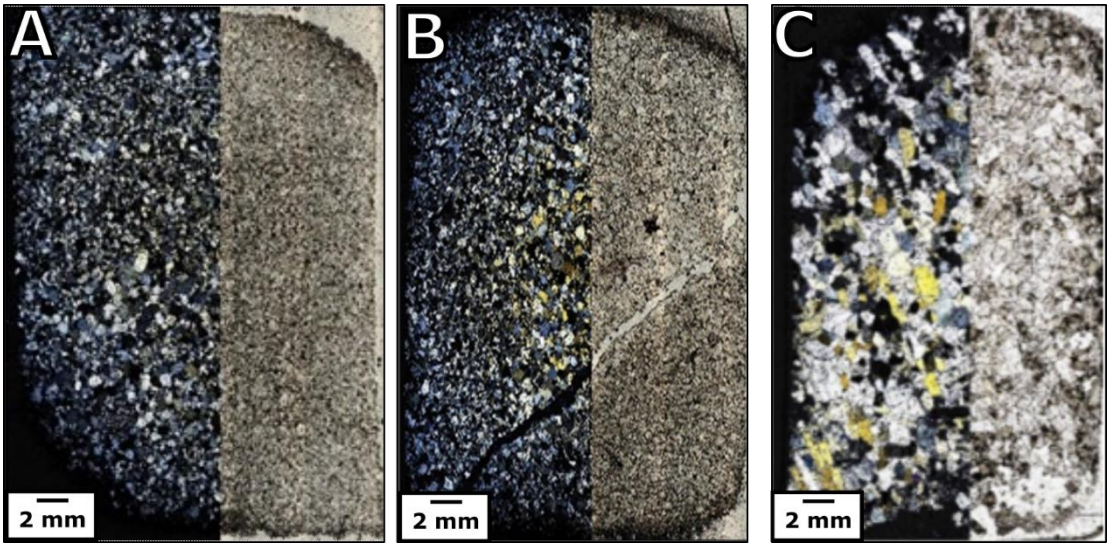

Figure 5.1: Cross and plain polarised light of samples A) S001, B) S001 exhibiting fracture and C) S004.

5.1.2 Area 2

Table 5.2 describes the geological samples that were collected for analysis in area 2 and Figure 5.2 shows the corresponding thin sections.

Table 5.2: Descriptions of geological samples for Area 2.

Sample	Outcrop/Loose	Hand sample description	Thin section description	Figure
S002	Highly weathered counterpart of S005. Outcrop exposed through agricultural digging.	Light grey to white colour, is extremely brittle, and contains micas (30 %) < 2 mm. The remaining grains within the sample are too small to identify.	Fine-grained (~ 0.5 mm) biotite grains (80 %). Visible within the thin section is a 2 mm grain of plagioclase which has evidence for zoning. Smaller subhedral grains (< 1 mm) of plagioclase (15 %) occurring in clusters (< 1 mm). The remaining grains (5 %) are opaques.	5.2 A
S005	Fine-grained sample (~ 1 mm) with much lower degree of weathering as compared to sample S002. Outcrop exposed through agricultural digging.	Micas accompanied by green, dark grey, and white grains.	Anhedral to subhedral grains (~ 1 mm) of orthopyroxene (50 %) within a plagioclase bearing intercumulus (20 %) in a poikilitic texture. Some orthopyroxene altered to tremolite (30 %) which have their characteristic green pleochroism, and fibrous texture while others display exsolution lamellae with the clinopyroxene. Within the intercumulus plagioclase, there are grains (< 0.5 mm) of clinopyroxene. All the grains within the sample are highly fractured.	5.2 B
S003	Loose samples.	Fine-grained (< 0.5 mm). Dark grey colour within no clear laminations present.	Sub-rounded to angular grains (< 0.5 mm) of quartz (90 %) hosted within an unknown matrix (10 %). Laminations (< 0.5 mm) are present within the sample and only visible in the thin section. A few grains show clear annealing with an overall granular texture.	5.2 C
S007	Loose samples.	Fine-grained (< 0.5 mm) sample that are dark grey to black and have light brown to orange veins (< 2 mm) that both cross-cut and follow the laminations (<0.5 mm).	Quartz (95%) and some unidentified minerals within the matrix. The veins (~ 0.8 mm) are quartz-rich and have recrystallized some of the surrounding grains allowing them to have an interlocking nature and become much larger (< 1 mm). The quartz grains further away from the veins maintain their angular to subrounded shape. Some of these veins follow the microfractures in the sample.	5.2 D

S006	Loose samples.	Dark grey to black colour with fine grains (< 0.5 mm). Laminations and micro fracturing are visible. Some of the grains (< 1 mm) within the sample have a shiny silvery colour and occur in a speckled nature throughout the sample.	Rounded to subrounded opaque grains (~ 75%) and random clusters of angular to sub-rounded grains (< 0.5 mm) of quartz (~ 20 %). Opague minerals identified as haematite nodules that follow the microfractures in some cases. Pyrite is also identifiable within the sample (< 5%) and consists of small blobs (< 0.5 mm) occurring in irregular patterns throughout the sample.	5.2 E

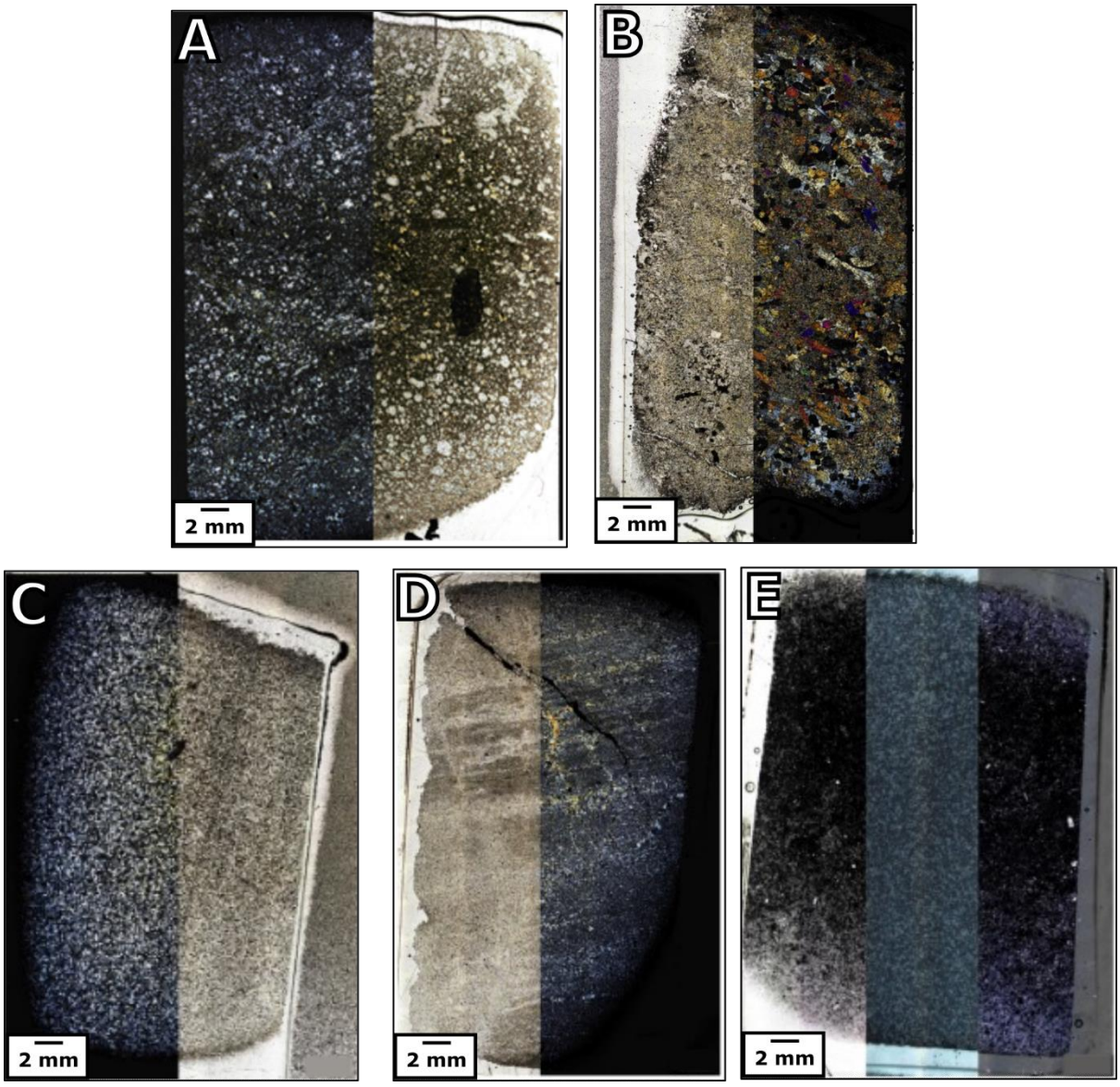

Figure 5.2: Cross and plain polarised light of samples A) S002, B) S005, C) S003, D) S007. E) S006 shows plain, cross polarised and reflect light.

5.2 Physical property data

The samples that were collected were cut into blocks to conduct each physical property measurement. Most of the samples were cut into multiple blocks to allow for repeat measurements. The results are listed in Table 5.3 and Table 5.4.

5.2.1 Area 1

Table 5.3: Physical property measurements for sample S001 and S004.

Possible rock type	Sample	Density (g/cm^3)	Resistivity (Ohm.m)	P-wave velocity (m/s)	P-wave Anisotropy (%)	S-wave velocity (m/s)	S-wave Anisotropy (%)	Susceptibility (E-06)
Quartzite	S001 A	2,62	1604,97	3567,53	7,58	1675,87	22,35	-10,08
	S001 B	2,63	1599,39	3553,17	8,64	1863,60	21,44	-8,94
	S001 C	2,63	2210,80	4067,97	16,42	1967,17	12,12	-10,19
	S001 D	2,61	1226,79	3935,67	18,05	1823,43	23,73	-8,60
	Average S001	2,62	1660,49	3781,03	12,67	1832,52	19,91	-9,45
Pyroxenite	Average S004 1	3,26	1802,52	5520,43	34,15	1603,43	62,78	504,41
	S004 2A	3,24	407,30	1787,83	34,68	483,83	24,33	552,24
	S004 2B	3,25	651,48	1894,97	28,67	486,03	22,36	523,31
	Average S0042	3,25	529,39	1841,40	32,50	484,93	36,49	537,77

5.2.2 Area 2

Table 5.4: Physical property measurements for samples S002, S003, S005, S006, S007 and S008.

Possible rock type	Sample number	Density (g/cm3)	Resistivity (Ohm.m)	P-wave velocity (m/s)	P-wave Anisotropy (%)	S-wave velocity (m/s)	S-wave Anisotropy (%)	Susceptibility (E-06)
Norite	S002 A	2,79	2007,94	5255,90	31,87	1880,93	67,42	364,85
	S002 B	2,80	4380	5670,57	11,85	2438,47	21,72	298,27
	S002 C	2,85	9021,95	6369,13	1,63	3053	13,27	421,78
	S002 D	2,80	2937,04	5765,47	9,18	1859,77	10,94	317,25
	Average S002	2,81	4586,83	5765,27	12,67	2308,04	19,91	350,54
	S005 A	3,13	2660,78	6213,57	17,86	2195,73	49,97	579,71
	S005 B	3,15	3371,38	6699,83	50,86	1971,10	15,78	487,61
	Average S005	3,15	3016,08	6456,70	34,36	2083,40	32,88	533,66
Siltstone	S003 A	2,71	5697,56	5704,83	8,36	2727,83	5,65	320,94
	S003 B	2,72	6636,85	5390,63	1,28	1937,53	22,88	346,48
	S003 C	2,71	7050,12	5452,63	6,83	2093,74	31,52	295,11
	Average S003	2,711	6461,51	5516,13	5,49	2248,32	20,02	320,83
	S006 A	2,98	6356,63	6638,47	3,82	1890,20	13,12	373,39
	S006 B	3,03	5254,01	6232,33	11,47	1890,20	8,12	616,40

	Average S006	3,01	5805,32	6435,40	7,64	1990	10,62	494,90
	S007 A	2,63	2746,86	5489,10	22,75	1932,67	33,17	1106,51
	S007 B	2,63	4457,47	5305,03	6,80	1944,63	33,95	1842,76
	Average S007	2,63	3602,16	5937,07	14,77	1938,65	33,56	1474.64

5.3 Field seismic data

The refraction tomography was primarily created to understand the velocities and thicknesses of the near-surface lithologies. The refraction tomography together with the ray tracing for each line can be found below.

5.3.1 Seismic line 1

The ray tracing (Figure 5.3 A) and the refraction tomography (Figure 5.3 B) for line 1 show the subsurface seismic velocities (ranging from 400 to 4400 m/s) with a total reliable depth penetration of ~ 20 m. Clear regions of equal seismic velocities are found in the seismic tomography which increase with depth. The shallow lithologies (< 10 m) consist of velocities lower than 2000 m/s while the deeper lithologies (> 10 m) consist mainly of velocities around 4000 m/s.

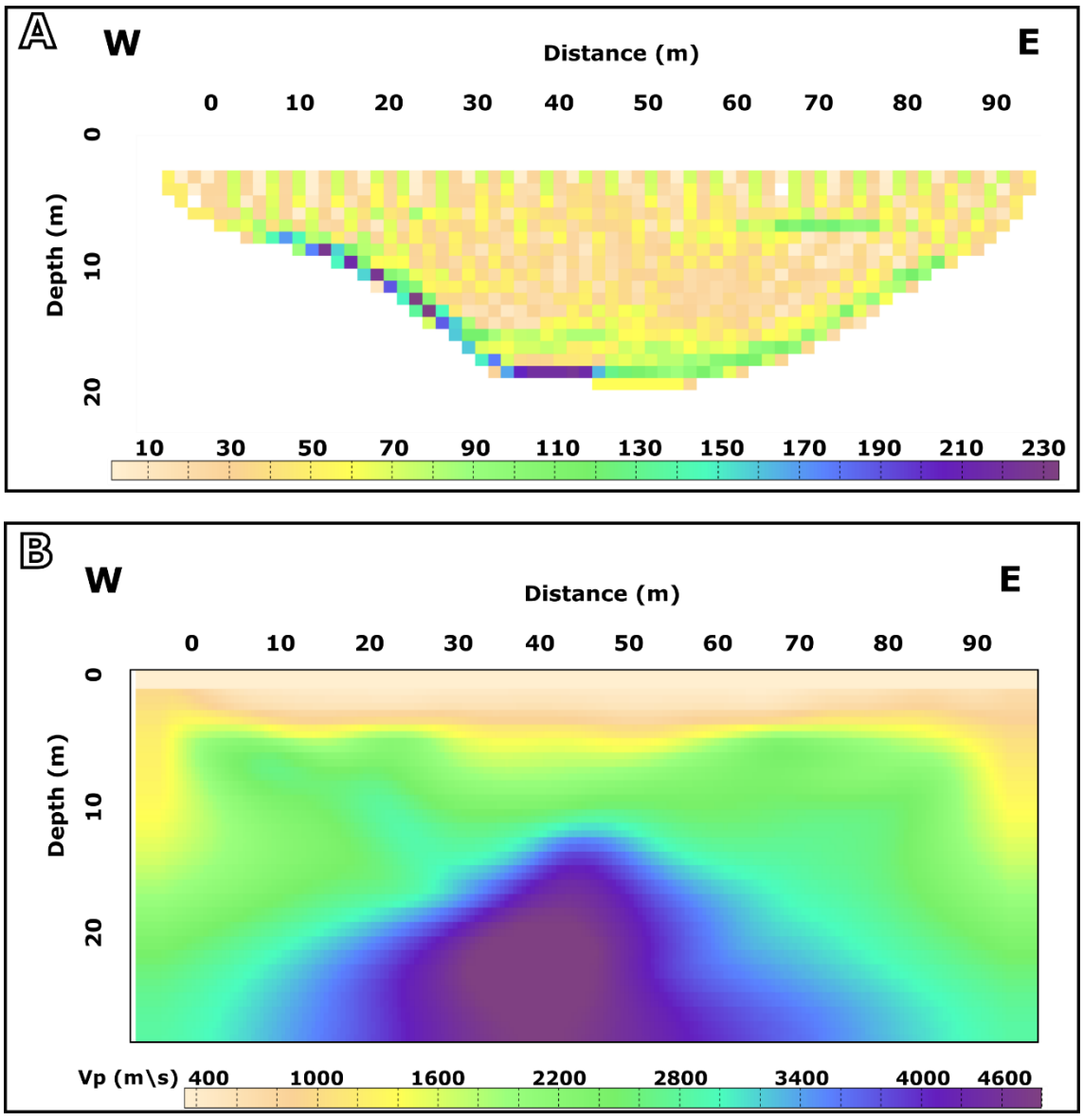

Figure 5.3: A) Ray tracing and B) seismic tomography of seismic line 1.

The final reflection seismic section for seismic line 1 (Figure 5.4).

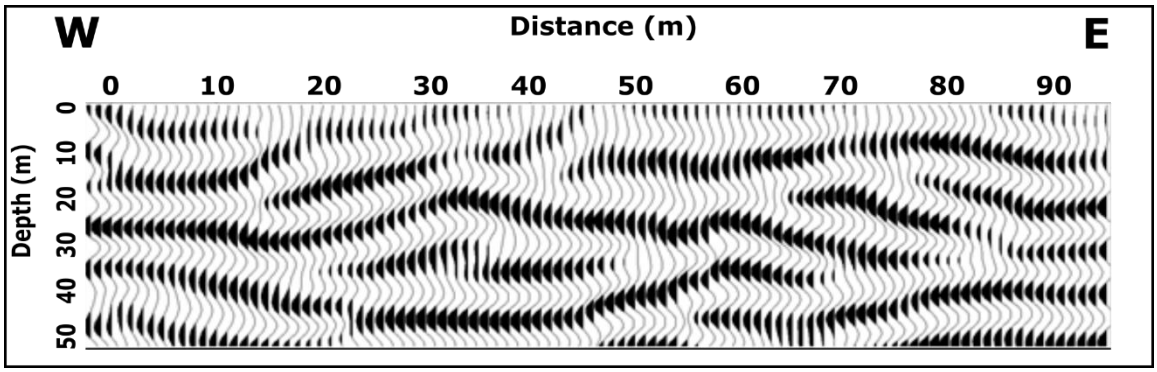

Figure 5.4: Seismic section for line 1.

The final frequency spectrum for line 1 shows that the frequency for the weight drop is significantly enhanced and preserved (Figure 5.5). This gives some confidence in the result that the correct frequency has been enhanced in the data.

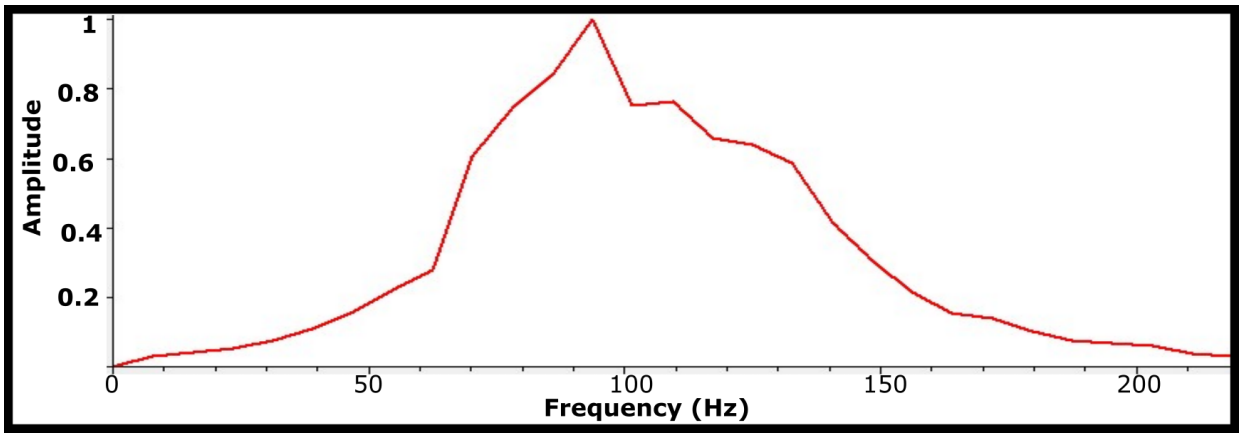

Figure 5.5: Frequency spectrum for the seismic section of seismic line 1.

5.3.2 Seismic line 2

The ray tracing (Figure 5.6 A) and the refraction tomography (Figure 5.6 B) for line 2 shows the seismic wave velocities (ranging from 400 to 3800 m/s) with a total reliable depth penetration of ~ 30 m.

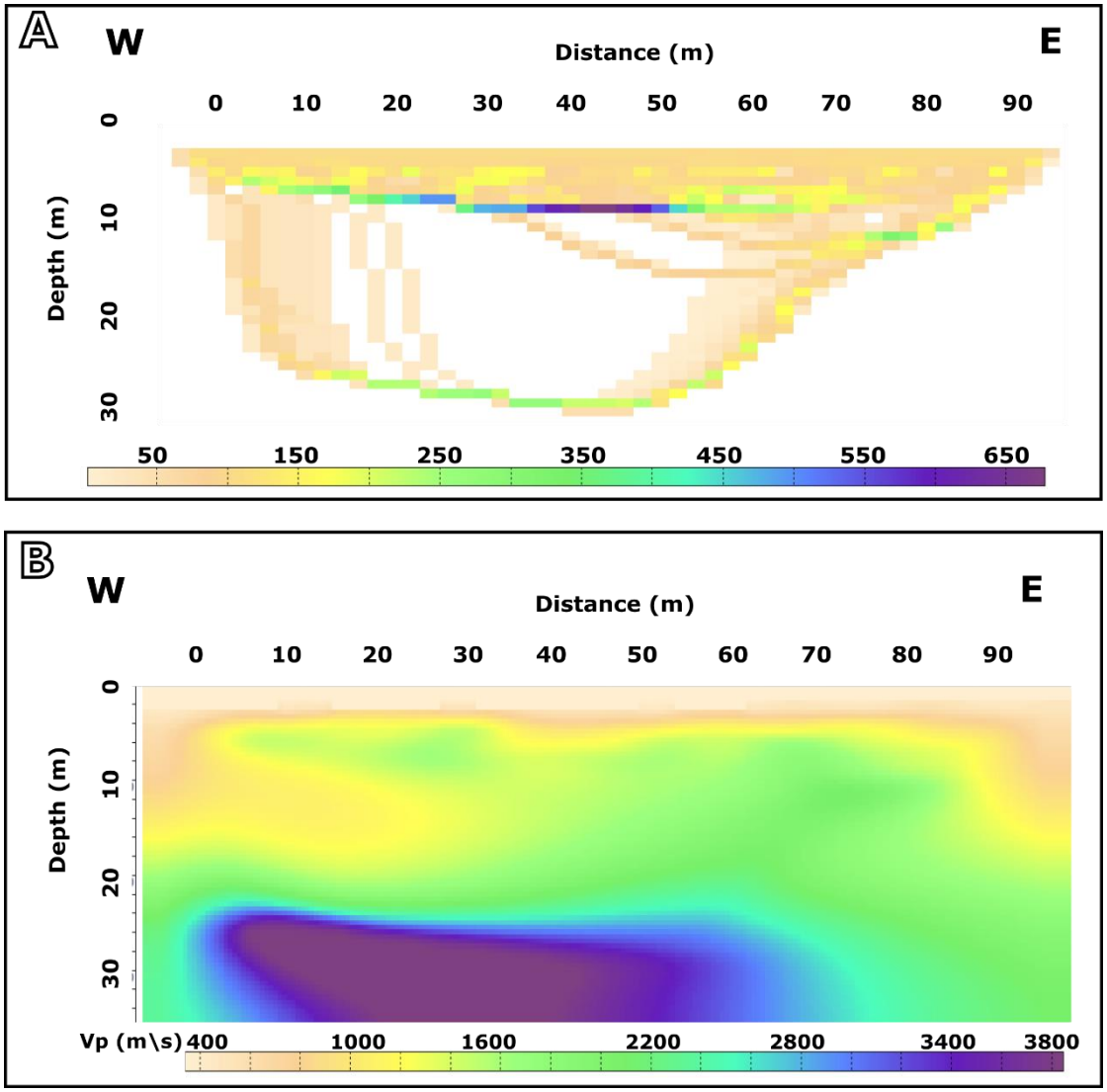

Figure 5.6: A) Ray tracing and B) seismic tomography of seismic line 2.

The shallow lithologies (< 10 m) have velocities less than 1200 m/s while the deeper lithologies (> 20 m) have velocities greater than 2000 m/s. In seismic line 2, there is a lithology below 20 m with a velocity greater than 3000 m/s.

Final seismic section for seismic line 2 (Figure 5.7).

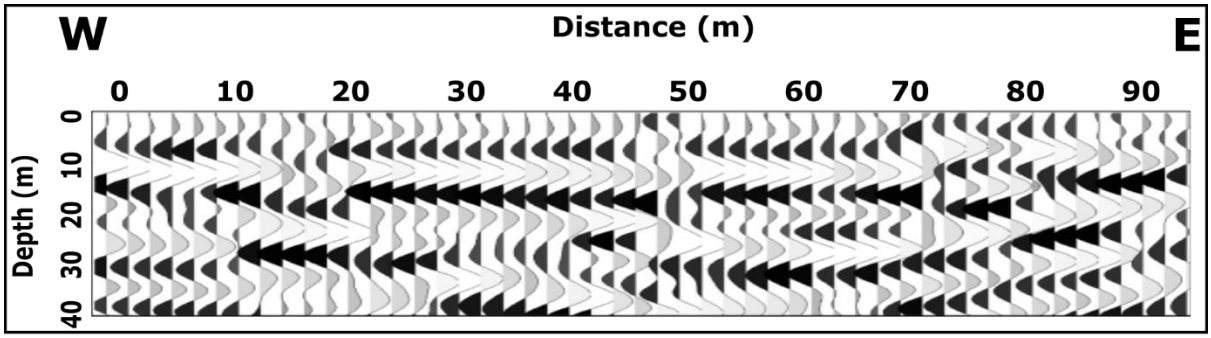

Figure 5.7: Seismic section for line 2.

The final frequency spectrum for line 2 shows that the frequency for the hammer is significantly enhanced and preserved (Figure 5.8).

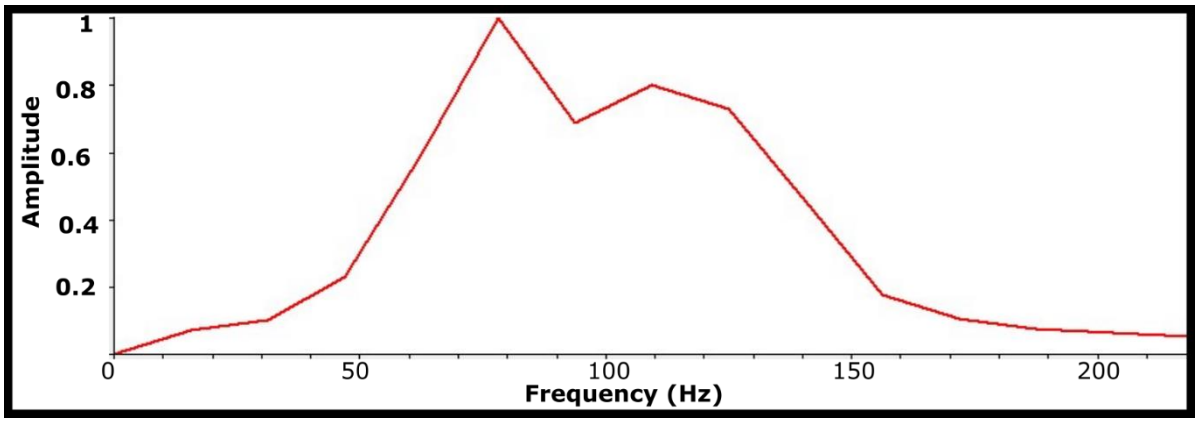

Figure 5.8: Frequency spectrum for the seismic section of seismic line 2.

5.3.3 Seismic line 3

The ray tracing (Figure 5.9 A) and refraction tomography (Figure 5.9 B) for line 3 shows the subsurface seismic velocities (ranging from 400 to 2200 m/s) with a total reliable depth penetration of ~ 25 m. Two irregular shaped anomalous features can be found in the shallow regions of the seismic tomography. The shallow lithologies (< 10 m) comprise of velocities lower than 1200 m/s while the deeper lithologies (> 10 m) comprise of velocities greater than 2000 m/s.

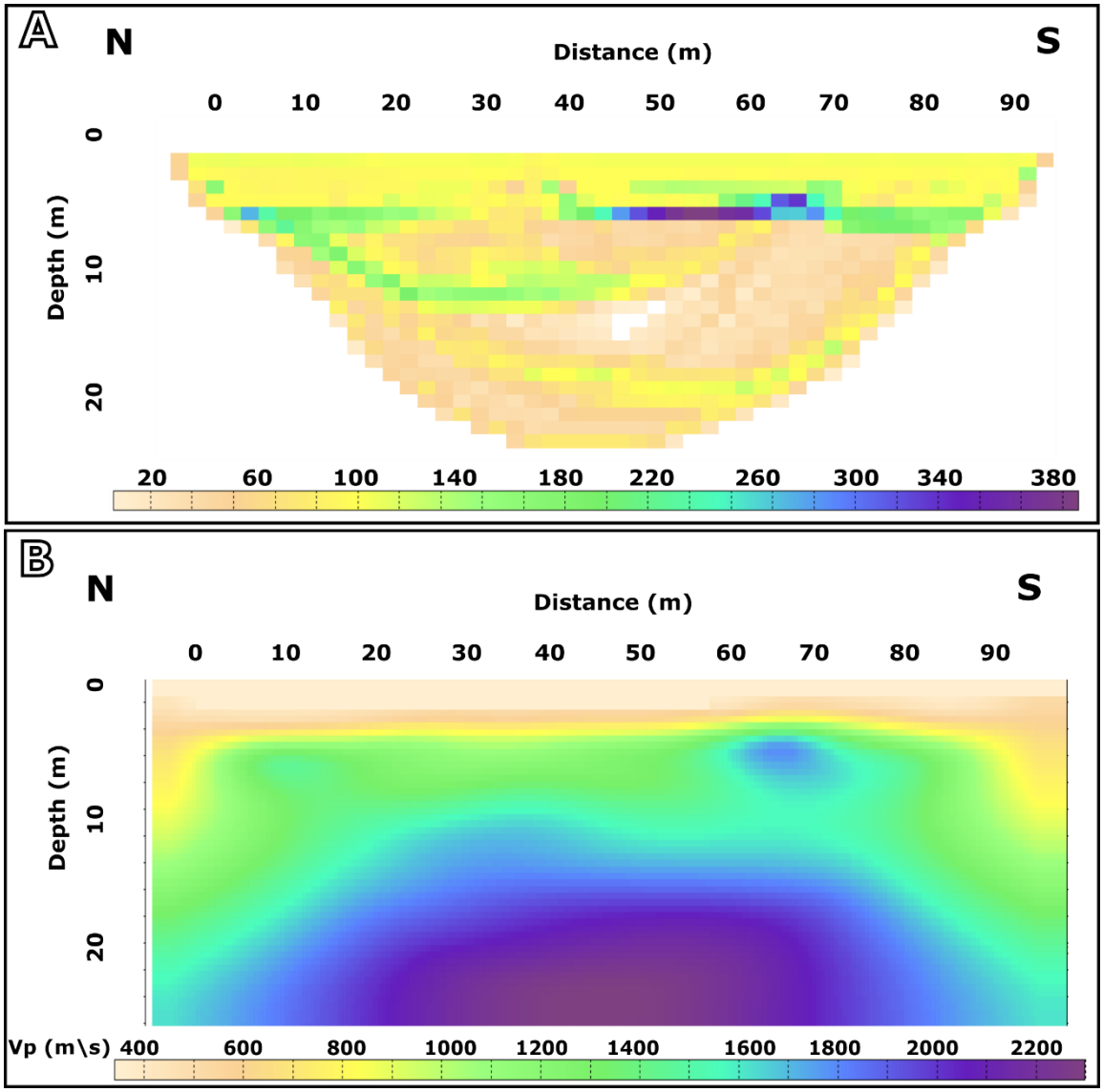

Figure 5.9: A) Ray tracing and B) seismic tomography of seismic line 3.

Reflection seismic section for seismic line 3 (Figure 5.10).

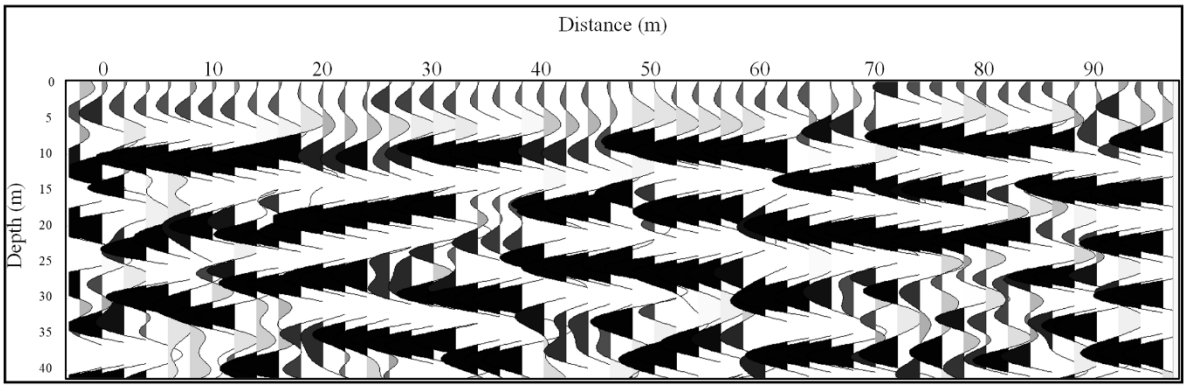

Figure 5.10: Seismic section for line 3.

The final frequency spectrum for line 3 shows that the frequency for the hammer is significantly enhanced and preserved (Figure 5.11).

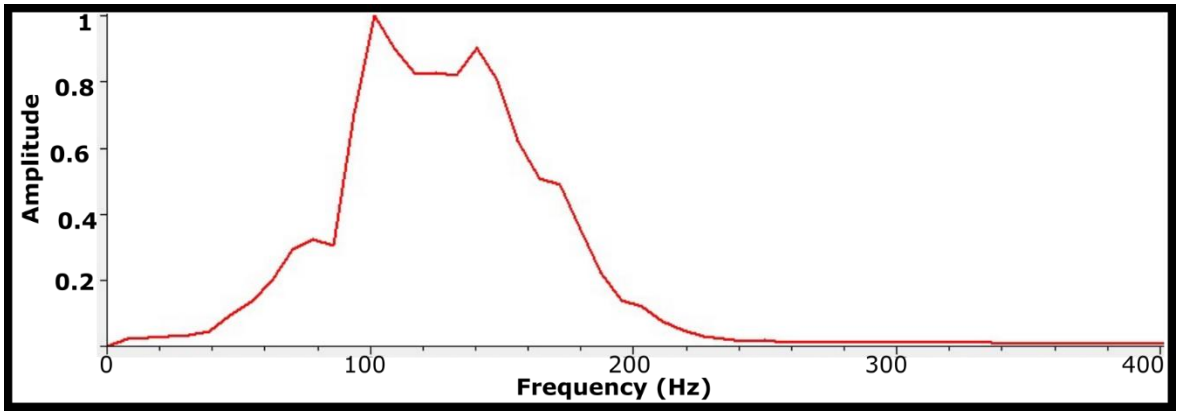

Figure 5.11: Frequency spectrum for the seismic section of seismic line 3.

5.4 Field resistivity data

Resistivity inversions were created in Res2Dinv. Bad data points were removed from the raw data before the inversions were completed. The coloured dashed lines found in the resistivity inversion sections separate regions with specific resistivity ranges that will be interpreted.

5.4.1 Resistivity line 1

Table 5.5 shows the parameters of resistivity data for resistivity line 1.

Table 5.5: Inversion results for resistivity line 1.

Method	Dipole-Dipole	Schlumberger
Data coverage	7 - 142 m	7 – 142 m
Max depth	31 m	29 m
Resistivity range	76 - 582 Ohm.m	90 – 1000 Ohm.m
Datum points	406	210
Data levels	28	14
Figure	5.12	5.13

The shallow region of the inversion section is dominated by a low resistivity (~ 76 Ohm.m) above the red dashed line for the Dipole-Dipole array (Figure 5.12). An irregular ovular feature (20 m in diameter and outlined by the orange dashed line between 35 – 55 m) has obtained a resistivity that grades outwards (~ 350 Ohm.m at its centre to ~ 200 Ohm.m). Resistivities increase with depth and have similar ranges between the remaining coloured dashed lines (~ 100 Ohm.m) although they are more stable (~ 500 Ohm.m) below the green dashed line. The low resistivities are found at a greater depth on the western side of the inversion section (up to 23 m).

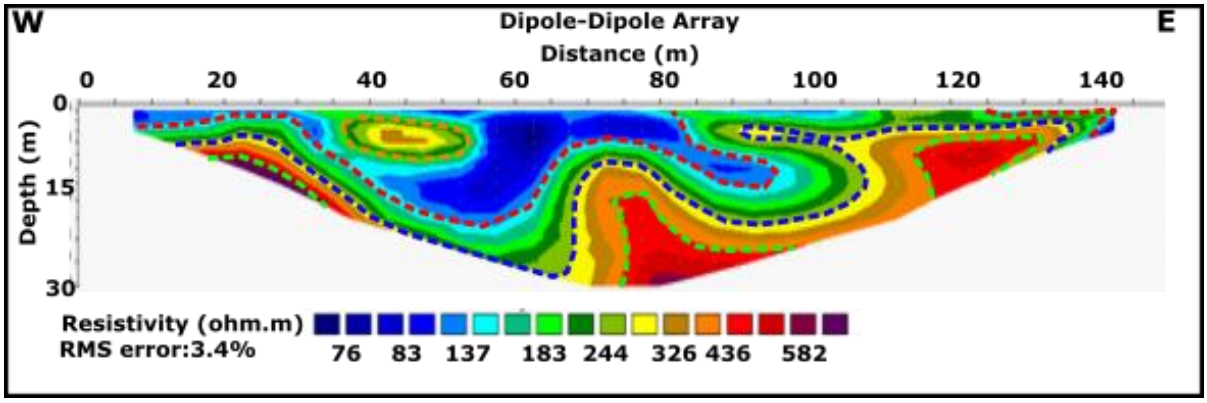

Figure 5.12: Dipole-Dipole array representing the resistivity inversion section of resistivity line 1.

Similar resistivity ranges are present in the Schlumberger array (Figure 5.13). The red dashed line underlines a low resistivity (~ 100 Ohm.m), the ovular is not well mapped in this inversion section and there is an increase in resistivity with depth (~ 200 Ohm.m to ~ 1000 Ohm.m).

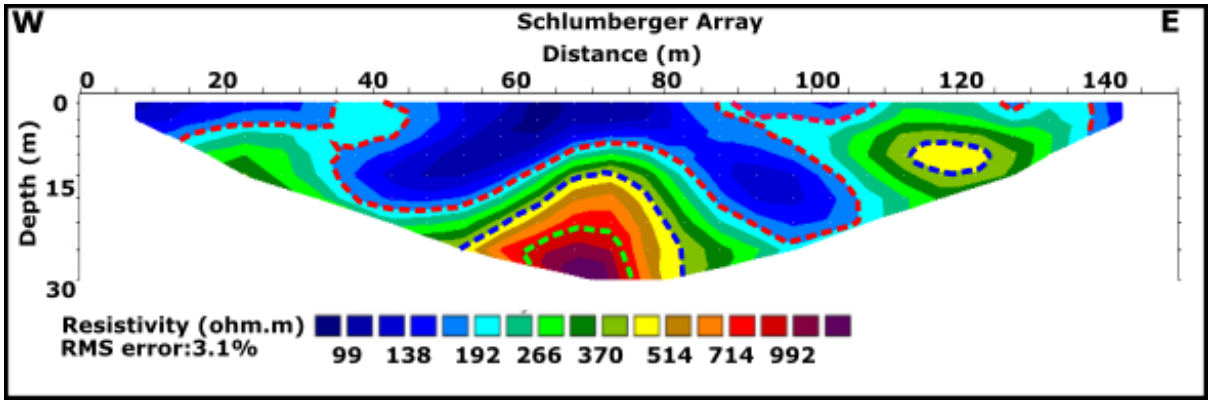

Figure 5.13: Schlumberger array representing the resistivity inversion section of resistivity line 1.

5.4.2 Resistivity line 2

Table 5.6 shows the parameters of the resistivity data for resistivity line 2.

Table 5.6: Inversion results for resistivity line 2.

Method	Dipole-dipole	Schlumberger
Data coverage	3 - 91 m	3 – 91 m
Max depth	18.6 m	18 m
Resistivity range	20 - 800 Ohm.m	35 – 850 Ohm.m
Datum points	1035	529

Data levels	45	23
Figure	5.14	5.15

The Dipole-Dipole array (Figure 5.14) again identifies a low resistivity (~ 36 Ohm.m) in the shallow surface above the red dashed line (up to 6 m thick). Resistivity increases with depth up to ~ 800 Ohm.m. A discontinuity in the low resistivity above the red dashed line is found towards the western side of the profile (~ 100 Ohm.m at its centre to a low resistivity ~ 60 Ohm.m at its rim) where agricultural digging has occurred. This occupies a small area in the inversion section (between 20 and 30 m at 3.4 m depth).

Another discontinuity (the pink dashed line) in the centre portion of the inversion section (around 48 m) has been identified. The region between the red and the blue dashed lines has a general trend of narrow resistivities (~ 2 m) in the range between 100 and 150 Ohm.m (excluding the feature indicated by the pink dashed line). Below this (between the blue and the green dashed lines), the broader resistivities (up to 6 m) can be found with a general increase in resistivity from ~200 to 500 Ohm.m. Below the green dashed line, there is a narrow (~ 2m) high resistivity (~ 800 Ohm.m).

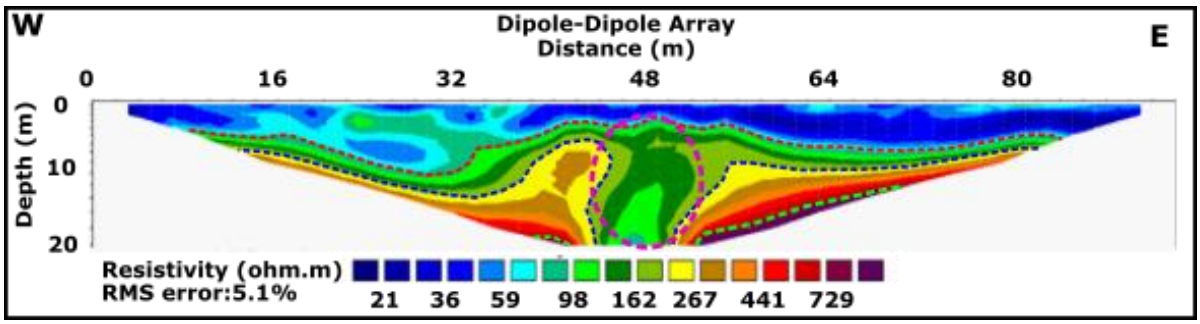

Figure 5.14: Dipole-Dipole array representing the resistivity inversion section of resistivity line 2.

The Schlumberger array also hosts a shallow low resistivities (~35 to 55 Ohm.m) above the red dashed line (up to 9 m) (Figure 5.15). Continuous resistivity bands are found with depth and range from ~ 90 to 220 Ohm.m (between the red and the blue dashed line**)** and from ~ 300 to 700 Ohm.m (between the blue and the green dashed lines). The highest resistivities of this inversion section is found below the green dashed line (~ 900 Ohm.m)

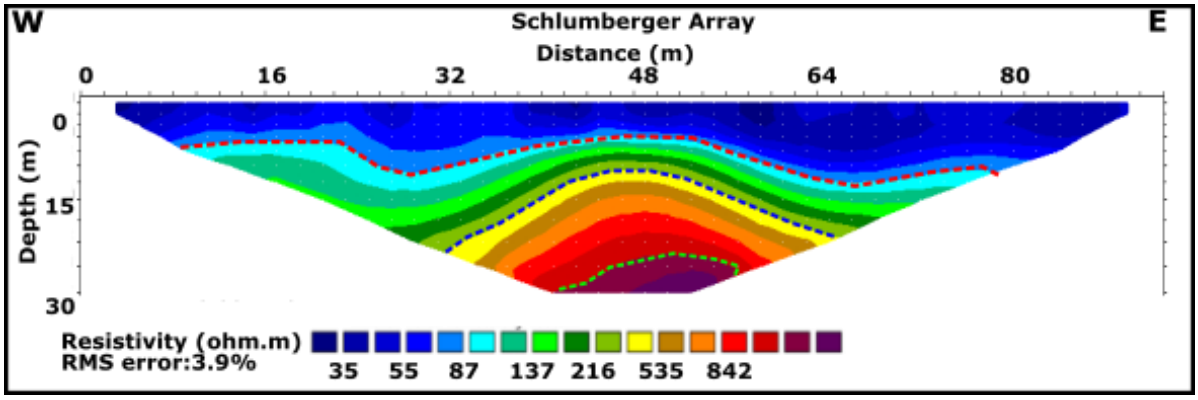

Figure 5.15: Schlumberger array representing the resistivity inversion section of resistivity line 2.

5.4.3 Resistivity line 3

Table 5.7 shows the parameters for the resistivity data for resistivity line 3.

Table 5.7: Inversion results for resistivity line 3.

Method	Schlumberger
Data coverage	3 – 89 m
Max depth	18 m
Resistivity range	15 – 250 Ohm.m
Datum points	506
Data levels	22
Figure	5.16

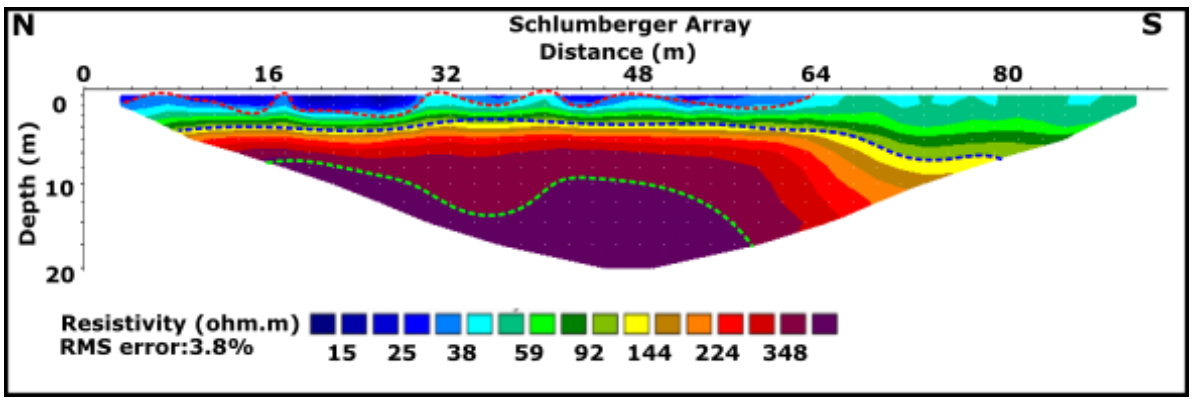

Figure 5.16: Schlumberger array representing the resistivity inversion section of resistivity line 3.

The resistivities in this inversion section (Figure 5.16) are narrow on the northern side then increase in size and begin to dip from 55 m within the profile. A shallow (> 5 m) low resistivity (~ 25 Ohm.m)

dominates above the red dashed line. Continuous bands of resistivities ranging from ~30 to 100 Ohm.m undulate close to the surface between the red and the blue dashed line. The resistivities continue to increase with depth up to ~ 350 Ohm.m below the green dashed line.

5.5 Field magnetic data

The Total Magnetic Intensity (TMI) map of survey area 1 contains 12 magnetics survey lines that cover a 400 by 500 m area (Figure 5.17). The line spacing is 25 m which all trend north-south. This map has a magnetic range of 500 nT. The data are collected over 2 days, with lines 1 to 3 (~ 400 m length) and line 7 to 12 (~ 280 m length) collected on the first day, and line 4 to 6 (~ 420 m length) collected on day 2. The survey lines don't follow the initial planned lines exactly due to the thick vegetation in the survey area.

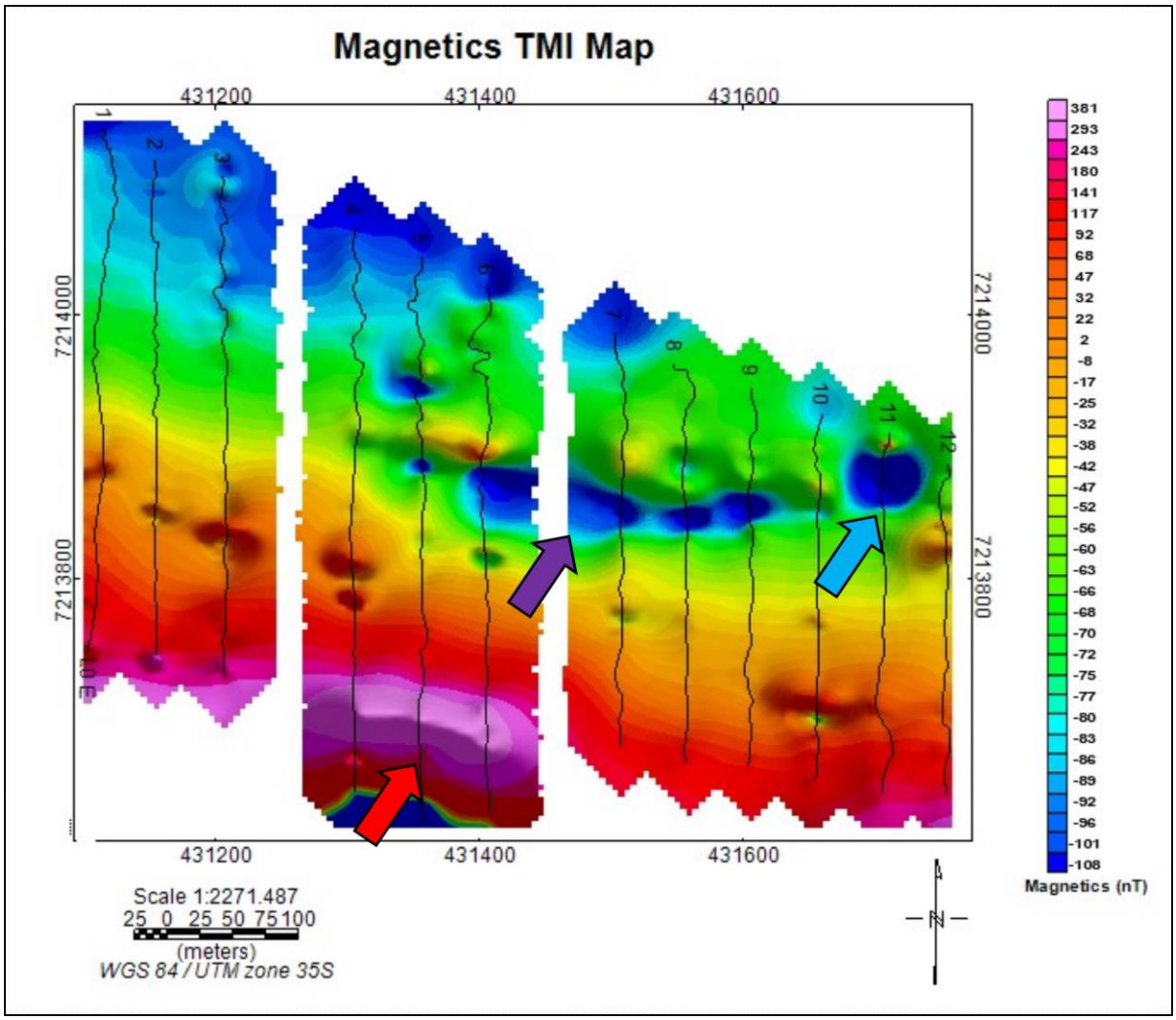

Figure 5.17: Raw magnetic data for Area 1 with high magnetic anomaly (red arrow) and low magnetic anomalies (blue and purple arrows) indicated.

An east-west trending high magnetic anomaly (red arrow) is mapped by lines 4 to 6 with total magnetic intensity of 257 nT, is approximately 75 m wide (above 243 nT) and has a curved shape. On the northern side of this anomaly, there is a gradual decrease in the magnetic intensity values over a distance of 50 m (from 381 nT to 92 nT at the end of the purple arrow). To the south of this magnetic high (Southern

portion of line 4 and 5, below the red arrow), there is a rapid decrease in the magnetic intensity over 50 m (from 381 nT to -108 nT).

Survey lines 6 to 9 mapped a low magnetic anomaly (purple arrow) that has a magnetic low of -108 nT and narrow from 50 m to 25 m from west to east. A similar low magnetic anomaly (blue arrow) has a semi-circular feature which has a radius of around 20 m.

The magnetic intensity continues to decrease towards the Northern section of the map from ~ -52 to -96 nT with line 1 to 7 containing the lowest magnetic intensities in the Northern section.

The diurnal variations that were recorded for day 1 (Figure 5.18 A) and day 2 (Figure 5.18 B) of data collection do not show any major variations or spikes which would have affected the recorded magnetic results. Both diurnals show minimal variations (120 nT and 40 nT the first and second day, respectively). which have been considered for in the results.

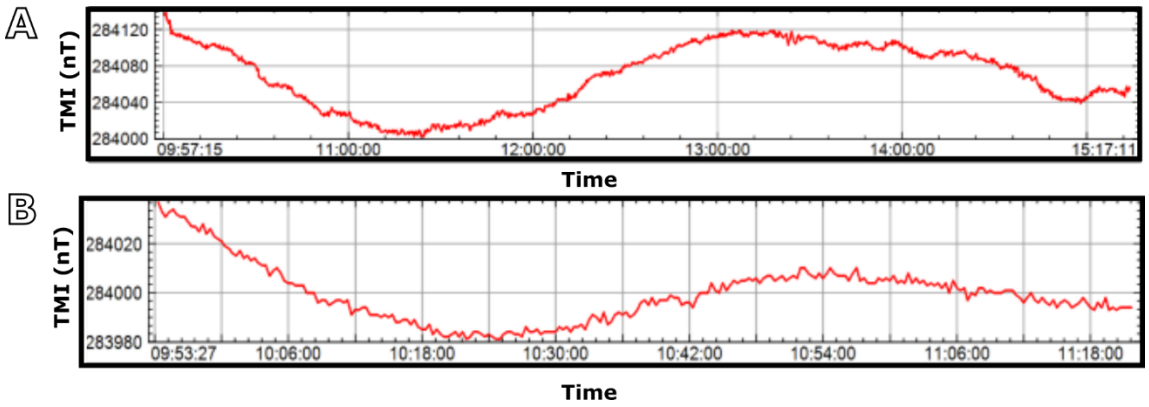

Figure 5.18: Diurnal data for day 1 (A) and day 2 (B) during the magnetic data acquisition (Geosoft map data).

5.6 Legacy 2D reflection seismic data

The legacy 2D reflection seismic surveys identified the subsurface lithologies. Horizons were mapped using the brightness of the reflection caused by the acoustic impedance contrast between them. Horizons were then identified based on their correlations with the outcrops along the rim of the Far Western Limb. The seismic profile of RZ-254 clearly shows the contact between the Black Reef Formation and the overlying Malmani Dolomites since they have the highest acoustic impedance contrast as shown in the previous analysis of the data (Tinker et al., 2002).

Ray tracing forms a means of determining which seismic velocities within the seismic tomography have a high confidence. A higher confidence in the calculated seismic tomography occurs when multiple rays reflect off of the same surface. Areas where there are few rays reflecting off the surface have a lower confidence in the seismic tomography velocities. A confidence map is thus created from the ray tracing.

Line RZ 254 was split into 4 sections (A-D). The ray tracing and the tomography for each section distinctly shows the confidence mapping and the velocities of the subsurface lithologies. The ray tracing for each section shows confidence up to 400 m in depth with the refraction tomography mapping velocities up to 6500 m/s within the subsurface. The velocities mostly range from 500 m/s to 6500 m/s within the first 100 m. There are some regions within the tomography that show the lower velocities at greater depths, but these changes still correspond well with the high confidence mapping. This shows that the data for the seismic tomography are reliable.

The ray tracing (Figure 5.19 A) and refraction seismic tomography (Figure 5.19 B) for section A has a total length of 27 km. The low velocities (< 500 m/s) extend laterally from 14 to 17 km and 20 to 26 km, with a maximum depth penetration of 70 m (red arrows). The region between 7 and 14 km has a velocity of 3000 m/s that is at the surface (blue arrow). The remaining area in the tomography contains a low velocity of 2000 m/s that is close to the surface and contains variable anomalies of high velocities (~ 4000 m/s). Below a depth of 100 m the high seismic velocities (6000 to 6500 m/s) dominate.

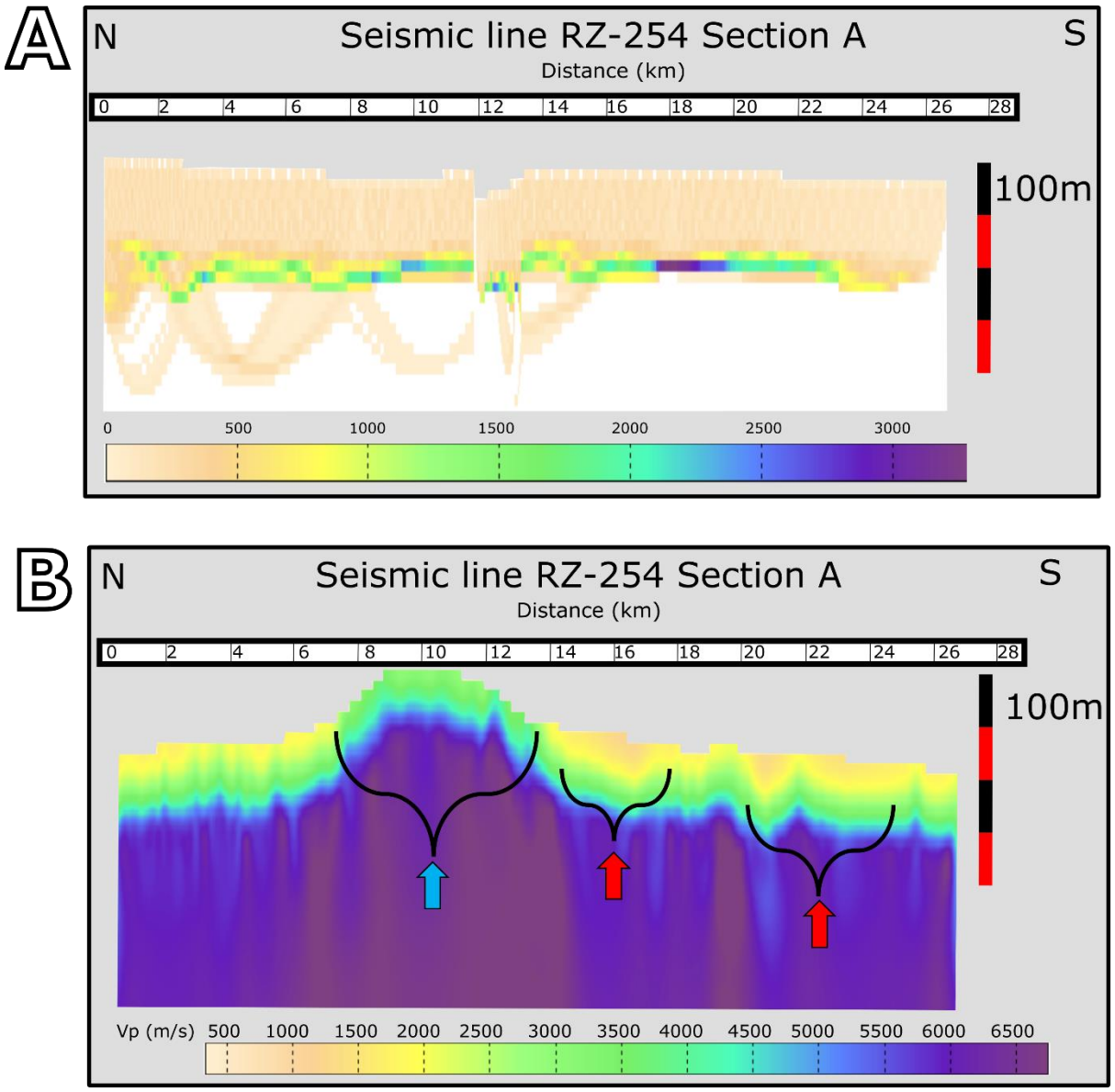

Figure 5.19: A) Ray tracing and B) refraction seismic tomography for section A of seismic line RZ-254.

The ray tracing (Figure 5.20 A) and refraction seismic tomography (Figure 5.20 B) for section B shows a total length of 29 km mapped. The low velocities (< 500 m/s) can be found from 4 to 6 and 14 to 19 km with a maximum depth penetration of 62 m (red arrows). The remaining area in the tomography contains a low velocity of 2000 m/s that is close to the surface and contains variable anomalies of high velocities (~ 4000 m/s). Below a depth of 160 m the high seismic velocities (6000 to 6500 m/s) dominate.

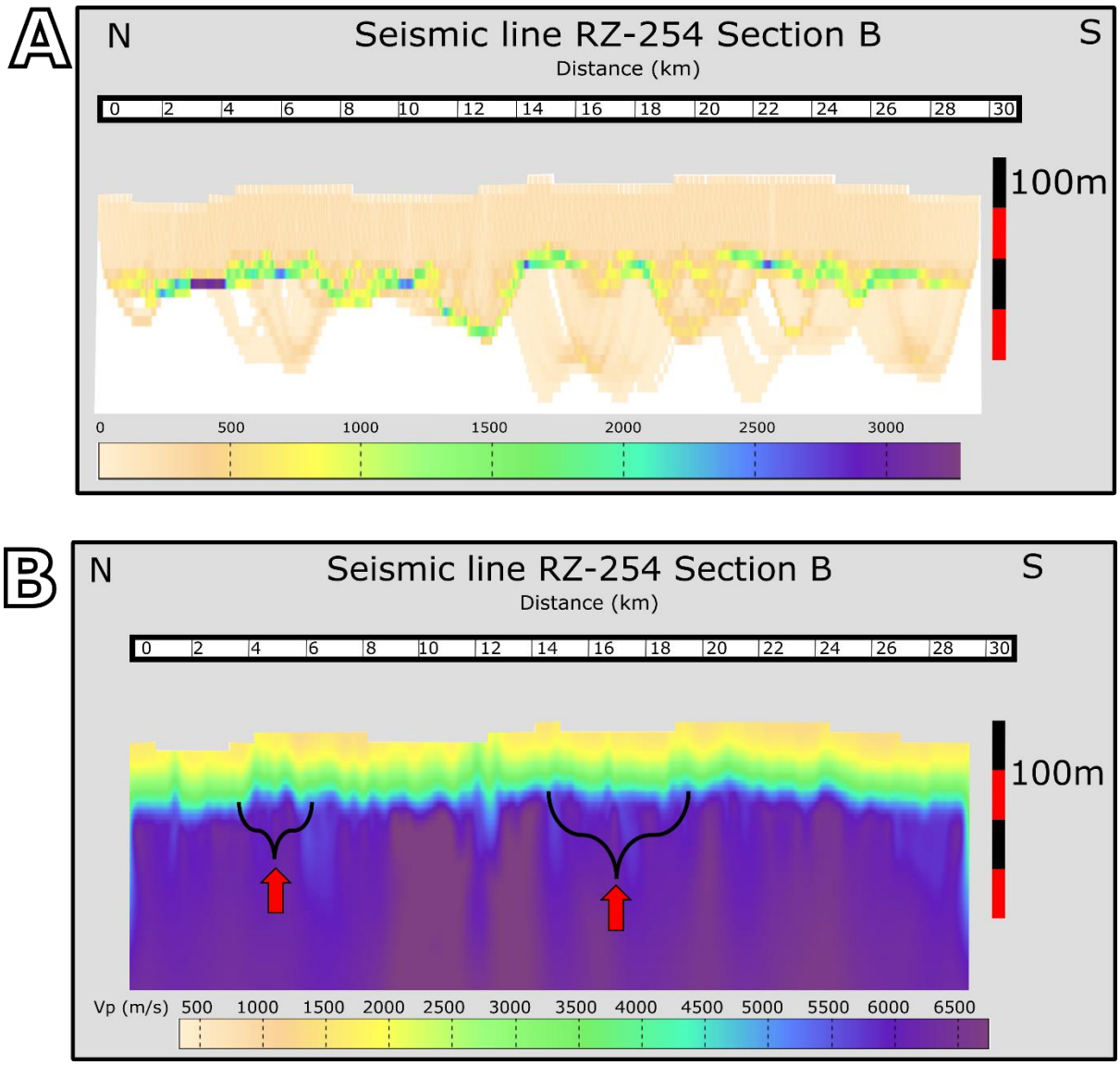

Figure 5.20: A) Ray tracing and B) refraction seismic tomography for section B of seismic line RZ-254.

The ray tracing (Figure 5.21 A) and refraction seismic tomography (Figure 5.21 B) for section C shows a total length of 20 km mapped. The low velocities (< 500 m/s) can be found from 0 to 3, 7 to 14 and 15 to 18 km with a maximum depth penetration of 90 m (red arrows). At 14 and 18 km there is a shallow velocity of 2500 m/s that is close to the surface (< 20 m) (blue arrows). The remaining area in the tomography contains a low velocity of 2000 m/s that is close to the surface and contains variable spikes of high velocities (~ 4000 m/s). Below a depth of 150 m the high seismic velocities (6000 to 6500 m/s) dominate.

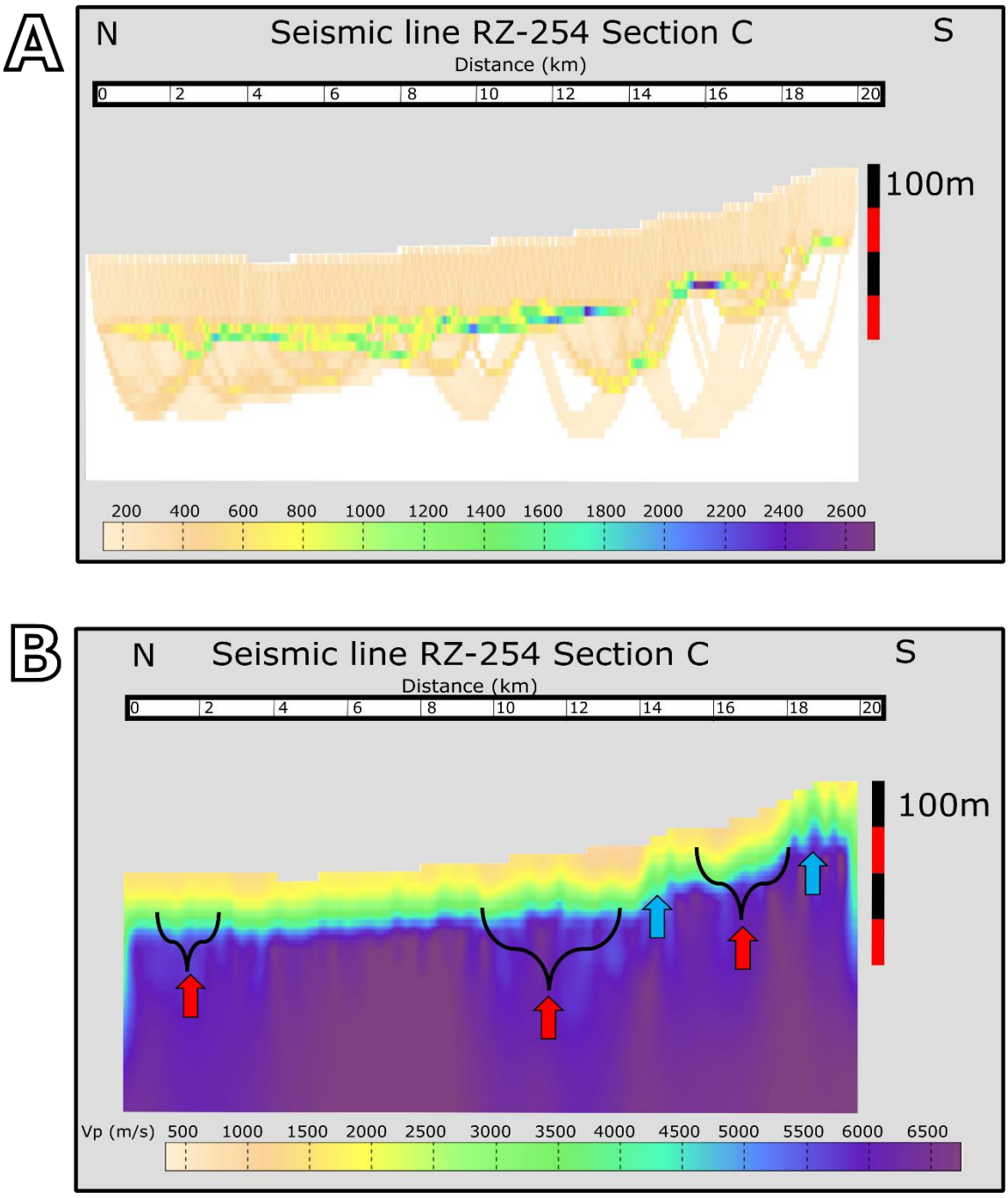

Figure 5.21: A) Ray tracing and B) refraction seismic tomography for section C of seismic line RZ-254.

The ray tracing (Figure 5.22 A) and refraction seismic tomography (Figure 5.22 B) for section D shows a total length of 30 km mapped. The low velocities (< 500 m/s) can be found from 12 to 15, and at 22 km with a maximum depth penetration of 75 m (red arrows). At 10 and from 26 to 30 km there is a shallow velocity of 3000 m/s that is close to the surface (< 10 m) (blue arrows). The remaining area in the tomography contains a low velocity of 2000 m/s that is close to the surface and contains variable spikes of high velocities (~ 3500 m/s). Below a depth of 133 m the high seismic velocities (6000 to 6500 m/s) dominate.

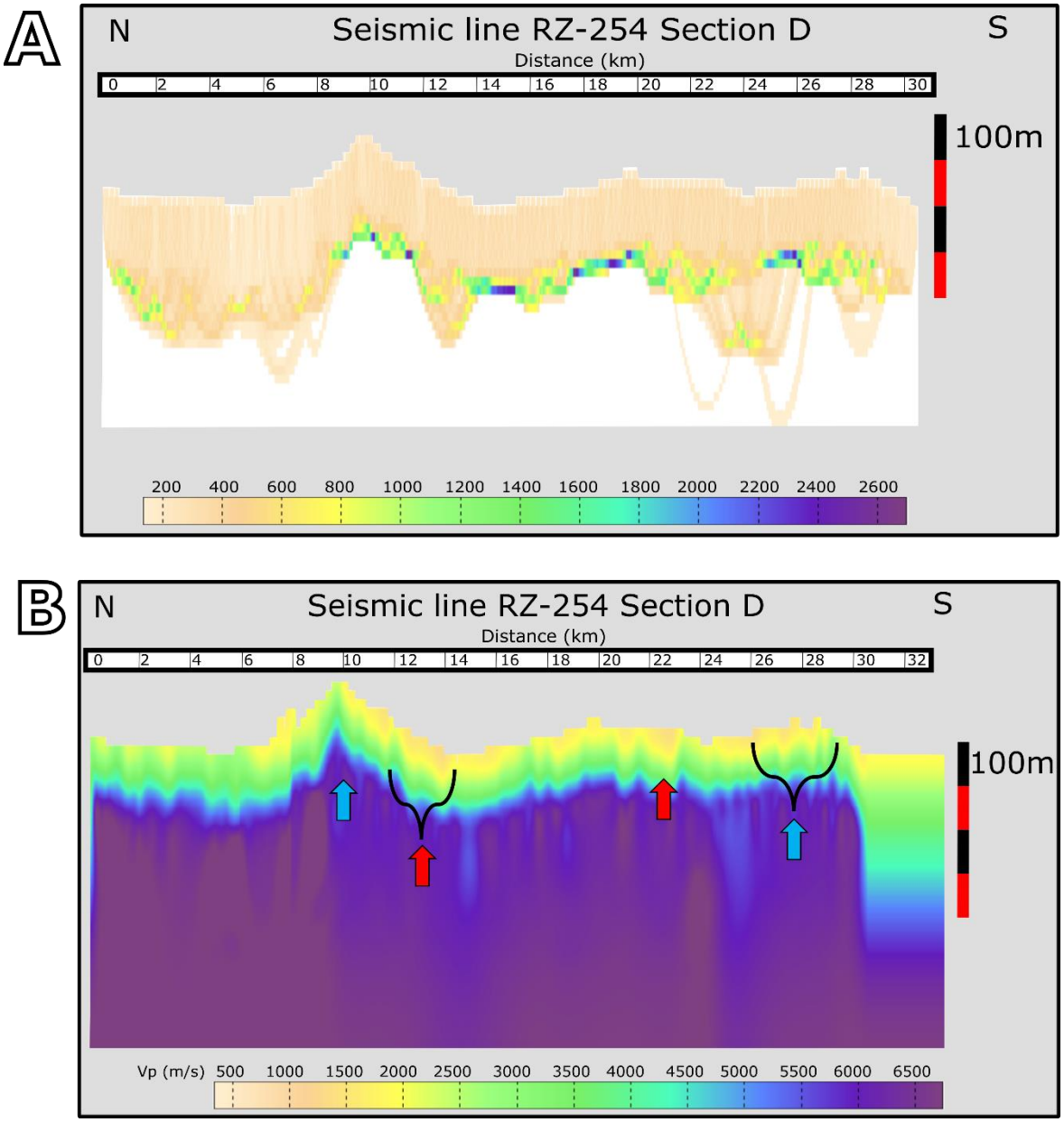

Figure 5.22: A) Ray tracing and B) refraction seismic tomography for section C of seismic line RZ-254.

6 Interpretation

This chapter shows the interpretations of the geological samples and the geophysical data that are used to characterise the subsurface of area 1 and 2.

6.1 Petrographic analysis

The thin section analysis of the samples collected from the field allows for the samples to be classified (Table 6.1).

Table 6.1: Sample Classifications.

Sample	Classification
S001	Quartzite
S002	Highly altered Gabbronorite
S003	Siltstone
S004	orthopyroxenite
S005	Altered-Gabbronorite
S006	Siltstone with haematite mineralization
S007	Veined and fractured siltstones

Surrounding lithologies in area 1 can be characterized by samples S001 (quartzite) and S004 (orthopyroxenite). Orthopyroxenite corresponds to the outcrop that occurs north of the study area (Figure 4.6) and that which is present in the local geological map (Figure 2.3) while the quartzite sample that has been analysed may correspond with the outcrop mapped further north (Figure 2.3).

The orthopyroxenite has evidence of annealing which shows an increase in pressure during the formation of the rocks. This provides insight into the diagenesis of the rocks in the area. The quartzite sample that was retrieved shows evidence of secondary alteration through the compaction and the annealing of the quartz grains.

Based on the geological maps of area 2 (Figure 2.3), there are small amounts of diabase and large amounts of sedimentary rocks from the Rayton Formation that occur as outcrops surrounding the area. The samples collected in area 2 represent both igneous and sedimentary rocks which could be correlated to the unidentified shallow subsurface lithologies.

The majority of the lithological samples collected consisted of highly weathered gabbronorite (sample S002 and sample S005) that was too brittle to retrieve. Measurements were made on samples that had a lower degree of weathering. The gabbronorite may correspond to one of the east-west trending dykes in the area.

The sedimentary samples that were collected consisted of a few pebbles of siltstone that were sparsely situated (around 1 sample for every three-square meters) within the gabbronorite samples. This shows that the siltstone samples could be xenoliths within the gabbronorite and occur deeper within the subsurface.

Sample S003 and S007 are classified as siltstone and have visible layering and quartz veining. They show evidence of low-grade metamorphism due to their annealing texture which occurs close to the quartz veining. The fractures within these samples occurred after the quartz veining occurred as they crosscut the veins. Sample S006 is also a siltstone that has diagenetic nodular haematite mineralization which follows the microfractures within the sample.

6.2 Geophysical data analysis area 1

6.2.1 Seismic line 1

The lithology identified in area 1 is orthopyroxenite. The weathered orthopyroxenite samples have an average P-wave seismic velocity of 1800 m/s while the fresh orthopyroxenite has a P-wave seismic velocity of 5520 m/s. These values correlate well with the low P-wave seismic velocities (< 2000 m/s) in the shallow regions of the tomography and the high P-wave seismic velocities (> 4000 m/s) in the centre of the tomography. There is confidence in this seismic tomography up to 20 m into the subsurface and in the high seismic anomalies found in the centre of this seismic profile based on the ray paths (Figure 5.3 A).

The P-wave seismic velocities increase with depth which may represent the degree of weathering. The shallowest region (< 5 m) of the tomography (Figure 6.1) is likely to represent the compacted (shown above the blue dashed line) and loose soil (shown above the red dashed line). These identified velocities fall well within the accepted values for the various weathering profiles (Kausarian et al., 2014). These soils overlay the weathered orthopyroxenite bedrock (shown between the blue and green dashed lines) and the semi-fresh bedrock (shown below the green dashed line).

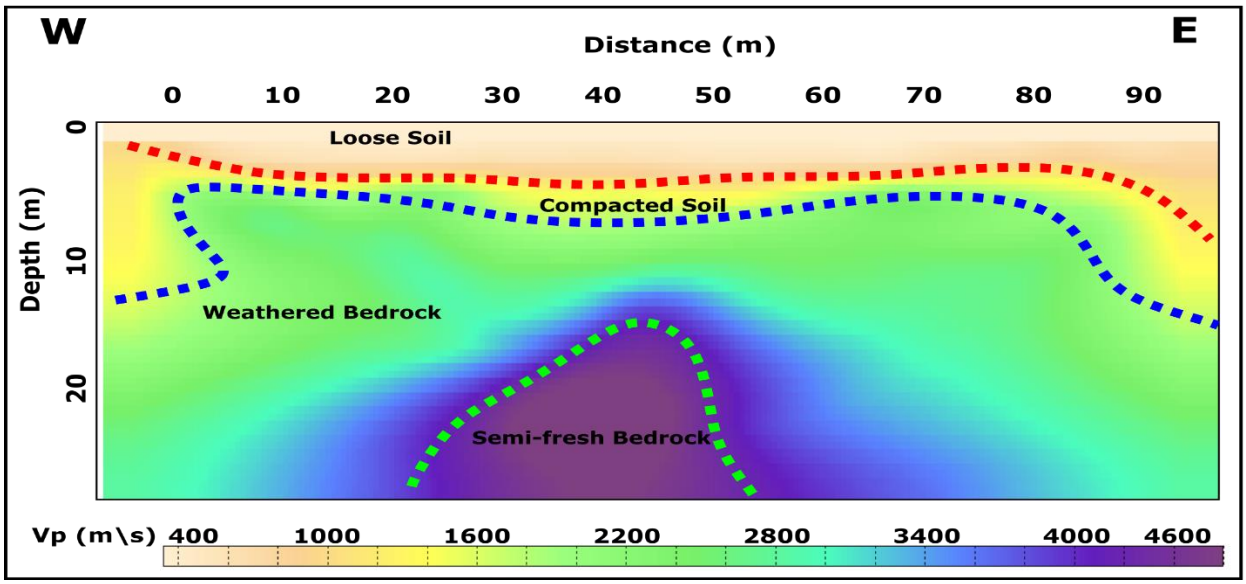

Figure 6.1: Interpreted seismic tomography for seismic line 1 with the different weathering surfaces marked.

The interpreted seismic section for line 1 (Figure 6.2) confirms the different weathering profiles identified in the seismic tomography and shows the subsurface mapping up to 20 m. The contacts between them (dashed coloured lines) are delineated by the strong reflections on the section. The base

of the top soil is at 4 m (yellow dashed line). The contact between the top soil and the weathered bedrock is between 10 and 20 m (green dashed lines). The contact between the weathered and the semi-fresh bedrock is at 28 m (purple dashed line).

Throughout the seismic section, there are clear subvertical discontinuities (blue dashed lines) in the reflections representing the different weathered surfaces. Most of these discontinuities trend from northeast to southwest. On the eastern side of the seismic section, the fresh bedrock is offset by a potential fault (red arrow).

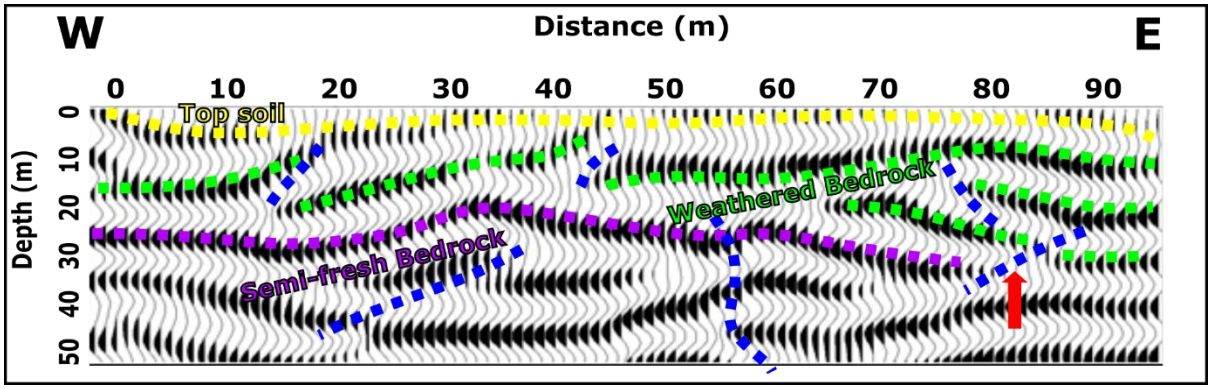

Figure 6.2: Interpreted seismic section for seismic line 1 with the different weathering surfaces marked, discontinuities (blue dashed lines) and indication of the potential fault (red arrow).

Integrating the seismic tomography with the seismic section shows the velocities responsible for the reflections in the data (Figure 6.3). The semi-fresh bedrock (purple dashed line) has a P-wave seismic velocity of 4000 m/s, the weathered bedrock (green dashed lines) has a P-wave seismic velocity of 2000 m/s, while the compacted soil (below yellow dashed line) has a P-wave seismic velocity of 1200 m/s. The top soil/loose soil has a P-wave seismic velocity of <1000 m/s.

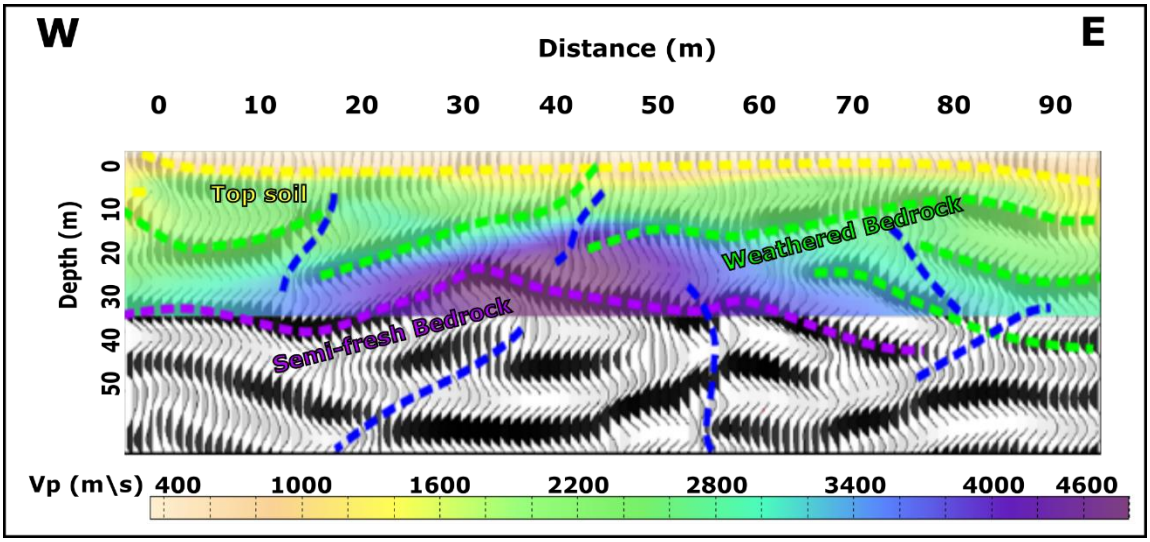

Figure 6.3: Integration between seismic section and tomography for seismic line 1with the different weathering surfaces marked and discontinuities (blue dashed lines).

Based on the velocities in the tomography, the weathering surfaces can be identified (Table 6.2).

Table 6.2: Velocity ranges and correlating thicknesses for the interpreted subsurface weathering profiles on seismic line 1.

Weathering profiles	Velocity range (m/s)	Thickness (m)
Loose top soil	< 1000	< 1
Compacted soil	1000-1800	~ 2
Weathered othropyroxenite bedrock	1800-4400	~ 15
Semi-fresh Orthopyroxenite bedrock	> 4400	> 2

6.2.2 Modelling for seismic line 1

The seismic model is based on the same geological model used for the resistivity data (discussed later in this section) which represents the contacts between the fresh and weathered bedrock, followed by the overburden. The shapes of the weathering profiles in this forward model does not necessarily follow that of the resistivity model, although it was modelled according to the seismic field data that was collected. A geological section (Table 6.3) shows the velocities and thicknesses that were used for this model and the synthetic seismograms. The densities of the samples and the velocity of the semi-fresh orthopyroxenite bedrock was used from the physical property data that was collected. The forward model was designed with fixed receivers: 50 sources spaced at 4 m along the profile and 48 receivers at 2 m spacing (Figure 6.4). The modelling was run at 65 Hz using the Ricker wavelet and recorded up to 2000 ms.

Table 6.3: Geological model for seismic line 1.

Lithological description	P-wave velocities (m/s)	Density (g/cm^3)	Estimated thickness (m)	Correlating reference
Top soil	1000	1,5	< 10	(Kausarian et al., 2014)
Highly weathered orthopyroxenite bedrock	2000	3,25	15	See Table 5.3
Semi-fresh orthopyroxenite bedrock	5500	3,26	> 2	

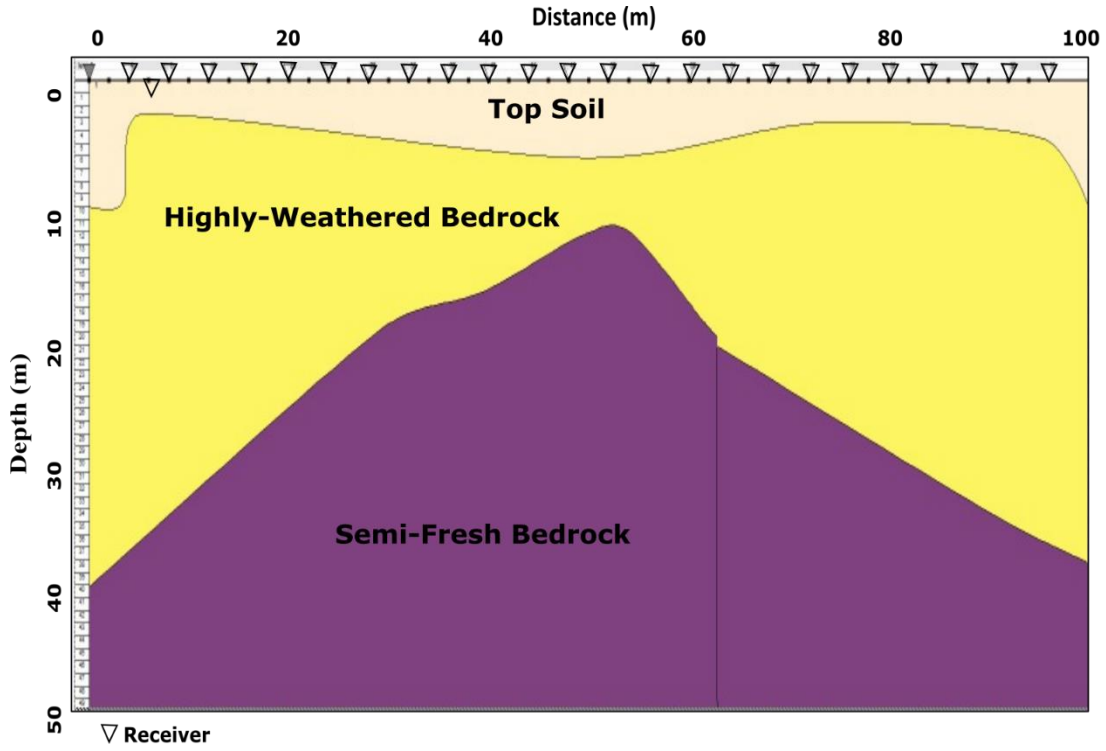

Figure 6.4: Geological model for seismic line 1.

Comparing the synthetic shot gathers for this model (Figure 6.5 A) with the processed shot gathers (Figure 6.5 B) shows a strong correlation with those from the field data. The velocities that were picked out from the field shot gathers were slightly lower than those from the model, although they did occur in similar positions. The first reflection with a velocity of 1000 m/s (yellow arrow) and the second reflection with a velocity close to 3000 m/s (green arrow).

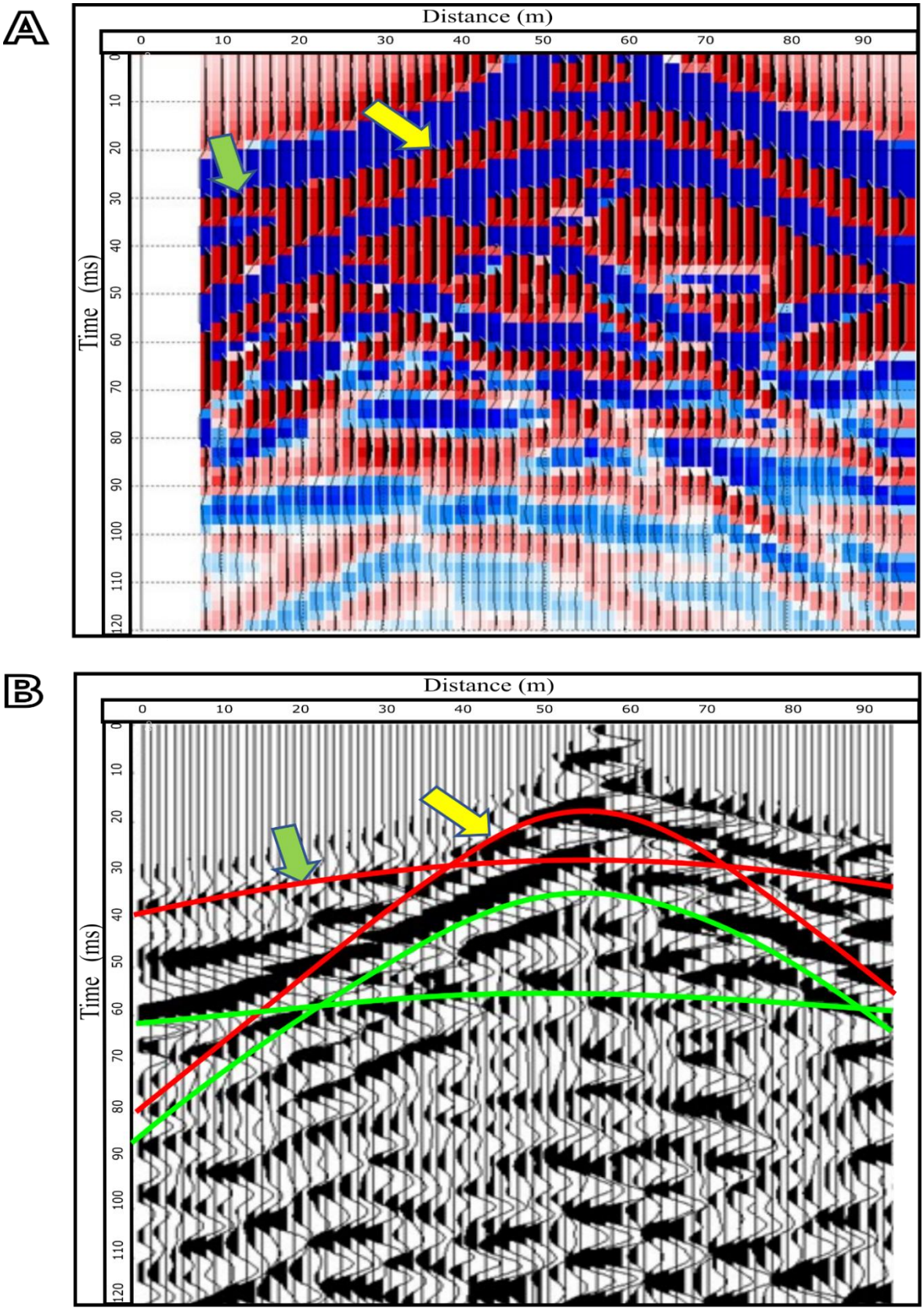

Figure 6.5: A) Synthetic shot gathers, B) Processed shot gathers for seismic line 1 showing reflections picked. Yellow arrow showing a velocity of 1000 m/s and the green arrow showing the velocity of 3000 m/s.

The synthetic seismogram created in SynthSeis shows that there will be some reflections from the proposed geological section (Table 6.4). This geological section adds a few more weathering surfaces.

Table 6.4: Geological section for reflectivity modelling in area 1.

Lithological description	Velocities (m/s)	Density (g/cm^3)	Estimated thickness (m)
Loose top soil	500	1,2	1
Compacted top soil	1200	1,3	4
Highly weathered orthopyroxenite bedrock	2000	1,5	5
Weathered orthopyroxenite bedrock	2600	3,25	6
Semi-fresh orthopyroxenite bedrock	4400	3,26	> 2

Two wavelets were considered for the synthetic seismogram modelling. The Minimum phase wavelet which has all its energy concentrated at the onset of the wavelet and the Ricker wavelet that has its energy concentrated at the centre of the wavelet. Various sampling rates and frequencies were used to enhance the reflections created by the lithological contacts identified in (Table 6.4). Additional reflections were observed within the synthetic seismogram when more weathering surfaces are introduced to the synthetic modelling. A higher sampling rate was applied to the Ricker wavelet seismogram to account for the added reflections and to honour the previous models. The Minimum phase wavelet seismogram showed the most reliable reflections at a high sampling frequency. The first synthetic seismogram was created using a sampling rate of 1 ms and the Minimum phase wavelet to enhance the shallow reflection and a frequency of 100 Hz (Figure 6.6).

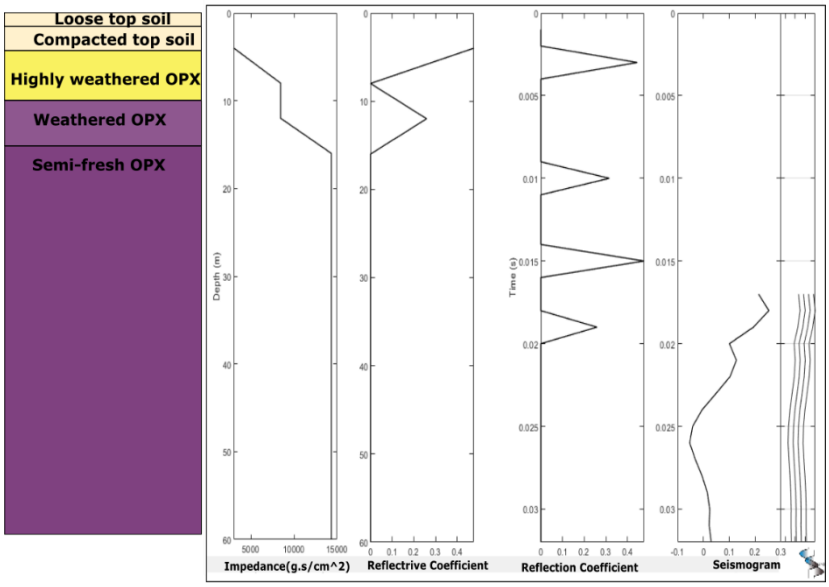

Figure 6.6: Synthetic seismogram using the minimum phase wavelet for area 1, OPX is the orthopyroxenite.

The second synthetic seismogram was created using a sampling rate of 4 ms, the Ricker wavelet and a frequency of 70 Hz to compare the reflections directly with those in the processed seismic data (Figure 6.7). Lower sampling rates (< 4 ms) were investigated and the most prominent reflection originated from the contact between the weathered and semi-fresh bedrock which was most visible in the

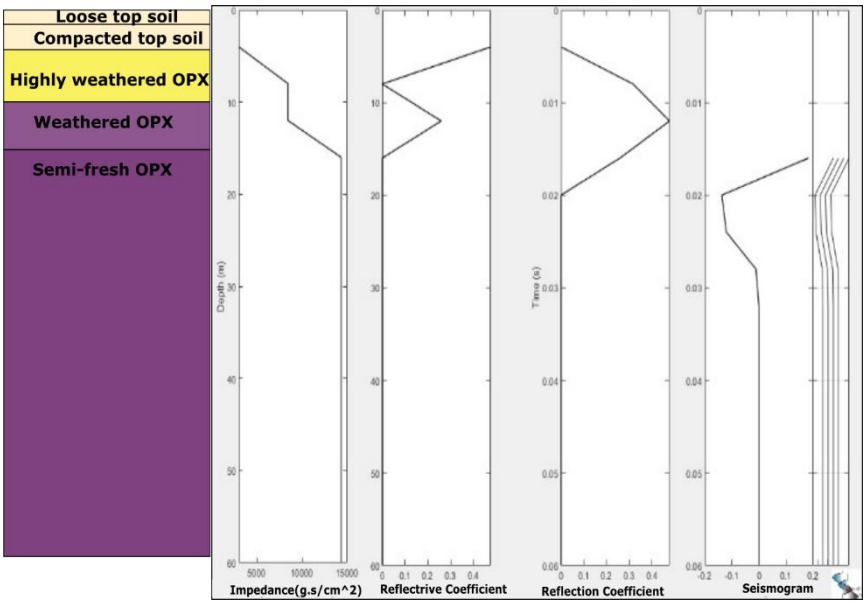

Figure 6.7: Synthetic seismogram using the Ricker wavelet for area 1, OPX is the orthopyroxenite.

The Ricker (R) and the Minimum Phase (MP) wavelet synthetic seismogram show relevant reflections with the Ricker wavelet showing a stronger correlation to the reflections in the seismic section (Figure 6.8).

Both wavelets show the strongest reflection from the contact between the weathered and the semi-fresh bedrock. This proves that the interpretations made on the seismic sections are valid and reliable.

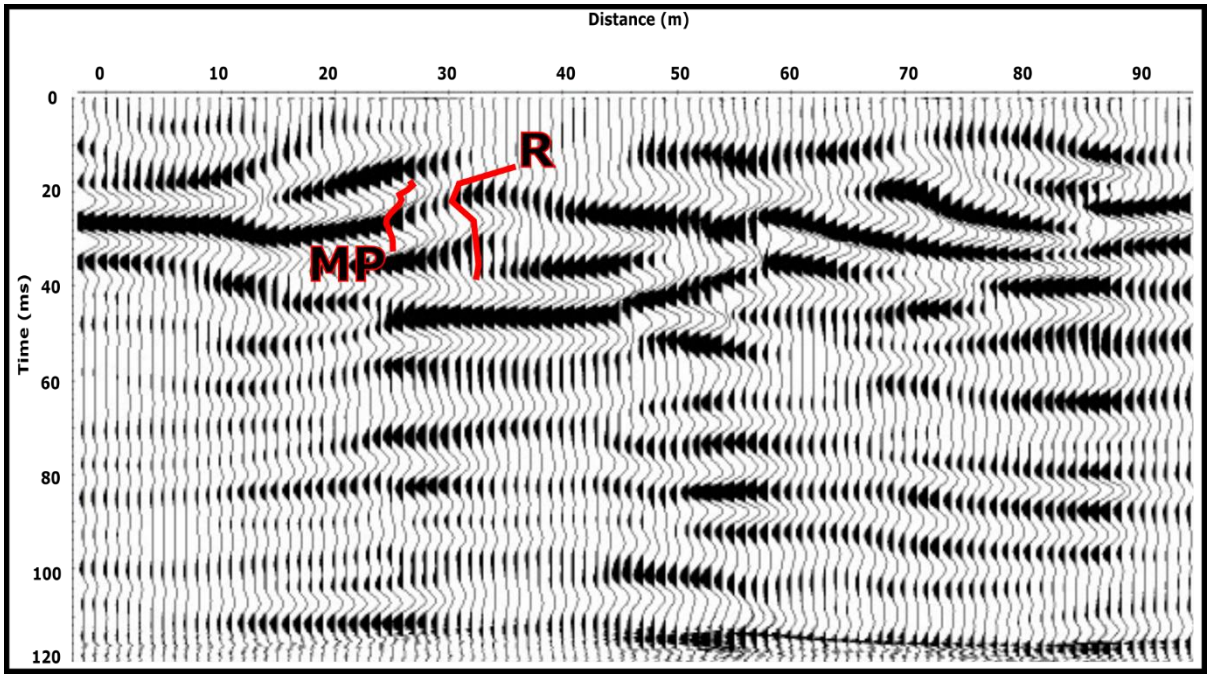

Figure 6.8: Correlation of the reflections in the seismic section with the minimum phase (MP) and ricker (R) synthetic seismograms for area 1.

6.2.3 DC Resistivity line 1

Various weathering layers within the subsurface have been identified in the interpreted section of the Dipole-Dipole array (Figure 6.9) in area 1.

Dipole-Dipole array

The resistivity measurements for the weathered orthopyroxenite samples collected in the area show an average of 500 Ohm.m, while the fresh orthopyroxenite has a resistivity of 1800 Ohm.m. The low resistivities that are found in the centre of the section correlate strongly with the weathered bedrock.

Water that has seeped into the subsurface creates the typical shape found for the low resistivity seen above the red dashed line Water has a low resistivity/high conductivity which allows for the low resistivity to be interpreted as loose soil containing water/ waterlogged soil (Figure 6.9). Weathering will increase towards the water as it would erode the subsurface layers. Naturally, the soil below the

top soil will become compacted due to the weight of the overburden. This may make it occur as if there is gradual increasing resistivity with depth, as seen between the red and blue dashed line.

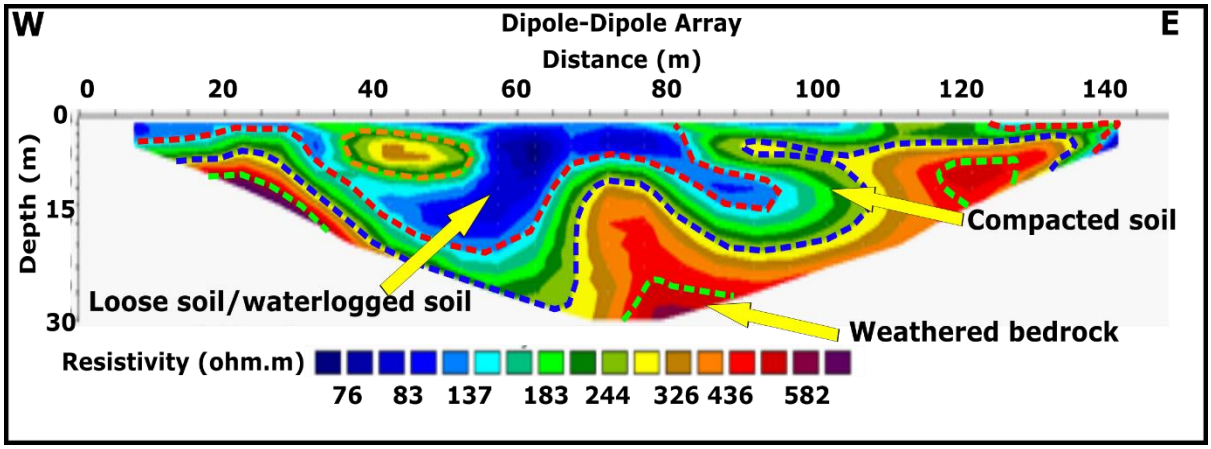

Figure 6.9: Interpreted resistivity section and marked weathering profiles for the Dipole-Dipole array from resistivity line 1.

Based on the resistivities in this section, the weathering surfaces can be identified (Table 6.5).

Table 6.5: Resistivity ranges and correlating thicknesses for the interpreted subsurface weathering profiles of the Dipole-Dipole array (resistivity line 1).

Weathering profiles	Apparent resistivity range (Ohm.m)	Thickness (m)
Loose top soil/ waterlogged soil	< 100	< 20
Compacted soil	100-200	~ 2
Weathered orthopyroxenite bedrock	200-500	~ 12

Schlumberger array

This section for the Schlumberger array (Figure 6.10) has a similar location of the high resistivities as that found in the Dipole-Dipole array (Figure 6.9). The top soil/loose soil containing water can be considered as the low resistivity above the red dashed line (Figure 6.10) Natural compaction of the top soil caused by the overburden will form the compacted soil (Figure 6.10, just below the red dashed line). The gradational resistivity increases is interpreted as the weathering surfaces that occur between the red and the green dashed lines. This is interpreted as the weathered bedrock (between the blue and the green dashed line) caused by the waterlogged soil which overlies the semi-fresh bedrock (higher resistivity ~ 1000 Ohm.m) below the green dashed line. This is expected with a decrease in the amount of weathering with depth.

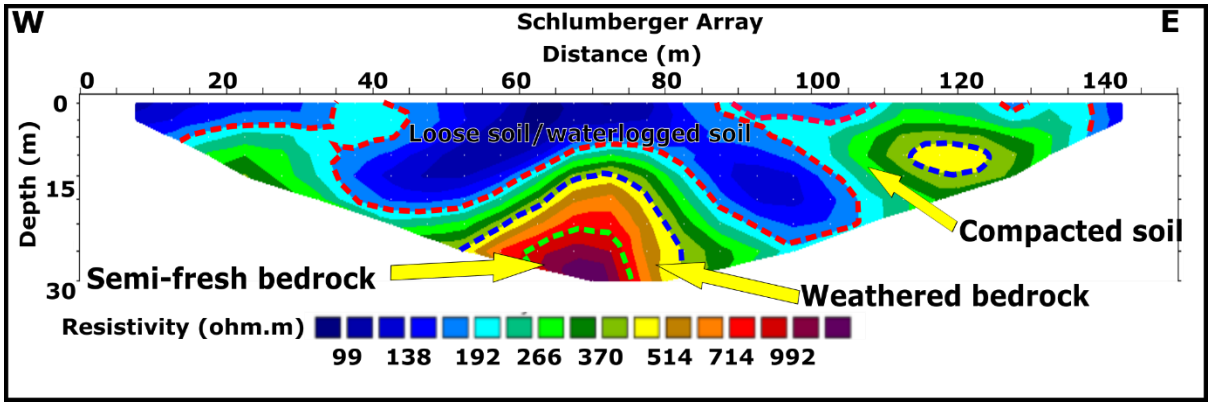

Figure 6.10: Interpreted resistivity section and marked weathering profiles for the Schlumberger array from resistivity line 1.

Based on the resistivities in this section, the weathering surfaces can be identified (Table 6.6).

Table 6.6: Resistivity ranges and correlating thicknesses for the interpreted subsurface weathering profiles of the Schlumberger array (resistivity line 1).

Weathering profiles	Apparent resistivity range (Ohm.m)	Thickness (m)
Top soil/ Loose soil/ waterlogged soil	< 100	< 20
Compacted soil	100-200	~ 2
Weathered orthopyroxenite bedrock	200-800	~ 14
Semi-fresh orthopyroxenite bedrock	~ 1000	> 5

When comparing the two sections, the bedrock seems to be recorded well with the Schlumberger array, while a higher resolution of the shallow subsurface is obtained by the Dipole-Dipole array. Based on the sections collected for area 1, the model below was created in order to further understand the subsurface lithologies in the study area. For line 1, the model describes the geological subsurface based on the field data and the physical properties collected (Table 6.7).

Table 6.7: Physical characteristics of lithological units in area 1 with their thicknesses found from interpreted data.

Lithological description	Resistivity properties (Ohm.m)	Estimated thickness (m)	Correlating reference
Loose soil	100	< 20	(Kausarian et al., 2014)
Compacted soil	100 – 200	2	
Highly weathered orthopyroxenite bedrock	200 - 700	14	See Table 5.3

Semi-fresh orthopyroxenite bedrock	> 1000	> 2	

Modelling for resistivity line 1

The geological model (created in Res2Dmod) (Figure 6.11) reveals the expected weathering profile in the field area based on the DC resistivity data collected from the field. The model is exaggerated both on the horizontal and vertical scales, therefore the depths reached on the resultant sections will be much higher and so will the recorded resistivities.

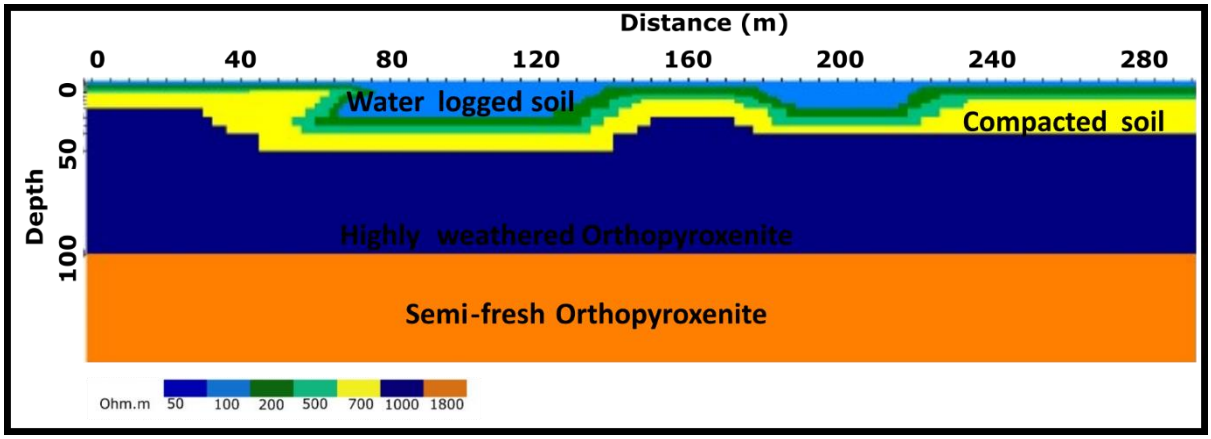

Figure 6.11: Geological model for Resistivity line 1.

The resistivity values were then calculated for this forward model for both the Dipole-Dipole array and the Schlumberger array. The Dipole-Dipole array for the geological model (Figure 6.12 A) shows a similar weathering profile to that seen from the field data (Figure 6.12 B). If only the first 31 m vertical depth of the section is considered, there is a match in the resistivities and the shape of the weathering profile.

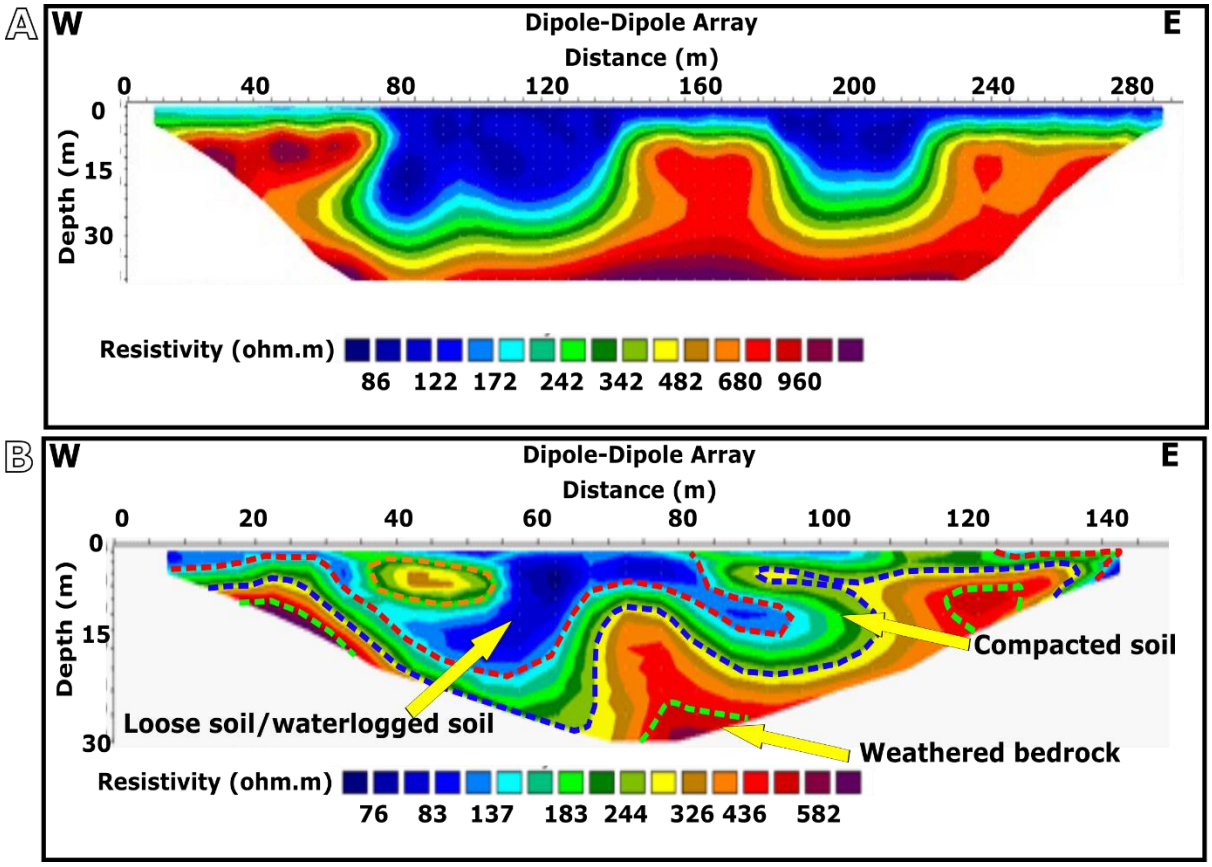

Figure 6.12: Dipole-Dipole array, comparison of: A) Forward model of the geological model for resistivity line 1; B) Inversion of the measured data.

The Schlumberger array for the geological model (Figure 6.13 A) shows a similar weathering profile to that seen from the field data (Figure 6.13 B). This model was exaggerated on a horizontal scale and therefore reached a deeper depth. If only the first 28 m vertical depth of the section is considered, there is a match in the resistivities and the shape of the weathering profile.

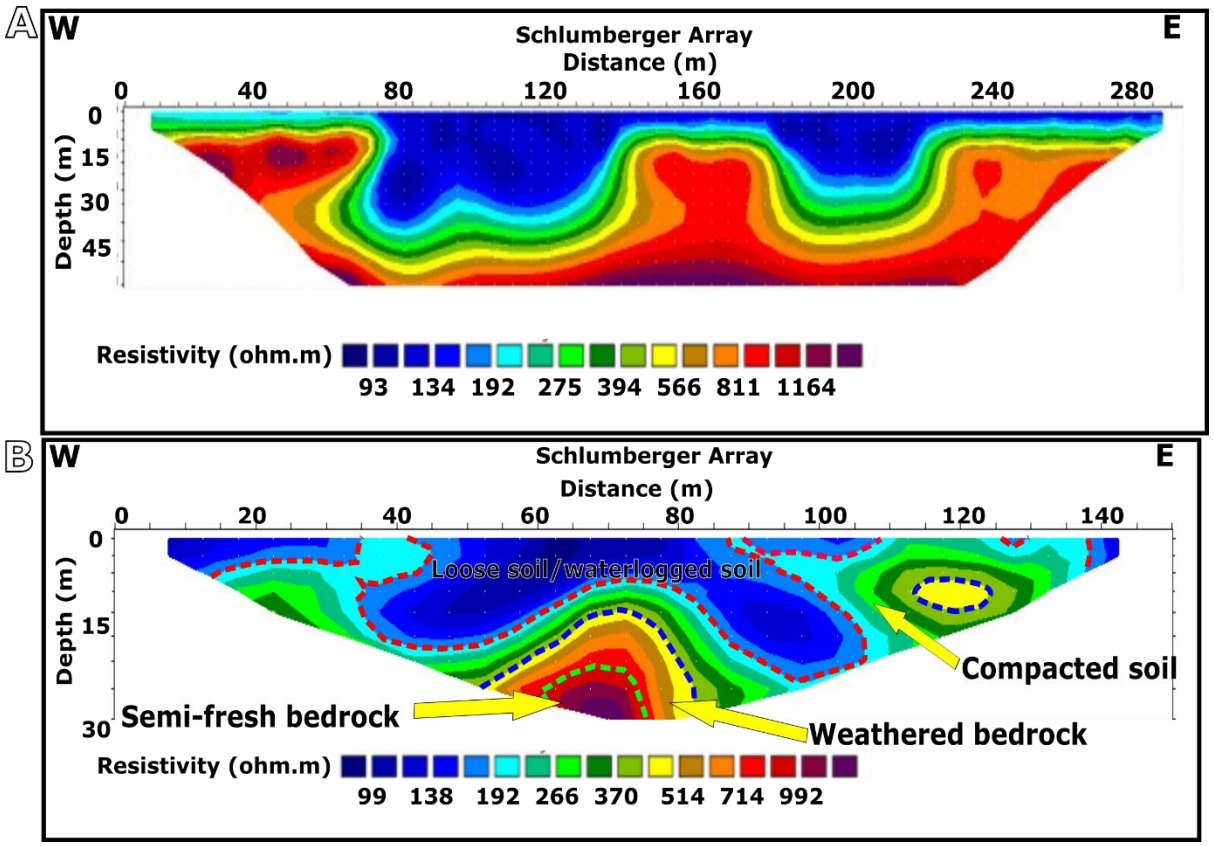

Figure 6.13: Schlumberger array, comparison of: A) Forward model of the geological model for resistivity line 1; B) Inversion of the measured data.

6.2.4 Magnetics

Regional magnetic data (Figure 6.14) were collected by the Council for Geosciences and show multiple magnetic anomalies of which no conclusion has been made. Multiple east-west trending magnetic highs are found, which one of the two study areas are found along.

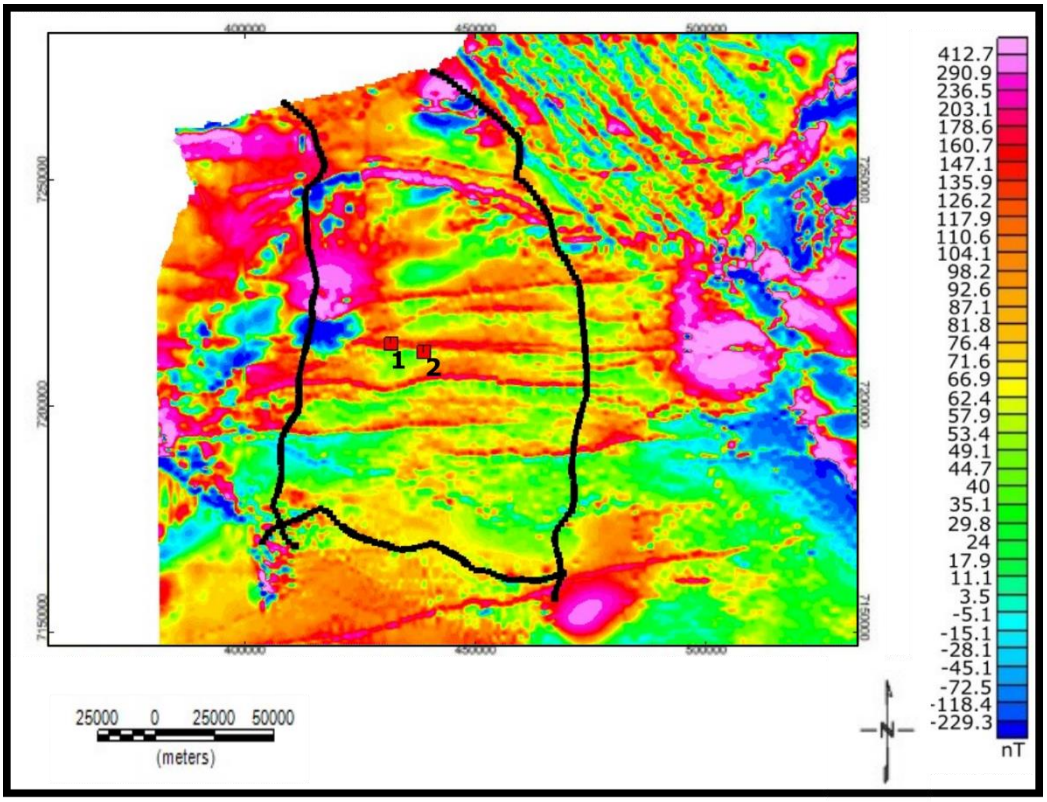

Figure 6.14: Regional magnetic map over the Far Western Limb with the legacy vibroseis seismic lines (Black lines) and the two study areas (Red blocks).

This survey therefore, allowed for high-resolution imaging of this magnetic anomaly (Figure 6.15).

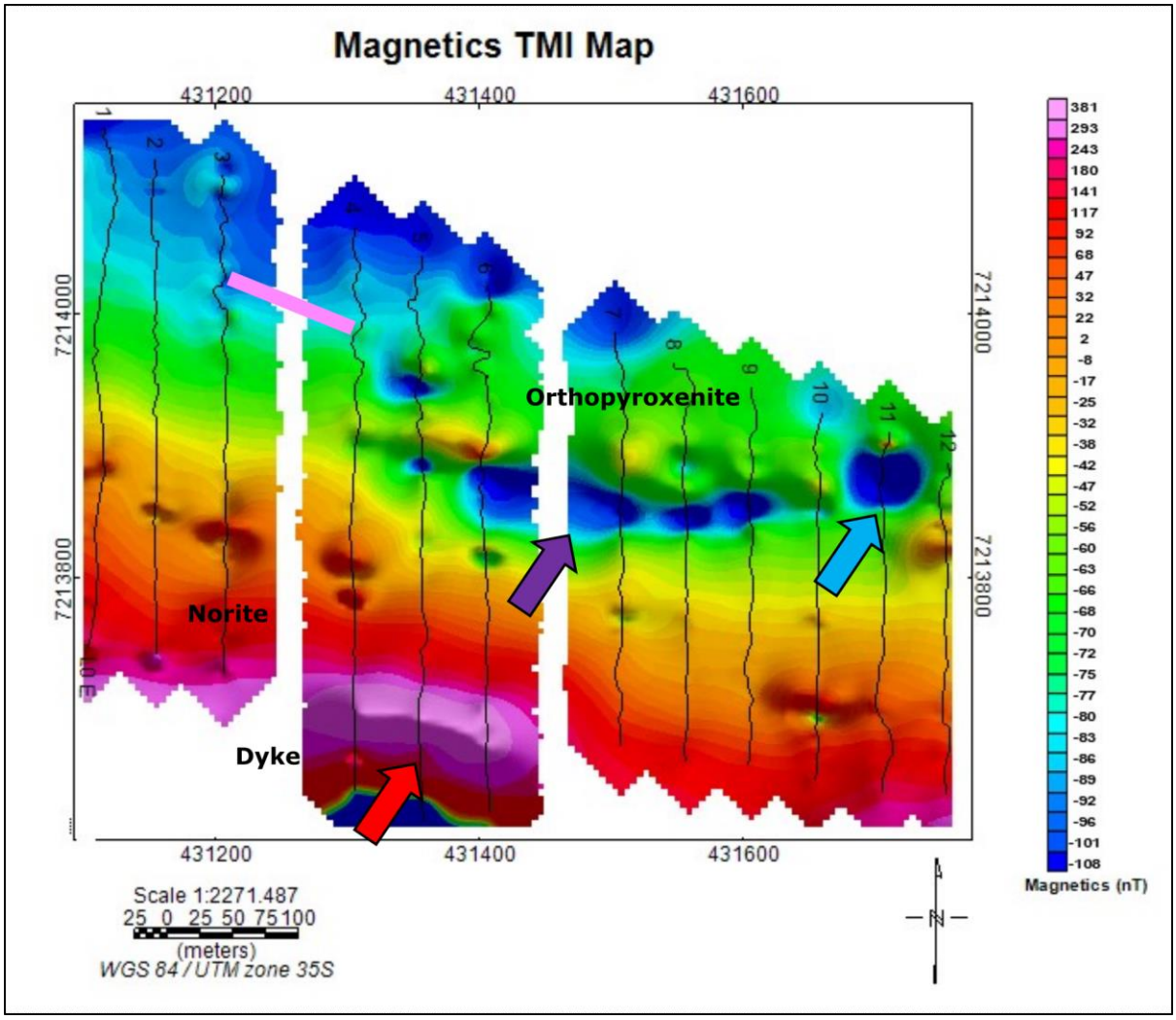

Figure 6.15: Interpreted Total Magnetic Intensity Map. Regions with less weathered Orthopyroxenite possibly shown by the purple and blue arrows. The green surrounding these less weathered orthopyroxenites may indicate a higher degree of weathering of these orthopyroxenites. The high magnetic anomaly (red arrow) is one of the east-west trending dykes that can be found in the regional magnetic data. The pink line shows the location of the seismic and resistivity lines in the area with the black lines showing the lines where the magnetic data are collected.

North of the surveyed area is the orthopyroxenite outcrop, which coincides with the magnetic low (approximately < -90 nT) in the data. It is important to note that there is a wire fence which borders the magnetic data.

The magnetic low in the centre of the survey area (indicated by the purple and blue arrow in Figure 6.15) is not continuous throughout the surveyed area. Given that it has similar values (< -90 nT) to the magnetic lows further north associated with the outcropping orthopyroxenites, this feature may be continuous.

The slightly higher magnetic values (~ -60 nT, green in Figure 6.15) surrounding these lows could be associated with weathering of these orthopyroxenites. As pyroxenite weathers it forms magnetite, which

has a higher susceptibility. Since the rate of weathering is unknown, the higher magnetic anomalies may be interpreted as the weathered orthopyroxenite to the north. The magnetisation of the magnetite at its time of formation would allow for variable magnetic response to be created.

The higher magnetic values towards the south of the map (- 40 nT to ~180 nT, yellow and red region in Figure 6.15) may indicate a contact between two different lithologies in the area, namely orthopyroxenite in the north and the potential contact with the underlying norite towards the south. This may indicate the contact between the Marginal Zone and the Lower Zone of the Rustenburg Layered Suite but cannot be confirmed as no outcrop was found in the area.

The high magnetic anomaly indicated by the red arrow (~ 293 nT) is identified as a dyke. This allows the remaining east-west trending high magnetic anomalies to also be considered as dykes. This dyke swarm continues towards the north and the south of the study area.

An integration of all of the collected data together with the models for area 1 can be found in Figure 6.16 below.

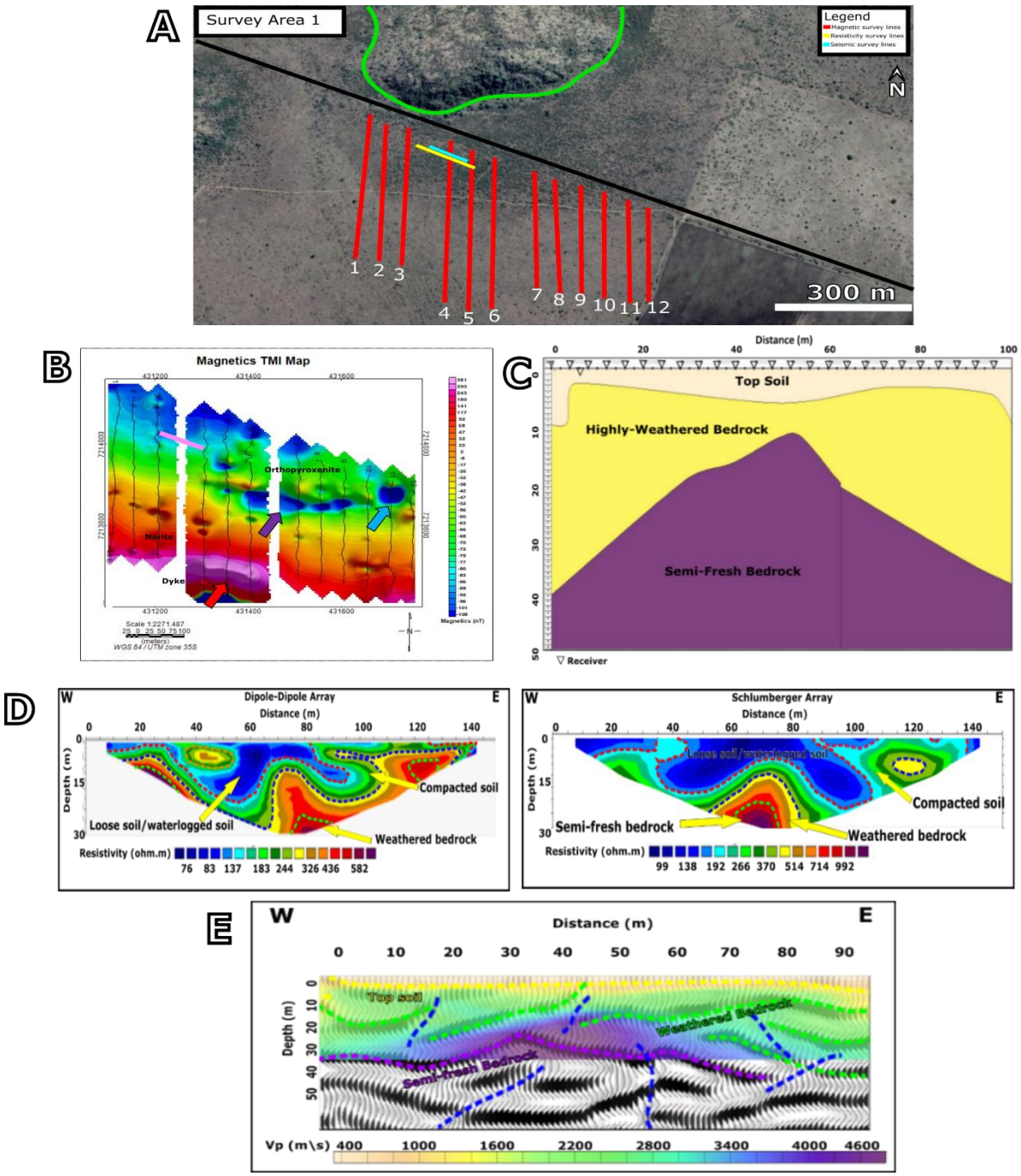

Figure 6.16: Integrated geophysical data for Area 1. A) The surveys lines used to collect the data; B) The interpreted magnetic data; C) the general geological model for the area; D) Interpreted resistivity data for resistivity line 1 and E) Interpreted seismic.

6.3 Geophysical data analysis for area 2

In this area, it is difficult to identify the lithologies responsible for the geophysical data collected. This is due to the lack of outcropping lithologies in the area. The samples retrieved from this area may be from the existing bedrock. By comparing the geophysical data and the physical property measurements it may be possible to find a relationship between the two.

6.3.1 Seismic line 2

The tomography for seismic line 2 shows the top soil (Figure 6.17, above black dashed line). The lithologies underlying this are the highly weathered gabbronorite samples (above the red dashed line) while the deeper higher P-wave velocities on the tomography represent semi-fresh gabbronorite (below the red dashed line). On either end of the tomography, the lower velocities extend deeper into the subsurface.

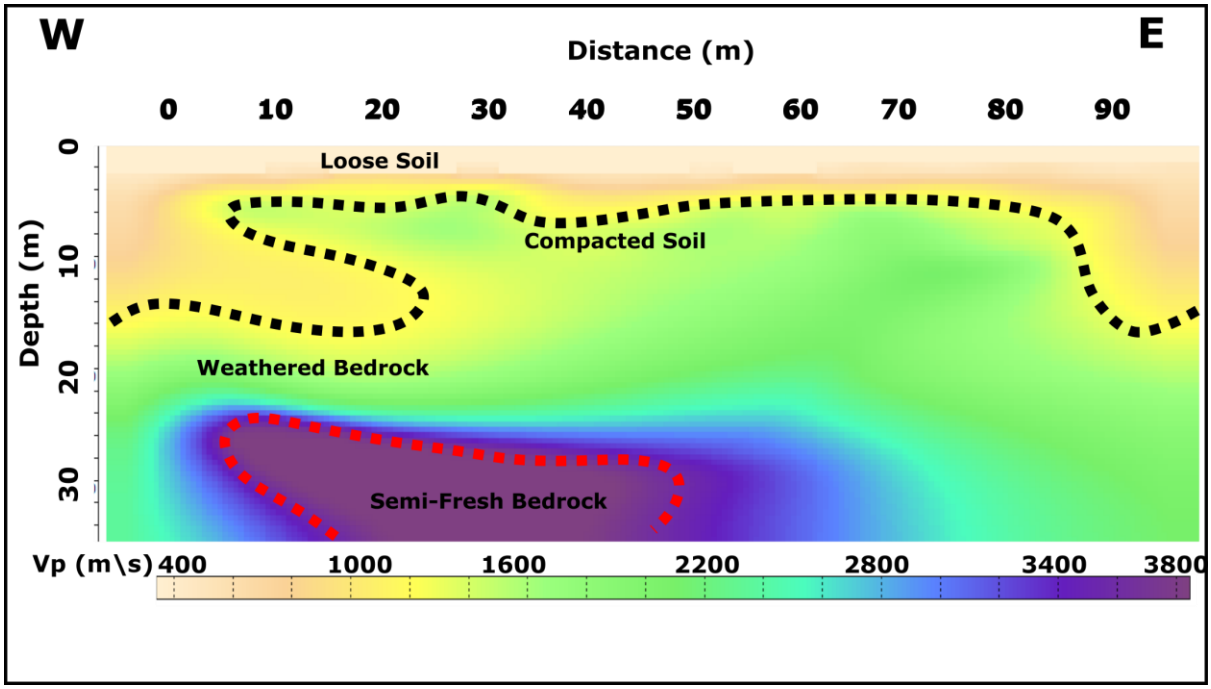

Figure 6.17: Interpreted seismic tomography for seismic line 2 with the different weathering surfaces marked.

The geological samples retrieved after agricultural digging between 37 and 54 m along the profile (pink dashed line in Figure 6.17) are sedimentary rocks (average P-wave velocity of 5500 m/s) and a gabbronorite intrusive (P-wave seismic velocity of 6500 m/s on the fresher samples).

The disturbance caused by the agricultural digging is seen by the lower confidence in the ray paths within the centre of the seismic data (Figure 5.6 A) and a discontinuity in the seismic section below the agricultural digging. Below this the ray paths show confidence up to 30 m into the subsurface.

The seismic section for line 2 (Figure 6.18) confirms the disturbance caused by the agricultural digging through the offsets seen in the section (pink dashed line) and the different weathering profiles identified on the tomography. The contact between the highly weathered gabbronorite bedrock and the top soil is found at 5 m (yellow dashed line). The potential contact between the highly weathered and the weathered gabbronorite bedrock is found at 15 m (green dashed line). This is followed by the contact

between the weathered and semi-fresh gabbronorite bedrock at 30 m (purple dashed line). Subvertical discontinuities in the seismic section (blue dashed lines) represent the potential faults in the seismic section.

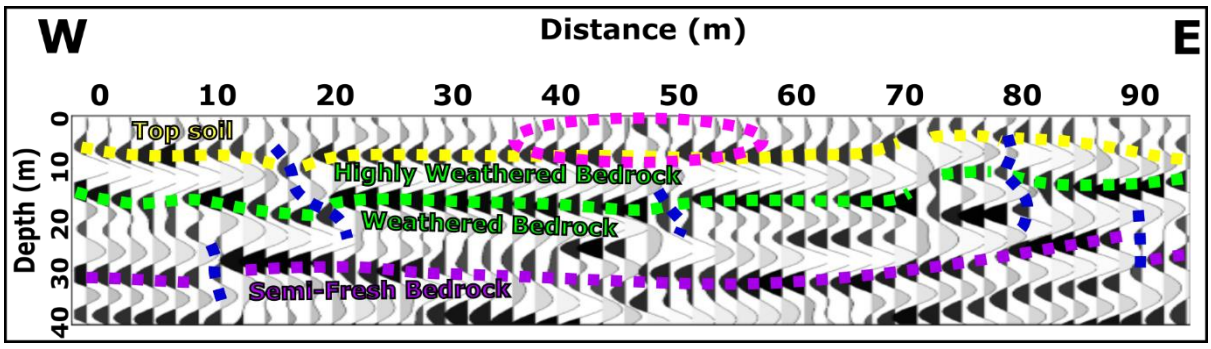

Figure 6.18: Interpreted seismic section for seismic line 2, with the different weathered surfaces, discontinuities (blue dashed line) and agricultural digging (dashed pink lines) marked.

Integrating the seismic section and the tomography (Figure 6.19) shows the velocities responsible for the reflections in the data. The top soil (yellow dashed line) has a P-wave velocity of 1000 m/s, the highly weathered gabbronorite bedrock (between the yellow and green dashed lines) has a P-wave velocity of 1600 m/s, the weathered gabbronorite (between the green and purple dashed lines) has a P-wave velocity of 2300 m/s and the semi-fresh gabbronorite bedrock (purple dashed line) has a reflection with a P-wave velocity of 3600 m/s. The pink dashed line in the seismic section represents the gaps within the data caused by the agricultural digging. The subvertical discontinuities in the data are associated with the lower velocities and show extensive weathering along them (blue dashed lines). In this area water would have run along these fractures and weathered the gabbronorite further.

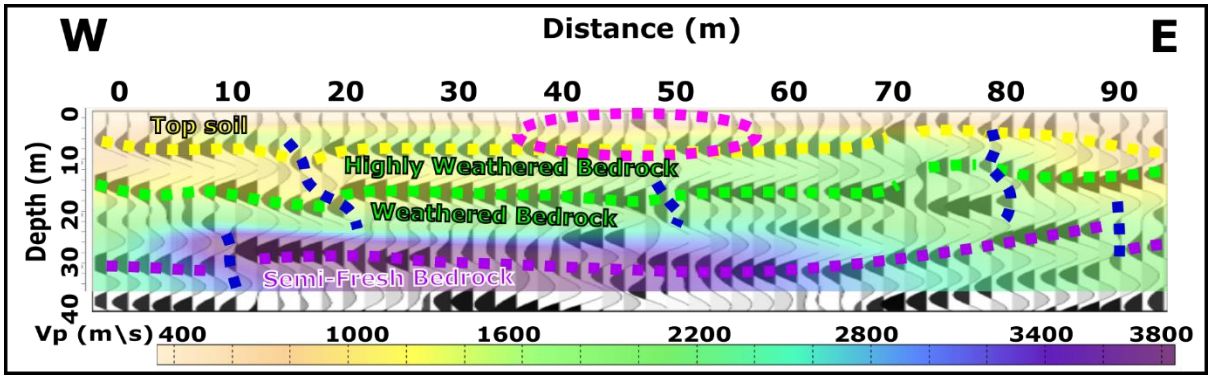

Figure 6.19: Integrated interpretations for seismic section and seismic tomography data along seismic line 2 with the weathering surfaces, discontinuities (blue dashed lines) and agricultural digging (dashed pink lines) marked.

Based on the seismic velocities, the weathering profiles can be identified as outlined in Table 6.8.

Table 6.8: Velocity ranges and correlating thicknesses for the interpreted subsurface weathering profiles on seismic line 2.

Weathering profiles	Velocity range (m/s)	Thickness (m)
Top soil	~1000	~5
Highly weathered gabbronorite bedrock	1600	~10
Weathered to semi-fresh gabbronorite bedrock	2300	~15
Semi-fresh gabbronorite bedrock	~3600	>2

6.3.2 Modelling for Seismic line 2

The seismic model in Figure 6.20 represents the contacts between the semi-fresh, weathered and highly weathered gabbronorite bedrock followed by the overburden. The shape of the weathering profile is based on the field data. The gabbronorite is expected to occur as a dyke that strikes in the east-west direction as found in the magnetic data north of area 2 (Figure 6.14), therefore the model for seismic line 2 shows a linear section along the dyke. Multiple fractures are found on the eastern side of the model and shows the weathered bedrock reaching a deeper depth. Sedimentary samples that were collected in this area have been excluded from this model as the samples collected from the field do not come from any outcrop or occur in a large quantity as compared to the gabbronorite. It is likely that the sedimentary samples occur deeper within the subsurface.

The geological section for this model is summarised in Table 6.9. A higher velocity was used for the semi-fresh bedrock to see the correlation with the measurements made on the samples. The forward model (Figure 6.20) was designed with fixed receivers: 50 sources spaced at 2 m along the profile and 48 receivers at 2 m spacing. The modelling was run at 60 Hz using the Ricker wavelet and recorded up to 500 ms.

Table 6.9: Geological model for seismic line 2.

Lithological description	P-wave velocities (m/s)	Density (g/cm^3)	Estimated thickness (m)	Correlating reference
Top soil	600	1,24	~4	(Kausarian et al., 2014)
Highly weathered gabbronorite bedrock	1600	2,68	~10-20	See Table 5.4
Weathered gabbronorite bedrock	2300	3	~5-20	
Semi-fresh gabbronorite bedrock	5764	3.15	>2	

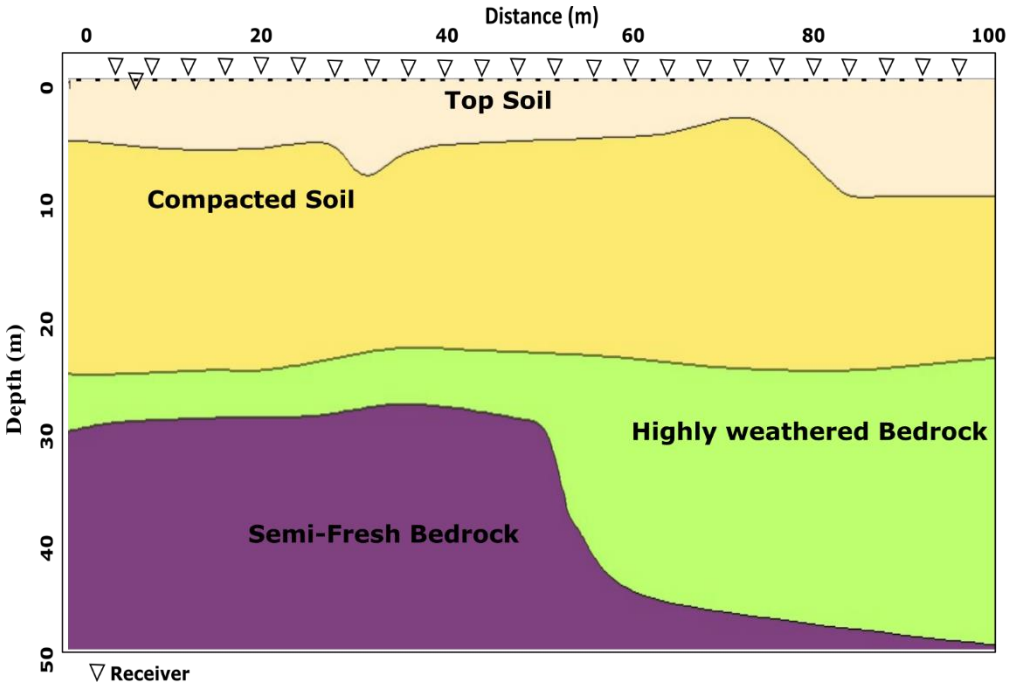

Figure 6.20: Model for seismic line 2.

Comparing the synthetic shot gathers (Figure 6.21 A) from this geological model with the processed shot gathers shows a strong correlation between the two (Figure 6.21 B). The reflections that were present in the processed shot gathers were also present in the synthetic shot gathers: the reflection with a velocity of 600 m/s (yellow arrow), the reflection with a velocity of 2000 m/s (green arrow) and the last reflection with a velocity of 3000 m/s (pink arrow). This shows that the model created is a reliable mapping of the subsurface lithologies in this area.

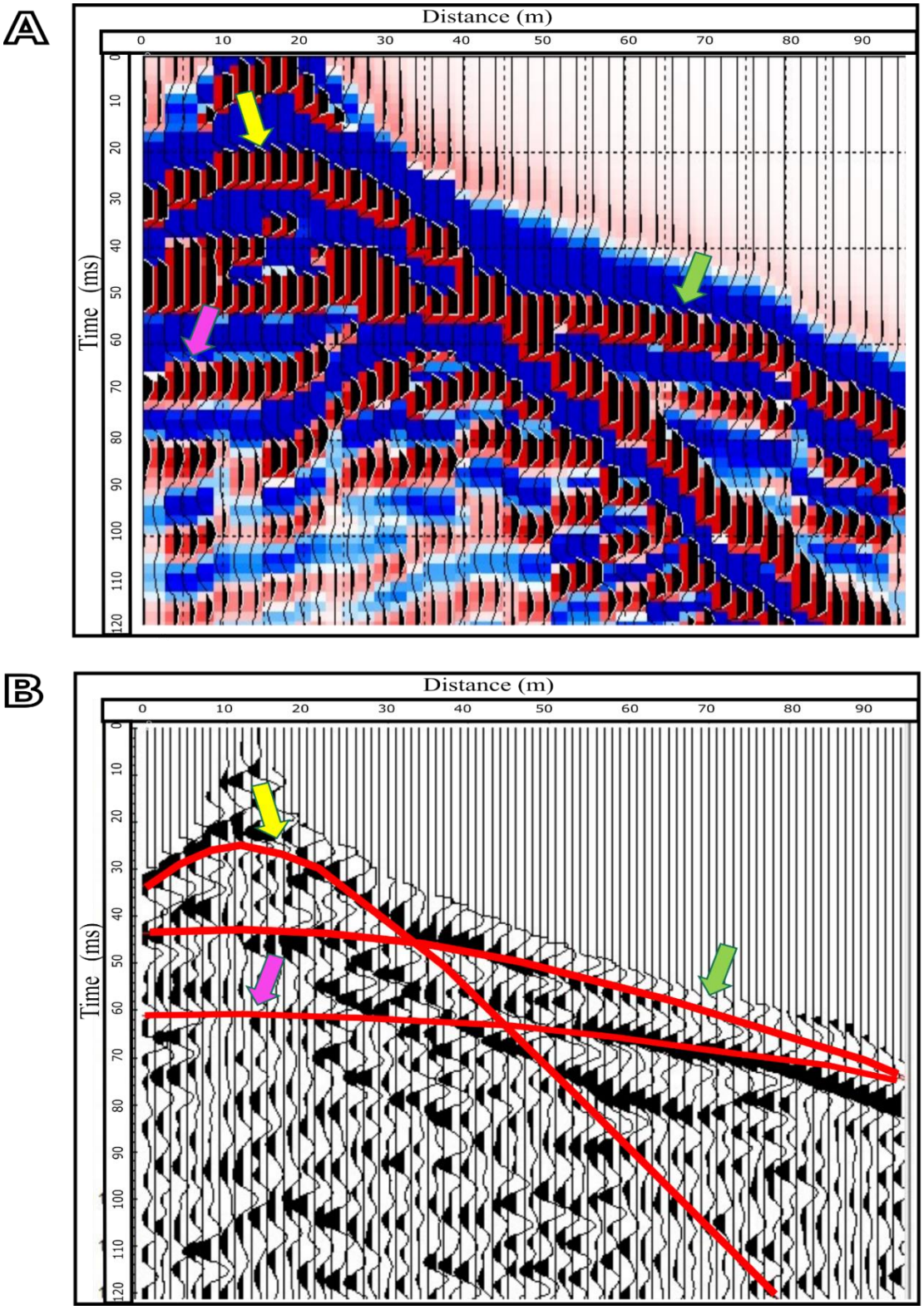

Figure 6.21: A) Synthetic shot gathers, B) Processed shot gathers for seismic line 2 showing reflections picked. Yellow arrow showing a velocity of 600 m/s, the green arrow showing the velocity of 2000 m/s and the pink arrow showing a velocity of 3000 m/s.

6.3.3 Seismic line 3

The tomography of seismic line 3 (Figure 6.22) images the top soil (above the red dashed line), potentially high degree of weathered gabbronorite bedrock (below red dashed line) and finally the weathered gabbronorite bedrock (below the black dashed line). The ray paths for this line shows confidence in mapping the velocities of the subsurface up to 24 m in depth. The highest confidence mapping falls within the first 10 m of the subsurface.

Agricultural digging along this line occurs between 35 and 54 m along profile (pink dashed line) with the disturbance found in both the seismic ray tracing and the seismic tomography up to 8 m in depth. The presence of the shallow high P-wave seismic velocity feature (~2000 m/s) confirms that the weathered gabbronorite bedrock is close to the surface and the agricultural digging may have exposed it.

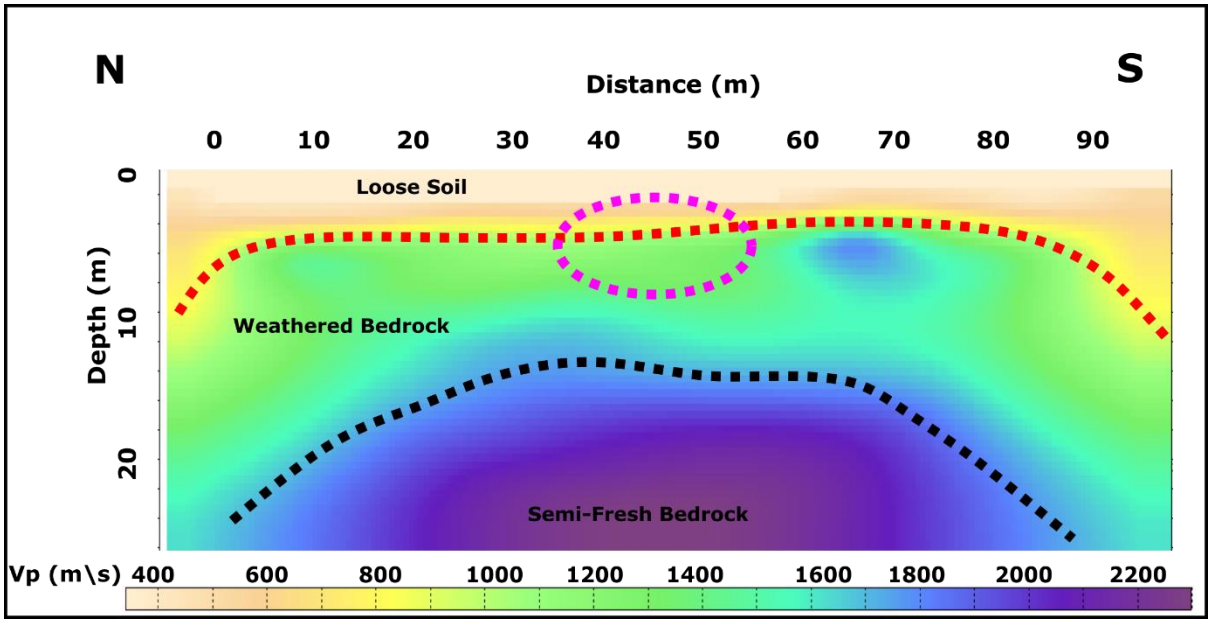

Figure 6.22: Interpreted seismic tomography for seismic line 3 with the different weathering surfaces marked.

The reflection seismic section (Figure 6.23) for this line shows contacts between the weathering surfaces (yellow, green and purple dashed lines) and confirms the disturbance caused by the agricultural digging (pink dashed line). The top soil (above the yellow dashed line) occurs within the first 10 m of the subsurface. The highly weathered gabbronorite bedrock (between the yellow and green dashed lines) occurs between 10 and 20 m, while the region below the weathered gabbronorite bedrock (between the green and purple dashed lines) represents the weathered gabbronorite bedrock. This is followed by the semi-fresh gabbronorite bedrock (below the purple dashed line) found at 30 m. Potential fractures in

the subsurface are identified through the discontinuities seen along the reflectors and mainly trend northeast to southwest (blue dashed lines).

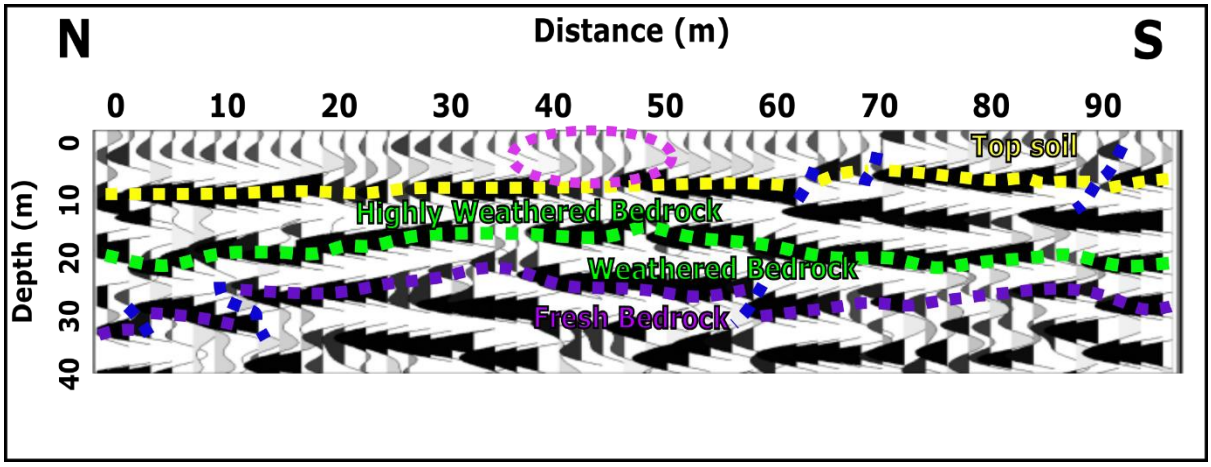

Figure 6.23: Interpreted seismic section for seismic line 3 with the different weathering surfaces, discontinuities (blue dashed lines) and agricultural digging (dashed pink line) marked.

Integrating the reflection seismic section with the seismic tomography (Figure 6.24) shows a good correlation between the weathering surfaces identified. The top soil (above the yellow dashed line) has a P-wave velocity of 1100 m/s, the highly weathered gabbronorite bedrock (between the yellow and green dashed lines) has a P-wave velocity of 1600 m/s and the weathered gabbronorite bedrock (between the green and purple dashed lines) has a P-wave velocity of 2100 m/s, while the semi-fresh gabbronorite bedrock (below the purple dashed lines) isn't clearly imaged on the tomography and has a velocity of >2100 m/s. The shallow areas where the fractures occur are associated with lower seismic velocities.

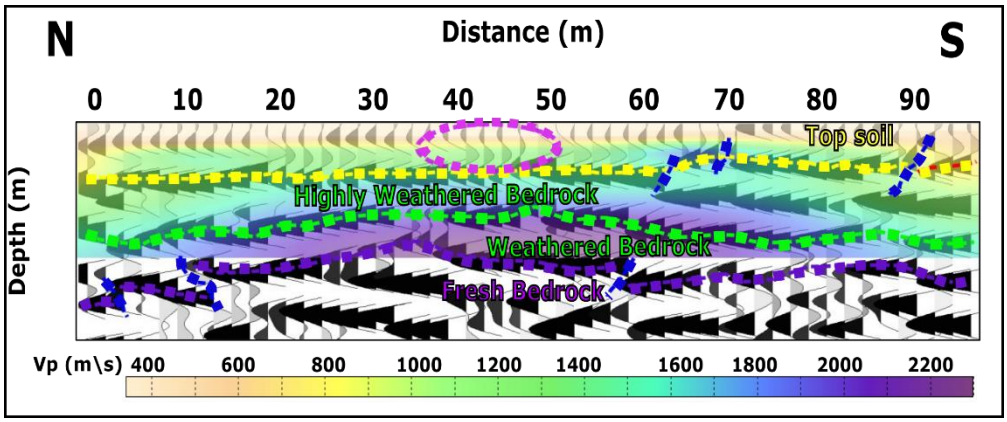

Figure 6.24: Integrated seismic section with the seismic tomography for seismic line 3 with the different weathering surfaces, discontinuities (blue dashed lines) and agricultural digging (pink dashed line) marked.

Based on the velocities in the tomography, the weathering surfaces can be identified as outlined in Table 6.10.

Table 6.10: Velocity ranges and correlating thicknesses for the interpreted subsurface weathering profiles on seismic line 3.

Weathering profiles	Velocity range (m/s)	Thickness (m)
Top soil	< 1000	< 10
Highly weathered gabbronorite bedrock	1000-1600	~10
Weathered gabbronorite bedrock	1600-2000	~5
Semi-fresh gabbronorite bedrock	> 2000	> 5

6.3.4 Modelling for seismic line 3

The seismic geological model (Figure 6.25) is based on the same geological model used for the resistivity data (discussed later in this section) which images the contacts between the weathered and highly weathered gabbronorite bedrock, followed by the overburden. The geological data for this line seemingly cross cuts the gabbronorite dyke, indicating the potential width of the gabbronorite dyke in the area. The geological section is summarised in Table 6.11, with the velocities, densities and thicknesses. These values were used to create a synthetic seismogram. The forward model was designed with fixed receivers; 50 sources spaced at 2 m along the profile and 48 receivers at 2 m spacing. The modelling was run at 60 Hz using the Ricker wavelet and recorded up to 500 ms. The sedimentary samples that were collected through the agricultural digging have not been included in the model as it may occur much deeper within the subsurface.

Table 6.11: Geological model for seismic line 3.

Lithological description	P-wave velocities (m/s)	Density (g/cm^3)	Estimated thickness (m)	Correlating reference
Top soil	600	1,25	5	(Kausarian et al., 2014)
Compacted soil	1100	1,35	2-15	
Highly weathered gabbronorite bedrock	1600	2,68	2	See Table 5.4
Weathered gabbronorite bedrock	2300	3	> 2	

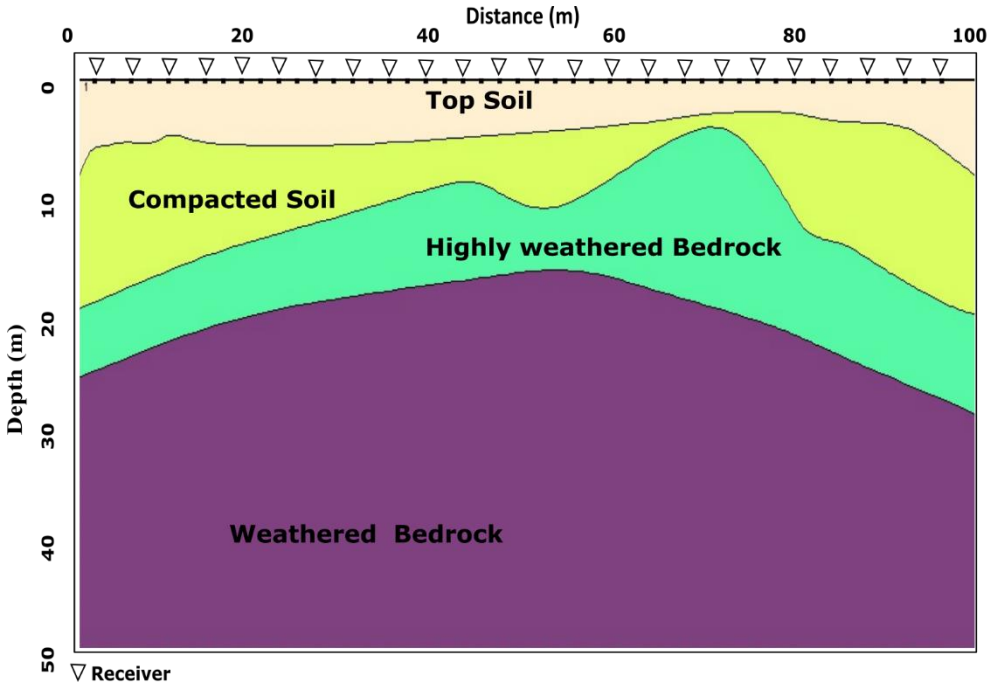

Figure 6.25: Geological model for seismic line 3.

Comparing the synthetic shot gathers created in SynthSeis (Figure 6.26 A) with the processed shot gathers (Figure 6.26 B) shows a strong correlation between the two namely: the first reflection between top soil and the compacted with a velocity around 600 m/s (yellow arrow), the second reflection at the contact between the compacted soil and the highly weathered gabbronorite bedrock with a velocity of 1000-1200 m/s (green arrow)and the third reflection at the contact between the highly weathered gabbronorite bedrock and the weathered gabbronorite bedrock with a velocity of 1600 to 2000 m/s (pink arrow).

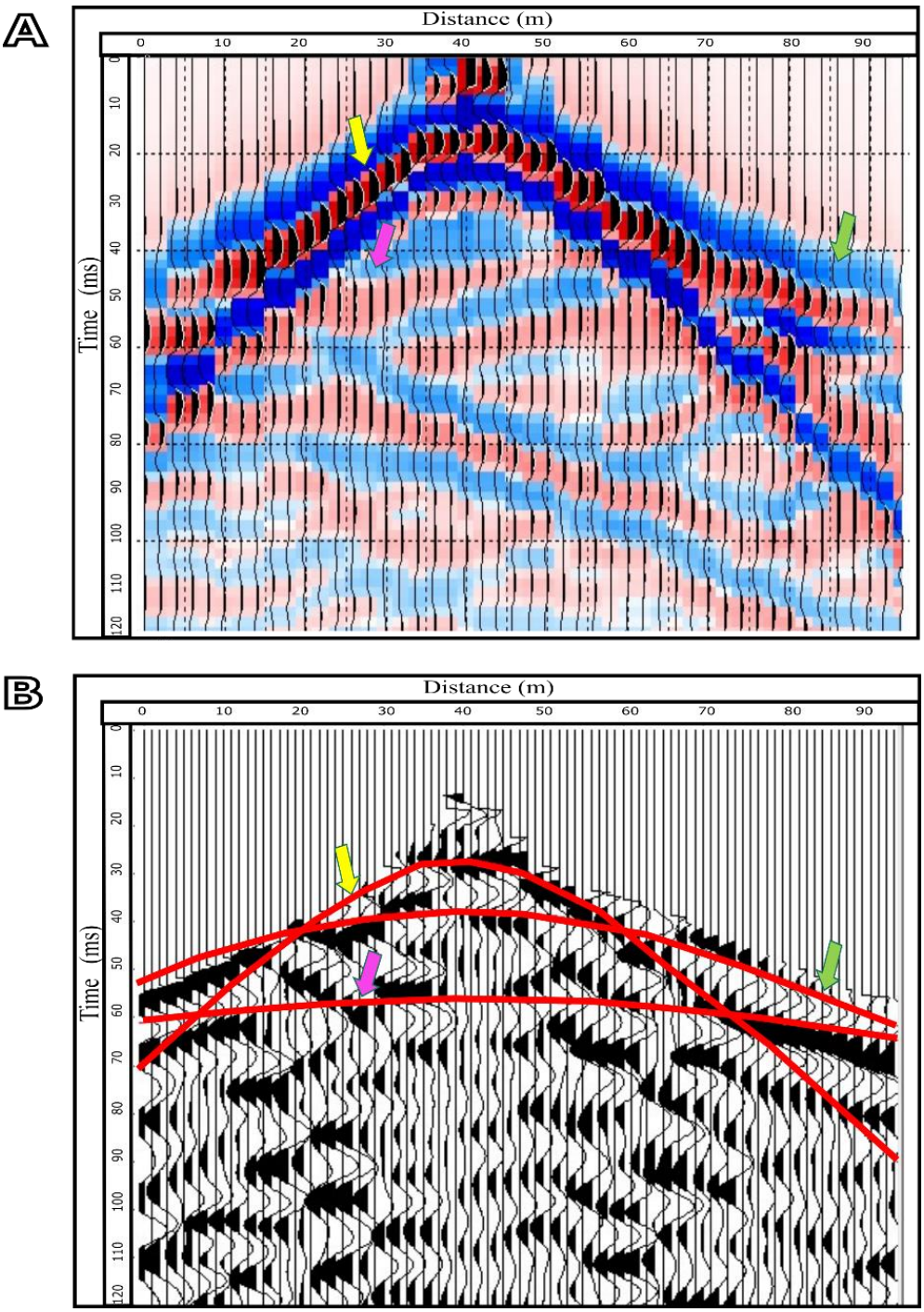

Figure 6.26: A) Synthetic shot gathers, B) Processed shot gathers for seismic line 3 showing reflections picked. Yellow arrow showing a velocity of 600 m/s, the green arrow showing the velocity of 1200 m/s and the pink arrow showing a velocity of 1600-2000 m/s.

The synthetic seismogram created in SynthSeis for seismic line 2 and 3 show that there will be some reflections from the proposed geological section (Table 6.12). This geological section adds a few more weathering surfaces.

Table 6.12: Geological section for reflectivity modelling in area 2.

Lithological description	Velocities (m/s)	Density (g/cm^3)	Estimated thickness (m)
Loose top soil	600	1,2	5
Compacted top soil	1200	1,71	10
Highly weathered gabbronorite bedrock	1600	2,68	2
Weathered gabbronorite bedrock	2300	3	3
Semi-fresh gabbronorite bedrock	3000	3	8
Fresh gabbronorite bedrock	5474	3,15	12

The seismogram was created using a sampling rate of 4 ms, the Minimum Phase wavelet to enhance the shallow reflection and a frequency of 60 Hz similar to that for which the data was acquired (Figure 6.27).

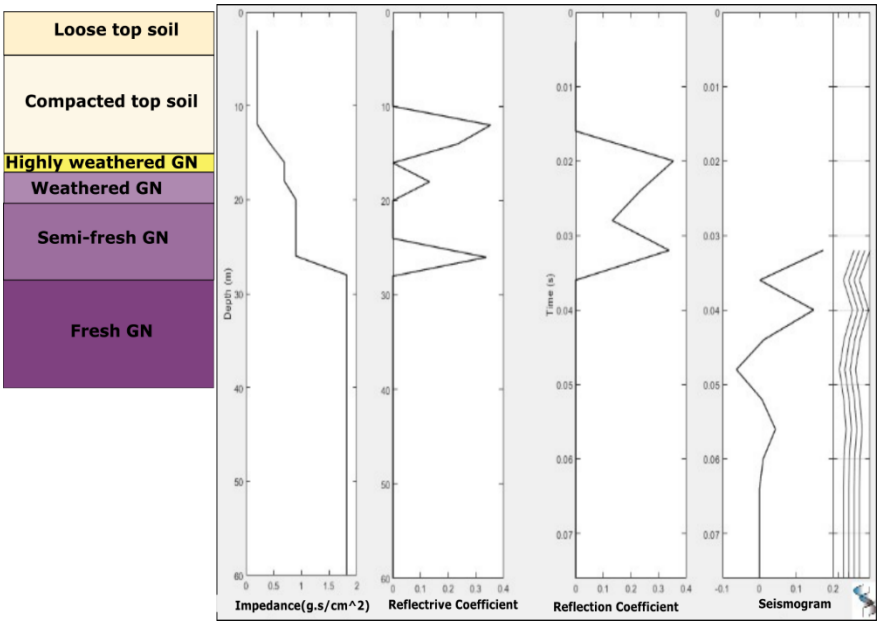

Figure 6.27: Synthetic seismogram using the minimum phase wavelet for area 2, GN represents gabbronorite.

Similarly, the Ricker wavelet was used in order to compare the reflections directly with those in the processed seismic data (Figure 6.28).

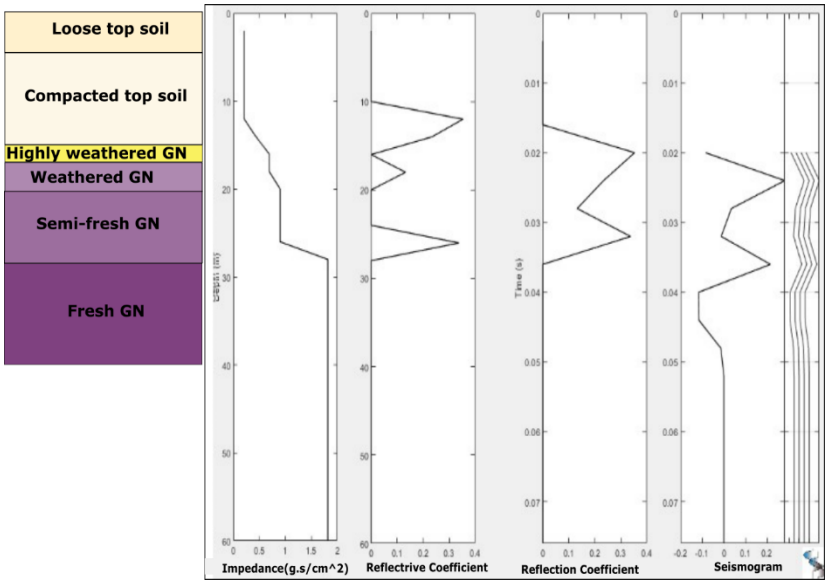

Figure 6.28: Synthetic seismogram using the Ricker wavelet for area 2, GN represents gabbronorite.

The Ricker and the Minimum Phase wavelet synthetic seismogram show two strong reflections. The first being the contact between the top/compacted soil and the highly weathered gabbronorite bedrock and the second being the contact between the semi-fresh and fresh gabbronorite bedrock. The Ricker wavelet shows a stronger correlation to the reflections in the seismic section (Figure 6.29) for seismic line 2 as compared to the Minimum Phase wavelet. The polarity of the Minimum Phase wavelet is opposite to that of the seismic section.

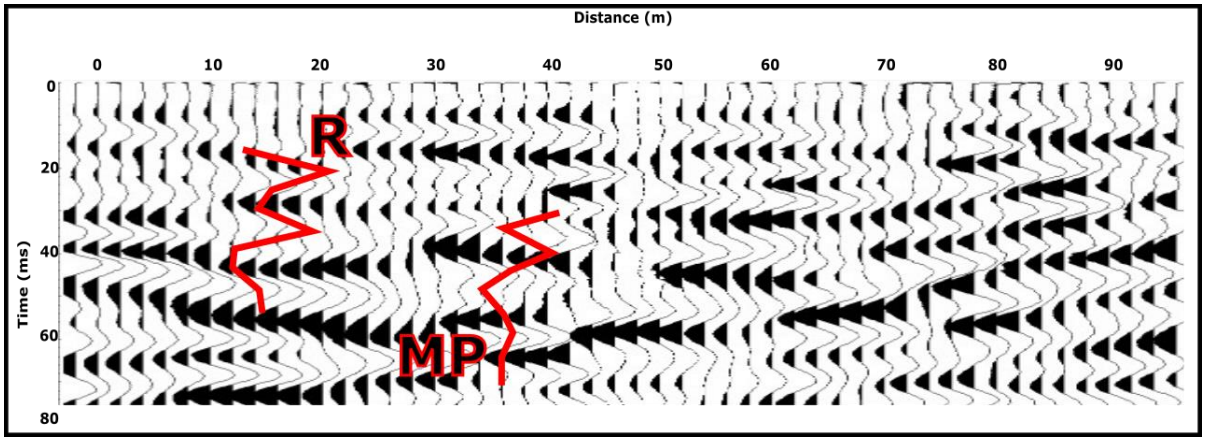

Figure 6.29: Correlation of the real and synthetic reflections in the seismic section with the with the minimum phase (MP) and ricker (R) synthetic seismograms for line 2 in area 2.

Similarly, the same weathering profiles/reflections are identified on seismic line 3 with the Ricker wavelet having a strong correlation (Figure 6.30). The Minimum Phase wavelet shows the polarity of the synthetic reflection to be opposite to that, as seen in the seismic section. This shows that the interpretations made on the seismic sections are valid and reliable.

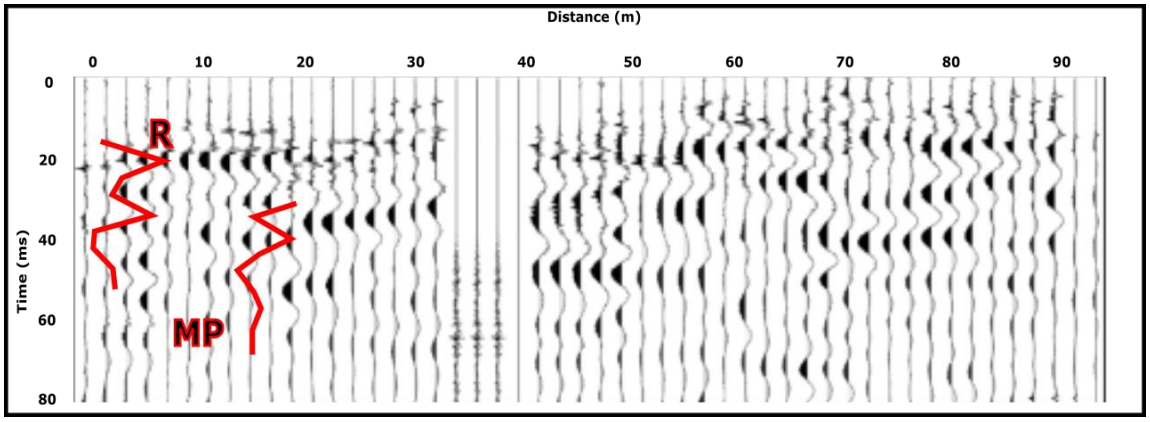

Figure 6.30: Correlation of the real and synthetic reflections in the seismic section with the with the minimum phase (MP) and ricker (R) synthetic seismograms for line 3 in area 2.

6.3.5 DC resistivity line 2

The gabbronorite samples on which measurements were made had a lower degree of weathering as compared to the majority of the gabbronorite samples revealed by the agricultural digging. Samples that have a higher degree of weathering showed resistivity values between 2000 and 9000 Ohm.m while the less weathered gabbronorite samples has resistivity of ~ 3000 Ohm.m. The sedimentary samples that were retrieved have an average resistivity range of 3500 Ohm.m to 6400 Ohm.m.

Different weathering layers within the subsurface are identified from the interpreted section of the Dipole-Dipole array (Figure 6.31). Resistivities that are picked up are however too low to be attributed to fresh bedrock.

Dipole-Dipole array

The shallow regions on the western side of the section (black circle) correlate with the agricultural digging where samples were retrieved. The waterlogged overburden within the subsurface is interpreted to occur above the red dashed line which may be where the water table is. Agricultural digging towards the western end of the section caused the varying resistivities found above the red dashed line. The landmass that was excavated added back into the cavity that was created.

The area on the section indicated by the pink dashed line may represent the water seeping into and eroding the bedrock through fractures, allowing for a higher degree of weathering on the gabbronorite bedrock.

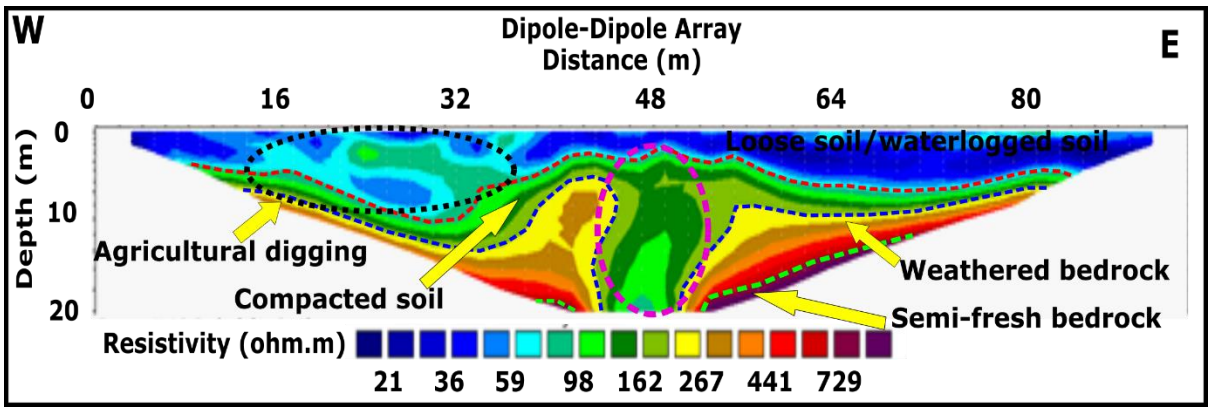

Figure 6.31: Interpreted resistivity section with marked weathering profiles, agricultural digging (black circle) and possible fractures (pink dashed line) for the Dipole-Dipole array from resistivity line 2.

The section below the blue dashed line could represent the fresher gabbronorite bedrock in the area (> 20 m). The sedimentary samples here may be found much deeper within the subsurface.
Based on the resistivities in this section, the weathering surfaces can be identified (Table 6.13).

Table 6.13: Resistivity ranges and correlating thicknesses for the interpreted subsurface weathering profiles of the Dipole-Dipole array (resistivity line 2).

Weathering profiles	Apparent resistivity range (Ohm.m)	Thickness (m)
Top soil/ loose soil/ waterlogged soil	<100	< 8
Compacted soil	100-200	~3
Highly weathered gabbronorite bedrock	200-800	~7
Semi-fresh gabbronorite bedrock	>800	>2

Schlumberger array

On the Schlumberger section (Figure 6.32) the low resistivity above the red dashed line is interpreted to represent the saturated loose soil. Between the red and the green dashed line, is assumed to be the highly weathered gabbronorite bedrock. This is followed by the semi-fresh gabbronorite bedrock below the green dashed line. The agricultural digging is not picked up on the Schlumberger array.

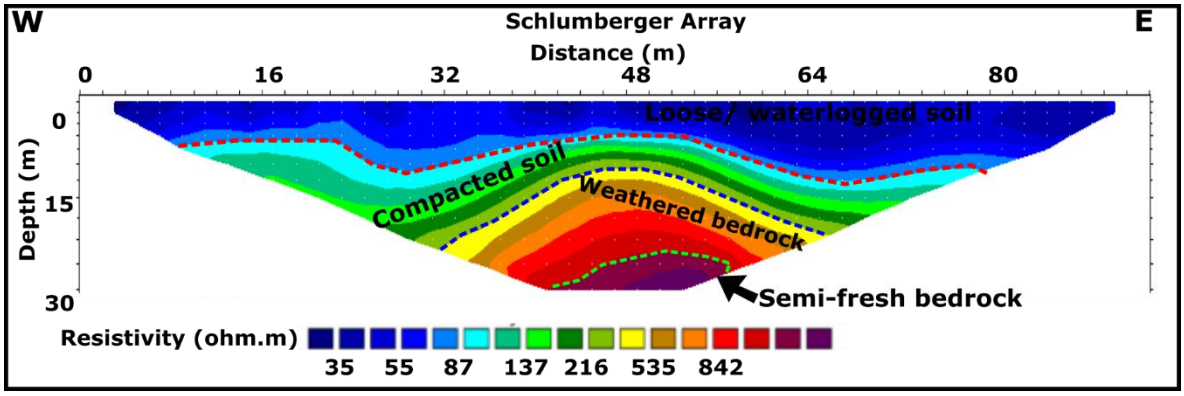

Figure 6.32: Interpreted resistivity section with marked weathering profiles for the Schlumberger array from resistivity line 2.

Based on the resistivities in this section, the weathering surfaces are summarised (Table 6.14).

Table 6.14: Resistivity ranges and correlating thicknesses for the interpreted subsurface weathering profiles of the Schlumberger array (resistivity line 2).

Weathering profiles	Apparent resistivity range (Ohm.m)	Thickness (m)
Top soil/ Loose soil/ waterlogged soil	<100	< 7
Compacted soil	100-200	~4
Highly weathered gabbronorite bedrock	200-800	~6
Semi-fresh gabbronorite bedrock	>800	>3

When comparing the two sections, the bedrock seems to be recorded well with the Schlumberger array, while a higher resolution of the shallow subsurface is obtained by the Dipole-Dipole array. The data indicates that the bedrock occurs within 10 m of the subsurface. The samples retrieved from the area indicate that the bedrock consists of the gabbronorite which may have intruded a sedimentary layer that is much deeper within the subsurface.

Modelling for resistivity line 2

A geological model for line 2 describes the geological subsurface based on the field data and the physical properties of the samples collected (Table 6.15).

Table 6.15: Physical characteristics of lithological units in area 2 with their thicknesses found from interpreted data.

Lithological description	Resistivity properties (Ohm.m)	Estimated thickness (m)	Correlating reference

Loose soil	100	<9	(Kausarian et al., 2014)
Compacted Soil	100 – 200	4	
Highly weathered gabbronorite bedrock	200 – 800	6	See Table 5.4
Semi-fresh gabbronorite bedrock	> 1000	> 3 (horizontal thickness)	

The geological model (created in Res2DMod) for resistivity line 2 of area 2 (Figure 6.33) reveals the expected weathering profile based on the resistivity data collected from the field. The model is exaggerated on both the horizontal and vertical scales, therefore, the depths reached on the resultant sections will be much higher and so will the recorded resistivities. This model was constrained using resistivity values for the gabbronorite. It can be assumed that the sedimentary samples were brought up to the surface with the gabbronorite although this was not added in the model as the exact depth to the layer has not been identified. The model itself is done considering that the survey line was done parallel to the regional dyke, therefore the typical idea of the dyke intruding the subsurface will not be seen in this model.

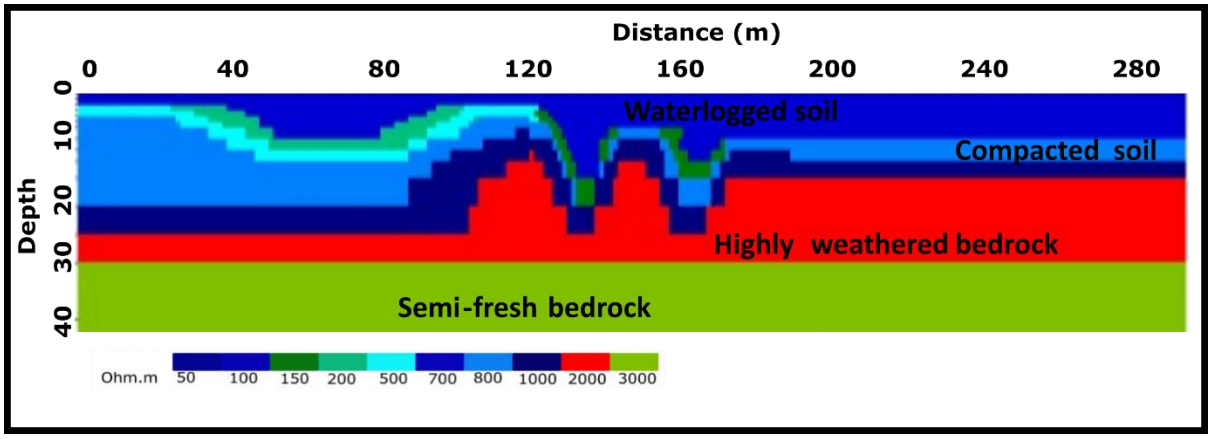

Figure 6.33: Geological model for resistivity line 2.

The resistivities were then calculated for this forward model for both the Dipole-Dipole array and the Schlumberger array. Both show a fair mapping of the structural features from the resistivity model. The Dipole-Dipole array (Figure 6.34 A) for this geological model shows the effect of the gabbronorite dyke. The shape of the sections match although the resistivities recorded do not match between the field data section (Figure 6.34 B) and the modelled data section.

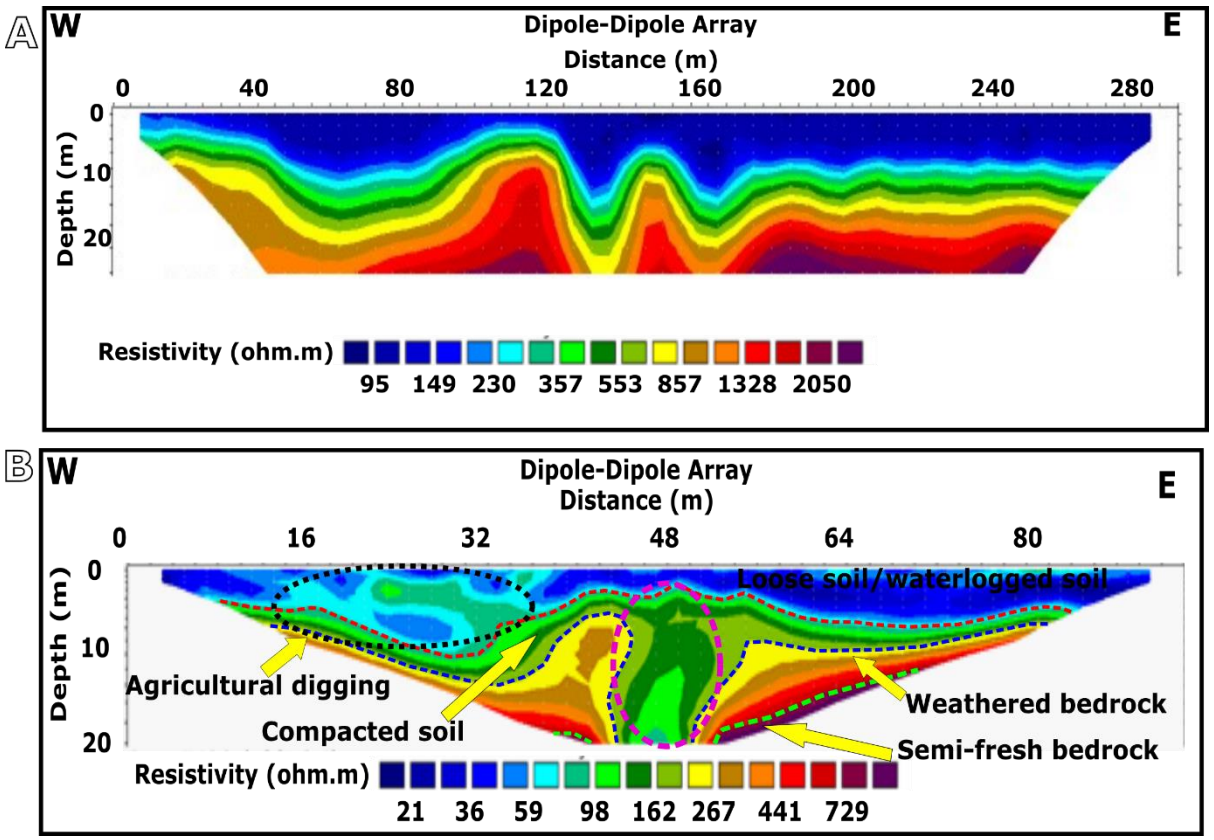

Figure 6.34: Dipole-Dipole section, comparison of A) Forward model of the geological model for resistivity line 2, B) Inversion of the measured data.

The Schlumberger array section (Figure 6.35 A) for the geological model matches the shape of the weathering profile of the field data (Figure 6.35 B). The resistivities that are recorded with the geological model sections are much higher than those picked up in the field data section as the model was for a longer length. If only the first 19 m of the modelled data is considered, then the resistivities and the weathering profiles match very well.

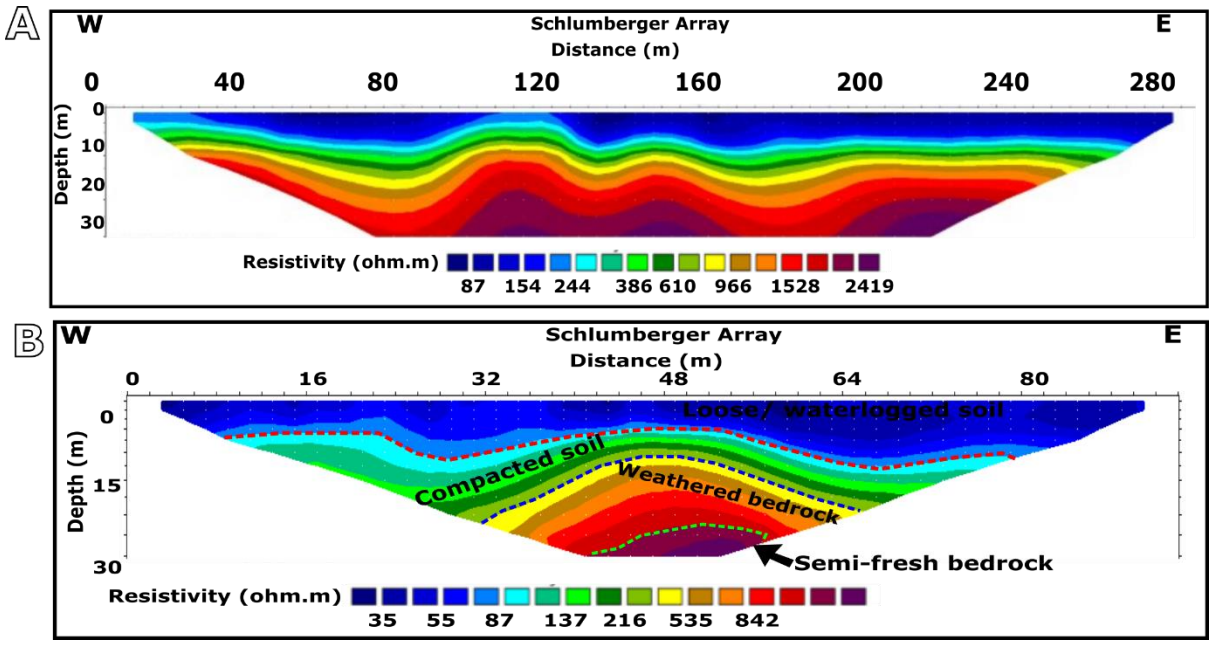

Figure 6.35: Schlumberger section, comparison of A) Forward model of the geological model for resistivity line 2, B) Inversion of the measured data.

Similar to the Dipole-Dipole modelled data, the values of the modelled section are higher. If only the first 19 m of this model are considered then the weathering profile and the resistivities match very well.

6.3.6 DC resistivity line 3

Similar to the previous resistivity line, the Schlumberger array (Figure 6.36) also shows the various weathering profiles for area 2.

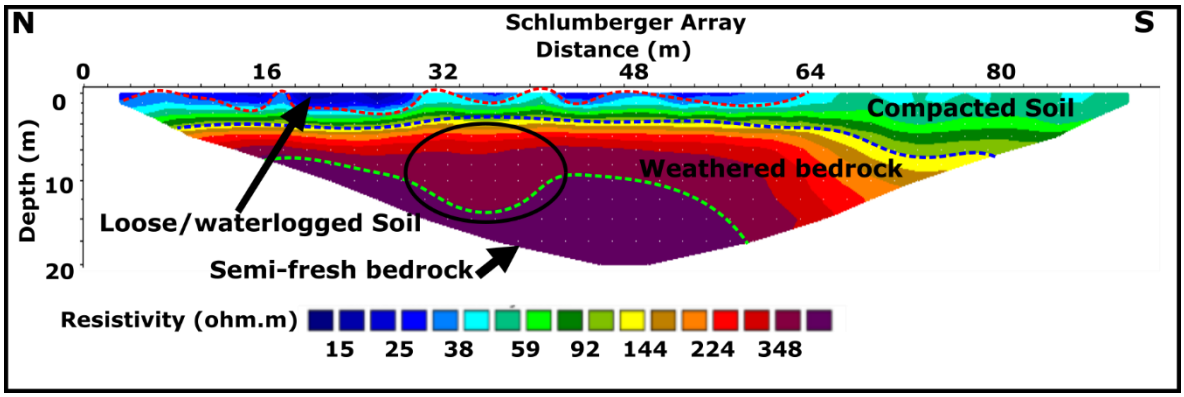

Figure 6.36: Interpreted resistivity section with marked weathering profiles and agricultural digging (black circle) for the Schlumberger array from resistivity line 3.

Similar to the previous sections, the waterlogged soil in the subsurface may be represented by the low resistivity above the red dashed line. The undulating nature of the resistivity bands between the red and

the blue dashed lines in the section may represent the compacted soil above which the water table may reside. The remaining region of the section may represent the highly weathered gabbronorite bedrock caused by water seeping into the subsurface as seen in the resistivity line 2 perpendicular to it. The southern portion of the section seems to be dipping towards the south and may delineate the edge of the gabbronorite bedrock.

Based on the resistivities in this section, the weathering surfaces can be identified (Table 6.16).

Table 6.16: Resistivity ranges and correlating thicknesses for the interpreted subsurface weathering profiles of the Schlumberger array (resistivity line 3).

Weathering profiles	Apparent resistivity range (Ohm.m)	Thickness (m)
Loose soil/ waterlogged soil	<100	< 6
Compacted soil	100-200	~4
Weathered bedrock	>200	>8

Modelling for resistivity line 3

A geological model for line 3 describes the geological subsurface based on the field data and the physical properties (Table 6.17) of the samples collected.

Table 6.17: Physical characteristics of lithological units in area 2 with their thicknesses found from interpreted data.

Lithological description	Resistivity properties (Ohm.m)	Estimated thickness (m)	Correlating reference
Loose soil	100	5	(Kausarian et al., 2014)
Compacted soil	100 – 200	9	
Highly weathered gabbronorite bedrock	200 – 800	10	See Table 5.4
Semi-fresh gabbronorite bedrock	> 800	> 2	

The geological model (created in Res2DMod) for resistivity line 3 of area 2 (Figure 6.37) reveals the expected weathering profile based on the resistivity data collected from the field. The model is exaggerated on both the horizontal and vertical scales, therefore, the depths reached on the resultant sections will be much higher and so will the recorded resistivities. The physical property measurements of the samples collected were too high to contribute to the subsurface. The model for this line, is perpendicular to the gabbronorite dyke and has been modelled to show the weathering profile of the gabbronorite dyke as well as the expected resistivities found with depth on the field data.

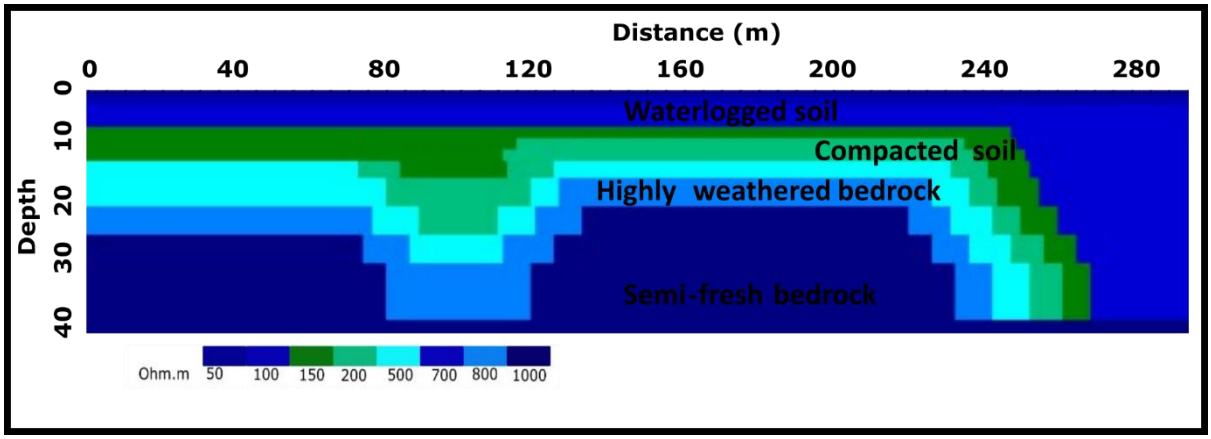

Figure 6.37: Geological model for resistivity line 3.

The forward models created for this geological model are only for the Schlumberger array. The Schlumberger array section (Figure 6.38 A) for the geological model shows a similar weathering profile to that of the field data section (Figure 6.38 B). The resistivities picked up in the modelled data are much higher and reach deeper into the subsurface. If only the first 19 m of the modelled data are considered, the weathering profile and the resistivities found in both the modelled data and the field data match very well.

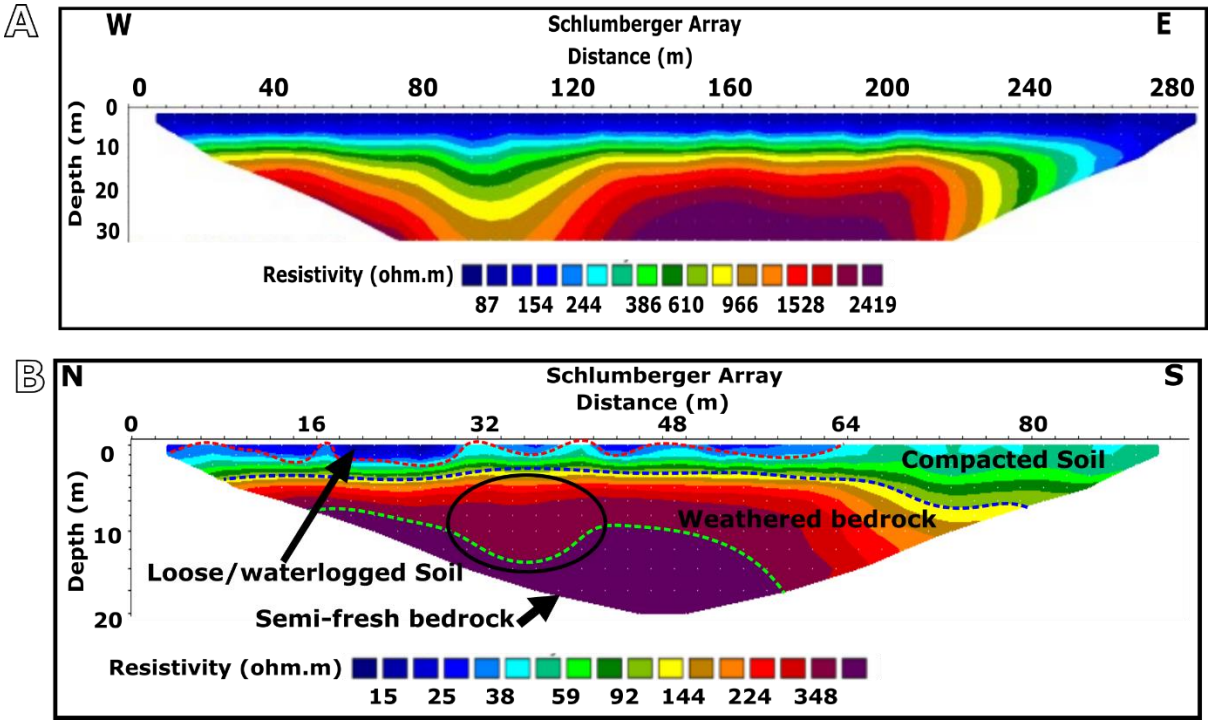

Figure 6.38: Schlumberger section, comparison of: A) Forward model of the geological model for resistivity line 3; B) Inversion of the measured data.

An integration of all of the collected data together with the models for area 2 can be found in Figure 6.39 below.

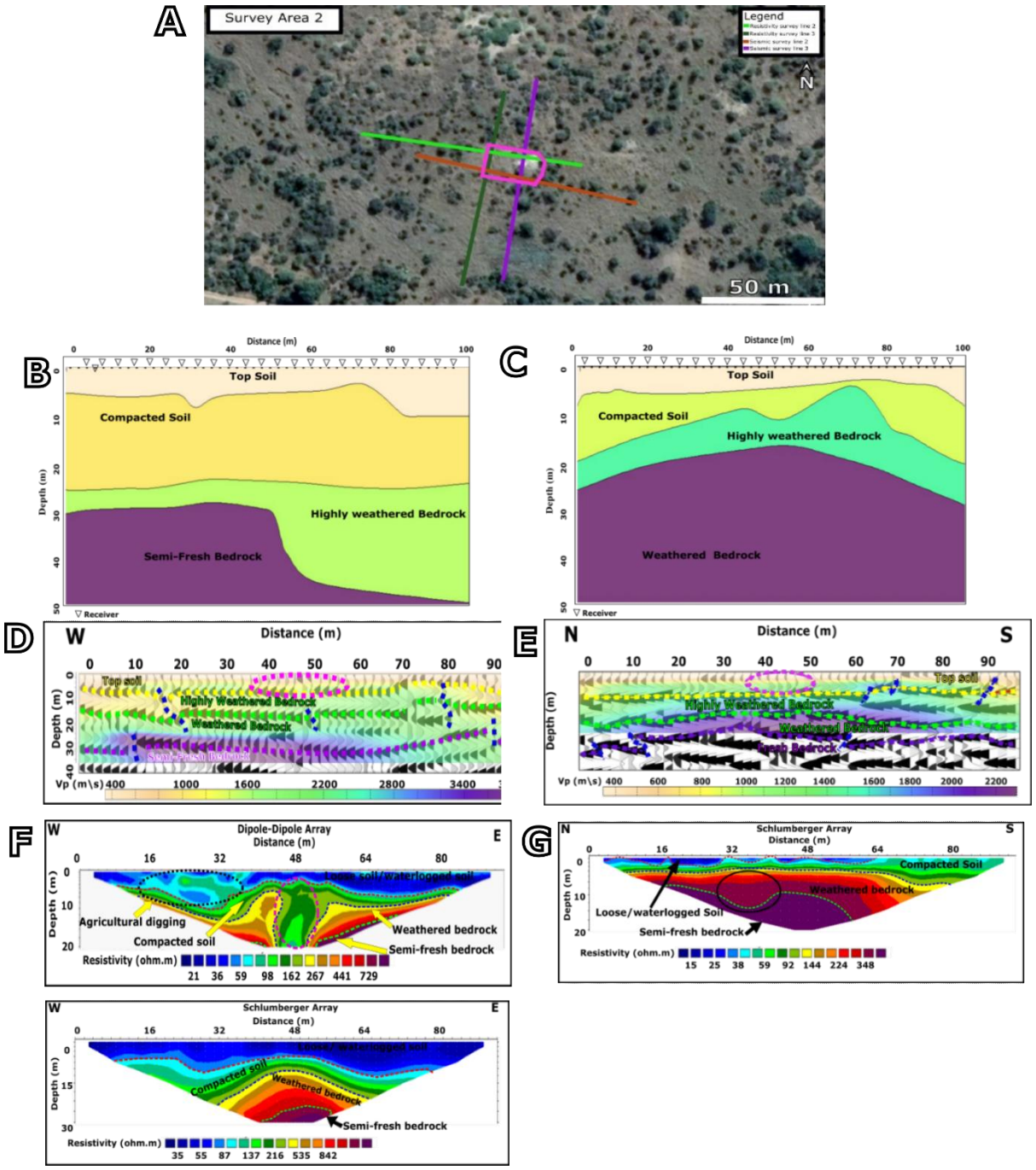

Figure 6.39: Integrated geophysical data for area 2. A) The surveys lines used to collect the data; B) Seismic models for the east-west trending line; C) Seismic models for the North-South trending line; D) Seismic data for the east-west trending seismic line; E) Seismic data for the North-South trending seismic line; F) Resistivity data for the east-west trending seismic line and G) Resistivity data for the North-South trending seismic line.

6.4 2D legacy seismic data analysis

The 4 sections that the legacy reflection seismic line was split into all overlap with one another giving a total mapping distance of 105 km.

The geological map shows that the seismic line runs over lithologies of the Transvaal Supergroup which contains highly resistant quartzite layers. These layers are responsible for mountainous peaks seen on either end of the elevation profile (red arrow in Figure 6.40). River valleys are easily identified by the valleys found along the elevation profile due to erosion and through the visible rivers found on Google Earth image. They are also useful in identifying the subsurface lithologies as they expose them further by weathering the overlying lithologies. These rivers also deposit the sediments that they carry which can lead to thick Quaternary deposits, as seen in the study area. Visible river channels have been identified (blue arrows in Figure 6.40) on the elevation profile for this seismic line (Figure 6.40).

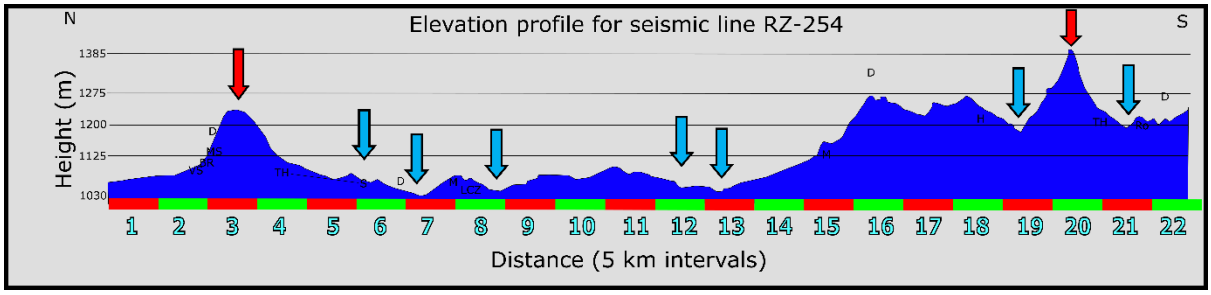

figure 6.40: Elevation profile for legacy seismic line RZ-254. Mountainous peaks represented by the red arrows and paleo river valleys represented by the blue arrows.

Observations are made by correlating the geological map with the seismic tomography of the legacy data (Figure 6.41) and described below. All refer to the P-wave velocities as seen on the seismic tomography. The thicknesses here are not the exact thicknesses of the respective lithological units. Since the stratigraphy of the Far Western Limb dips 9° towards the north in the southern rim and 25° towards the south in the northern rims of the basin (Engelbrecht, 1985), the thicknesses observed here are the apparent thicknesses.

6.4.1 P-wave refraction tomography analysis

Low P-wave velocity zones (< 500 m/s) identified on the seismic tomography are interpreted as the Quaternary cover in the area. When correlating the seismic line with the geological map, it clearly indicates that some of the low velocity zones correlate with the active rivers in the area. The rivers drain into the basin of the Far Western Limb and eventually deposit their sediments. The remaining low velocity zones can also be attributed to the rivers in the area, however those have dried up and run their course.

The Dominion Group (DG) outcrops in the northern end of the seismic line (border of section 1 and section 2) and shows shallow high velocities (~ 2000 m/s) within the seismic tomography. The outcrop is ~ 3 km wide on the surface according to the geological map. Moving along the seismic line, the Ventersdorp Supergroup (VS) follows the Dominion Group (section 2). It is ~ 3 km wide showing a high shallow seismic velocity of ~ 3000 m/s.

The Black Reef Formation (BR) is < 1 km wide showing a shallow seismic velocity of ~ 2000 m/s and follows the Ventersdorp Supergroup in section 2. A large deposit (~ 7 km wide) of the Malmani Subgroup (MS) follows which has a shallow velocity of ~ 4000 m/s (section 3).

The Timeball Hill Formation (TH) (~ 5 km wide) serves as a cap for the Malmani Subgroup and allows for the hill to form in the area (section 4). It has a seismic velocity of ~ 6000 m/s amongst its shallow lithologies. Thereafter is the Boshoek Formation (B) which is covered by the Quaternary cover due to a river flowing along it (section 4). The highest velocity is ~ 2000 m/s. The Hekpoort Formation (H) has a velocity ~ 2000 m/s, the Daspoort Formation (Das) has a velocity ~ 2500 m/s which host the Strubenkop Formation (S) which has a velocity ~ 1500 m/s, all occurring within a 4 km range (section 5). The overlying Silverton Formation (Sil) (~ 2 km wide) is covered by Quaternary sediments (section 6). The Magaliesberg Formation (M) is ~ 2 km wide and has a shallow velocity of ~ 3000 m/s (section 6). A large section of Quaternary cover is shown on for the next 6 km although the shallow velocities range 500 to 3000 m/s.

The next outcrop is again that from the Magaliesberg Formation (~ 1 km wide) with a shallow velocity of ~ 2000 m/s (section 7) which now alternates with the Lower Critical Zone (LCZ) of the Rustenburg Layered Suite that has a velocity of ~ 2300 m/s (sections 7 and 8). This is then followed by small (< 1 km wide) outcrops of the Rayton Formation (R) which have a seismic velocity of ~ 2000 m/s (within section 9 and 12). The high east-west trending linear magnetic anomalies that are found in the regional magnetic data (red D) display shallow seismic velocities ~ 1800 m/s (section 12). The Lower Zone (LZ) of the Rustenburg Layered Suite (~ 1 km wide) has a velocity ~ 2300 m/s (section 13).

The Magaliesberg Formation towards the end of the seismic line has a thick outcrop ~ 5 km wide split by a deep river deposit. It has a slightly lower velocity of ~ 2800 m/s (section 15). The Silverton Formation then follows which has a low velocity of ~ 2000 m/s and is ~ 2 km wide (section 16). A 1 km thick Daspoort Formation (section 17) with a shallow velocity of ~ 3000 m/s outcrops after a thick Quaternary deposit (~ 6 km wide). The ~ 4 km wide Hekpoort Formation with shallow velocities ~ 2500 m/s is rimmed by a 1 km wide Dwaalheuwel Formation (Dwa) with a velocity of ~ 2000 m/s (section 18).

This is followed by a narrow valley (~ 4 km wide in section 19) and a ~ 25 km wide deposit of the Timeball Hill Formation with a shallow seismic velocity of ~ 4000 m/s (section 20). Within the Timeball Hill Formation a < 3 km wide deposits of the Rooihoogte Formation (Ro) outcrops with a shallow seismic velocity of ~ 3500 m/s (section 21).

The mapped diabase on the geological map in the area (D) are less than a kilometre thick with high seismic velocities of 3500 m/s (section 22). They occur as spikes throughout the seismic line.

Table 6.18 summarizes the lithological correlation with the P-wave seismic velocities found in the Legacy seismic data and Figure 6.41 shows the geological map with the interpreted legacy seismic tomography for line RZ-254.

Table 6.18: Lithological correlation with the P-wave seismic velocities found in the legacy seismic data together with their horizontal thickness and location along the legacy seismic tomography.

Stratigraphic unit	Naming	P-wave velocity (m/s)	Thickness	Section number
Quaternary Cover		<500		
Lower Critical Zone	LCZ	2300		7 and 6
Lower Zone	LZ	2300	1	13
Rayton Formation	R	2000	<1	9
Magaliesburg Formation	M	3000	2	6
		2800	5	15
		2000	1	7
Silverton Formation	Sil	Covered by Quaternary	2	6
		2000	2	16
Daspoort Formation	Das	2500		5
		3000	1	17
Strubenkop Formation	S	1500		5
Dwaalheuwel Formation	Dwa	2000	1	18
Hekpoort Formation	H	2000		5
		2500	4	18
Boshoek Formation	B	2000		4
Timeball Hill Formation	TH	6000	5	4
		4000	25	20
Rooihoogte Formation	Ro	3500	<3	21
Malmani Subgroup	MS	4000	7	3
Black Reef Formation	BR	2000	<1	2
Ventersdorp Supergroup	VS	3000	3	2
Wits Supergroup	WS			
Dominion Group	DG	2000	3	1 and 2

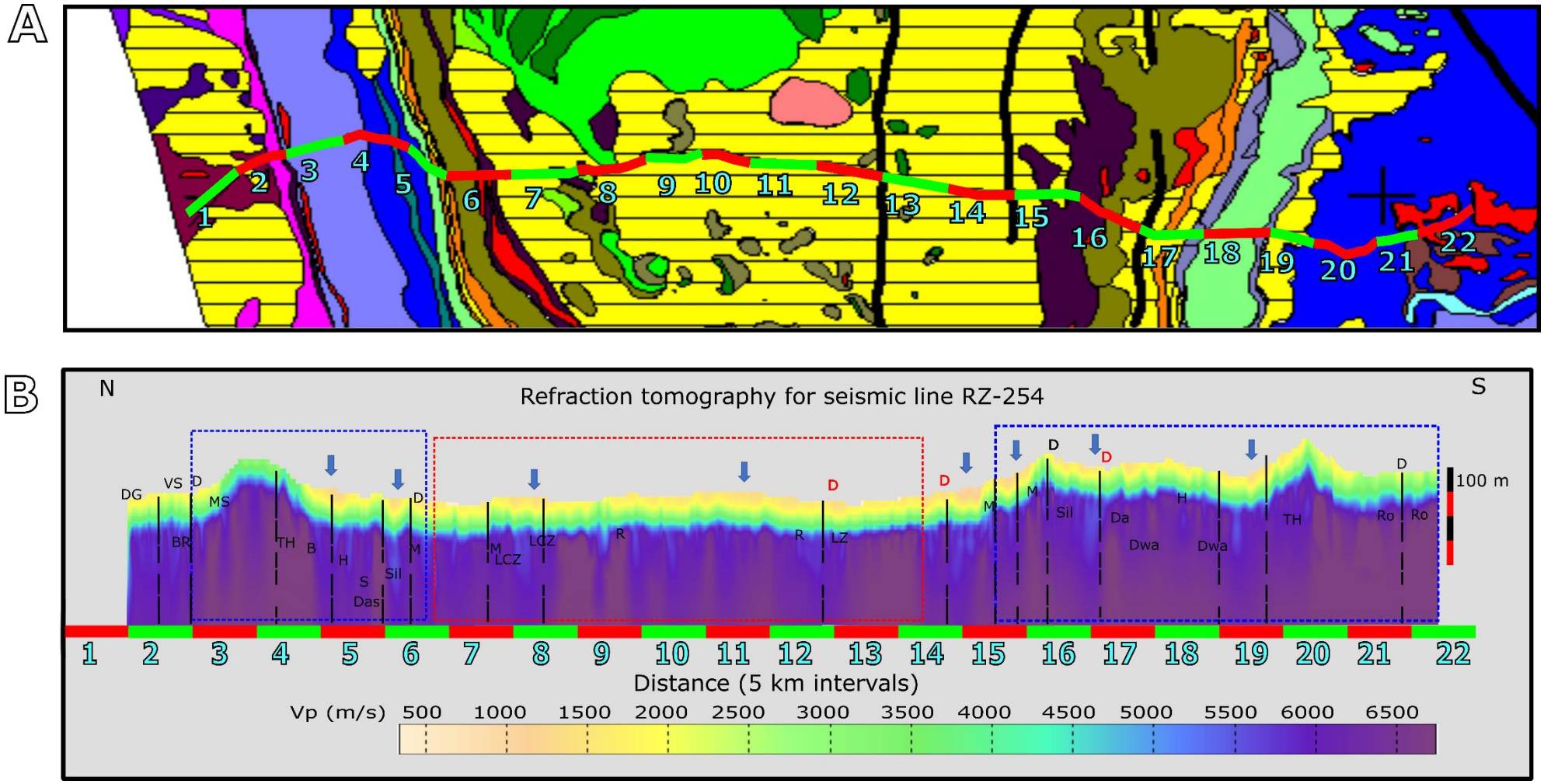

Figure 6.41: A) Geological map with legacy seismic line RZ-254 interpolated (with 5 km intervals marked in red and green), high magnetic anomalies from the regional magnetic data represented (black line); B) the interpreted legacy P-wave refraction seismic tomography of the RZ-254 seismic line. The blue boxes indicate the area where the Transvaal Supergroup lithologies occur. Similarly, the red box indicates with the Bushveld Complex lithologies occur. The blue arrows indicate where the paleo river valleys were found on the Google Earth imagery and the descriptions of the lithologies contacts are as in Table 6.18.

The seismic tomography for seismic line RZ 254 reveals clear mapping of the near surface P-wave velocities of the lithologies along the line. Through the correlation with the geological map of the area, a clear understanding of the lithologies that are responsible for the different seismic velocities has been found. The mapped geological dykes create sharp peaks throughout the seismic tomography.

6.4.2 Geological description of lithologies along the legacy seismic line

The Ventersdorp Supergroup consists of a volcano-sedimentary sequence. This explains why high seismic velocities in the tomography are close to the surface. The Black Reef Formation hosts a lower seismic velocity close to the surface as it mostly consists of marine deposits that are susceptible to a higher rate of weathering. The Malmani Subgroup consists mainly of dolomite which is very susceptible to weathering although due to the Timeball Hill Formation unconformably capping the dolomites, it allows for the dolomites to become more prominent and have less exposure to weathering.

Pretoria Group

The Rooihoogte Formation consists mainly of quartzites and mudrocks which allow for it to be more resistant to weathering and for the high seismic velocities to be found close to the surface.

The Timeball Hill Formation which also mainly consists of quartzites and mudrocks is responsible for the sharp peaks in the area. This formation also hosts the Bushy Bend Lava Member which contributes to the lithologies becoming more resistant to weathering as compared to the sedimentary rocks in the area.

The Boshoek Formation consists of the conglomerates and sandstones which are susceptible to high degrees of weathering. This is why the river runs over the outcrop and why there is a large Quaternary deposit over it.

The Hekpoort Formation consists of andesites which are less resistant to erosion. Which is why high seismic velocities are close to the surface. The Dwaalheuwel Formation consists of sandstones and conglomerates which weather away easily. This is why the velocities are much lower closer to the surface. The Strubenkop Formation consists of mudrocks which is why it has a low seismic velocity and causes valleys between the more resistant lithologies. The Daspoort Formation consists of sandstones therefore being more resistant to erosion and closer to the surface allowing for the high seismic velocities to be picked up on the seismic tomography. The Silverton Formation mainly consists of shales and therefore usually can be found in valleys where the rivers run over it. This is why it has thick Quaternary deposits over it. The Magaliesberg Formation mainly consists of sandstones and wherever it outcrops, there are high seismic velocities close to the surface as the sandstone is less

resistant to weathering. The Rayton Formation mainly consists of mudrocks which weathers away easily. This is why it has low velocities associated with the subsurface where it outcrops.

Rustenburg Layered Suite

The Lower Zone consists mainly of pyroxenites and harzburgites which are igneous rocks that have high seismic velocities. This allows for the high seismic velocities to be close to the surface. The Lower Critical Zone lithologies are ultramafic rocks which have high seismic velocities. The area where the outcrop is covered by a river which is why the seismic velocities close to the surface do not represent that of the ultramafic lithologies but rather river sediments.

6.4.3 Integration with the regional magnetic data

The regional magnetic survey over the Far Western Limb can assist in finding the extent of the lithological units by correlating the magnetic responses with the lithological units (Figure 6.42).

The majority of the sedimentary lithologies have low magnetic susceptibilities and therefore do not correlate with magnetic anomalies. While some of the sedimentary lithologies in the study area correlate with low magnetic anomalies, it was found that the lowest belonged to the Silverton Formation outcrop (green arrow, Figure 6.42).

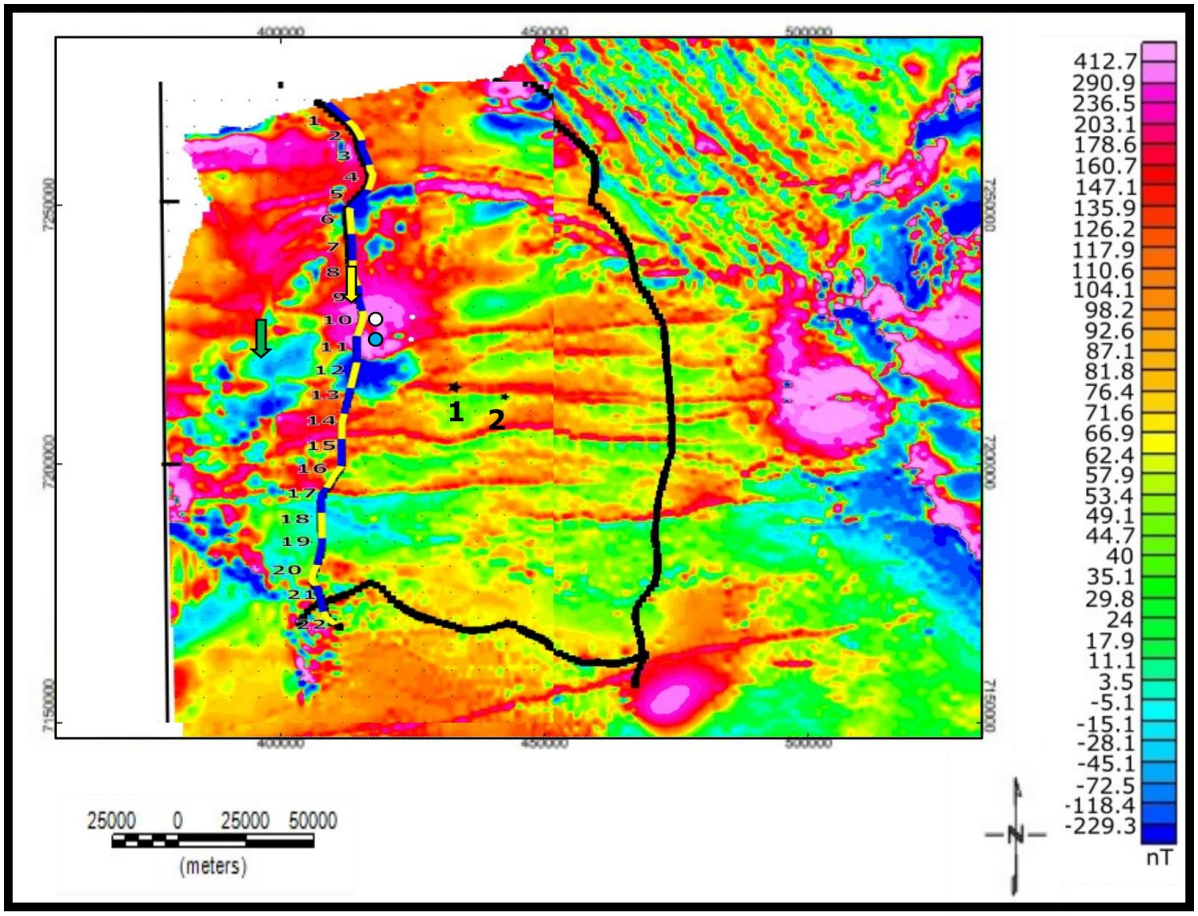

Figure 6.42: Regional magnetic data over the Far Western Limb with seismic line RZ254 running over it (5 km intervals marked in yellow and blue). Black stars represent the survey areas 1 and 2, blue and white circles represent boreholes in the area. Green and yellow arrow indicating Silverton Formation and Goudini Complex, respectively.

The late intrusives (diabase and Goudini Complex) in the area are associated with high magnetic anomalies on the regional magnetic map. The Goudini Complex outcrop on the geological map correlates with a ± 15 km wide magnetic high (> 290 nT) (magnetic anomaly from 9 to 11 indicated by the yellow arrow in Figure 6.42), which has a large (> 6 km) shallow high P-wave velocity (~ 6000 m/s) that is within the first 300 m of the subsurface found in the legacy seismic tomography (yellow arrow in Figure 6.43). This could overshadow the low magnetic anomalies of the Lower Zone lithologies and those from the diabase.

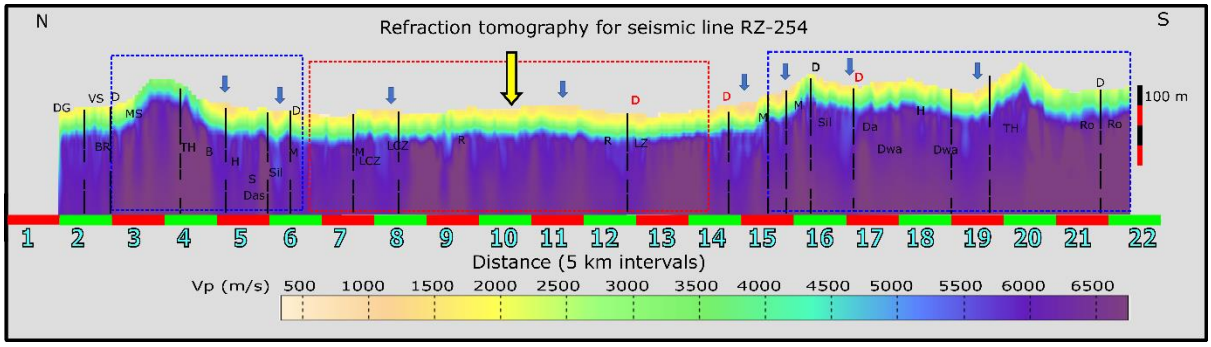

Figure 6.43: Interpreted seismic tomography for legacy seismic data showing the position of the Goudini Complex (yellow arrow) and the potential contact between the Transvaal Supergroup and the Rustenburg layered Suite in the North (red arrow).

This extension of the high magnetic anomaly of the Goudini Complex seen in Figure 6.42 could be evidence for the subsurface extent of the Goudini Complex in the study area.

The boreholes that exist close to the legacy seismic line are represented by the white (borehole 1) and blue circles (borehole 2) in Figure 6.42. Borehole 2 shows that the Lower Zone has a thickness of 790 m with the Marginal Zone having a thickness of 1050 m. This is then followed by the contact with the Transvaal Supergroup. These boreholes also occur just off the magnetic high associated with the Goudini Complex.

7 Discussion

This chapter integrates and discusses all of the geological and geophysical data that have been found collected and processed for area 1 and area 2. It also discusses the results and findings from the processing of the 2D legacy seismic tomography.

7.1 Geochemical vs physical property data

The anisotropic characteristics of the geological samples can be attributed to the modal abundance of the minerals present in each sample. Table 7.1 below shows the average seismic anisotropy that has been calculated for each samples together with the modal abundance of their minerals.

Table 7.1: Average seismic anisotropy together with the modal abundance for each geological sample collected.

Sample	Minerals and abundance	Average P-wave Anisotropy per sample (%)	Average S-wave Anisotropy per sample (%)
Area 1			
Quartzite	Quartz (90%) Matrix (10%)	12,67	19,91
Orthopyroxenite	Orthopyroxene (90%) Clinopyroxene (10%) Opague (5%)	34,15	62,78
Orthopyroxenite with higher degree of weathering	Orthopyroxene (90%) Clinopyroxene (10%)	32,50	36,49
Area 2			
Highly altered Gabbronorite	Biotite (80%) Plagioclase (15%) Opague (5%)	13,63	28,34
Altered Gabbronorite	Orthopyroxene (50%) Plagioclase (20%) Tremolite (30%)	34,36	32,88
Siltstone	Quartz (90%) Matrix (10%)	5,49	20,02
Siltstone with haematite	Haematite (75%) Quartz (20%) Pyrite (5%)	7,64	10,62
Veined and fractured siltstone	Quartz (95%) Matrix (5%)	14,77	33,56

7.1.1 Area 1

Quartzite

The grains mainly consist of quartz which are uniaxial. This shows that the quartz grain may account for some of the anisotropy found in the sample. The overgrowth and compaction of the quartz grains together with the granular texture, varying grain sizes and the minor fracturing in these samples may be the reason for the anisotropic behaviour in the acoustic measurements.

Orthopyroxenite

This orthopyroxenite contains clinopyroxene and orthopyroxene grains which are both biaxial minerals which may be a major factor in the high anisotropy measured in these samples. The varying shapes, sizes and fracturing of the grains cause the variations in the acoustic measurements as they provide a preferable orientation for the acoustic signals to move along which affects the seismic anisotropy.

7.1.2 Area 2

Gabbronorite

The highly altered gabbronorite contains biotite and plagioclase while the fresher gabbronorite contains othropyroxene which has altered into tremolite, plagioclase and clinopyroxene. All of these minerals are biaxial which may contribute to the anisotropy in the sample. The less weathered gabbronorite contains large (≈ 1mm) orthopyroxene crystals that do not necessarily show preferential orientations although they do have varying sizes which contribute to the higher anisotropy.

Siltstones

The siltstone contains mainly quartz grains which are uniaxial crystals. It does have fine laminations and evidence for secondary physical alteration which are the likely causes for the seismic anisotropy. These features do not present themselves strongly and are possibly the reason as to why the seismic anisotropy is small.

The siltstone with haematite consists predominantly of haematite nodules which are chemically isotropic. The remaining grains are quartz which are uniaxial and pyrite which is isotropic. The only physical contribution to the anisotropy in this sample is the laminations which have micro-fracturing and the irregular orientation of the pyrite showing that the anisotropy is not largely dependent on the layering in the sample.

This veined and fractured siltstone contains mostly quartz grains which includes quartz veins which have recrystalized, some of the grains such that they gained a larger size. This explains the significant increase in the seismic anisotropy of these samples as the grains have been physically altered within the veins.

The physical property data that has been collected were not on fresh samples that were retrieved from drill cores or physical outcrop. This would have significantly affected the seismic velocity and the resistivity measurements that were made on the samples. Weathering also plays a significant role in the seismic anisotropy. A higher degree of weathering causes a decrease in both the P- and S-wave seismic anisotropy. This could be attributed to the physical structure of the sample losing its integrity and the decrease in the size of the minerals with an increase in the degree of weathering.

7.2 Comparison of the physical properties with existing datasets

The density vs velocity plot of the previously identified gabbronorite samples from the Bushveld Complex lithologies (Shithigona et al., 2018) together with those found in the study area shows some correlation between the two datasets (Figure 7.1). The trendlines describing the 2 datasets (y=0.44x for the old data and y=0.317x for the new data collected) are within 27%. This shows that the gabbronorite samples collected from this study may not be representative of the lithologies from the Bushveld Complex. The weathered samples of the local gabbronorite show similar properties to magnetite bearing gabbronorites from the previous studies. They occur within 5% of the seismic velocities and densities of those found in the previous study (Shithigona et al., 2018). The fresh gabbronorite samples however do not show much of a correlation to the known Bushveld Complex data.

It is possible that the cause of the offset between the 2 datasets is that the samples were not fresh samples collected from outcrops and that the samples on which the previous data are collected were on a different unit within the Bushveld Complex.

Alternatively, the gabbronorite that has been surveyed may not belong to the Bushveld Complex. The MHS is known to contain sills and dykes that are chemically distinct from that of the Marginal Zone of the Bushveld Complex but still originating from the parent magma of the Bushveld Complex (Engelbrecht, 1990).

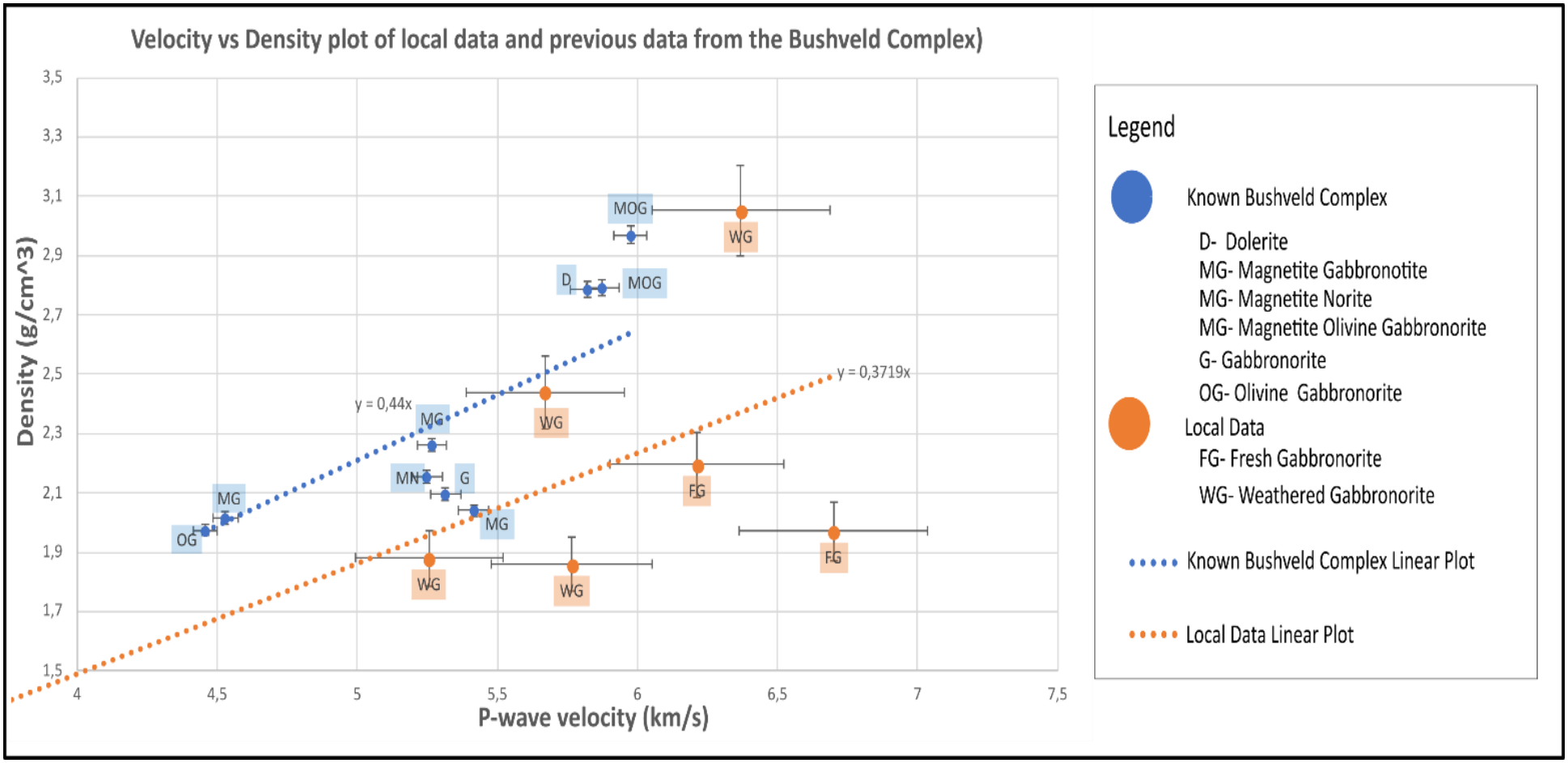

Figure 7.1: Velocity vs Density plot of the local data and the previous data collected from the Bushveld Complex (Shithigona et al., 2018). Trendlines show the relationship between the 2 dataset that have been plotted.

7.3 Correlation between the physical property and the field geophysical data

7.3.1 Area 1

The collected samples indicated that there are orthopyroxenite and quartzite lithologies present in the area. Based on the geophysical data collected in the area, it is clear from velocity and the resistivity values of the samples that the survey lines only cover orthopyroxenite.

The large orthopyroxene crystals seen in thin section are a sign that the parent magma had sufficient time to cool slowly. These crystals were then subjected to an increase in pressure due to the increase in the thickness of the overburden and eventually, the magma cooled forming the clinopyroxene intercumulus.

The quartzite collected was a boulder, therefore, contributes to the idea that there are no outcrops in the immediate area but may still represent the lithologies in the surrounding area. As mentioned, there are outcrops of it to the west of the study area therefore it may have been transported to the east. These samples did undergo secondary alteration and were also exposed to some tectonic activity as shown by the fractures. The compaction in the grains simply represents the increase in the overburden while the quartzite was being formed. The annealing indicates that it may have experienced an increase in temperature once it formed.

To the west of the study area, there is a large linear feature (orange dashed line, Figure 7.2) which may represent an unmapped fault and is picked up by the desktop studies. It is significantly continuous in the area and may correlate to one of the tectonic events that the area has undergone. This feature separates the outcrops of the pyroxenites to the north of the study area from the outcrop to its left (not seen in Figure 7.2) and may be linked to the tectonic event that caused the fractures in the quartzite sample.

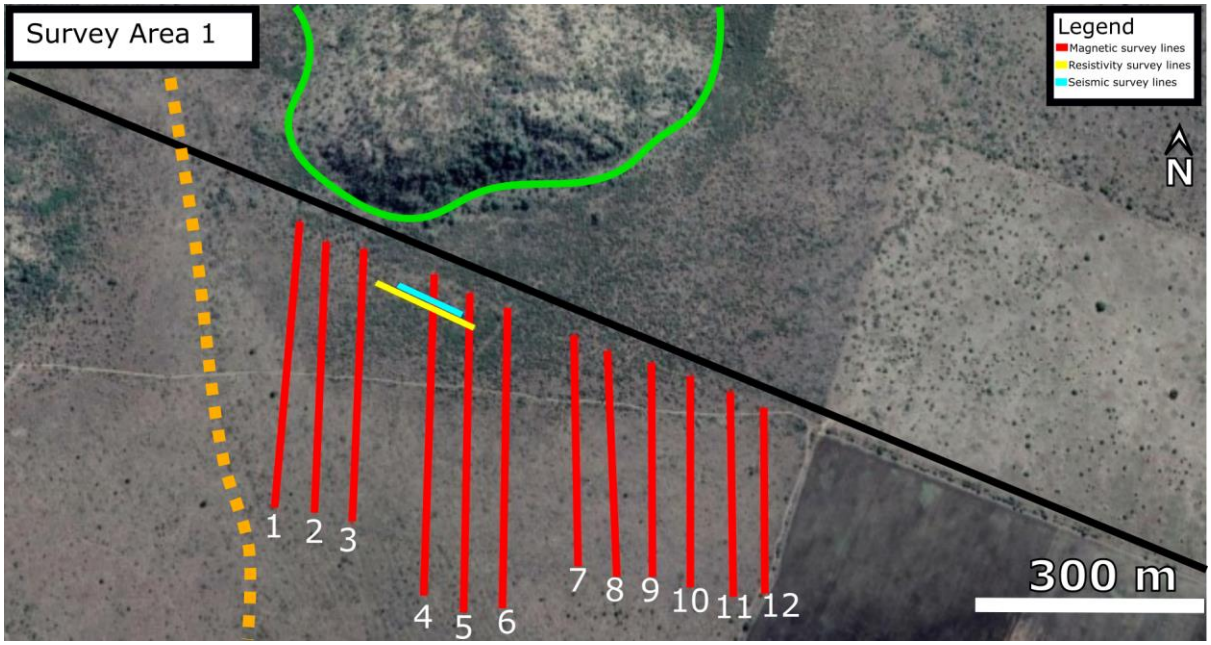

Figure 7.2: Survey lines for area 1 with the potential fault (orange dashed line) offsetting the outcrops to the North (green outline).

The weathering profiles and thickness ranges identified using seismic and resistivity methods correlate. The high seismic velocities correlate with the high resistivities and the low seismic velocities correlate with the low resistivities. This data shows that along the survey line the semi-fresh to fresh bedrock is picked up from below 10 m depth within the subsurface. Above this is compacted soil and the top soil. The semi-fresh bedrock shallows in the middle of the line (10 m depth compared to 20 m) or is just more strongly weathered near the start and end of the profile, showing variation in the weathering profile. The seismic tomography and the Schlumberger array section (Figure 7.3) show the extent of the weathering profile to reach further into the subsurface on the eastern side indicating that there is more weathering on the eastern side as compared to the western side.

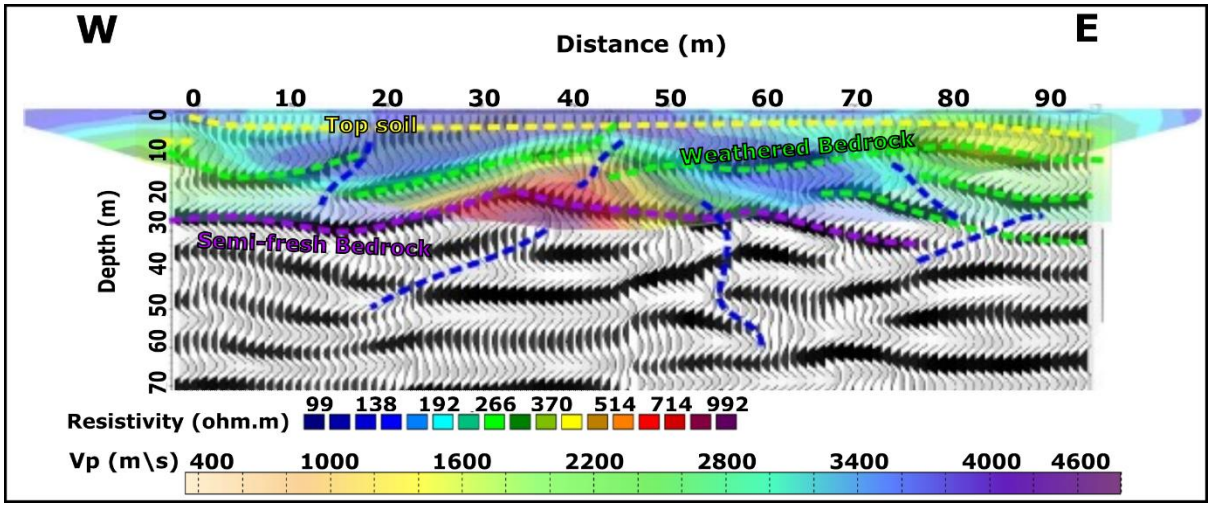

Figure 7.3: Integration of the seismic and resistivity profile for area 1 showing the weathered profiles within the subsurface and discontinuities (blue dashed lines).

This correlates with the magnetic data along the profile. Figure 7.4 shows the interpreted magnetic data. There is a higher magnetic response on the eastern side of the seismic and resistivity profile as compared to the western side of it. The susceptibilities of the samples show an increase in the susceptibility with the degree of weathering of the orthopyroxenite. This indicates that the higher magnetic anomalies surrounding the low magnetic anomalies in the northern regions of the magnetic data represented the weathered orthopyroxenite.

The two low magnetic anomalies in the centre of the magnetic data may indicate the extension of the orthopyroxenite into the subsurface or it may represent the quartzite which has a negative susceptibility. Since no quartzite samples were collected from outcrops, a conclusion cannot be made on the extent of it.

The high magnetic anomaly in the southern area of the magnetic map is interpreted as a dyke that matches one of regional east-west trending high magnetic anomalies. A potential contact with the underlying norite may be present in the data but there is no surface evidence to prove this.

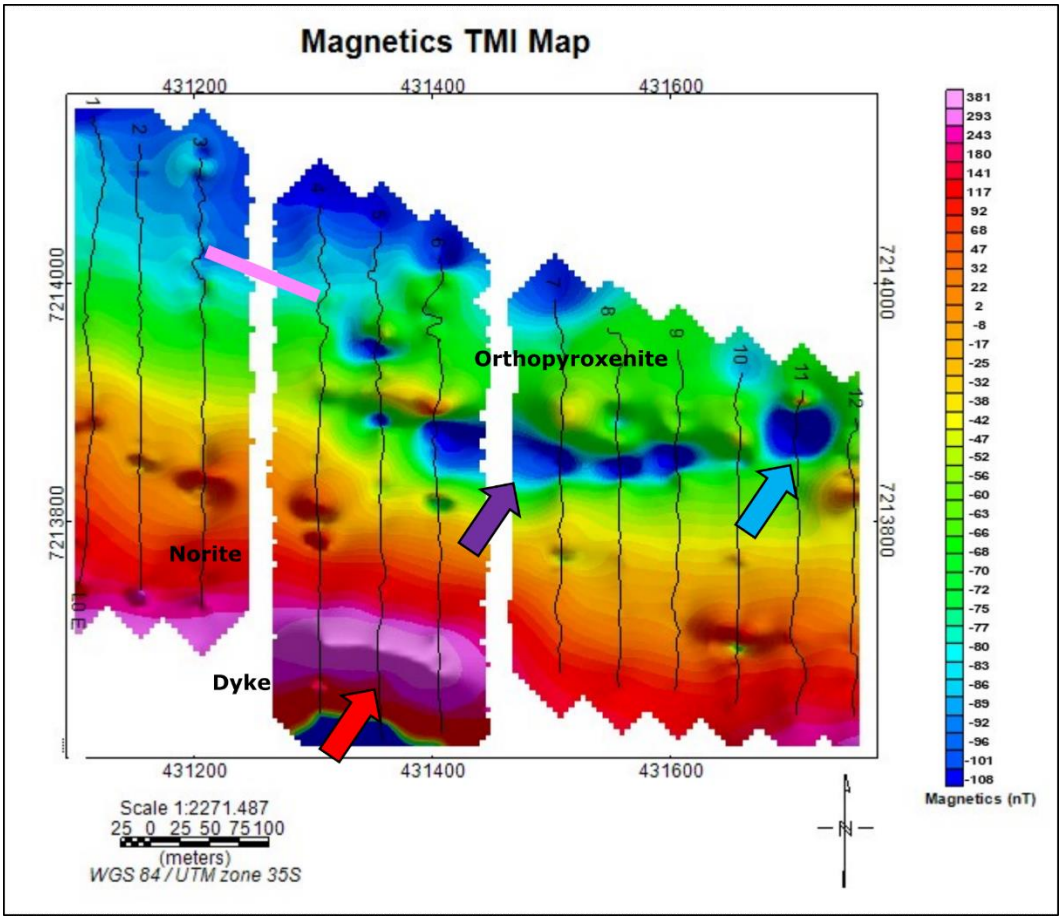

Figure 7.4: Interpreted magnetic data collected in area 1. Less weathered Orthopyroxenite (purple and blue arrows) with a higher degree of weathering (green surrounding these less weathered orthopyroxenites). East-west trending dyke (red arrow) identified in the regional magnetic data. Position of the seismic and resistivity lines (pink line) in the area and the magnetic survey lines (black lines).

7.3.2 Area 2

In this area gabbronorite and siltstone samples were retrieved through the agricultural digging that occurred along the profiles. The texture from the less weathered gabbronorite samples collected in the area indicates that the gabbronorite magma had sufficient time to form its large euhedral orthopyroxene crystals. Exsolution lamellae within the pyroxenes of the gabbronorite indicate they have undergone slow cooling. This was followed by rapid cooling to form the plagioclase intercumulus. The amount of weathering indicated by the highly altered samples shows that the gabbronorite has been exposed to surface conditions for a sufficient period.

The line 2 seismic data and the Schlumberger section (Figure 7.5) are ~ 13 m apart and still correlate well regarding their weathering profiles. The high seismic velocities correlate with the high resistivities and the low seismic velocities correlate with the low resistivities. The velocities and resistivities increase with depth and show that the majority of the samples in this area consist of the highly weathered

gabbronorite bedrock. The fresh gabbronorite bedrock in the area is expected to be below 25 m depth based on the strong reflections in the seismic section.

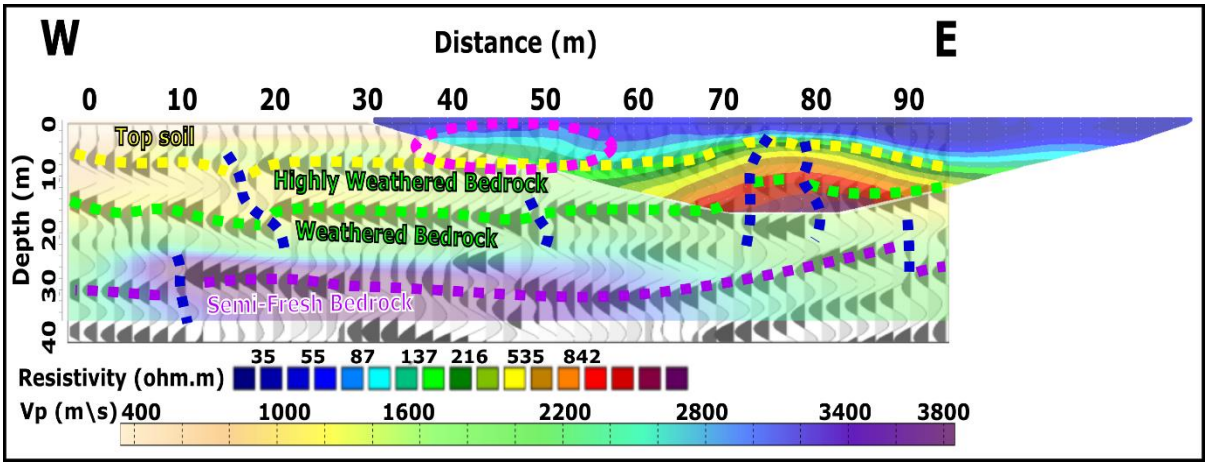

Figure 7.5: Integration of seismic line 2 with Schlumberger array for resistivity line 2 showing the weathered profiles within the subsurface, discontinuities (blue dashed lines) and the agricultural digging (pink dashed lines).

The Dipole-Dipole array section for line 2 (Figure 7.6) shows a greater resolution of the shallow lithologies as expected. The effect of the agricultural digging is clearer within the Dipole-Dipole data. It shows the region where the agricultural digging has occurred and an increase in the resistivities in that area (~100 Ohm.m) due to the gabbronorite samples being closer to the surface. The values do not correlate with the data from the gabbronorite samples collected from the area which have a much higher resistivity (~ 3000 Ohm.m), however, the majority of the gabbronorite samples were highly weathered at the surface. Similarly, the P-wave seismic velocities picked up in the agricultural digging are much lower (~ 2000 m/s) than the fresh gabbronorite bedrock (~ 6500 m/s).

The low resistivity (162 Ohm.m) in the centre of the section correlates with the low P-wave seismic velocity (~ 2000 m/s) in the seismic tomography. This feature may be the gabbronorite bedrock that has obtained a lower resistivity and seismic values due to the fractures found in the seismic data allowing water to erode the bedrock further into the subsurface.

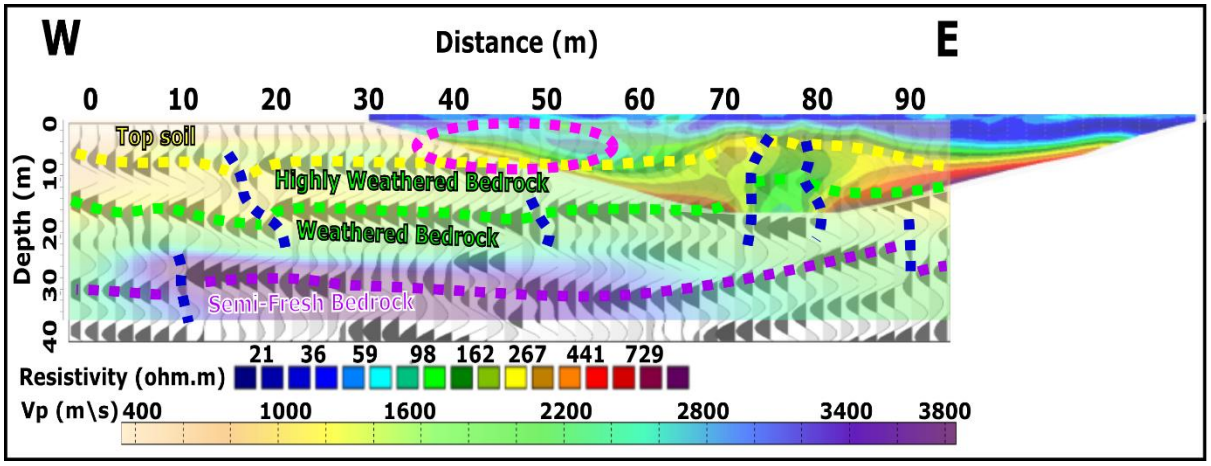

Figure 7.6: Integration of seismic line 2 with dipole-dipole array for resistivity line 2 showing the weathered profiles within the subsurface, discontinuities (blue dashed lines) and the agricultural digging (pink dashed lines).

The seismic velocities mapped along seismic line 3 are much lower than those along seismic line 2 as the seismic tomography did not reach as far into the subsurface however, the velocities match in the region where they overlap. Similar to seismic line 2, the bedrock consists of gabbronorite with the P-wave seismic velocities (> 2100 m/s) and resistivities (>350 Ohm.m) being lower than the fresh gabbronorite samples retrieved. The majority of the samples in this area consist of the highly weathered gabbronorite bedrock which reaches down to 20 m depth within the subsurface. This weathered layer is covered by the overburden and is only exposed once the overburden is removed, in this case the agricultural digging that occurred. It shows that the gabbronorite may be much closer to the surface than the surrounding lithologies in this small area.

Resistivity line 3 and seismic line 3 (Figure 7.7) are ~ 8 m apart and have weathering profiles that match well. Based on the seismic velocities and the resistivities that were recorded, it is likely that the fresh bedrock is below 25 m within the subsurface as seen in the seismic data. The fresh bedrock seems to be deeper on the northern and southern side of the profile in both surveys (>28 m). The effect of the agricultural digging can also be seen along these survey lines through the disturbance in the reflections within the seismic section, the low P-wave seismic velocities (~ 1200 m/s) and the disturbance seen in the resistivity data.

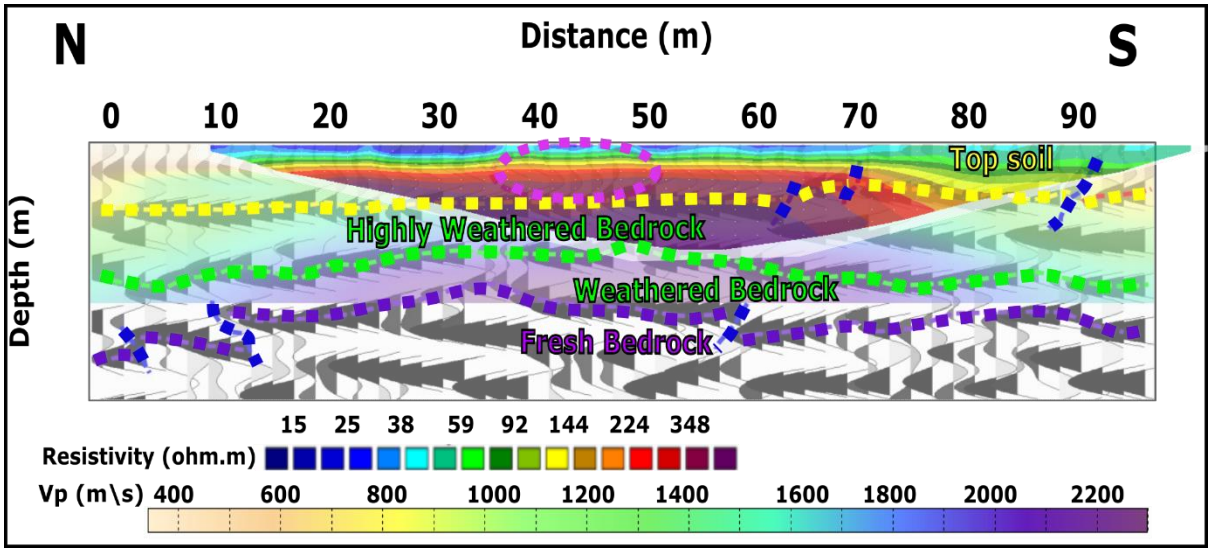

Figure 7.7: Integration of seismic line 3 with Schlumberger array for resistivity line 3 showing the weathered profiles within the subsurface, discontinuities (blue dashed lines) and the agricultural digging (pink dashed lines).

7.4 Assessment of the regional legacy seismic data

The thickness of the Quaternary cover varies across the study area. The legacy reflection seismic line has a thicker Quaternary cover (~ 80 m) while in areas 1 and 2 it is between 10 and 20 m. This shows that the Quaternary cover thins towards areas 1 and 2, which is not unexpected since the Rustenburg Layered Suite outcrops just north of these areas while it is mostly shallow along the seismic line.

The geological maps (Figure 7.8 A) integration with the 2D legacy seismic tomography of line RZ-254 (Figure 7.8 B) reveals the different lithological units and their shallow P-wave seismic velocities that are found along the line. When comparing the legacy reflection seismic section (Figure 7.8 C) to its tomography, the unknown lithological unit (green arrow in Figure 7.8 C) in the reflection seismic section falls within the region where the Rustenburg Layered Suite and the Rayton Formation lithologies outcrop. The remaining outcropping lithologies correlate well with the previous interpretations. The lithologies that outcrop along within the region of the unknown unit is specifically that from the Lower Zone (LZ) (dark green in Figure 7.8 A), the Lower Critical Zone (LCZ) (light green in Figure 7.8 A) and the Rayton Formation (R) (grey in Figure 7.8 A). This shows that the contact between the Rustenburg Layered Suite and the Transvaal Supergroup falls within this unit.

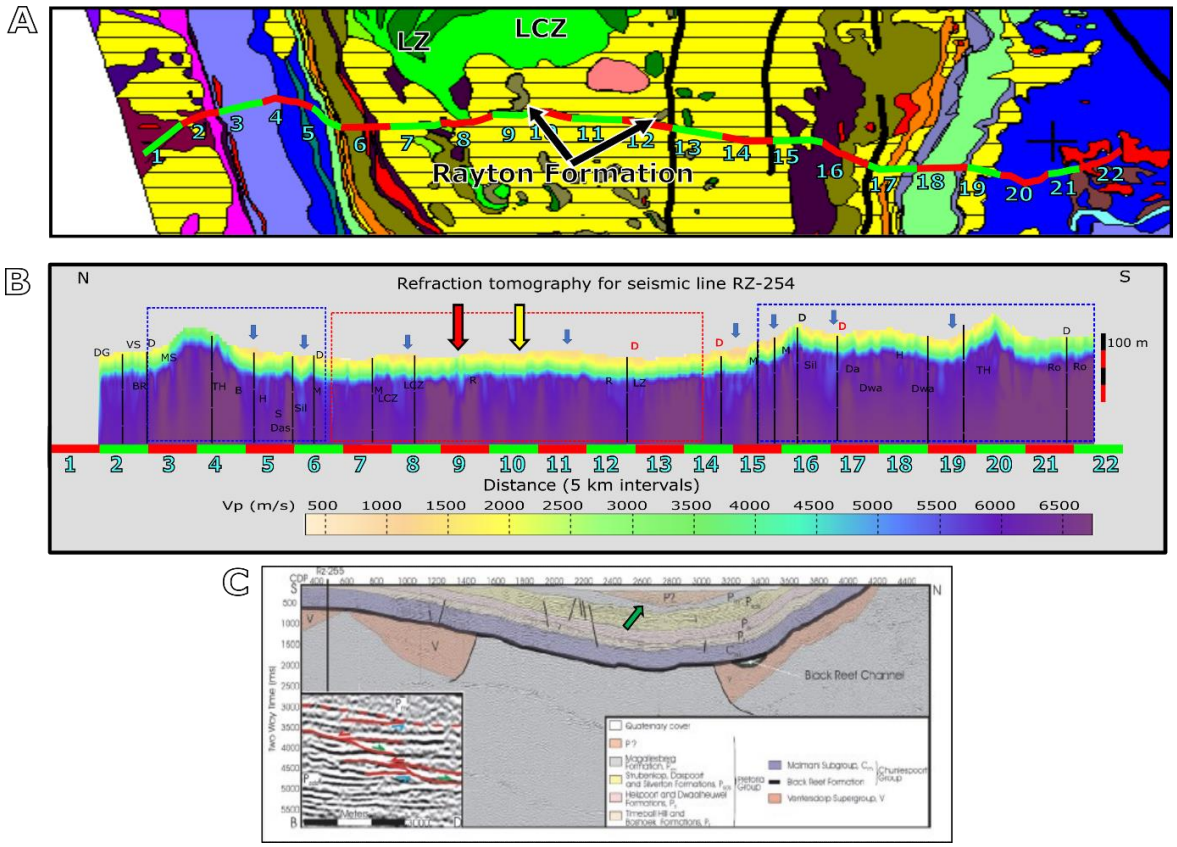

Figure 7.8: A) Geological map showing the lithologies present along the legacy seismic line; B) Interpreted refraction tomography of the legacy seismic line and C) 2D reflection seismic data tending North-South over the entire Far Western Limb (modified after Tinker et al., 2002) with the interpreted seismic data and the suggested lithologies responsible for the reflections present.

7.5 Integration of the legacy seismic data with the local geophysical survey

To identify the contact between the Rustenburg Layered Suite and the Transvaal Supergroup the physical property data and the ground geophysical survey need to be correlated with the 2D legacy seismic tomography of seismic line RZ-254.

Area 1 hosts orthopyroxenite that possibly belongs to the Lower Zone of the Rustenburg Layered Suite as seen from the surrounding outcrops in Figure 7.9. The lithologies that are close to the legacy seismic line along the same latitude are also from the Lower Zone (LZ) (dark green at 13, Figure 7.8 A). A comparison of the orthopyroxenite P-wave velocities that were measured in area 1 with the shallow velocities of the Lower Zone of the Rustenburg Layered Suite on the legacy seismic refraction tomography, show that the shallow subsurface velocities correlate. The Orthopyroxenite has a P-wave velocity of ~ 2000 m/s while the Lower Zone has a P-wave velocity of ~ 2300 m/s. This shows that the Lower Zone may be continuous all the way to area 1 from its contact seen along the legacy seismic tomography along line RZ-254 but is mostly covered by the Quaternary cover.

Figure 6.42 shows an east-west trending magnetic high (between 135 and 160 nT) on the regional magnetics map is picked up on the local magnetic data in area 1. The gabbronorite found in area 2 also occurs close to this east-west trending lineament and has a higher magnetic susceptibility than the siltstones it was collected with. This lineament is expected to extend west towards the legacy seismic line where a shallow high P-wave velocity feature is measured (~ 3000 m/s). This velocity correlates with that measured in this study for the gabbronorite samples, which were in excess of 3000 m/s. Various smaller outcrops of diabase (gabbronorite) were also mapped in close vicinity to area 2 as seen on a local geological map (Figure 2.3). This allows for the high magnetic anomaly to be considered as a gabbronorite that has be exposed in area 2.

This gabbronorite high magnetic anomaly could be similar to those from the Marico Hypabyssal Suite which are suggested to have formed near the contact between the Transvaal Supergroup and the Bushveld Large Igneous Province (Engelbrecht, 1990). The physical property data also show that the gabbronorite in area 2 may be chemically distinct from the Bushveld Complex contributing to the idea that the highly magnetic lineament is a gabbronorite dyke that formed separately from the Bushveld Complex.

Figure 7.8 A shows the high magnetic anomaly (between 12 and 13 in Figure 7.8 A) occurring close to outcrops of both the Rayton Formation of the Transvaal Supergroup and the Lower Zone of the Bushveld Complex. If this magnetic high is used to delineate the contact between the Rustenburg Layered Suite and the Transvaal Supergroup, a linear magnetic high (similar to the gabbronorite feature)

is expected on the northern side of the seismic tomography where the Lower Critical Zone is outcropping with traces of the Transvaal Supergroup close by.

A shallow, high P-wave seismic velocity feature can be found between the Lower Zone and Rayton Formation outcrop in the north (red arrow in Figure 7.8 B) similar to that between 12 and 13 (Figure 7.8 B). This could delineate an additional contact between the Transvaal Supergroup and the Rustenburg Layered Suite. Correlating this with the regional geophysical data shows at this position the high magnetic anomaly from the Goudini Complex which could be shadowing the lower magnetic response of the potential lineament.

Figure 6.42 also shows evidence for the potential extension of the Goudini Complex to the west of the 2D legacy seismic line RZ-254 as the magnetic anomaly where it occurs, extends towards the western side of the seismic line. This shows that it is possible that the Rustenburg Layered Suite can be found deep within the subsurface west of the legacy seismic line, with the Quaternary cover and Goudini Complex simply shadowing its presence.

The magnetic high lineament that has been surveyed in area 2 may be that originating from the MHS and has a gabbronorite composition which is known to form at the contact between the Rustenburg Layered Suite and the Transvaal Supergroup. Using the shallow P-wave velocity of this gabbronorite allows for a similar contact to possibly be identified towards the north. This allows for a potential contact between the Transvaal Supergroup and the Rustenburg Layered Suite to be delineated showing the possible extension of the Rustenburg Layered Suite to the west of its existing outcrop (red dashed outline, Figure 7.9) based on the extent of the outcrops in the geological map. Evidence for the potential contact is found in the legacy seismic tomography and its integration with the geophysical and physical property data that were collected.

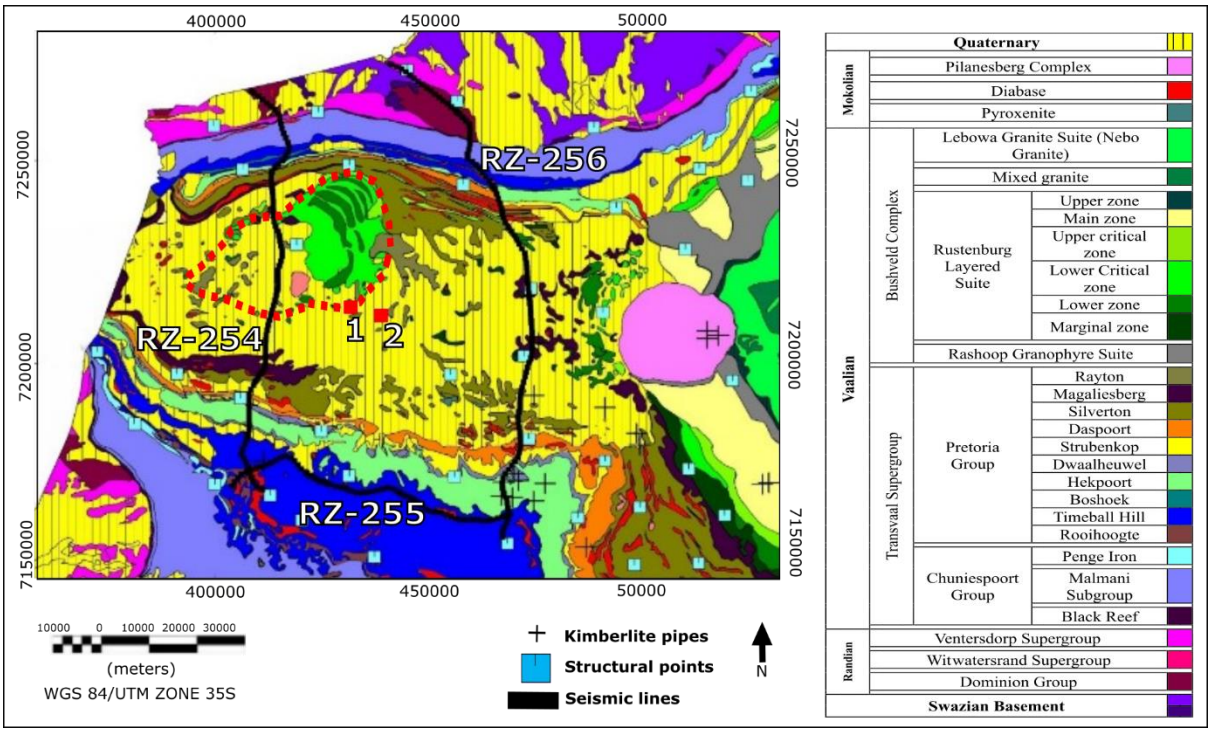

Figure 7.9: Regional geological map with the study areas and the potential contact between the Lower Zone of the Bushveld Complex and the Rayton Formation of the Transvaal Supergroup (Red dashed line).

8 Conclusion

The Far Western Limb of the Bushveld Complex is approximately 80 km west of the Western Limb of the complex. The continuity between these two limbs and their relationship with the surrounding Transvaal sedimentary rocks is not clear due to Quaternary cover. While deeper imaging is needed to understand this connection, in this study we investigate the near-surface to understanding shallow lithologies within the Far Western Limb.

This study shows that near surface reflection seismic, DC resistivity and magnetic surveys were successful in mapping the near surface lithologies and identifying the depth to the bedrock. The data shows that the bedrock in area 1 and area 2 reaches up to 20 m and 30 m respectively with some fractures offsetting the bedrock within the subsurface. Petrographic analysis of samples allowed for the identification of the orthopyroxenite bedrock in area 1 and the gabbronorite bedrock in area 2.

The physical properties helped constrain both the reflection seismic and DC resistivity models by obtaining the P-wave velocities and DC resistivity of both the fresh orthopyroxenite (5520 m/s and 1800 Ohm.m) and gabbronorite (6500 m/s and 3000 Ohm.m). The synthetic seismograms allowed for clear identification of the weathering profiles and the reflections found in the seismic sections.

The DC resistivity and reflection seismic modelling assisted in identifying the shape of the weathering profiles within the subsurface. Area 1 and 2 showed simple weathering of the bedrock along fractures within the subsurface.

These shallow studies will aid future exploration in this region for chromitites of the Critical Zone, as the thickness of the overburden is defined.

A legacy reflection seismic line that was previously used to investigate the deep structure in the Far Western Limb, was reprocessed and the shallow near-surface was focused on (first 100 m). This allowed for the identification of a previously unknown lithological unit on the interpreted legacy seismic section consists of lithologies from the Rayton Formation, the Rustenburg Layered Suite (Lower Zone, Lower Critical Zone and potentially the Marginal Zone).

A gabbronorite high magnetic anomaly that occurs close to the contact between the Rustenburg Layered Suite and the Transvaal Supergroup has been identified by integrating the physical property and geophysical data collected with the refraction tomography of the legacy seismic data. This allowed for the potential contact between the Rustenburg Layered Suite and the Transvaal Supergroup to be mapped towards the western side of its outcrop which is covered by Quaternary sediments. An in-depth

geochemical analysis of the gabbronorite samples is required to confirm these findings, together with more geophysical ground surveys on the western side of the existing outcrops.

This study shows potential evidence that the gabbronorite dykes from the Marico Hypabyssal Suite occur as highly magnetic lineaments in the regional magnetic data. More detailed ground geophysical studies are required to prove this concept and to gain a better understanding of the tectonic history in the Far Western Limb of the Bushveld Complex.

8.1 Recommendations

The following recommendations are made:

- Shallow boreholes should be drilled to see the thickness of lithologies that are sub-outcropping in the Far Western Limb. Boreholes drilled over the sub-outcropping Lower Critical Zone to the West could identify the thickness of the zone and therefore provide further insight into the continuity of the chromite sub-outcrops. A possible site would also be directly into the shallow region along the centre of the legacy seismic line to confirm the presence of the newly discovered lithological units that it may consist of.
- Extended reflection seismic, magnetic and DC resistivity surveys over areas where the Quaternary cover is thin will also allow for a further investigation of the subsurface lithologies. Reflection seismic, DC resistivity and magnetic surveys towards the South and West of the previous survey lines in Area 1 will be beneficial in investigating the relationship of the orthopyroxenite with its surrounding lithologies. Similar surveys around the survey lines in Area 2 will also provide more information on the extent of the gabbronorite dyke.
- Physical property measurements on core samples from the boreholes that have been drilled will allow for large scale model to be created and constrained to the local lithologies in the area.

9 References

- Armstrong, R, A., Compston, W., Retief, E, A., Williams, I, S., Welke, H, J., 1991. Zircon ion microprobe studies bearing on the age and evolution of the Witwatersrand triad: Precambrian Research, **53**, 243-266.
- Barton, E.S., Altermann, W., Williams, I.S. and Smith, C.B., 1994. U-Pb zircon age for a tuff in the Campbell Group, Griqualand West Sequence, South Africa: implication for Early Proterozoic rock accumulation rates: Geology, **22**, 343-346.
- Basson, I., 2019. Cumulative deformation and original geometry of the Bushveld Complex: Tectanophysics, **750**, 177-202.
- Beukes, N. J., 1987. Facies relations, depositional environments and diagenesis in a major Early Proterozoic stromatollitic carbonate platform to basinal sequence, Campbellrand Subgroup, Transvaal Supergroup, Southern Africa: Sedimentary Geology, **54**, 1-46.
- Beukes, N.J., 1983. Paleoenvironmental setting of iron formations in the depositional basin of the Transvaal Supergroup, South Africa. In: Trendall, A.F., Morris, R.C. (Eds.), Iron Formation: facts and problems. Elsevier, Amsterdam, 131-210.
- Biesheuvel, K., 1970. An interpretation of a gravimetric survey in the area west of the Pilanesberg in the western Transvaal: Geological Society of South Africa Special Publication, **1**, 266-282.
- Bilijon, W, J., 1976. Goud is nie waar dit gevind word nie! ‘n Oorsig van die struktuur, gesteentes en ertsafsettings van die Transvaal: Transactions of the Geological Society of South Africa, **79**, 155-167.
- Buchanan, P.C., 2006. The Rooiberg Group: The Geology of South Africa Chapter 12.
- Buchanan, P.C., Reimold, W.U., Koeberl, C., Kruger, F.J., 2004. Rb-Sr and Sm-Nd isotopic compositions of the Rooiberg Group, South Africa: early Bushveld-related volcanism: Lithos, **75,** 3-4, 373-388.
- Buick, I.S., Maas, R., Gibson, R., 2001. Precise U-Pb titanite age constraints on the emplacement of the Bushveld Complex: South Africa. Journal of the Geological Society, **158**, 1, 3-6.
- Burger, H. R., A. F. Sheenan and C. J. Jones, 1992. Introduction to applied geophysics- Exploring the shallow subsurface: W. W. Norton & Company, 1-308.
- Bumby, A, J., Eriksson, P, G., Catuneanu, O., Nelson, D, R., Rigby, M, J., 2012. Meso-Archaean and Palaeo-Proterozoic sedimentary sequence stratigraphy of the Kaapvaal Craton: Marine and Petroleum Geology, **33**, 92-116.
- Carney, J. N., Aldiss, D. T. and Lock, N. P., 1994. The Geology of Botswana: Geological Survey Botswana Bulletin, **37**, 1-13.
- Cawthron, R, G., McKenna, N., 2006. The extension of the western limb, Bushveld Complex (South Africa), at Cullinan Diamond Mine: Mineralogical Magazine, **70**, 3, 241-256.

- Cheney, E.S., Twist, D., 1991. The conformable emplacement of the Bushveld mafic rocks along a regional unconformity in the Transvaal succession of South Africa: Precambrian Research, **52**, 115-132.
- Clendenin, C.W., 1989. Tectonic influence on the evolution of the early Proterozoic Transvaal Sea, southern Africa. PhD thesis, University of the Witwatersrand, South Africa, 367.
- Clendenin, C.W., Henry, G., Charlesworth, E.G., 1991. Characteristics of and influences on the Black Reef depositional sequence in the eastern Transvaal South Africa: Journal of Geology, **94**, 321-327.
- Clendenin, C.W., Maske, S., Charlesworth, E.G., 1988. Resurgent basin development within an early Proterozoic successor basin sequence, southern Africa: Geocongress '88 Durban, South Africa, Abstract nos. 105-108.
- Coertze, F, J., Jansen, H., Walraven, F., 1997. The transition from the Transvaal Sequence to the Waterberg Group: Transactions of the Geological Society of South Africa, **80**, 145-156.
- Crockett, R. N., 1969. The geological significance of the margin of the Bushveld Basin in Botswana. Ph.D. dissertation: University of London, UK, 273.
- Crockett, R. N., 1971. Some aspects of post-Transvaal system tectogenesis in south eastern Botswana with particular reference to the Lobatse and Ramotswa areas: Geological Society of South Africa, **74**, 211-235.
- Crowson, P., 2001. Minerals Handbook 2000-01: Statistics and Analyses of the World's Minerals Industry: Mining Journal Books Ltd.
- Dentith, M., and S. T. Mudge, 2015. Geophysics for the mineral exploration geoscientist: Cambridge University Press, 89-96.
- Dobrin, B, M., 1976, Introduction to Geophysical prospecting: McGraw-Hill, Inc, 25-581.
- Eales, H.V., Cawthorn, R.G., 1996. The Bushveld complex. Cawthorn, R.G. (Ed.), Layered Intrusions. Elsevier, Amsterdam, 181–230.
- Engelbrecht, J, P., 1988. The tectonic setting of the Bushveld Complex in the Marico district, Western Transvaal, South Africa: South African Journal of Science, **84**, 770-774.
- Engelbrecht, J. P., 1985. The Chromites of the Bushveld Complex in the Nietverdiend Area: Economic Geology **80**, 4, 896-910.
- Engelbrecht, J. P., 1990. The Marico Hypabyssal Suite and the marginal zone of the Bushveld Complex in the Marico District, western Transvaal, South Africa: Journal of Geology, **93**, 2, 318-328.
- Eriksson, P. G., Van Der Merwe, R., Bumby, A. J., 1998. The Paleoproterozoic Woodlands Formation of eastern Botswana-northeastern South Africa: lithostratigraphy and relationship with Transvaal Basin inversion structures: Journal of African Earth Science, **27**, 349-358.

- Eriksson, P.G., Altermann, W., Hartzer, F.J., 2006. The Transvaal Supergroup and its precursors. In: Johnson, M.R., Anhaeusser, C.R., Thomas, R.J. (Eds.), The Geology of South Africa. Geological Society South Africa, Council for Geoscience, Pretoria, Johannesburg, 237–260.
- Eriksson, P.G., Reczko, B.F.F., Corner, B., Jenkins, S.L., 1996. The Kanye axis, Kaapvaal craton, southern Africa: a postulated Archaean crustal architectural element inferred from three-dimensional basin modelling of the lower Transvaal Supergroup: Journal of African Earth Sciences, **22**, 223-233.
- Eriksson, P.G., Schreiber, U.M., Van der Neut, M., 1991. A review of the sedimentology of the Early Proterozoic Pretoria Group, Transvaal Sequence, South Africa: implications for tectonic setting: Journal of African Earth Sciences, **13**, 107-119.
- Eriksson, P.G., Schweitzer, J.K., Bosch, P.J.A., Schreiber, U.M., Van Deventer, J.L., Hatton, C.J., 1993. The Transvaal Sequence: an overview: Journal of African Earth Sciences, **16**, 25-51.
- Eriksson, G. P., Altermann, W., 1998. An overview of the geology of the Transvaal Supergroup dolomites: Environmental Geology, **36,** 1-2, 179-188.
- Eriksson, G. P., Hattingh, J. P., & Altermann, W., 1995. An overview of the geology of the Transvaal Sequence and: Mineralium Deposita, 98-111.
- Fanchi, F., Brown, R., Mapeo, M., 2019. Evolution of an Archaean intracratonic basin: A review of the Transvaal Supergroup lithostratigraphy in Botswana: Earth-Science Reviews, **191**, 273-290.
- Geometrics, Inc., 2004. G-822A and G-823A & B CESIUM MAGNETOMETER Operation manual: https://www.aseg.org.au/sites/default/files/G-822A%20G-823A%20G-823B%20Operation%20Manual%20%28GR%29.pdf, accessed 1 November 2019.
- Hannah, J.L., Bekker, A., Stein, H.J., Markey, R.J., Holland, H.D., 2004. Primitive Os and 2316 Ma age for marine shale: implications for Paleoproterozoic glacial events and the rise of atmospheric oxygen: Earth and Planetary Science Letters, **225**, 43–52.
- Hanson, R, E., Gose, W, A., Crowley, J., Ramezani, S, A., Bowring, D, S., Hall, R, P., Pancake, J, A., Mukwakwami, J., 2004. Paleoproterozoic intraplate magmatism and basin development on the Kaapvaal Craton: age, paleomagnetism and geochemistry of ~1.93 to ~1.87 Ga post-Waterberg dolerites: South African Journal of Geology, **107**, 233-254.
- Harmer, R.E., Armstrong, R.A., 2000. New precise dates on the acid phase of the Bushveld and their implications: Abstract, Workshop on the Bushveld Complex, 18th-21st November 2000, Burgersfort. University of Witwatersrand, Johannesburg.
- Harmer, R.E., Farrow, D., 1995. An isotopic study on the volcanics of the Rooiberg Group: age implications and a potential tool: Mineralium Deposita, **30**, 188-195.
- Hartzer, F. J., 1995. Transvaal Supergroup inliers: geology, tectonic development and relationship with the Bushveld complex, South Africa: Journal of African Earth Sciences, **21**, 52l-547.

- Hatton, C.J. and von Gruenewaldt, G., 1989. The geological setting and petrogenesis of the Bushveld chromitite layers. In: Chromite deposits through time. (Eds.), C. W. Stowe: International Geological Congress, Washington, 109-142.
- Hatton, C.J., Schweitzer, J.K., 1995. Evidence for synchronous extrusive and intrusive Bushveld magmatism: Journal of African Earth Sciences, **21**, 579-594.
- Heiland, A, C., 1940. Geophysical Exploration: PENTICE-HALL, INC, 442-446.
- Henry, G., Clendenin, C.W., Charlesworth, E.G., 1990. Depositional facies of the Black Reef Quartzite Formation in the eastern Transvaal: Geocongress '90 (Cape Town, South Africa) Abstract nos. 230-233.
- Hollos, S., and J. R. Hollos, 2008. How to build a proton precession magnetometer: Exstrom Laboratories LLC, 150.
- Irvine, T. N., 1977, Origin of the chromitite layers in the Muskox intrusion and other stratiform intrusions: a new interpretation: Geology, **5**, 273-277.
- Jansen, H., 1982. The geology of the Waterberg Basin in Transvaal, Republic of South Africa: Memoirs of the Geological Survey of South Africa, **71**, 98.
- Kausarian, H., Shamsudin, A, R., Yaskar, Y., 2014, Geotechnical and Rock Mass Characterization Using Seismic Refraction Method at Kajang Rock Quarry, Semenyih, Selangor Darul Ehsan: Journal of Ocean, Mechanical and Aerospcace, **13**, 12-17.
- Key, R.M., 1983. The geology of the area around Gaborone and Lobatse, Kweneng, Kgatleng, Southern and South East Districts: District Memoir Geological Survey of Botswana, 5, 229.
- Kinnaird, J.A., 2005. The Bushveld Large Igneous Province: http://www.largeigneousprovinces.org/LOM.html [February 2020].
- Kinnaird, J.A., Kruger, F.J., Nex, P.A.M., Cawthorn, R.G., 2002. Chromitites of the Bushveld Complex – processes of formation and PGE enrichment: Economic Geology Research Institute Information Circular, **369**.
- Kruger, F.J. and Marsh, J.S., 1982. The significance of 87Sr/86Sr ratios in the Merensky cyclic unit of the Bushveld Complex: Nature, **298**, 53-55.
- Kruger, F.J., 2005. Filling the Bushveld Complex magma chamber: lateral expansion, roof and floor interaction, magmatic unconformities, and the formation of giant chromitite, PGE and Ti-V-magnetitite deposits: Mineralium Deposita **40**, 5, 451–472.
- Lenhardt, N., Erikkson, P, G., Catuneanu, O., 2012. Nature of and controls on volcanism in the ca. 2.32-2.06 Ga Pretoria Group, Transvaal Supergroup, Kaapvaal Craton, South Africa: Precambrian Research, **214-215**, 106-123.
- Mapeo, R.B.M., Armstrong, R.A., Kampunzu, A.B., Modisi, M.P., Ramokate, L.V., Modie, B.N.J., 2006. A ca. 200 Ma hiatus between the Lower and Upper Transvaal Groups of southern Africa:

SHRIMP U–Pb detrital zircon evidence from the Segwagwa Group, Botswana: implications for Palaeoproterozoic glaciations: Earth Planetary Science Letters, **244**, 113–132.

- Maré, L, P., Eriksson, P, G., Améglio, L., 2006. A plaeomagnetic study of the lower part of the Paleoproterozoic Waterberg, South Africa: Journal of African Earth Sciences, **44**, 1, 21-36.
- Milson, J., Eriksen, A., 2011, Field Geophysics: Wiley-Blackwell, 65-270.
- Rasmussen, B., Bekker, A., Fletcher, I, R., 2013. Correlation of Paleoproterozoic glaciations based on U–Pb zircon ages for tuff beds in the Transvaal and Huronian Supergroups: Earth and Planetary Science Letters, **382**, 173-180.
- Richards, R.J., 1987. A geological investigation of upper Transvaal sequence rocks in the northern portion of the Rooiberg Fragment: MSc thesis, University of Pretoria.
- Roberts, J.L., 1970. The intrusion of magma into brittle rocks. In: Newall, G. & Rast, N. (Eds.), Mechanism of Igneous Intrusion: Gallery Press, Liverpool, 287-338.
- Schreiber, U.M., Eriksson, P.G., Van der Neut, M., Snyman, C.P., 1992. Sedimentary petrography of the Early Proterozoic Pretoria Group, Transvaal Sequence, South Africa: implications for tectonic setting: Sedimentary Geology, **80**, 89-103.
- Schűrmann, L.W., Grabe, P-J and Steenkamp, C.J., 1998. Chromium: In Wilson, M.G.C. and Anhaeusser, C.R. (Eds.), The mineral resources of South Africa: Handbook, Council for Geoscience, **16**, 740.
- SCINTREX., 2012, CS-VL Caesium Vapour Magnetometer Sensor OPERATION MANUAL: https://scintrexltd.com/wp-content/uploads/2017/02/CS-VL-Manual-773701-Rev0.pdf, accessed 1 November 2019.
- Schweitzer, J.K., Hatton, C.J., de Waal, S.A., 1995. Regional lithochemical stratigraphy of the Rooiberg Group, upper Transvaal Supergroup: a proposed new subdivision: South African Journal of Geology, **98**, 245-255.
- Scoates, J.S., Friedman, R. M., 2008. Precise age of the plantiferous Merensky Reef, Bushveld Complex, South Africa, by the U-Pb zircon chemical abrasion ID-TIMS technique: Economic Geology, **103**, 465-471.
- Scoon, R.G. and Teigler, B. 1994. Platinum Group element mineralisation in the Critical Zone of the western Bushveld Complex: 1. Sulphide-poor chromitites below the UG2: Economic Geology, **89**, 1094-1121.
- Shithigona, O., Manzi, M.S.D., Ashwal, L.D., Bybee, G.M.,Webb, S.J., 2018. Experimental studies of elastic wave velocities and densities in rocks from the Bushveld Complex, South Africa: implications for deep reflection seismic surveys: South African Journal of Geology, **121**, 3, 311-326.

- Stamsnijder, J., 2017. New geochronological constraints on the Klipriviersberg Group:defining a new Neoarchean large igneous province on the Kaapvaal Craton, South Africa: Dissertation Geology, Lund University, 524, 21.
- Telford, M, W., Geldart, P, L., Sheriff, E, R., 1990, Applied Geophysics Second Edition: Cambridge University Press, 62-577.
- Tinker, J., de Wit, M., Brotzinger, J., 2002. Seismic Stratigraphic Constraints on Neoarchean-Paleoproterozoic Evolution of the Western Margin of the Kaapvaal Craton: South African Journal of Geology, **105**, 2, 107-134.
- Trendall, A.F., Compston, W., Williams, I.S., Armstrong, R.A., Amdt, N.T., McNaughton, N.J., Nelson, D.R., Barley, M.E., Beukes, N.J., de Laeter, J.R., Retief, E.A., and Thome, A.M., 1990. Precise zircon U-Pb chronological comparison of the volcano-sedimentary sequences of the Kaapvaal and Pilbara cratons between about 3.1 and 2.4 Ga: 3rd International Archean Symposium, Perth. Department of Geology, University of Western Australia, Perth, 81-83.
- Twist, D., 1985. Geochemical Evolution of the Rooiberg silicic lavas in the Loskop Dam area, southeastern Bushveld: Economic Geology, **80**, 1153-1165.
- Twist, D., French, B.M., 1983. Voluminous acid volcanism in the Bushveld Complex: a review of the Rooiberg felsite: Bulletin Volcanologique, **46**, 225-242.
- Viljoen, M.J., Schurmann, L.W., 1998. Wilson, M.G.C., Annhaeusser, C.R. (Eds.), Platinum-group metals: The Mineral Resources of South Africa, 6th edition. Council for Geoscience, 532–568.
- Visser, H. N., de Villiers, J., 1961. The geology of the area between Middelburg and Cullinan, Transvaal: Geological Survey-Department of mines, 62-68.
- Walraven, F., 1997. Geochronology of the Rooiberg Group, Transvaal Supergroup, South Africa. Information Circular: Economic Geology Research Unit, University of the Witwatersrand, Johannesburg, South Africa, **316**.
- Walraven, F., Martini, J., 1995. Zircon Pb-evaporation age determinations for the Oak Tree Formation, Chuniespoort Group. Transvaal Sequence: implications for Transvaal-Griqualand West basin correlations, South African Journal of Geology, **98**, 58–67.

Appendix A

Table 10.1.1: Dimensions of the physical property testing blocks.

Sample number	Dimensions of the samples (cm)			Volume ($cm^{3)}$
	X orientation	Y orientation	Z orientation	
S001A	2.3	2.1	2.2	10.626
S001B	2.1	2.1	2.2	9.702
S001C	2.4	2.3	2.1	11.592
S001D	2.4	2.1	2.2	11.088
S002A	2.5	2.1	1.9	9.975
S002B	2.4	2.0	1.8	8.64
S002C	2.4	2.1	2.4	12.096
S002D	2.3	1.7	1.8	7.038
S003A	2.2	2.0	2.0	8.8
S003B	1.9	2.0	2.0	7.6
S003C	2.2	2.0	1.7	7.48
S0042A	2.5	2.4	2.0	12
S0042B	2.5	2.4	2.1	12.6
S0041A	1.9	2.2	2.1	8.778
S005A	2.1	2.2	2.1	9.702
S005B	2.2	2.2	2.1	10.164
S006A	2.2	1.9	2.1	8.778
S006B	2.2	2.1	2.0	9.24
S007A	2.2	2.1	1.9	8.778
S007B	1.9	2.0	2.1	7.98
S008A	21	22	21	9.702